A measurement of the $ZZ \rightarrow \ell^{-}\ell^{+}\nu\bar{\nu}$ cross section at 8 TeV and limits on anomalous neutral triple gauge couplings with the ATLAS detector

Steven Adam Kaneti

Department of Physics

University of Cambridge

This dissertation is submitted for the degree of

Doctor of Philosophy

King's College October 2015

This thesis is dedicated to the memory of my grandparents Arthur and Lenore, and to the memory of my mother June, who was with me every step of the way.

Declaration

I hereby declare that except where specific reference is made to the work of others, the contents of this dissertation are original and have not been submitted in whole or in part for consideration for any other degree or qualification in this, or any other University. This dissertation is the result of my own work and includes nothing which is the outcome of work done in collaboration, except where specifically indicated in the text. This dissertation contains fewer than 65,000 words including appendices, bibliography, footnotes, tables and equations and has fewer than 150 figures.

Steven Adam Kaneti
October 2015

Preface

This thesis summarises the work undertaken by the author, as part of the Standard Model electroweak subgroup within the ATLAS collaboration. The work was performed over a four-and-one-half year period from October 2010 to March 2015. Studies were performed using ATLAS data taken during the full 2012 run at a centre-of-mass energy of $\sqrt{s} = 8$ TeV, corresponding to an integrated luminosity of $20.3\,\text{fb}^{-1}$.

The thesis first presents a brief evolution of the Standard Model in Chapter 1 up through the discovery of the Higgs boson. An introduction to diboson physics, including previous experimental results is given in Chapter 2.

A brief description of the LHC accelerator complex is given at the beginning of Chapter 3, followed by an overview of the ATLAS detector and the most relevant sub-systems for the *ZZ* analysis Section 3.2. The reconstruction of objects such as electrons, muons, jets, missing energy, and photons within ATLAS is described in Chapter 4. The specific definitions of the objects used to define the *ZZ* signal are given in Chapter 5. The author summarises the methods used to estimate the major backgrounds to the $ZZ \to \ell\ell\nu\bar{\nu}$ sub-channel in Chapter 6. The major results of the thesis are the first measurements of the *ZZ* production cross section at 8 TeV as measured by ATLAS. Limits at 95% confidence-level on anomalous neutral triple-gauge couplings obtained with data in the $ZZ \to \ell^-\ell^+\nu\bar{\nu}$ sub-channels are presented in Chapter 8.

The author's contributions to the *ZZ* analysis at 8 TeV are listed as follows:

- Chapter 5: The author was involved in the choice of selection requirements and object selection at the beginning of the 8 TeV analysis. Using the ATLAS event data model, the author implemented all the criteria to select *ZZ* events at reconstruction-level and particle-level. Full calibration using official ATLAS tools was performed on all objects.

- Chapter 6: The *Z*+jet background is expected to make a relatively small contribution to the total number of observed events. However, this background contribution is often difficult to estimate directly from simulation without a large number of events, and it can be subject to large uncertainties. A data-driven technique reweighting kinematics of photon to Z bosons is discussed. The author implemented full photon selecton and reweighting procedure to estimate the Z+jet background to the $ZZ \to e^-e^+\nu\bar{\nu}$ and $ZZ \to \mu^-\mu^+\nu\bar{\nu}$ sub-channels.

- Chapter 7: The ZZ production cross section is measured in a fiducial phase space and is then extrapolated to a larger, more inclusive phase space. The components used for the measurement of the cross section include quantities calculated from simulation of the signal process, such as the fiducial efficiency correction, C_{ZZ} (Section 7.3), and the acceptance, A_{ZZ} (Section 7.4). The author performed studies of the theoretical uncertainties on these quantities, in particular the QCD scale uncertainties, and the effects of parton showering on the acceptance. The author produced and analysed all samples for these studies independently. The author also developed the statistical model which is used to extract the measured cross sections. The statistical model accounts for correlations between uncertainties across different sub-channels and implements a fit to the data by a minimisation of a likelihood function profiled over all nuisance parameters. For the 7 and 8 TeV ATLAS ZZ analyses, the $ZZ \to \ell^-\ell^+\nu\bar{\nu}$ analysis has been combined with the $ZZ \to \ell^-\ell^+\ell^-\ell^+$ analysis to increase the precision of the cross section measurement. In addition to the measurement of the cross sections in the two $ZZ \to \ell^-\ell^+\nu\bar{\nu}$ sub-channels, the author measured cross sections in the three $ZZ \to \ell^-\ell^+\ell^-\ell^+$ sub-channels and a combined ZZ measurement in the sub-channels. A study was also performed by the author regarding a correction to the efficiency of the jet veto in the event selection, including theoretical and experimental uncertainties. The effect of the correction factor to the jet veto and its impact on C_{ZZ} and the cross sections in the $ZZ \to \ell^-\ell^+\nu\bar{\nu}$ sub-channels is given at the end of the chapter for comparison to the nominal values of the cross section.

- Chapter 8: Typically, ATLAS diboson measurements also include limits on anomalous neutral triple-gauge couplings. The author constructed a statistical model similar to that used for the cross section calculation to implement a procedure for frequentist limit setting based on a profile-likelihood statistic with data from the $ZZ \to \ell^-\ell^+\nu\bar{\nu}$ sub-channels. The author also contributed to the parametrisation of the signal yield via matrix element reweighting procedure and validation of the signal parametrisation.

Acknowledgements

When working on a project as large-scale as ATLAS is, there will naturally be many people to thank, especially given that the author list is longer than most academic papers.

This work would not have been possible without the help of Professor Andy Parker of the High Energy Physics Group at the Cavendish Laboratory. Andy was my point of contact before I decided to make the trip across the pond. It is hard to tell how a graduate student will evolve over the course of their degree, especially one who you've never seen face to face. I would like to thank Andy for always showing support for me and believing that I could contribute both to the group in Cambridge and the ATLAS collaboration.

I am tremendously indebted to my supervisor, Pat Ward, for all of her help over the last four and one-half years. Pat has been an incredible supervisor and has been rock-solid in terms of her support to help me put out the best work possible. She has always made herself available to discuss my work and seems to have a knack for knowing where bugs and problems turn up and finds ways to test ideas to fix those problems. I have learned a lot about what it means to make a precision measurement and the level of work and detail necessary in order to obtain a precise result. Pat has always provided solid advice and has always had my interests at the forefront. Thank you Pat. Richard Batley has effectively been a second supervisor, and his years of experience have helped me tremendously in understanding both Standard Model electroweak physics and beyond-Standard-Model searches.

I would also like to thank the high energy physics group in Cambridge, in particular Val Gibson for making my time with the HEP group such that I could focus on work and my thesis instead of more menial, but necessary tasks. I would like to thank Nick Barlow for answering my often-times obvious questions while sitting next to me for 18 months at CERN. Every graduate student I have come across has access to more senior students and post-docs that show them how to do their research in an effective way. For me, those excellent students/post-docs were Will Buttinger, Teng-Jian Khoo, John Chapman, and Dave Robinson. I would also like to thank Jonatan Rostén for working with me closely for several months to obtain the most interesting and important (and naturally, the most difficult to get right!) results. Thanks to Thibaut Mueller and Tom Gillam for taking time to talk about different background estimation techniques, and Dave Sutherland for many enlightening discussions about elementary particle theory. Thank you all for your help on topics ranging from analysis and statistics to the ATLAS software framework, SCT operation, and of course, missing energy. Many thanks to John Hill and Steve Wotton for providing a very reliable computing environment, no matter how many times we tried to outsmart the system and take it down with memory leaks, forked processes, poorly-written shell scripts, etc. The group has always been a pleasure to be a part of, and the cohesion of the group and the quality of the students and staff are the reasons it maintains its tremendous reputation.

I would also like to acknowledge people who have shown me how to become part of an ATLAS analysis and how to make an impact within such a large collaboration, especially during my time at CERN. I'd like to thank Nick Edwards (Edinburgh) and Andrew Nelson (UC Irvine) for showing me how one even begins to start undertaking an analysis within ATLAS from the very first steps like implementing a basic (or not so basic) selection. Many thanks are owed to Josh Kunkle (Maryland) for showing me the details of a very interesting method of photon reweighting and for many discussions on background estimation and other analysis techniques. I would like to thank Josh Moss (Cal State, Sacramento) and Sofia Chouridou (Athens) for taking on the role of analysis contact at 8 TeV. I'd also like to thank Jochen Meyer (Nikhef) and Vasiliki Kouskoura (BNL) for their help. Special thanks go to Lailin Xu (Michigan) for being available just about any time of day to discuss the analysis, and for putting in a tremendous amount of work for the both 7 and 8 TeV analyses. I would also like to thank Jake Searcy (Michigan) analysis for helping steer the 8 TeV analysis as the sub-convener.

I could not appreciate how important the college would be to my experience during my time at Cambridge. Indeed, some of my best friendships were formed with people I would only have met at a place as unique as King's College. I would like to thank my very good friend Krishna Kumar not only for providing me with a wonderful template used to write this thesis, but for being a tremendous friend willing to drop everything to help no questions asked. We speak the same language (computer code) and understand each other despite his refusal to put error bars on his plots. I would like to extend many thanks to my colleague and office mate for three years (in CERN and in Cambridge) Sarah Williams for teaching me how to adjust to life in Cambridge and how to make my time there (or pretty much anywhere) much more enjoyable. I would also like to thank Anna Bachmann, Renate Fellinger, Nicole Grunstra, Josh Keeler, Adam Reid, Alex Ridge, Max Hewkin-Smith, and all of my friends from King's College for keeping me inspired. The staff at King's have always been extremely kind and generous. I would like to thank Caroline White and Peter Pride for always finding time to answer my questions.

Lastly, I would like to thank my family. They have always been supportive and extremely proud of what I have done, even if at times I feel it doesn't merit any special attention. Many thanks to my cousin Alain Gabai-Maillet and his wonderful family in France for taking me in and making me feel welcome during my nearly 18 months away from Cambridge. Special thanks go to my aunts, uncles and cousins (big and little) in Turkey, Israel, and (of course) the USA for their support. This thesis represents the completion of a journey I started in 2005 when I returned to New York from Michigan to continue my studies, switching fields to physics from chemistry. My father, sister and step-mother never doubted the path I had set for myself and always pushed me forward to the next phase, with nothing but support and love. Their only serious question was, "when are you coming home?" The answer now is the same as it has always been: "Soon."

Abstract

This thesis presents a measurement of the ZZ diboson production cross section using the dataset from proton-proton collisions at $\sqrt{s} = 8$ TeV collected in 2012 by the ATLAS experiment at the Large Hadron Collider at CERN, corresponding to a total integrated luminosity of $20.3\,\text{fb}^{-1}$. The ATLAS detector and its component subsystems are described, with particular focus on the subsystems which have the largest impact on the analysis.

Events are selected by requiring one pair of opposite-sign, same-flavour leptons and large missing transverse momentum, consistent with on-shell ZZ production. Two separate measurements of the $pp \to ZZ$ cross section are made first in a restricted ("fiducial") phase space in each of the decay modes $ZZ \to e^-e^+\nu\bar{\nu}$ and $ZZ \to \mu^-\mu^+\nu\bar{\nu}$ to give:

$$\sigma^{\text{fid}}_{pp\to ZZ} = 4.99\,^{+0.76}_{-0.71}\,(\text{stat})\,^{+0.45}_{-0.38}\,(\text{syst})\,^{+0.20}_{-0.15}\,(\text{lumi})\text{ fb}\quad (ZZ \to e^-e^+\nu\bar{\nu})\,,$$
$$\sigma^{\text{fid}}_{pp\to ZZ} = 4.67\,^{+0.70}_{-0.65}\,(\text{stat})\,^{+0.45}_{-0.35}\,(\text{syst})\,^{+0.19}_{-0.15}\,(\text{lumi})\text{ fb}\quad (ZZ \to \mu^-\mu^+\nu\bar{\nu}).$$

A theoretical cross section is calculated using the POWHEGBOX and gg2VV generators. Using the detector acceptance and reconstruction efficiency extracted in each decay mode, the measurements are then extrapolated to a more inclusive phase space requiring both Z bosons to be in the mass range $66 < m_{\ell\bar{\ell}} < 116$ GeV to give two independent measurements of the $pp \to ZZ$ cross section:

$$\sigma^{\text{extrapolated}}_{pp\to ZZ} = 8.99\,^{+1.37}_{-1.28}\,(\text{stat})\,^{+0.95}_{-0.78}\,(\text{syst})\,^{+0.36}_{-0.28}\,(\text{lumi})\text{ pb}\quad (ZZ \to e^-e^+\nu\bar{\nu})\,,$$
$$\sigma^{\text{extrapolated}}_{pp\to ZZ} = 8.68\,^{+1.29}_{-1.21}\,(\text{stat})\,^{+0.94}_{-0.73}\,(\text{syst})\,^{+0.35}_{-0.27}\,(\text{lumi})\text{ pb}\quad (ZZ \to \mu^-\mu^+\nu\bar{\nu}).$$

Another measurement of the extrapolated cross section is made that incorporates events in two $ZZ \to \ell^-\ell^+\nu\bar{\nu}$ ($e^-e^+\nu\bar{\nu}$, $\mu^-\mu^+\nu\bar{\nu}$) and three $ZZ \to \ell^-\ell^+\ell^-\ell^+$ ($e^-e^+e^-e^+$, $e^-e^+\mu^-\mu^+$, $\mu^-\mu^+\mu^-\mu^+$) decay modes to give

$$\sigma^{\text{extrapolated}}_{pp\to ZZ} = 7.30\,^{+0.38}_{-0.37}\,(\text{stat})\,^{+0.28}_{-0.25}\,(\text{syst})\,^{+0.23}_{-0.20}\,(\text{lumi})\text{ pb}\,.$$

Finally, limits are set on anomalous neutral ZZV couplings ($V = Z, \gamma$), within an effective Lagrangian framework. The expected signal yield as a function of coupling strength is

obtained via a procedure which reweights events produced with aTGCs to events produced by Standard Model processes. Expected and observed limits on these parameters are set at 95% confidence-level, with observed limits in the range

$$\begin{aligned} -0.0047 < f_4^\gamma < 0.0046, -0.0040 < f_4^Z < 0.0040\,, \\ -0.0048 < f_5^\gamma < 0.0047, -0.0040 < f_5^Z < 0.0041\,. \end{aligned}$$

Table of contents

List of figures

List of tables

Chapter 1

Theoretical background

1.1 The Standard Model and its particle content

One of the crowning achievements in all of physics is the knowledge of elementary particle physics contained in the Standard Model. This model evolved over the course of several decades, and was refined in the light of new discoveries and confirmations of theoretical predictions. There is no real consensus amongst scientists on when the "modern" era of particle physics began, or exactly when the Standard Model actually became the one we know today, but the sum of the knowledge gained over nearly a century reflects an impressive understanding of nature and an ability to quantitatively predict a wide range of physical phenomena. One could argue that the modern era of particle physics was ushered in at the start of the 1970's [1]. This is for several reasons most notably (but certainly not restricted to) the discovery of the J/ψ in 1974 [2, 3], the discovery of weak neutral currents [4, 5], the discovery of the b quark in 1977 [6], and the discovery of the τ lepton [7]. Prior to the 1970's the only gauge theory to successfully stand up to experimental validation was quantum electrodynamics (QED). However, deep inelastic scattering experiments shed light on proton structure, and served to further validate quantum chromodynamics (QCD) as a gauge theory of the strong interactions. The twenty years that followed would see the milestone observations of the W and Z, the top quark [8], and the tau neutrino [9], which served to solidify the Standard Model as a model for fundamental particle interactions.

1.1.1 Particle content

The particle content of the Standard Model consists of spin-$\frac{1}{2}$ particles (fermions) called quarks and leptons, spin-1 gauge bosons, and a fundamental scalar (spin-0) boson, the Higgs particle. Each of the fermions and the charged gauge bosons has an associated anti-particle, that is, a particle with the same mass and spin, but with opposite electric charge. The symmetry group for the electroweak sector of the Standard Model is $SU(2) \otimes U(1)$. Chiral states are obtained as projections of the corresponding Dirac spinor ψ as follows

$$\psi_L = \frac{1-\gamma_5}{2}\psi, \quad \psi_R = \frac{1+\gamma_5}{2}\psi. \tag{1.1}$$

The symmetry transformations act differently on left handed and right handed fermion fields. Furthermore, the fermions are grouped by their transformations under $SU(2)$ (referred to as "weak isospin"), and posess quantum numbers Y and T_3, with the groupings referred to as "generations":

$$\begin{matrix} \begin{pmatrix} e \\ \nu_e \end{pmatrix}_{\mathrm{L}} & \begin{pmatrix} \mu \\ \nu_\mu \end{pmatrix}_{\mathrm{L}} & \begin{pmatrix} \tau \\ \nu_\tau \end{pmatrix}_{\mathrm{L}} \\ \begin{pmatrix} u \\ d \end{pmatrix}_{\mathrm{L}} & \begin{pmatrix} c \\ s \end{pmatrix}_{\mathrm{L}} & \begin{pmatrix} t \\ b \end{pmatrix}_{L} \end{matrix} \tag{1.2}$$

The matter field content of the Standard Model fermions and their representations under the gauge groups $SU(3)_C$, $SU(2)_L$, and $U(1)_Y$ is summarised in Table 1.1.

Field	$SU(3)_C$	$SU(2)_L$	$U(1)_Y$
$L = \begin{pmatrix} e \\ \nu_e \end{pmatrix}_{\mathrm{L}}$	**1**	**2**	-1
e_{R}	**1**	**1**	-2
$Q = \begin{pmatrix} u \\ d \end{pmatrix}_{\mathrm{L}}$	**3**	**2**	$\frac{1}{3}$
u_{R}	**3**	**1**	$\frac{4}{3}$
d_{R}	**3**	**1**	$-\frac{2}{3}$

Table 1.1 The matter field content of the Standard Model and their representations under the groups $SU(3)_C$, $SU(2)_L$, and $U(1)_Y$. The other generations of quarks and leptons follow the same patterns in terms of gauge quantum numbers. Bold numbers indicate multiplicity (singlet, doublet, triplet), in the fundamental representation. The last number represents the weak hypercharge quantum number Y.

The Standard Model lagrangian is invariant under the transformations of the form

$$U = e^{\frac{i\alpha^a \sigma^a}{2}}, \quad \{a = 1,2,3\} \tag{1.3}$$

where the σ^a are the generators of the $SU(2)$ group. The right-handed states

$$e_\mathrm{R}, u_\mathrm{R}, d_\mathrm{R} \qquad \mu_\mathrm{R}, c_\mathrm{R}, s_\mathrm{R} \qquad \tau_\mathrm{R}, t_\mathrm{R}, b_\mathrm{R} \tag{1.4}$$

are singlets with weak isospin $I = 0$ and are invariants under such a transformation. It should be noted that there are no right-handed neutrinos in the Standard Model; they are taken to be exactly massless in the Standard Model, although experiment has shown that they do have some small, but finite mass. For collider experiments, where centre-of-mass energies far exceed the small neutrino mass by several orders of magnitude, the massless approximation is valid.

1.2 Fundamental forces and the gauge bosons

Within quantum field theory, forces arise from exchange of particles resulting in momentum transfer. Currently, four fundamental forces are known; the gravitational force, the weak force, the electromagnetic force, and the strong force. Each force mediates a particular type of interaction. The gravitational force is by far the weakest, and is not accounted for by the Standard Model. The weak force is responsible for nuclear beta decays and flavour-changing processes involving quarks. Electromagnetic interactions are mediated by the photon. There are two gauge fields responsible for the electroweak interaction, W^a_μ and B^μ. The actual physical states are realised via transformations of the W^3_μ and B fields to give the fields Z^μ and A^μ. The field A_μ remains massless after symmetry breaking, and is identified as the photon, that is, the gauge boson with $U(1)_\mathrm{em}$ symmetry. The strong force is mediated by gluons, of which there are eight. Because gluons carry the charge (colour) corresponding to the force that is mediated, gluons may interact with each other. This is a consequence of the non-abelian nature of the $SU(3)_C$ gauge group which lies at the heart of QCD.

A guiding principle behind the Standard Model is that of local gauge invariance; a general Lagrangian can be obtained by identifying a global symmetry of the free-field Lagrangian, making the symmetry local by changing the covariant derivative ∂_μ with the gauge-covariant derivative D_μ (which contains a vector, or spin-1 field) and adding a kinetic term for the vector field [10].

1.3 Quantum chromodynamics

1.3.1 The gauge structure of QCD

As mentioned above, the theory which describes strong interactions is called quantum chromodynamics (QCD). Quantum Chromodynamics [11] is a gauge theory based on the special unitary group $SU(3)$. There are eight generators of the group $(3^2 - 1)$. The "charge" that is carried by the quarks and gluons is the colour charge. Stable hadrons exist as colour singlets and carry no net colour. This force serves to bind quarks into hadrons and acts to produce different dynamic reactions as quarks approach one another with given momentum and energy [12]. For a single flavour of quark, the QCD Lagrangian is given by [12, 13]

$$\begin{aligned}\mathscr{L}_{\mathrm{QCD}} = \sum_{a,b=1}^{3} [\bar{\psi}_a(x)(i\gamma^\mu[D_\mu]_{ab} - m\delta_{ab})\psi_b(x)] - \frac{1}{4}F_{\mu\nu}(x)\cdot F_{\mu\nu}(x) - \\ \frac{1}{2\lambda}(\partial_\mu \boldsymbol{A}^\mu(x)\cdot\partial_\nu \boldsymbol{A}^\nu(x)) + \sum_{A,B=1}^{8}(\partial^\mu \eta_A(x))\left[D_\mu\right]_{AB}\eta_B(x)\,.\end{aligned} \tag{1.5}$$

The eight components of the field strength tensor $F_{\mu\nu}$ and covariant derivatives are defined by

$$F^A_{\mu\nu} = [\partial_\mu A^A_\nu(x) - \partial_\nu A^A_\mu(x) - g_s f^{ABC} A^B_\mu(x) A^C_\nu(x)] \tag{1.6a}$$

$$\left[D_\mu\right]_{ab} = \delta_{ab}\partial_\mu + ig[\boldsymbol{t}]_{ab}\cdot \boldsymbol{A}_\mu(x) \tag{1.6b}$$

$$\left[D_\mu\right]_{AB} = \delta_{AB}\partial_\mu + ig\,[\boldsymbol{T}]_{AB}\cdot \boldsymbol{A}_\mu(x). \tag{1.6c}$$

Here $\boldsymbol{t}$ and $\boldsymbol{T}$ are the colour matrices of the quarks and gluons, respectively. The masses of the quarks appear as free parameters, and are different for each flavour.

The QCD Lagrangian posesses a number of symmetries. The well-established conservation laws of parity, charge conguation, quark number for each flavour follow from Equation 1.5. If the masses of the first-generation quarks (u,d) are equal, the Lagrangian is also invariant under the isospin $SU(2)$ flavour transformations $q \rightarrow Uq$ where $q = u,d$ only. This is referred to as chiral symmetry.

1.3.2 The running of the coupling constant and the renormalisation scale

In QCD, ultraviolet divergences must be removed by the renormalisation of the fields and couplings. Different schemes exist for this, including dimensional regularisation. Two common schemes, which are linked to dimensional regularisation are the (MS) scheme, and the modified (often referred to as $\overline{\mathrm{MS}}$) scheme [13].

The renormalisation formalism leads to the running of the coupling constants described by the renormalisation group equation

$$\frac{d\alpha_s(\mu_R)}{d\ln\mu_R^2} = \beta\left(\alpha_s(\mu_R)\right), \tag{1.7}$$

where the renormalisation group beta function $\beta(\alpha_s)$ has the perturbative expansion

$$\beta(\alpha_s) = -\left(b_0\alpha_s^2 + b_1\alpha_s^3 + b_2\alpha_s^4 + b_3\alpha_s^5 + ...\right), \tag{1.8}$$

where the coefficients depend on the number of active quark flavours, n_{Flavour}. It is here that the renormalisation scale μ_R appears, which can be interpreted as an energy scale. The coupling $\alpha_s(\mu)$ is the coupling constant describing strong interactions at an energy scale μ_R or a distance scale $1/\mu_R$. The leading order coefficients of the beta function are positive, which leads to a decrease of the coupling with increasing energy μ_R. At energies sufficiently above 1 GeV, the coupling is relatively small and perturbative calculations can be performed to predict cross sections. For energies around 1 GeV and lower, the coupling becomes large and perturbative methods break down and can no longer be applied to calculate observable quantities. There are many ways the strong coupling can be measured, including hadronic decays of the tau lepton, observed spectra of bound states of heavy quarks, and deep inelastic scattering. A convenient and often-used scale is the mass of the Z boson [14]. At this scale, the strong coupling constant takes a value $\alpha_s\left(m_Z^2\right) = 0.1184 \pm 0.0007$ [15].

1.3.3 The factorisation scale

The role of the factorisation scale, μ_F, in calculation of an observable is similar to the renormalisation scale. It is an arbitrary parameter and can be thought of as the scale which separates long and short-distance physics. For instance, a parton (quark or gluon), emitted within a hadron with a small transverse momentum less than this scale is absorbed into the parton distribution [13]. A parton emitted at a large transverse momentum relative to this scale is considered part of the short-distance hard process. An observable, such as a cross section, cannot be dependent on a choice of “artificial scale.” The more terms that are included in the perturbative expansion, the weaker the dependence of the observable on the factorization scale will be.

1.3.4 Observables at hadron colliders

As mentioned above, one of the features of QCD is that the ability to calculate processes involving high momentum transfer (Q^2) can be “factorised”; that is, it can be broken into a perturbatively calculable short-distance subprocess involving partons and non-perturbative quantities like parton distribution functions [10]. This has particular relevance at a high energy collider, where the centre-of-mass energy scales allow for perturbative treatment of partonic processes. Thus a cross section, for instance, of a final state X in proton-(anti)proton collisions, may be expressed as

$$\sigma_{pp\to X} = \sum_{i,j,k} \int f_i\left(x_1;\mu\right) f_j\left(x_2;\mu\right) \times \hat{\sigma}_{ij\to k}\left(x_1, x_2, z, Q^2, \alpha_s(\mu), \mu\right) D_{k\to X}\left(z,\mu\right) dx_1 dx_2 dz, \tag{1.9}$$

where $f_i(x_a,\mu)$ are the parton distribution functions for hadrons 1 and 2, respectively taken at some scale μ, $\hat{\sigma}_{ij\to k}\left(x_1, x_2, z, Q^2, \alpha_s(\mu), \mu\right)$ is the partonic cross section for a given process to go to intermediate state k, and $D_{k\to X}\left(z,\mu\right)$ represents the fragmentation function for an intermediate state k to go to a hadronic final state X. Here the factorization (μ_f) and renormalization (μ_r) scales are taken to be the same. Physical observables such as a cross section cannot depend on these scales, which means that any residual dependence on μ in $\sigma_{pp\to X}$ has to be of a higher order than that of the cross section calculation.

1.4 Spontaneous symmetry breaking and the Higgs mechanism

The idea of spontaneous symmetry breaking made a significant impact in the context of superconductivity as described in the theory of Bardeen, Cooper, and Schreiffer [16]. The idea of spontaneous symmetry breaking was introduced into particle physics in the 1960 by Y. Nambu [17], who argued that the low mass and low-energy interactions of pions could be understood as a reflection of a spontaneously broken chiral symmstery. In 1964, Englert and Brout introduced the concept of spontaneous breaking of gauge symmetries [18]. P.W. Higgs would publish two papers [19, 20] independently within months of the paper by Englert and Brout. Papers by Guralnik, Hagen and Kibble would appear as well in the months that followed. The paper by Higgs is the first to mention explicitly the existence of a massive scalar particle associated with the effective potential that determines the vacuum expectation value of the charged field [21]. The other major step towards formation of the Standard Model as it is known today was the incorporation by Weinberg [22] and Salam [23] of non-Abelian spontaneous breaking into Glashow's unified $SU(2) \otimes U(1)$ model of the weak and electromagnetic interactions. The Higgs mechanism, and electroweak unification, along with QCD form the foundation of the Standard Model as it is known today. A brief summary and discussion is given in the following sections.

1.4.1 A basic example of spontaneous symmetry breaking

Consider a real scalar field ϕ that interacts with itself. The Lagrangian density for this field is given by

$$\mathscr{L} = \frac{1}{2}\left(\partial_\beta \phi)(\partial^\beta \phi\right) - \frac{1}{2}\mu^2|\phi|^2 - \frac{1}{4}\lambda|\phi|^4. \tag{1.10}$$

Since ϕ occurs only in even powers, $\mathscr{L}$ is invariant under all transformations of the form $\phi \to -\phi$. Higher powers of the field ϕ would lead to infinities in physical quantities. The description of the system starts with the determination of the ground state followed by perturbations near the ground state (the vacuum is called the ground state while excited states are identified as particles).

The Euler-Lagrange equations for this system can then be solved. Since $\mathscr{L}$ is the difference in kinetic and potential energy, the two right terms may be identified with a potential V. The cases $\mu^2 > 0$ and $\mu^2 < 0$ must be considered. In the first case there is only a minimum, which is located at the origin. In the second case there are two minima at

$$\phi = \pm\sqrt{-\mu^2/\lambda}, \tag{1.11}$$

that is, there exists a degeneracy in the ground state.

Suppose that a particle is in its ground state. Then there is a degeneracy at the two minima. The symmetry of the system is "spontaneously" broken. The ground state value is denoted by v. To investigate the excited states near the vacuum, so the field ϕ is then set to

$$\phi(x) = v + \eta(x). \tag{1.12}$$

The state may be expanded about the point $\eta = 0$. Insertion into the Lagrangian density gives

$$\begin{aligned}\mathscr{L} =& \frac{1}{2}\left(\partial_\alpha \eta \partial^\alpha \eta\right) \\ &- \left[\frac{v^2}{2}\left(\mu^2 + \frac{1}{2}\lambda v^2\right) - +\eta v\left(mu^2 + \lambda v^2\right) + \frac{\eta^2}{2}\left(\mu^2 + 3\lambda v^2\right) + \lambda v \eta^3 + \frac{1}{4}\lambda \eta^4\right].\end{aligned} \tag{1.13}$$

Using the relationship for the ground state in Eq. (1.11) the terms proportional to η are eliminated, which gives

$$\mathscr{L} = \frac{1}{2}\partial_\alpha \eta \partial^\alpha \eta - \lambda\left(v^2\eta^2 + v\eta^3 + \frac{1}{4}\eta^4\right). \tag{1.14}$$

Since the system is only considered for small values of η, higher powers of η can be neglected. There remains a mass term of the form

$$m_\eta^2 = 2\lambda v^2 = -2\mu^2. \tag{1.15}$$

The choice of the minimum of the potentials enables one to ignore the constant terms. The two small terms proportional to η^3 and η^4 can be interpreted as as interactions. The case $\mu^2 < 0$ leads leads to spontaneous symmetry breaking and a mass for the boson.

Now consider the case of a complex scalar potential $\phi = \frac{1}{\sqrt{2}}\left(\phi_1 + i\phi_2\right)$ with the same Lagrangian density as before, and with ϕ_1 and ϕ_2 as scalar potentials. For $\mu^2 < 0$, one obtains a circle in the $\phi_1 - \phi_2$ plane. This describes the vacuum

$$\frac{1}{\sqrt{2}}\left(\phi_1^2 + \phi_2^2\right) = \frac{-\mu^2}{\lambda} = v^2. \tag{1.16}$$

If a vacuum state is at any point of the circle, the symmetry is broken. For example, one may arbitrarily choose the point $\phi_1 = \phi_2 = 0$ and expand v about this point. The next step is to make the transformations $\phi_1 = v + \eta\left(x\right)$ and $\phi_2 = \rho\left(x\right)$ with η and ρ purely real. These are used in the Lagrangian density:

$$\begin{aligned}\mathscr{L} =& \frac{1}{2}\left(\partial_\beta \rho\right)^2 + \frac{1}{2}\left(\partial_\beta \eta\right)^2 \\ &+ \mu^2\eta^2 - \lambda v\left(\eta\rho^2 + \eta^3\right) - \frac{\lambda}{4}\left(2\eta^2\rho^2 + \eta^4 + \rho^4\right) + \text{const.}\end{aligned} \tag{1.17}$$

There is now a mass term

$$m_\eta^2 = 2|\mu|^2 > 0. \tag{1.18}$$

It is worth noting that the corresponding term in ρ^2 disappears; there is a mass term for the η field but no corresponding mass term for ρ. This is an example the Goldstone theorem [24], which states that during a spontaneous symmetry breaking of a continuous, global symmetry, massless bosons with zero spin appear.

1.4.2 Spontaneous breaking of a local symmetry

A spontaneous symmetry breaking of a global symmetry for the case of a complex scalar field was discussed in the previous section. It was shown that the symmetry breaking yields massive gauge bosons at the expense of introducing massless scalars (Goldstone bosons). A very interesting case is that of spontaneous symmetry breaking of a local gauge transformation. The Lagrangian density for a complex scalar field is

$$\mathscr{L} = \left(\mathscr{D}_\beta \phi\right)^* \left(\mathscr{D}^\beta \phi\right) - \frac{1}{4} F^{\beta\gamma} F_{\beta\gamma} - \mu^2 \phi^* \phi - \lambda \left(\phi^* \phi\right)^2, \tag{1.19}$$

where $\mathscr{D}$ is the covariant derivative:

$$\mathscr{D} = \partial_\mu + igA_\beta. \tag{1.20}$$

The field-strength tensor $F_{\beta\gamma}$ can be ignored, as it does not contribute to the mass-generation mechanism. As before, the case $\mu^2 < 0$ is considered. There are four independent fields: the two scalar fields ϕ_1 and ϕ_2 and the two transverse polarization states of the vector field A_α. The scalar fields ϕ_1 and ϕ_2 are chosen as follows:

$$\phi_1 = v + h(x), \tag{1.21}$$

$$\phi_2 = 0. \tag{1.22}$$

One has the freedom to choose the rotation angle $\alpha(x)$ so that the second condition is satisfied. Substitution back into the Lagrangian gives

$$\begin{aligned} \mathscr{L} =& \frac{1}{2} \left(\partial_\beta h\right) \left(\partial^\beta h\right) + \frac{1}{2} g_1^2 v^2 A_\beta A^\beta - \lambda v^2 h^2 - \lambda v h^3 \\ & - \frac{1}{4} \left(\lambda h^4 - 4 g_1^2 v h A_\beta A^\beta - 2 g_1^2 h^2 A_\beta A^\beta + F_{\beta\gamma} F^{\beta\gamma}\right). \end{aligned} \tag{1.23}$$

The mass of the gauge bosons is then the root of the coefficient in front of the terms quadratic in the field $\frac{1}{2} A_\beta A^\beta$, that is:

$$m_A = g_1 v. \tag{1.24}$$

The Lagrangian density is gauge invariant but the vacuum is not, because a special point was chosen as the ground state.

1.5 The Standard Electroweak Model

Following the previous section, the Standard Electroweak Model of Glashow, Weinberg [22], and Salam is developed. Consider a complex doublet of fields:

$$\phi = \left(\phi^+, \phi^0\right), \tag{1.25}$$

with

$$\phi^+ = \frac{1}{\sqrt{2}}\left(\phi_1 + i\phi_2\right) \tag{1.26}$$

and

$$\phi^0 = \frac{1}{\sqrt{2}}\left(\phi_3 + i\phi_4\right). \tag{1.27}$$

As before, the potential $V\left(\phi\right)$ is invariant under the local gauge transformation of the field variable

$$\phi\left(x\right) \to \phi'\left(x\right) = \phi\left(x\right) e^{i\frac{\boldsymbol{\alpha}(x)\cdot\boldsymbol{\tau}}{2}}. \tag{1.28}$$

where $\boldsymbol{\alpha}\left(x\right)$ are three rotation angles which now depends on the coordinate x (thus it is a local gauge transformation), and the $\boldsymbol{\tau} = \left(\tau_1, \tau_2, \tau_3\right)$ are the Pauli spin matrices. Again, the case $\mu^2 < 0$ and $\lambda > 0$ is considered, then the minimum for $V\left(\phi\right)$ is given by:

$$\phi^\dagger\phi = \frac{-\mu^2}{2\lambda} = \frac{v^2}{2} = \frac{\phi_1^2 + \phi_2^2 + \phi_3^2 + \phi_4^2}{2}. \tag{1.29}$$

This implies that there are many ways to form the vacuum state. A point in $SU(2)$ space is chosen as follows:

$$\phi_1 = \phi_2 = \phi_4 = 0, \qquad \phi_3^2 = -\frac{\mu^2}{\lambda} = v^2, \tag{1.30}$$

with $T = 1/2$, $T_3 = -1$, and $Y = 1$, with T the weak isospin (and T_3 the third component) and Y is the weak hypercharge. This has the effect of breaking the $SU(2)$ symmetry. The field $\phi(x)$ can now expanded about this particular choice of vacuum:

$$\phi_0 = \frac{1}{\sqrt{2}}\begin{pmatrix} 0 \\ v \end{pmatrix}. \tag{1.31}$$

To examine the spectrum of particle states, gauge invariance allows the field to expanded about the ground state again using the ansatz

$$\phi_3 = v + h(x)\,. \tag{1.32}$$

The result is that of the four scalar fields, the only one that remains is the Higgs field $h(x)$.

The choice of an isospin doublet of complex scalar fields was made to break the $SU(2)$ symmetry. However, any choice of ϕ_0 which breaks the symmetry would have generated a mass for the corresponding gauge bosons. However, if the vacuum ϕ_0 is still left invariant by some subgroup of gauge transformations, then the gauge bosons of the subgroup will remain massless. The particular choice of weak isospin and weak hypercharge made above breaks both $SU(2)$ and $U(1)_Y$ symmetries. There is a relationship between the electric charge Q, the third component of the isospin under the $U(1)$ and weak hypercharge given by (in analogy to the Gell-Mann-Nishijima relation)

$$Q = T_3 + \frac{Y_H}{2}. \tag{1.33}$$

If the vacuum state ϕ_0 is to remain neutral,

$$Q\phi_0 = \left(T_3 + \frac{Y_H}{2}\right)\frac{1}{\sqrt{2}}\begin{pmatrix}0\\ v\end{pmatrix} = 0. \tag{1.34}$$

This means that the vacuum invariant under transformations of the form

$$\phi_0 \to \phi_0' = \phi_0 e^{i\alpha(x)Q}, \tag{1.35}$$

which correspond to those of the gauge group $U(1)_{em}$.

The masses of the gauge bosons are generated through the coupling of the Higgs field via the covariant derivative:

$$\left(\mathscr{D}_\mu\phi\right)^\dagger\left(\mathscr{D}^\mu\phi\right) = \phi^\dagger\left(ig\frac{\boldsymbol{\tau}}{2}\cdot\mathbf{W}_\mu + i\frac{g'}{2}YB_\mu\right)^\dagger\left(ig\frac{\boldsymbol{\tau}}{2}\cdot\mathbf{W}^\mu + i\frac{g'}{2}YB^\mu\right)\phi, \tag{1.36}$$

where the $\mathscr{D}$ are the covariant derivatives expressed in Eq. (1.20), $\boldsymbol{\tau}$ are the generators of the weak isospin $SU(2)$ symmetry, $\boldsymbol{W}(x)$ are three new gauge fields, and B is a gauge field contained in the field-strength tensor.

The masses of the gauge bosons can be found by inserting Eq. (1.31) into Eq. (1.36). The relevant term for the boson masses is

$$\begin{aligned}\frac{1}{8}&\left|\begin{pmatrix} gW_\mu^3+g'B_\mu & g\left(W_\mu^1-iW_\mu^2\right) \\ g\left(W_\mu^1+iW_\mu^2\right) & -gW_\mu^3+g'B^\mu \end{pmatrix}\begin{pmatrix}0\\ v\end{pmatrix}\right|^2 \\ &=\frac{1}{8}v^2g^2\left[\left(W_\mu^1\right)^2+\left(W_\mu^2\right)^2\right]+\frac{1}{8}v^2\left(g'B_\mu-gW_\mu^3\right)^2 \\ &=\frac{1}{2}v^2\left(gW_\mu^3-g'B_\mu\right)^2+0\left(g'W_\mu^3+gB_\mu\right)^2+\left(\frac{1}{2}vg\right)^2W_\mu^+W^{-\mu}, \quad (1.37)\end{aligned}$$

where

$$W^\pm=\frac{1}{\sqrt{2}}\left(-W^1\mp iW^2\right), \quad (1.38)$$

$$W^0=W^3. \quad (1.39)$$

The mass matrix of the neutral fields is off-diagonal in the (W_μ^3,B) basis. The last term of the last equation can be intrepreted as the mass term expected for a charged boson

$$\left(\frac{1}{2}vg\right)^2W_\mu^+W^{-\mu}, \quad (1.40)$$

therefore, the mass of the $W^\pm$ is given by

$$m_{W^\pm}=\frac{1}{2}vg. \quad (1.41)$$

One of the eigenvalues of the 2×2 matrix is zero. The physical fields Z_μ and A_μ diagonalise the mass matrix. The normalised neutral mass eigenstates are therefore

$$A_\mu=\frac{g'W_\mu^3+gB_\mu}{\sqrt{g'^2+g^2}}, \quad (1.42)$$

$$Z_\mu=\frac{g'B_\mu+gW_\mu^3}{\sqrt{g'^2+g^2}}, \quad (1.43)$$

with

$$m_Z=\frac{1}{2}v\sqrt{g^2+g'^2}, \quad (1.44)$$

and

$$m_A = m_\gamma = 0. \tag{1.45}$$

The relations

$$\cos\theta_W = \frac{g}{\sqrt{g'^2 + g^2}}, \tag{1.46a}$$

$$\sin\theta_W = \frac{g'}{\sqrt{g'^2 + g^2}}, \tag{1.46b}$$

define the weak mixing angle (also referred to as the Weinberg-angle, or the electroweak mixing angle). This must be measured experimentally using measured values of the W and Z masses. The fundamental electric charge e can be written in terms of the couplings as follows:

$$e = \frac{g'g}{\sqrt{g'^2 + g^2}}. \tag{1.47}$$

1.5.1 Gauge boson self-couplings

The electroweak theory specifies the self-couplings of the gauge bosons. The "kinetic" terms for the W fields (Section 1.5) are obtained by a generalisation of the electromagnetic field strength tensor $\mathbf{F}_{\mu\nu}$:

$$\mathbf{F}_{\mu\nu} = \partial_\mu \mathbf{W}_\nu - \partial_\nu \mathbf{W}_\mu - ig[\mathbf{W}_\mu, \mathbf{W}_\nu], \tag{1.48}$$

with the N components

$$F^a_{\mu\nu} = \partial_\mu W^a_\nu - \partial_\nu W^a_\mu + g f^{abc} W^b_\mu W^c_\nu. \tag{1.49}$$

The fields transform as

$$\mathbf{F}_{\mu\nu} \rightarrow \mathbf{F}'_{\mu\nu} = U \mathbf{F}_{\mu\nu} U^{-1}, \tag{1.50}$$

where U is a unitary transformation. The "weak" portion is given by the Yang-Mills Lagrangian

$$\mathscr{L}_W = -\frac{1}{2} Tr\left(\mathbf{F}_{\mu\nu}\mathbf{F}^{\mu\nu}\right). \tag{1.51}$$

When expanded, the weak Lagrangian becomes

$$\begin{aligned}\mathscr{L}_W = &-\frac{1}{4}\left(\partial_\mu W_\nu^a - \partial_\nu W_\mu^a\right)\left(\partial^\mu W^{a,\nu} - \partial^\nu W^{a,\mu}\right)\\ &-\frac{g}{2} f^{abc}\left(\partial_\mu W_\nu^a - \partial_\nu W_\mu^a\right) W^{b,\mu} W^{c,\nu}\\ &-\frac{g^2}{4} f^{abc} f^{ade} W_\mu^b W_\nu^c W^{d,\mu} W^{e,\nu}.\end{aligned} \tag{1.52}$$

In the $SU(2)$ theory of electroweak interactions the structure functions f^{abc}, f^{ade} are given by the fully antisymmetric Levi-Civita (alternating) tensor, ε_{abc}. It is the cubic and quartic terms which describe the self-interactions between the vector bosons. It is important to note that the Lagrangian above describes *massless* gauge bosons, as mass terms of the form $\frac{1}{2}m^2 W_\mu^a W^{a,\mu}$ spoil gauge invariance.

The electroweak theory discussed above has been a resounding success since its introduction in describing a wide range of experimental results; the electroweak sector with QCD forms the foundation of the $SU(3)_C \otimes SU(2)_L \otimes U(1)_Y$ gauge group which forms the foundation of the Standard Model. Despite its successes, one of the unsatisfying aspects of the Standard Model is the lack of prediction of the mass of the Higgs boson itself. However, upper bounds can be placed indirectly via experimental observations.

1.5.2 WW scattering and unitarity: arguments for TeV -scale physics

Amplitudes for scattering in theories with massive spin-1 particles can exhibit bad high-energy behaviour. The propagator for a longitudinally-polarised massive spin-1 field has a term which does not decrease with increasing momentum [25]:

$$\varepsilon_L^\mu = \left(\frac{q}{m}, 0, 0, \frac{E}{m}\right) \approx \frac{q^\mu}{m} + \mathscr{O}(m/E). \tag{1.53}$$

Consider the case of longitudinal scattering of two W bosons. The relevant diagrams at leading order are given below.

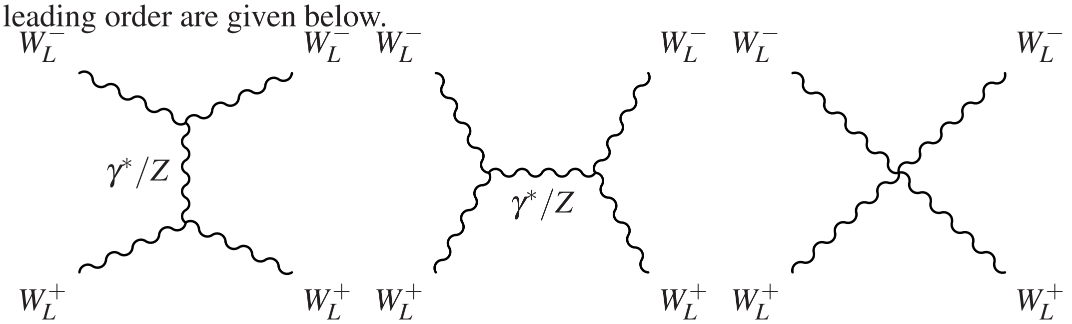

Fig. 1.1 Tree-level Feynman diagrams for longitudinally polarised WW scattering.

Direct calculation of the matrix elements reveals that the individual diagrams diverge as s^2/m_W^4, although the divergence of the sum of the individual matrix elements is smaller:

$$\mathscr{M}\left(W_L^+W_L^- \to W_L^+W_L^-\right) \sim \frac{s}{m_W^2} \qquad \text{as } s \to \infty$$

Thus the cross section tends to infinity at high centre-of-mass energies. Massive leptons do not resolve the divergence. The only way to keep the theory renormalisable is to introduce a massive scalar which cancels the residual divergences of the form [26]:

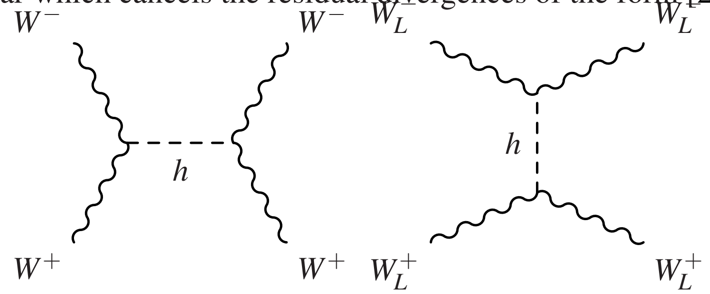

Fig. 1.2 WW scattering proceeding through an s-channel annihilation to a Higgs boson.

It is this scalar particle which is taken as the Higgs. Even if it were not introduced within the context of mass generation and electroweak symmetry breaking one would have to introduce a scalar particle. Furthermore, cancellations of the divergences mentioned above can only be obtained if the Higgs exchange graphs are included with the couplings predicted by the eletroweak model, which are proportional to the masses of the respetive particles coupling to the Higgs; in this case: $g_{HW^+W^-} = gm_W$ and $g_{He^+e^-} = gm_e/2m_W$.

The scattering of vector bosons can be used to place an upper limit on the mass of the SM Higgs boson. As the Higgs mass increases, the amplitude for s-wave WW scattering via Higgs exchange continues to increase and the contribution from the lowest order diagrams (Fig. 1.2) exceeds the perturbative unitarity limit at an energy of about 1 TeV [27, 28], giving an idea as to the energy of a collider experiment required to observe a SM Higgs.

1.6 Confirmation of the Standard Model; Discovery of the Higgs particle

In an unbroken gauge theory, all particles should be massless, which clearly goes against observation. The masses of the W and Z particles were predicted with the GWS theory and measured in 1983 at the CERN SPS Collider [29–31]. It is the symmetry breaking in the Higgs sector of the Standard Model which allows the electroweak gauge bosons (as well as the fermions) to acquire mass while keeping the photon massless. Furthermore, the couplings to electroweak bosons and fermions are proportional to the mass of the Higgs particle. The production and decay modes are determined by the mass of the Higgs; once known these can all be calculated and compared with experiment. Unlike the Z and the W bosons, the mass of the Higgs is not predicted by the Standard Model, and as a result, it was unclear from the outset whether previous generations of colliders had sufficient centre-of-mass energy to produce Higgs bosons. Although the mass was unknown, approximate upper and lower bounds on the mass were placed using unitarity arguments. For instance, longitudinal $W_\mathrm{L}W_\mathrm{L}$ scattering places the limit at around 1 TeV.

1.6.1 Searches at LEP and the Tevatron

A comprehensive search program was carried out by the experiments at the LEP and LEP II colliders. Searches were performed looking for the "Higgs-strahlung" process $e^+e^- \rightarrow Z^* \rightarrow ZH$ in various Z and H decay modes in collisions at centre-of-mass energies between 189 and 209 GeV. The efforts of the searches by the LEP collaborations placed a lower bound at 114.4 GeVat 95% confidence level [32].

Searches were also conducted by the Tevatron in $p\bar{p}$ collisions at 1.96 TeV. Datasets of ever increasing size (up to $10\,\mathrm{fb}^{-1}$ as of 2011) were acquired in hopes of discovering the elusive Higgs particle. The nature of the collisions at the Tevatron made it much more difficult to search for the Higgs than LEP; the background cross section is much higher than at LEP, and furthermore the bunch spacing (approximately 400 ns) severely limits the triggering capabilities. Searches in roughly 90 different selections were put in place by both CDF and DØ. As of March 2012, combined datasets from both experiments using 10 fb^{-1} were used to exclude the mass ranges $100 < m_H < 106$ GeV, and $147 < m_H < 179$ GeV, and a slight excess was seen in the range $115 < m_H < 135$ GeV [33]. The Tevatron was eventually shut down as the Large Hadron Collider (LHC) reached energies of 7 TeV; running stopped in August 2011 and the focus shifted towards the Large Hadron Collider at CERN.

1.6.2 Discovery at the LHC

After an incident on the 19th of September 2008 in which a faulty electrical connection caused a quench which severely damaged several magnets and led to a helium leak in the LHC tunnel [34], the LHC resumed operation one year later. Data were acquired at a centre-of-mass energy of 7 TeV (the highest energy of any accelerator up to that time) starting from around march 2010. Naturally, Higgs searches were of the utmost priority and results from both ATLAS and CMS had appeared by the summer putting out exclusion limits reasonably

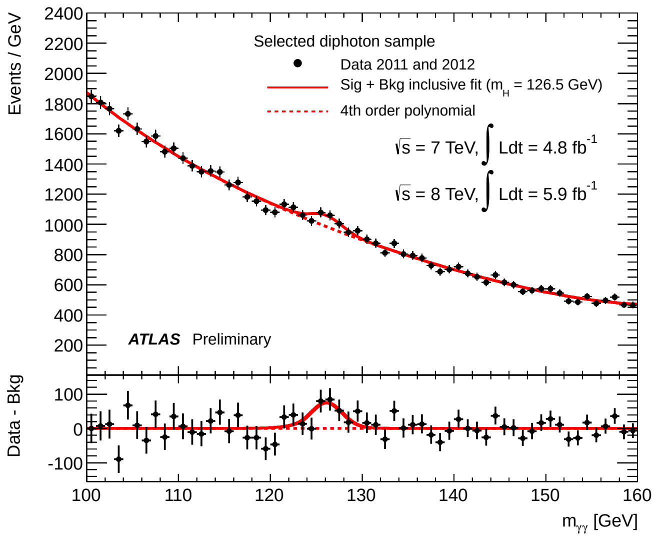

Fig. 1.3 Mass distribution for the di-photon channel in the 2012 ATLAS Higgs analysis at 7 and 8 TeV (4.9 + 5.9 fb^{-1}, respectively) [39]. The smooth dotted line traces the background from known processes. The solid line traces a statistical fit to the signal plus background.

close to and eventually more stringent than those of the Tevatron [35, 36]. Further data saw the range narrow down to 115 $< m_H <$ 135 GeV. At the end of 2011, as over 4.5 fb^{-1} had been collected by each experiment, evidence began accumulating showing an excess around 125 GeV, although the excess was not sufficiently statistically significant to be able to claim discovery.

In 2012, the centre-of-mass energy of the LHC was increased to 8 TeV. Higgs analyses for both ATLAS and CMS had resumed with the turn on of the collider in February of that year. On July 4th, a special seminar was announced to coincide with the start of the International Conference on High Energy Physics (ICHEP). Representatives from the ATLAS and CMS collaborations gave talks outlining search methodologies and results from their respective Higgs analyses [37]. Both representatives gave evidence from the diphoton ($\gamma\gamma$) and the ZZ diboson decay modes, claiming observation of a new fundamental scalar particle at 125 GeV[38]. The diphoton invariant mass spectrum is shown below in Fig. 1.3.

This represented the culmination of nearly fifty years of searching for the Higgs boson and a true milestone in physics. Although physicists were careful to not explicitly call the newly discovered scalar the Higgs, this discovery lended even more validity to the Standard Model, confirming that there was a fundamental scalar with a mass at the electroweak scale.

1.6.3 Updated Higgs measurements

Since the initial Higgs findings in 2012, experimental efforts have served to focus attention on measuring Higgs production in virtually all accessible decay channnels including $H \to \gamma\gamma$, $H \to b\bar{b}$, $H \to \tau\tau$, $H \to W^+W^-$, $H \to Z\gamma$ [40–42].

As of April 2014, the width of the Higgs boson has been constrained by results of the CMS collaboration. Using an analysis involving off-shell production to four charged leptons, or two charged leptons and two neutrinos, an upper limit on the Higgs boson width of $\Gamma_{\mathrm{H}} < 4.2 \times \Gamma_{\mathrm{H}}^{\mathrm{SM}}$ at 95% confidence level was obtained assuming $\Gamma_{\mathrm{H}}^{\mathrm{SM}} = 4.15\,\mathrm{MeV}$ significantly improving results over previous experimental measurements [43].

1.7 Shortcomings of the Standard Model

Despite all of its success, the Standard Model is not believed by most particle physicists to be a fundamental description of matter. There are 25 free parameters in the Standard Model that cannot be derived from first principles; the twelve quark, lepton, anti-quark and anti-lepton masses, three coupling constants describing the strengths of the gauge interactions (α, G_F, and α_s), the two parameters describing the Higgs potential (μ and λ), the eight mixing angles of the PNMS (θ_{12}, θ_{13}, θ_{23}, δ) and CKM matrices (λ, A, ρ, η). Furthermore, the QCD Lagrangian can contain a phase which could lead to CP violation in the strong interaction; this is usally referred to as θ_{CP}, and while small is not necessarily zero. Including θ_{CP} as a fundamental parameter would bring the count to 26. In addition, the Standard Model makes no mention of the gravitational force, or why the scale of gravity is so much (10^{43} times) weaker than that of the other fundamental forces at a given energy scale, or separation. Any attempts at a unified theory must incorporate all known fundamental forces. Other open questions in particle physics are, to name a few, the nature of dark matter, physics at the grand unified (GUT) scale, and whether neutrinos are Majorana or Dirac particles.

1.7.1 The dark matter puzzle

Since the mid-1930s, analysis of galactic rotation curves led to hypotheses (first by Oort, later made by Zwicky) that most of the mass of the galaxies under observation was not visible. Since then, indirect evidence for dark matter has been accumulating in various cosmological and astrophysical measurements such as velocity dispersions of galaxies, X-ray analysis and gravitational lensing effects in galaxy clusters, and angular fluctuations in the cosmic microwave background (CMB). Currently, the favoured candidate for dark matter is a Weakly Interacting Massive Particle, or WIMP. There is a strong relationship (or preference, some would say) between WIMP candidates and new physics at the TeV scale. Direct searches for WIMP dark matter come in a wide range of experiments, from nuclear recoil experiments, to direct productions at colliders such as the LHC. Currently, there is no clear statistically significant evidence for dark matter in direct-detection experiments, although newer experiments with increased sensitivity are continuously being planned and put into operation.

1.7.2 Supersymmetry

The Higgs particle is the only fundamental scalar in the Standard Model. Scalar particles have the property their masses receive large radiative first-order corrections; the first-order correction to the squared Higgs boson mass gives quadratically divergent terms which arise from fermion loops. The divergences are handled by typical methods of renormalisation, and the renormalised masses become inputs to the model. However, when the Standard Model is embedded in a theory that is valid up to higher energy scales (10^{16} GeV or higher), the corrections become very large, and it is no longer natural to have a light Higgs boson. This is referred to as the “hierarchy problem”. Supersymmetry attempts to address this problem by proposing additional particles to those of the Standard Model. For every particle loop there would be a super particle (“sparticle”) loop which would cancel the divergences by providing a correction with the opposite sign to those of a particle loop. At the core of Supersymmetry lies a relation between fermions and bosons which extends the Lie algebras in gauge theories to graded Lie algebras with commutation and anticommutation relations that connect SUSY generators to the Poincare generators. The SUSY algebra has a spin-$\frac{1}{2}$ Majorana generator that changes total angular momentum J by one half-unit and turns boson fields into fermion fields and fermions to boson fields. Thus each boson has a fermionic superpartner and each fermion has a bosonic superpartner.

If SUSY were an unbroken symmetry, the sparticle masses would be the same as the Standard Model particle masses. Experiments have shown that this is not the case, implying that SUSY is a badly broken symmetry. While the scale of SUSY breaking is unknown, theoretical arguments tend to favour the scale at around 1 TeV[44–46]. SUSY searches have been carried out since the LEP experiments in various channels [47]. Likewise for the Tevatron, SUSY searches have served to extend limits out to sparticle masses of several hundred GeV[48, 49], exploring a wide range of scenarios such as the MSSM [50–52], mSUGRA, and gauge-mediated supesymmetry breaking (GMSB) . The LHC experiments have a comprehensive program of direct SUSY searches. Current limits place mass limits at the order of 1 TeV within various SUSY scenarios. Although model-independent limits are easier for reinterpretation, limits are also set for several minimalistic SUSY scenarios, such as the MSSM and PMSSM [53]. A summary of the results after Run 1 of the LHC is shown in Fig. 1.4.

Although the picture for discovery of supersymmetry is quite a sombre one at the moment, what can be said is that the LHC has completed a tremendous first run. The reach for potential discovery will be increased in the second run as the Large Hadron Collider will be run at 13 and eventually 14 TeV. The theoretical underpinnings of the Standard Model will face a stringent test yet again, whether it survives unscathed remains to be seen.

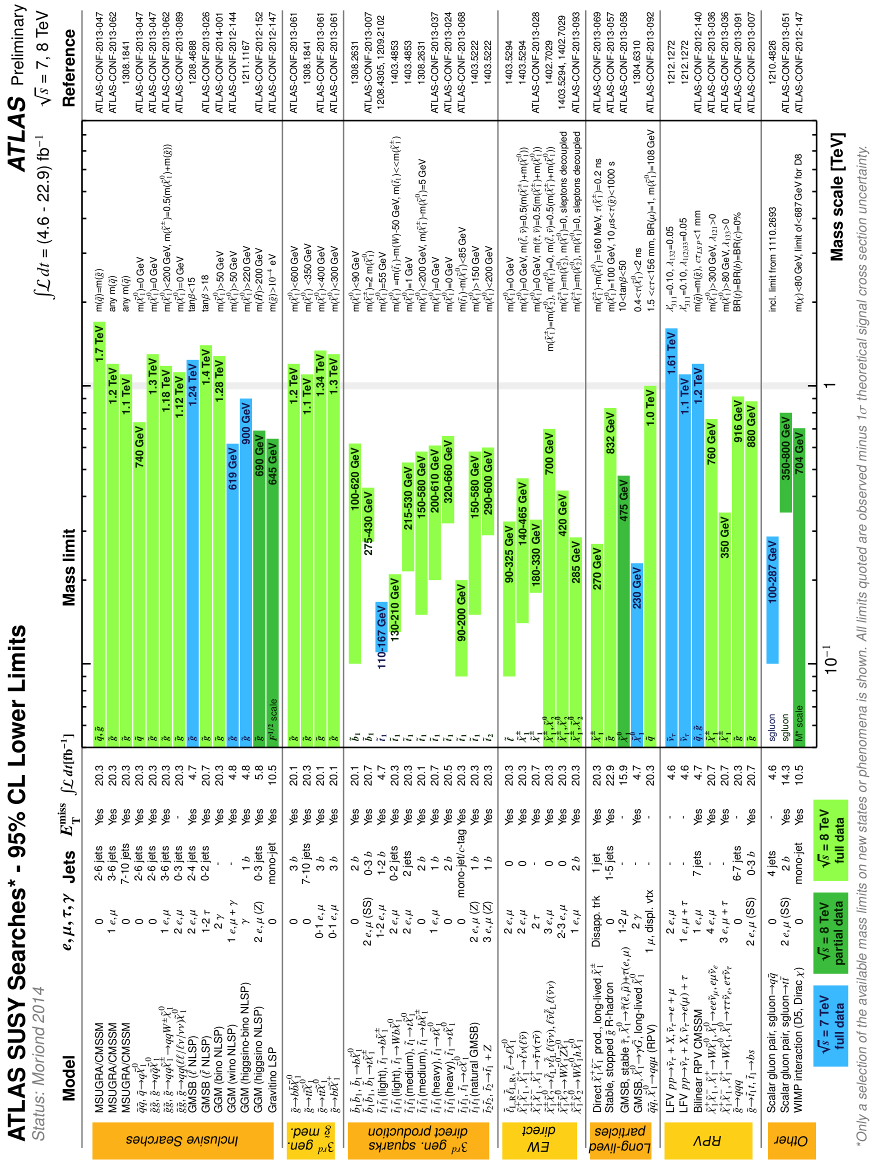

Fig. 1.4 Mass reach of ATLAS supersymmetry searches run 1 of the LHC.

Chapter 2

Diboson physics and ZZ production

This chapter gives an overview of the main mechanisms for producing ZZ dibosons. Anomalous neutral triple gauge couplings are introduced in the context of an effective Lagrangian which respects Lorentz invariance. Previous diboson measurements at the Large Electron Positron Collider (LEP) as well as the Tevatron and the Large Hadron Collider (LHC) are discussed, and previous results from ATLAS and CMS are also given.

2.1 Diboson physics

Diboson physics, as used in modern collider physics terminology, refers to the production of pairs of spin-1 electroweak gauge bosons. Possible diboson states include $W\gamma$, $Z\gamma$, WW, WZ, and ZZ. The nature of a particular collider determines the accessible diboson states; all diboson states are accessible at a hadron collider, but only neutral states are accessible at an e^-e^+ collider. After the centre-of-mass energy of the LEP accelerator was raised above 161 GeV in 1996, this paved the way for production of W pairs. As a result, the reaction $e^+e^- \to WW$ was studied extensively by the detector experiments at LEP-II between 1996 and 2000 by all four collaborations (OPAL, DELPHI, ALEPH, and L3) [54].

The first observations of diboson production at a hadron collider were at Fermilab in the mid 1990s. The CDF collaboration published the first observation of WW production in $p\bar{p}$ collisions in 1996 [55]. Since then, the Tevatron has made a series of cross section measurements in various diboson channels, including all the diboson channels mentioned above. Comprehensive overviews can be found in [56–60].

2.2 Introduction to diboson production

At an electron-positron collider (at lowest order in the weak coupling) dibosons are produced through s, t, and u-channel processes. For example, leading order diagrams for W pair production are shown in Fig. 2.1.

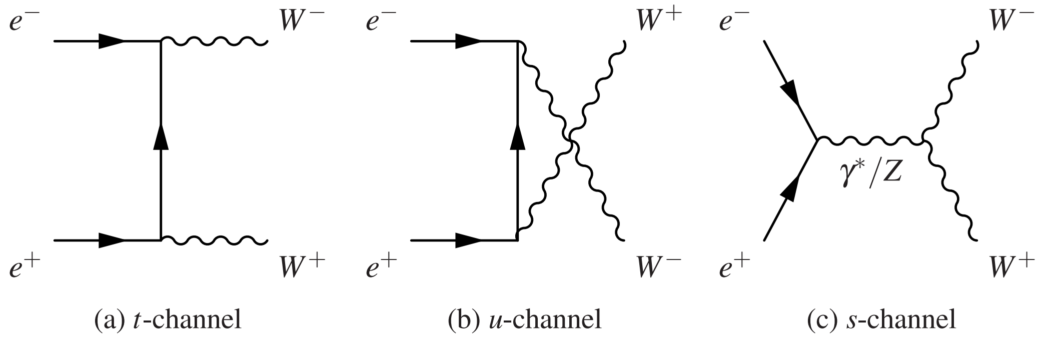

(a) t-channel (b) u-channel (c) s-channel

Fig. 2.1 Tree-level Feynman diagrams for WW diboson processes in e^+e^- collisions.

At hadron colliders, quarks, anti-quarks, and gluons, replace electrons and positrons in the initial state. The main mechanism of diboson production at a hadron collider is quark anti-quark annihilation via a t-channel or u-channel process. For the case of ZZ production, there is no s-channel process at tree-level, as this would involve a neutral triple gauge vertex. Neutral triple gauge vertices such as γZZ, ZZZ, and $Z\gamma\gamma$ are forbidden in the Standard Model at lowest order. The lowest-order (LO) gluon-induced processes involve quark loops. The relevant Feynman diagrams are shown in Fig. 2.2.

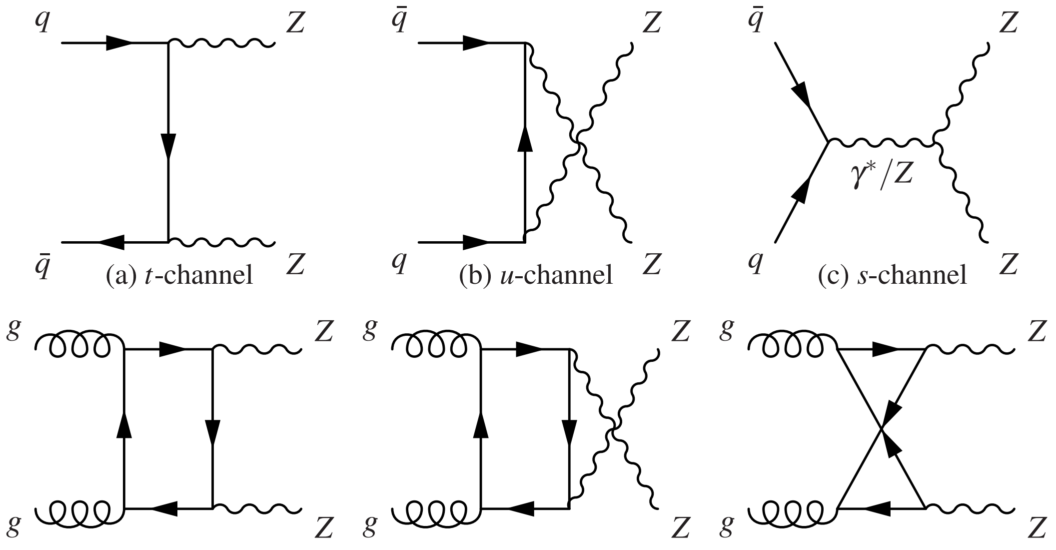

(a) t-channel (b) u-channel (c) s-channel

(d) (e) (f)

Fig. 2.2 Feynman diagrams for ZZ production. The first two figures in the top row show the t and u-channels which contribute to ZZ production at lowest order. The s-channel diagram is forbidden at tree-level, as it contains a neutral ZZV vertex ($V = Z$ or γ). The bottom figures show one-loop contributions to ZZ production via gluon pairs.

For WW and ZZ production, in addition to the production diagrams listed above, there are contributions from (possibly off-shell) Higgs bosons which may subsequently decay to one or more off-shell vector bosons $W^{(*)}W^{*}$ or $Z^{(*)}Z^{*}$. At hadron colliders such as the LHC and the Tevatron, the predominant mechanism of Higgs production, namely gluon-gluon fusion [61] via a Higgs intermediate state, should be included as "Standard Model production" of dibosons. However, Higgs analyses generally consider only processes with Higgs intermediate states as signal, while continuum production of diboson without a Higgs is considered background; the opposite is true in case of Standard Model production which considers $q\bar{q} \to ZZ$ and $gg \to ZZ$ as signal. A lowest-order diagram showing $gg \to H \to ZZ$ via a quark-loop is given in Fig. 2.3. Theoretical total Higgs production cross sections at the LHC have been studied extensively in various production channels including gluon-gluon fusion and vector boson fusion [62]. Moreover, further studies on benchmark cuts for signal-to-background optimisation and comparison of differential distributions were also performed [63]. Precision calculations of diboson production are currently under active development, although higher-order calculations become increasingly more difficult.

2.3 *ZZ* decay modes

The decay modes of the ZZ system give rise to both hadronic and leptonic final states. The leptonic channels have reduced background due to lepton energy and momentum resolution

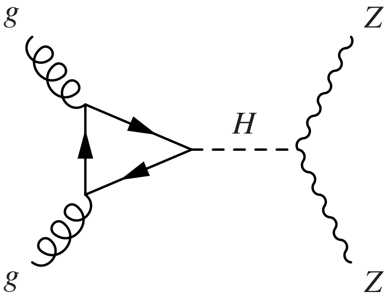

Fig. 2.3 Lowest-order $gg \to H \to ZZ$ diagram which proceeds via a fermion loop.

being better than jet energy resolution, however they have lower branching ratios. Analyses which use purely leptonic final states will see fewer events as a result and hence be subjected to a larger statistical uncertainty in their measurements compared to a semi-leptonic ($ZZ \to \ell^-\ell^+ + \text{jets}$) analysis. The four charged lepton final state, $\ell^-\ell^+\ell'^-\ell'^+$, where $\ell = e, \mu$, is the channel with the least background, but also suffers from the smallest branching fraction. Furthermore, not considering τ decays further reduces the final event counts after selection. Fig. 2.4 shows the branching ratios for ZZ diboson pairs to decay to various hadronic, semi-leptonic, and fully-leptonic final states.

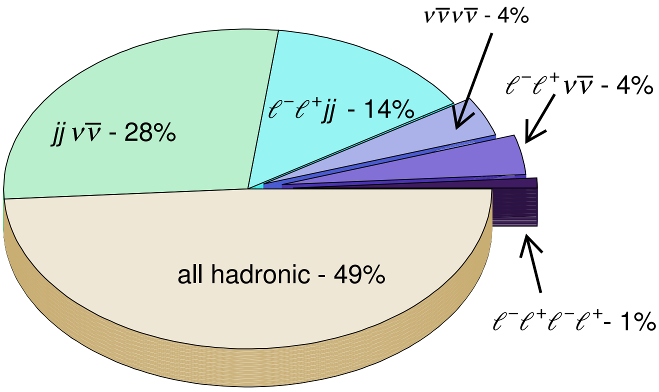

Fig. 2.4 Branching ratios of ZZ to hadronic, semi-leptonic, and fully-leptonic final states, as calculated from data from the Particle Data Group [15]. The hadronic final states have the largest branching ratios, while the $ZZ \to \ell^-\ell^+\nu\bar{\nu}$ and $ZZ \to \ell^-\ell^+\ell^-\ell^+$ channels have the smallest branching ratios at approximately 4% and 1% respectively. Here, the leptonic decay modes include e, μ, and τ.

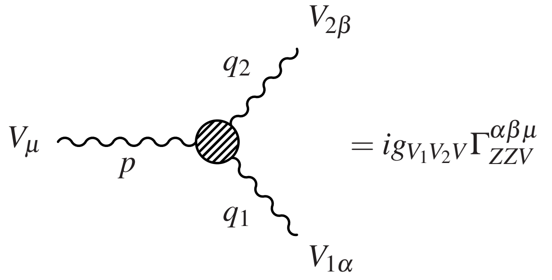

Fig. 2.5 The Feynman rule for an anomalous ZZV vertex where $V = Z$ or γ. Here p is the incoming momentum of the (generally off-shell) resonant vector boson $V^\mu = Z/\gamma$, q_1 and q_2 are the outgoing momenta of the on-shell Z bosons.

2.4 Anomalous neutral *ZZV* triple gauge couplings

The gauge boson self-couplings are given by the cubic and quartic terms of the kinetic portion of the weak Lagrangian (Eq. (1.52)). This forbids couplings of the form ZZV, where $V = Z$ or γ, at tree-level. However, triple gauge vertices can be generated via contributions from beyond Standard Model processes, the simplest models of which would involve heavy fermion loops from a new generation of fermions [64].

2.4.1 A framework for neutral triple gauge couplings

Including anomalous couplings would require the addition of the s-channel contribution. In the massless fermion limit, a reasonable approximation for hadron collider processes, the most general form of the $Z^\alpha(q_1)Z^\beta(q_2)V^\mu(p)$ vertex function, where the outgoing Z bosons are on-shell and $V = Z$ or γ is in general off-shell, which respects Lorentz invariance and electromagnetic gauge invariance may be written as [65]

$$g_{ZZV}\Gamma^{\alpha\beta\mu}_{ZZV} = e\frac{p^2 - m_V^2}{m_Z^2}\left[if_4^V\left(p^\alpha g^{\mu\beta} + p^\beta g^{\mu\alpha}\right) + if_5^V\varepsilon^{\mu\alpha\beta\rho}\left(q_1 - q_2\right)_\rho\right], \tag{2.1}$$

where m_Z is the mass of the Z boson, e is the proton charge, p is the centre-of-mass energy of the resonant boson, and q_1 q_2 represent the momenta of the outgoing bosons, as shown in Fig. 2.5. Here, two new couplings (f_4^V, f_5^V) have been introduced; they are dimensionless complex functions of q_1^2, q_2^2, and p^2. All couplings violate charge conjugation C. CP invariance forbids f_4^V so contributions to the helicity amplitudes will not interfere with Standard Model ZZ production. Parity conservation requires that f_5^V vanishes. At tree-level, f_4^V and f_5^V are zero in the Standard Model, while contributions of these couplings are of the order of $\mathscr{O}\left(10^{-4}\right)$ at one-loop level. The effective Lagrangian generating the vertex function is

$$\mathscr{L}_{\text{effective}} = \frac{e}{m_Z^2}\left[f_4^V\left(\partial_\mu V^{\mu\beta}\right)Z_\alpha\left(\partial^\alpha Z_\beta\right) + f_5^V\left(\partial^\sigma V_{\sigma\mu}\widetilde{Z}^{\mu\beta}Z_\beta\right)\right], \tag{2.2}$$

where the couplings and charges are as before, $V_{\sigma\mu} = \partial_\sigma V_\mu - \partial_\mu V_\sigma$ and the dual tensor $\widetilde{Z}_{\mu\nu} = \frac{1}{2}\varepsilon_{\mu\nu\rho\sigma}Z^{\rho\sigma}$ [66].

There are four $Z\gamma Z$ couplings (i.e, one outgoing photon and one outgoing Z). These are referred to as $h_i^Z(i = 1,2,3,4)$ and give rise to anomalous $Z\gamma$ production, where the Z is assumed to be on-shell. These are independent of the ZZV couplings. If all three bosons are allowed to be off-shell, then a total of seven couplings may contribute [67].

An example of BSM contributions to anomalous couplings is the MMSSM. This model is “simple” in that the only new fermions are charginos and neutralinos. If the MSSM provides a solution to the gauge hierarchy problem, it is possible for at least some of the charginos and neutralinos to be present not very far from the electroweak scale. The two charginos $\chi_{1,2}^{\pm}$ contribute to the f_5^γ and f_5^Z couplings, while the four neutralinos $\chi_{1\ldots4}^0$ contribute only to f_5^Z. Charginos couple to the gauge bosons through both their gaugino and higgsino components, whereas neutralinos only contribute through their higgsino components [64].

One issue that arises is how to maintain unitarity at high energies. The parton-level diboson production cross sections continue to grow with increasing (partonic) centre-of-mass energy, $\sqrt{\hat{s}}$. However, the unitarity of the S matrix places restrictions on the ZZV couplings to their SM values at very high energies; to ensure this, a momentum dependence is often introduced to the couplings which makes them decrease to their SM values at energies much larger than m_Z. To parametrise the $\hat{s}$ dependence of the couplings, the bare coupling f_{i0}^V is multiplied by a form factor [68]:

$$f_i^V(\hat{s}) = \frac{f_{i0}^V}{\left(1+\frac{\hat{s}}{\Lambda_{\mathrm{FF}}^2}\right)^n} \quad (i = 4,5). \tag{2.3}$$

Here Λ_{FF} is the scale of new physics generating the anomalous couplings, and n is a constant. The choice of n is related to the preservation of unitarity in relation to Λ_{FF}, a common choice for n is 3 [69]. In the case of the Tevatron and the LHC analyses, Λ_{FF}, is in the energy scale of several TeV.

2.5 Precision electroweak measurements with dibosons

2.5.1 Precision measurements at LEP

Dibosons played a very prominent role in the physics programme at LEP. The raising of the threshold energy of LEP-II allowed for the first observations of WW events by July 1996. The first evidence for doubly-resonant production of Z bosons was observed during 1997 [70], when the LEP-2 accelerator reached a centre-of-mass energy near 183 GeV. Measurements of ZZ dibosons by the four LEP collaborations were made with data collected between 1997 and 2000 using all visible decays: $q\bar{q}q\bar{q}$, $\nu\bar{\nu}qq$, $\ell^-\ell^+qq$, $\ell^-\ell^+\ell'^-\ell'^+$and $\ell^-\ell^+\nu\bar{\nu}$. Cross section measurements of ZZ are summarized below in Fig. 2.6. Limits at 95% confidence level (CL) on the neutral aTGC's f_4^V and f_5^V were also set using the combination of results from all four LEP experiments. Each experiment provided the negative log-likelihood as a function of the parameter being combined, which was then minimised to find the best combined limit. Limits on neutral ZZV aTGC's in the range as set by the combined LEP experiments are shown in Table 2.1.

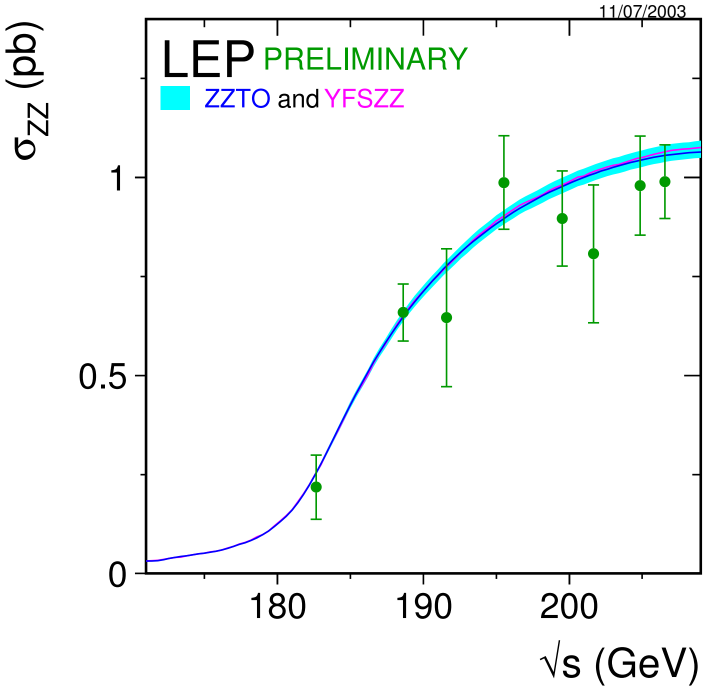

Fig. 2.6 ZZ production cross section measured as a function of $\sqrt{s}$ using all decay channels combined for all four LEP experiments [71].

Parameter	95% C.L.
f_4^γ	[-0.17, 0.19]
f_4^Z	[-0.30, 0.30]
f_5^γ	[-0.32, 0.36]
f_5^Z	[-0.34, 0.38]

Table 2.1 The 95% CL intervals ($-\Delta \ln L = 1.92$) obtained combining the results from all four LEP experiments in a one-parameter analysis [71].

2.5.2 Precision measurements at the Tevatron

The Tevatron at Fermilab also had an impressive programme of electroweak physics and diboson measurements. Measurements of the $W\gamma$, $Z\gamma$, WW and WZ cross sections were made by the CDF and DØ collaborations. The ZZ state was the last of the diboson states to be observed at the Tevatron. More recently, the ZZ analysis has been updated using a much larger dataset of $9.6\,\mathrm{fb}^{-1}$ as of 2013 [72]. CDF also updated measurements in both the $ZZ \to \ell^-\ell^+\ell^-\ell^+$ and $ZZ \to \ell^-\ell^+\nu\bar{\nu}$ channels using the full dataset of $9.7\,\mathrm{fb}^{-1}$. The diboson cross sections as reported by both the CDF and DØ collaborations are summarised in Fig. 2.7.

2.6 Diboson measurements at the LHC

Diboson measurements have played a key role in the physics programmes of both the ATLAS and CMS experiments at the LHC from the beginning of operation. The first diboson results from ATLAS were released in 2010/2011. The first analyses used small datasets of approximately $34\,\mathrm{pb}^{-1}$ [74, 75]. These analyses were superseded by the full 2011 dataset, which used approximately $4.6\,\mathrm{fb}^{-1}$ of data.

2.6.1 ZZ measurements at ATLAS and CMS

The first measurement of ZZ production was made in 2011 using the four-charged lepton channel at $\sqrt{s} = 7$ TeV [76]. Limits on neutral anomalous ZZV couplings were set using a dataset of $1.02\,\mathrm{fb}^{-1}$. Using an expanded dataset of $4.6\,\mathrm{fb}^{-1}$, the measurement was extended to include the $ZZ \to \ell^-\ell^+\nu\bar{\nu}$ channel. The total cross section for ZZ events produced with both Z bosons in the mass range $66 < m_Z < 116$ GeV was measured to be $\sigma_{\mathrm{tot}}^{ZZ} = 6.7 \pm 0.7(\mathrm{stat.}) \pm^{0.4}_{0.3}(\mathrm{syst.}) \pm 0.3(\mathrm{lumi.})\,\mathrm{pb}$ compared to a NLO calculation of $5.89^{+0.22}_{-0.18}\,\mathrm{pb}$. [77].

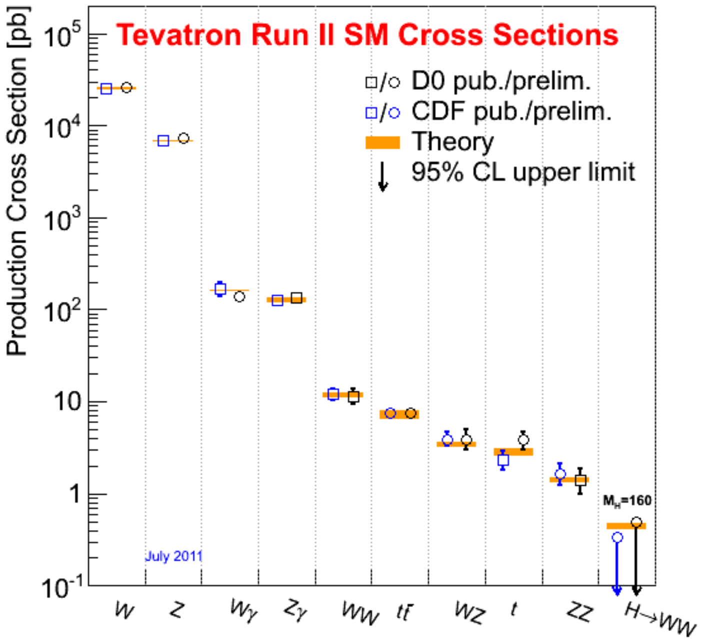

Fig. 2.7 Single boson, diboson and top production cross sections as measured with up to 8 fb^{-1} of Tevatron Run II data by the CDF and DØ collaborations [73].

Anomalous TGC limits for neutral ZZV couplings extracted from both ZZ channels with the full 2011 dataset at $\sqrt{s} = 7$ TeV are shown in Fig. 2.8. The ATLAS limits served to tighten the range of aTGC parameters for anomalous neutral trilinear ZZV couplings by nearly a factor of 10. In 2013, the ATLAS collaboration measured the ZZ production cross section in the four charged lepton channel at a centre-of-mass energy of 8 TeV with a dataset consisting of over 20 fb^{-1} [78]. The cross section in a fiducial phase space corresponding to detector acceptance in the invariant mass window $66 < m_Z < 116$ GeVwas measured to be $20.7^{+1.3}_{-1.2}(\text{stat.}) \pm 0.8(\text{syst.}) \pm 0.6(\text{lumi.})$ fb, and the total cross section was measured to be $7.1^{0.5}_{-0.4}(\text{stat.}) \pm 0.3(\text{syst}) \pm 0.2(\text{lumi})$ pb, compared to a Standard Model expectation of $7.2^{-0.3}_{+0.2}$ pb calculated from simulation. The ZZ cross sections as measured at the LHC are shown along with the corresponding Tevatron measurements in Fig. 2.9.

The first measurement of the ZZ cross section by CMS was made in 2011 using 1.1 fb^{-1} of data at $\sqrt{s} = 7$ TeV, with $\sigma(pp \to ZZ + X) = 3.8^{+1.5}_{-1.2}(\text{stat}) \pm 0.2(\text{syst.}) \pm 0.2(\text{lumi})$pb [80]. An updated measurement at 8 TeV was performed in 2013 [81]. In 2013, a measurement in the $ZZ \to \ell^-\ell^+\nu\bar{\nu}$ channel was made with 5.1 fb^{-1} at 7 TeV and 19.6 fb^{-1} at 8 TeV giving $\sigma(pp \to ZZ + X) = 5.0^{+1.5}_{-1.4}(\text{stat})^{+1.3}_{-1.0}(\text{syst.}) \pm 0.2(\text{lumi})$pb at 7 TeV and

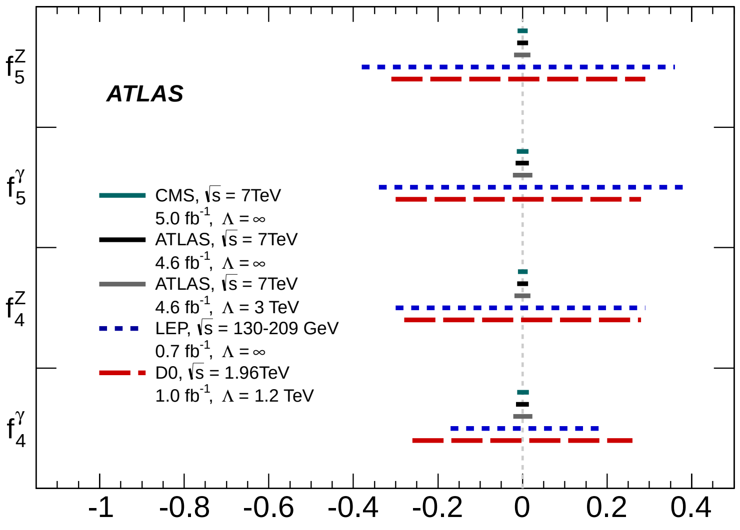

Fig. 2.8 95% confidence limits on neutral anomalous triple gauge coupling parameters f_4^V and f_5^V ($V = Z, \gamma$) using both the $ZZ \to \ell^-\ell^+\ell^-\ell^+$ and $ZZ \to \ell^-\ell^+\nu\bar{\nu}$ channels. ATLAS limits are set using a form factor $\Lambda = 3$ TeV and with no form factor. Limits from ATLAS and CMS are compared to previous limits set by both the combination of LEP experiments and the limits from the DØ experiment [77].

$\sigma(pp \to ZZ+X) = 6.8^{+0.8}_{-0.8}(\text{stat})^{1.8}_{-1.4}(\text{syst.}) \pm 0.3(\text{lumi})\text{pb}$ at 8 TeV. Measurements in the $ZZ \to \ell^-\ell^+\ell^-\ell^+$ channel were made at 7 and 8 TeV[82, 83]. The tightest limits on netural ZZV aTGCs are found in [83], and are summarized in Table 2.2.

A summary of Standard Model cross sections, including WW, WZ, and ZZ dibosons measured in ATLAS is given in Fig. 2.10. The corresponding measurements as made by CMS are given in the summary plot Fig. 2.11. No significant (larger than 3σ) deviations from theoretical predictions have been observed yet, indicating that there is no obvious tension with the Standard Model predictions in the electroweak sector.

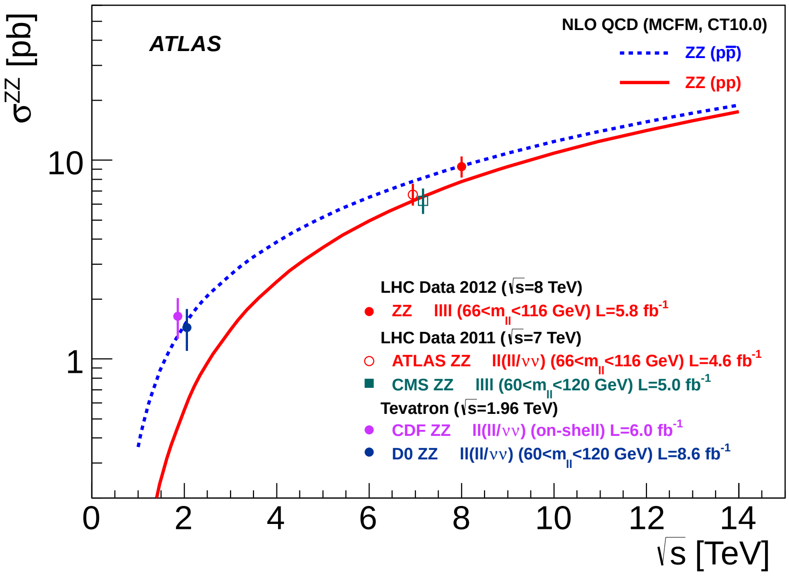

Fig. 2.9 *ZZ* diboson cross sections as a function of the centre-of-mass energy $\sqrt{s}$ at both the LHC (proton-proton) and the Tevatron (proton-antiproton) [77]. The theory curves are derived using NLO QCD calculations from cross section calculator MCFM [79].

Parameter	95% C.L.
f_4^{γ}	[-0.005, 0.005]
f_4^{Z}	[-0.004, 0.004]
f_5^{γ}	[-0.005, 0.005]
f_5^{Z}	[-0.004, 0.004]

Table 2.2 One-dimensional 95% C.L. intervals on neutral *ZZV* aTGCs obtained by the CMS collaboration in the $ZZ \to \ell^-\ell^+\ell^-\ell^+$ channel ($\ell = e,\mu, \ell' = e,\mu,\tau$) with 19.6 fb^{-1} at $\sqrt{s} =$ 8 TeV [83].

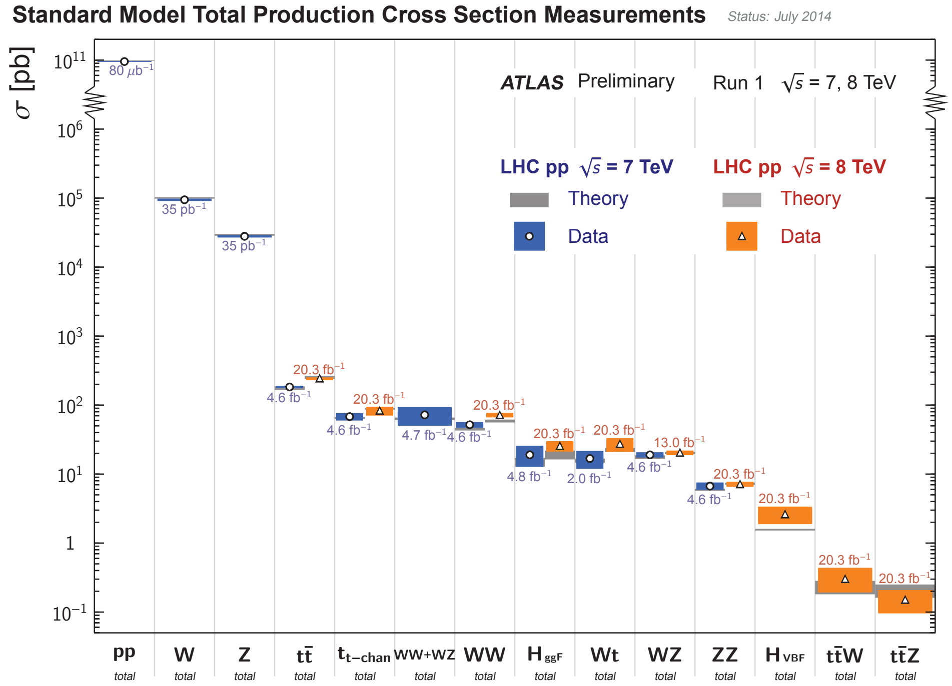

Fig. 2.10 A summary of several Standard Model single boson, diboson, and top total production cross section measurements, corrected for leptonic branching ratios. The comparison is made to theoretical predictions at next-to-leading order in the diboson states [84].

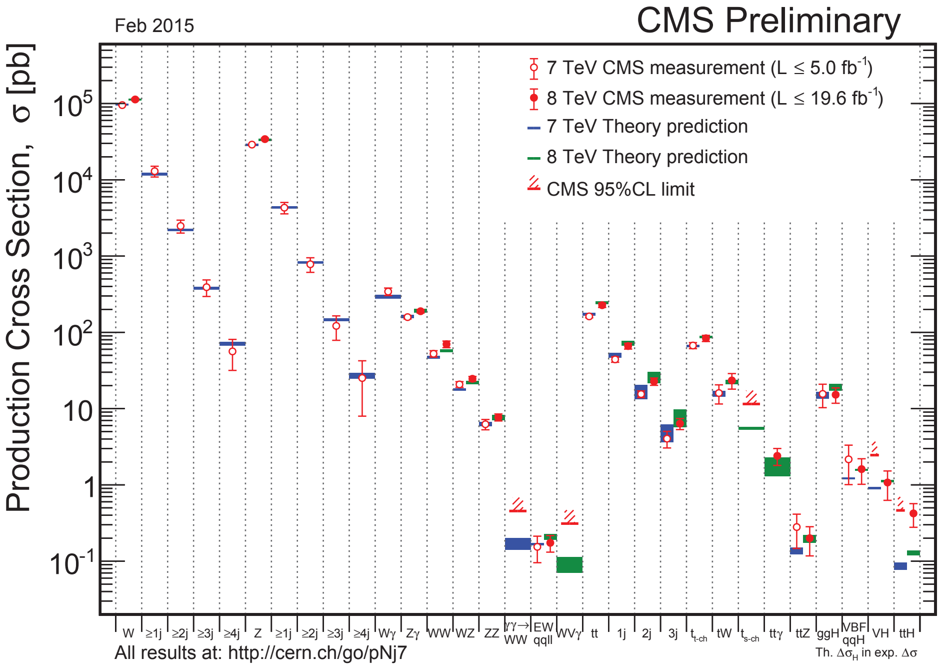

Fig. 2.11 A summary of several Standard Model single boson, diboson, and top total production cross section measurements, corrected for leptonic branching ratios, as measured by the CMS collaboration. The comparison is made to theoretical predictions at next-to-leading order in the diboson states.

2.7 Conclusion

This chapter presented an overview of diboson physics, and in particular, *ZZ* production. An effective Lagrangian framework was introduced whereby new couplings allow for both on-shell and off-shell *ZZ* production via anomalous triple *ZZV* couplings. Limits from the LEP experiments, the Tevatron experiments, and the general purpose experiments at the LHC were shown, showing that the size of the couplings within this framework are constrained to better than the percent-level. The method of limit extraction using the full 8 TeV ATLAS dataset is explained in Chapter 8.

Chapter 3

The LHC and the ATLAS experiment

This chapter presents an overview of the LHC accelerator. The ATLAS experiment is briefly described including the detector subsystems, trigger, and coordinate conventions. Performance of the various subsystems including the Inner Detector is discussed.

3.1 The Large Hadron Collider

The LHC is currently the highest energy collider constructed. After the Superconducting Supercollider (SSC) was cancelled in 1993 due to severe funding problems, the LHC was approved by the CERN council in 1994 [85]. The conceptual design of the LHC was first proposed in 1995 [86]. The technical proposals for the ATLAS [87] and CMS [88] experiments were approved in 1996 and formal approval of the experiments to move to the construction phase took place in late 1997. Assembly of the experiments began in 2000. The LEP accelerator was shut down in the fall of that year to make way for the LHC. The magnet system would be assembled and installed over the next seven years, with the last of the LHC dipole magnets being installed in 2007. The first beam was circulated in the LHC ring on the 10th of September, 2008, marking a new era in accelerator physics [89]. Unfortunately, on the 19th of September, 2008, a faulty electrical connection between two of the accelerator's magnets in Sector 3-4 of the LHC ring caused a rapid temperature increase and a release of about 7 MJ of energy, enough to rip the 35 t magnet from the floor. This incident caused a huge setback to the operation of the LHC. Most of 2009 was spent on repairing the damage caused by the incident and fixing vacuum leaks. Beams were not resumed until November 2009. On November 30th, the LHC achieved 1.18 TeV per beam to become the world's highest energy accelerator. Successful operation of the LHC has led to many new and interesting physics results over the past five years from all LHC experiments.

3.1.1 The accelerator complex

The LHC uses the same tunnel as LEP, which completed operation at the end of 2000 after 11 years of operation [90]. The tunnel is roughly 100 m underground and 26.6 km in circumference, passing through the French-Swiss border. A schematic overview of the Geneva area showing the scale of the LHC is shown in Fig. 3.1. Nearly 22 km of the LHC tunnel consists of curved sections that allow bending dipole magnets to be installed. The remaining 5 km consists of eight straight sections that provide space for the installation of the experiments, injection and extraction elements for the proton beams, and acceleration and "cleaning" devices to protect the superconducting magnets [92]. Protons are produced in a duoplasmatron device and accelerated in a linear accelerator to 50 MeV; from there the beam is injected into four Proton Synchrotron Booster rings, ramped to 1.4 GeV and transferred to the Proton Synchrotron (PS) where the beam energy grows to 25 GeV [93]. The LHC base bunch

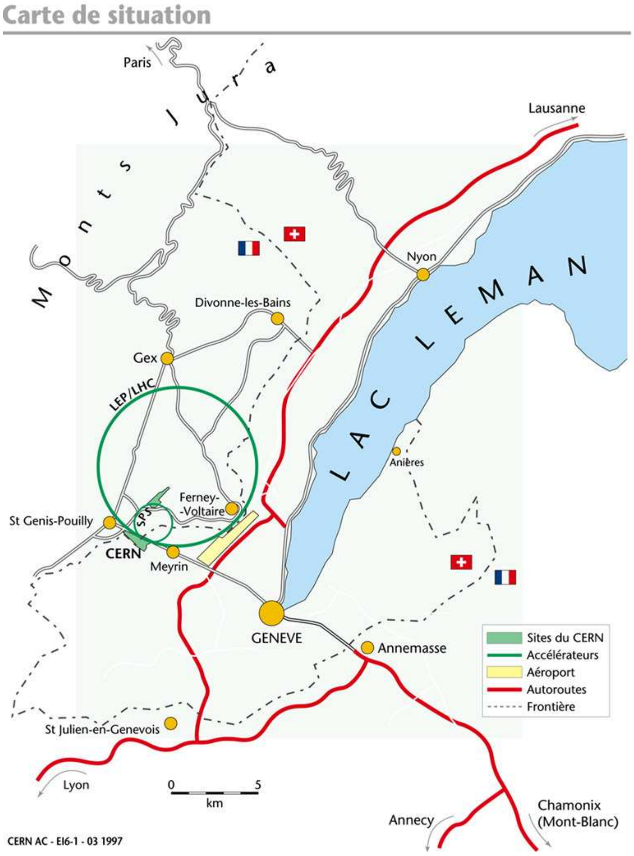

Fig. 3.1 An aerial schematic of the LHC in relation to Geneva and the French-Swiss border. The LHC straddles the border between Switzerland and France. Most of the accelerator ring passes through France. Point 1 of the LHC is located on the CERN main site in Meyrin. The ring is approximately 27 km in circumference [91].

structure of bunches with 50 ns spacing is applied[1]. The protons then enter the Super Proton Synchrotron, with a circumference of 6911 m, which accelerates the proton bunches to 450 GeV. The protons are injected into the main ring at this energy via beam transfer lines, and are further accelerated to the operational energy, 3.5 TeV per beam for the 2011 run and 4 TeV per beam for the 2012 run. A schematic of the LHC injection complex is shown in Fig. 3.2. The design energy of the LHC is 14 TeV seven times larger than that of its nearest competitor, the Tevatron at Fermilab, which has been out of operation since September 2011. The design luminosity of the LHC is approximately $10^{34}\,\mathrm{cm}^{-2}\,\mathrm{s}^{-1}$ which, when taken over the course of the year would give an integrated luminosity of $10^{41}\mathrm{cm}^{-2}/\mathrm{yr} = 100\,\mathrm{fb}^{-1}/\mathrm{yr}$ [94].

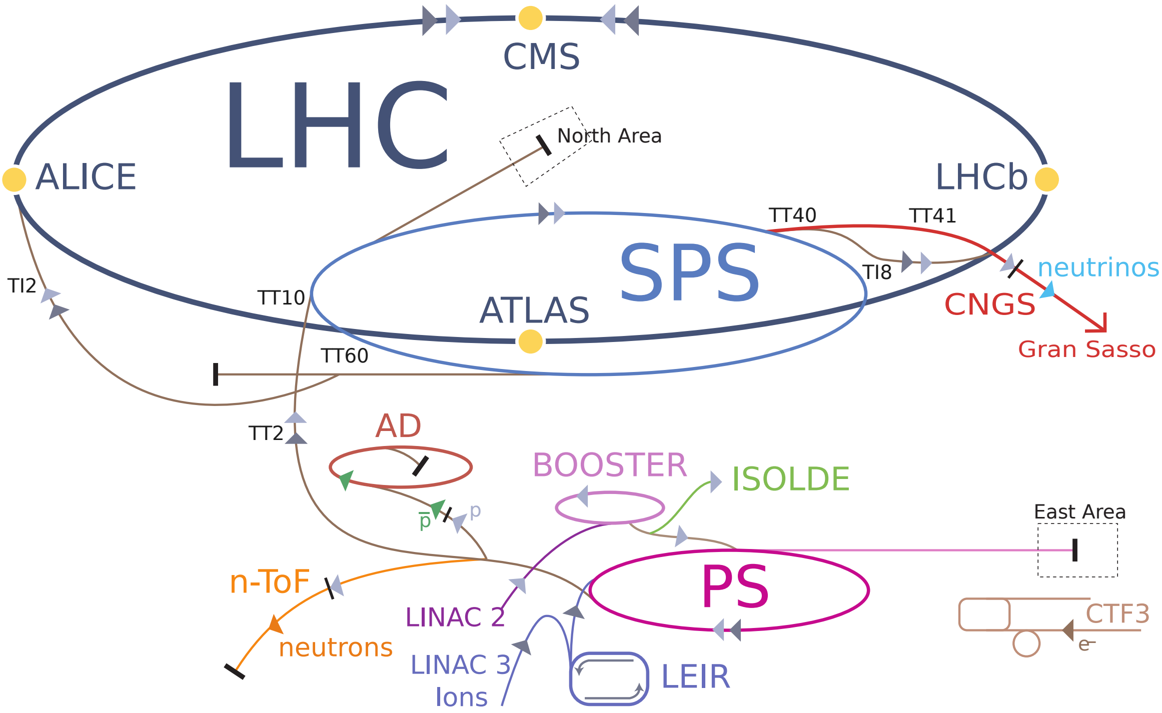

Fig. 3.2 A schematic layout of the LHC accelerator complex. Figure courtesy of CERN's public web [95].

3.1.2 The magnet system of the LHC

Several different types of magnet are employed by the LHC to achieve The first prototype bending magnet for the LHC reached a field of 8.73 T in 1994 [96], which is higher than the 8.3 T used for operations during run 1 of the LHC. Several different types of magnet

---

[1] During the first run of the LHC during 2011 and 2012, the bunch spacing was set at 50 ns with approximately 1380 bunches per fill.

are employed by the LHC, the largest of which are the main dipole magnets. There are 1232 main dipoles in the LHC tunnel. Each superconducting dipole is about 14.3 m long and has two apertures (one for each counter-rotating beam). The dipoles operate in a static bath of superfluid helium II at a temperature of 1.9 K [97]. The total energy of each beam is a function of the number of the number of bunches injected into the ring, the number of protons in each bunch, and the energy to which the protons are accelerated. At the maximum design intensity, with 2808 bunches per beam, 1.15×10^{11} protons per bunch accelerated to an energy of 7 TeV, each beam would have roughly 360 MJ of energy. A schematic cross section of a LHC dipole magnet is shown in Fig. 3.3. In an accelerator such as the LHC, particles are accelerated by a high-frequency standing wave which is excited in an accelerating cavity. The frequency of these waves is typically in the radio frequency range, and the cavities are called RF cavities. The cavities serve to keep the proton bunches tightly spaced to ensure high instantaneous luminosity. Each cavity in the LHC is tuned to oscillate at 400 MHz. There are 16 RF cavities (8 per beam) in the LHC that are housed in four cylindrical refrigerators called cryomodules [99]. High-power klystrons drive each RF cavity, and a high power electron beam inside the klystron modulates at 400 MHz delivering an accelerating field of 5 MV m^{-1}.

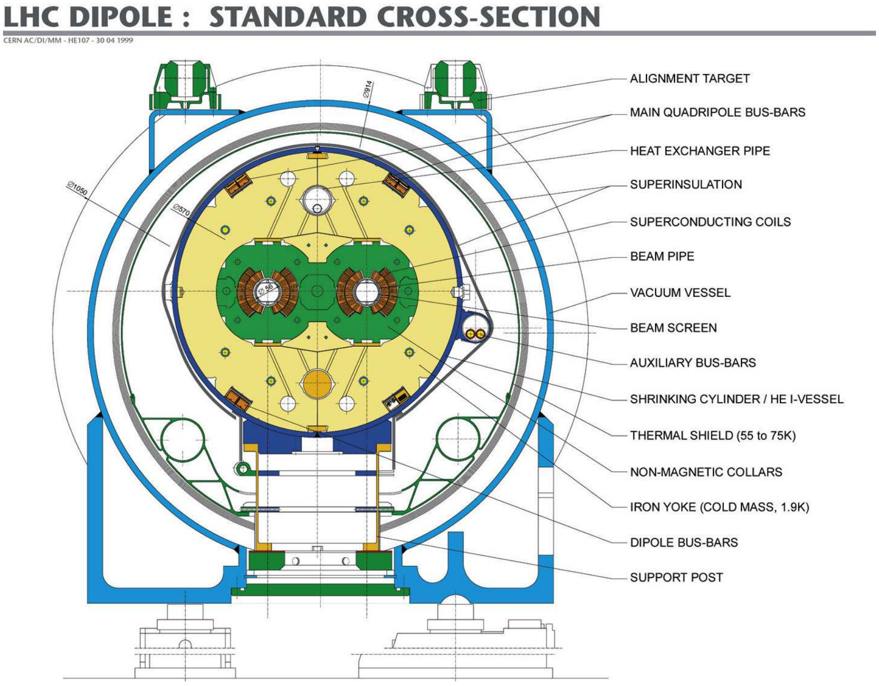

Fig. 3.3 A schematic cross section of an LHC dipole magnet [98].

3.1.3 Performance of the LHC: 2010-2012

Proton-proton collisions in Run I of the LHC ended December 2012, and the final heavy ion collisions took place between January and February 2013. The LHC entered its first planned long shutdown (LS I) shortly after, where maintenance and upgrades were performed on the magnets for a period of about two years. From the first collisions to the end of Run I, the LHC was able to deliver an increased luminosity each year. The first year was primarily devoted to machine performance. Initially, LHC started running at low luminosity, with only one pair of colliding bunches, with a bunch size of of about 1×10^{11} protons per bunch [100]. The proton run for the year finished with beams of 368 bunches of around 1.2×10^{11} protons per bunch and a peak instantaneous luminosity of $2.1 \times 10^{32}\,\mathrm{cm}^{-2}\,\mathrm{s}^{-1}$. The total integrated luminosity for both ATLAS and CMS in 2010 was around $0.04\,\mathrm{fb}^{-1}$.

The beam energy remained at 3.5 TeV in 2011. The number of bunches in the machine was tested with a 50 ns bunch spacing, which would eventually be the bunch spacing for the remainder of the physics run. A peak instantaneous luminosity of $2.4 \times 10^{33}\,\mathrm{cm}^{-2}\,\mathrm{s}^{-1}$ was achieved in 2011. ATLAS and CMS had each received around $5.6\,\mathrm{fb}^{-1}$ by the end of proton–proton running for 2011, with approximately $4.7\,\mathrm{fb}^{-1}$ good for physics in the ATLAS dataset after data quality criteria were applied. LHCb collected a total of $1.1\,\mathrm{fb}^{-1}$.[2] In early 2012 the decision was made by the LHC division to stay at a 50 ns bunch spacing with around 1380 bunches. The accelerator delivered an integrated luminosity at the rate of roughly $1\,\mathrm{fb}^{-1}$ per week. This allowed a total of about $23\,\mathrm{fb}^{-1}$ to be delivered to both ATLAS and CMS during a long operational year with the proton-proton run extended until December (in previous years, heavy ion runs took place in December). The high number of collisions was very important for analyses such as Higgs searches. Plots of integrated luminosity in 2012 for both the ATLAS and CMS collaborations are shown in Fig. 3.4.

---

[2] Substantially less luminosity is delivered to LHCb compared to the general purpose detectors.

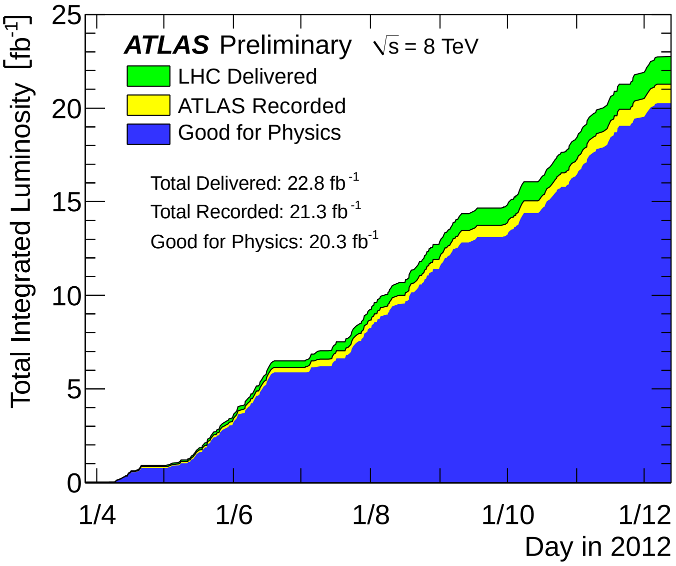

(a)

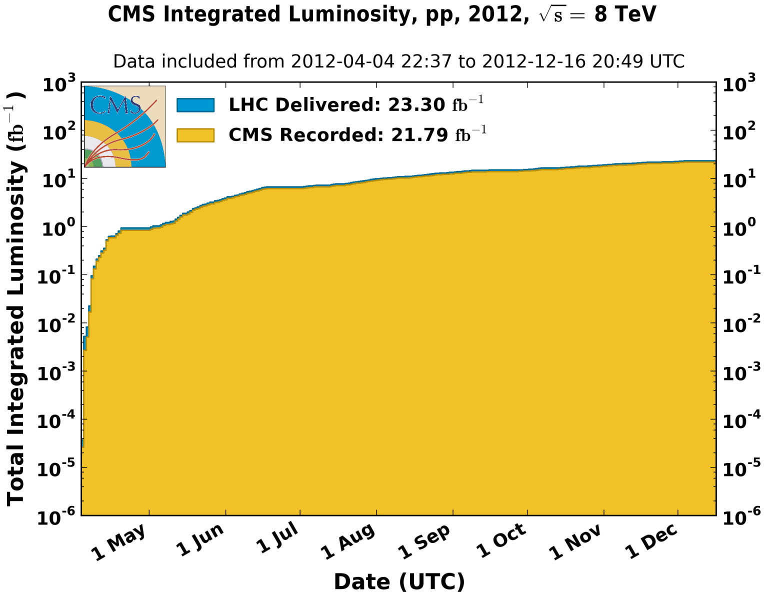

(b)

Fig. 3.4 (a) Cumulative integrated luminosity versus time delivered by the LHC (green), as recorded by ATLAS (yellow), and certified to be good quality data (blue) during stable beams for proton-proton collisions at 7 TeV centre-of-mass energy for the year 2012 [101]. Total delivered luminosity for ATLAS is approximately 22.8 fb^{-1} in 2012. The corresponding plot for CMS is shown in (b) [102].

3.2 The ATLAS experiment at the LHC

There are four primary experiments at the LHC: ATLAS [103], CMS [104], LHCb [105] and ALICE [106]. ATLAS and CMS are general purpose detectors suitable for both proton-proton and heavy ion collisions. LHCb is a detector dedicated to measuring physics involving bottom quarks. The ALICE detector is specifically designed for heavy ion (Pb-Pb) reactions. The principles used to build each detector are the same, although the technology used to achieve a desired measurement resolution varies between experiments. Modern particle detectors follow a layered structure, and the LHC experiments are no different. The general detector structure consists of tracking (usually silicon strips and/or pixels and or wire chambers) very close to the collision point, followed by calorimetry (electromagnetic and hadronic calorimeters). The outer-most part of most modern detectors is a detector subsystem used for measuring the momentum of muons, which have sufficient energy to go completely through the detector.

ATLAS, (**A** **T**oroidal **L**HC **A**pparatu**S**), shown in Fig. 3.5, is a general purpose detector that sits at Point 1 of the LHC ring (Fig. 3.6). As it is a general-purpose detector, ATLAS follows the pattern of having tracking systems closest to the interaction point, followed by calorimetry, and tracking of muons as the outermost detector subsystem.

The detector is approximately 44 m long and 25 m in diameter and weighs over 7000 t. ATLAS consists of several detector subsystems, discussed briefly in the following sections.

3.2.1 Coordinate conventions and kinematic variables in ATLAS

ATLAS uses a right-handed orthogonal coordinate system in which the z-axis is directed along the beam pipe (with positive z from point 1 to point 8), the x-axis points from the collision point to the centre of the LHC ring, and the y-axis points upward from the collision point. The y-axis is slightly tilted with respect to the vertical due to the general tilt of the tunnel. The origin of this ATLAS “global frame” is the nominal interaction point. In addition to the conventional Cartesian axes used, a polar coordinate system (r, θ, ϕ) is also used quite frequently for physics analyses. The coordinate r is the radial distance from the collision point, ϕ is the azimuthal angle with x-axis taken to be zero, and θ is the polar angle [103]. The polar angle θ is defined with respect to the global z-axis. Kinematic variables frequently used to describe the location and the energy state of particles are transverse momentum, rapidity[3] and pseudorapidity. Transverse momentum p_T is defined as the com-

---

[3] The rapidity of a particle is defined in terms of its four-momentum components E and p_z through the relation

$$y = \frac{1}{2}\ln\left(\frac{p_0 + p_z}{p_0 - p_z}\right). \tag{3.1}$$

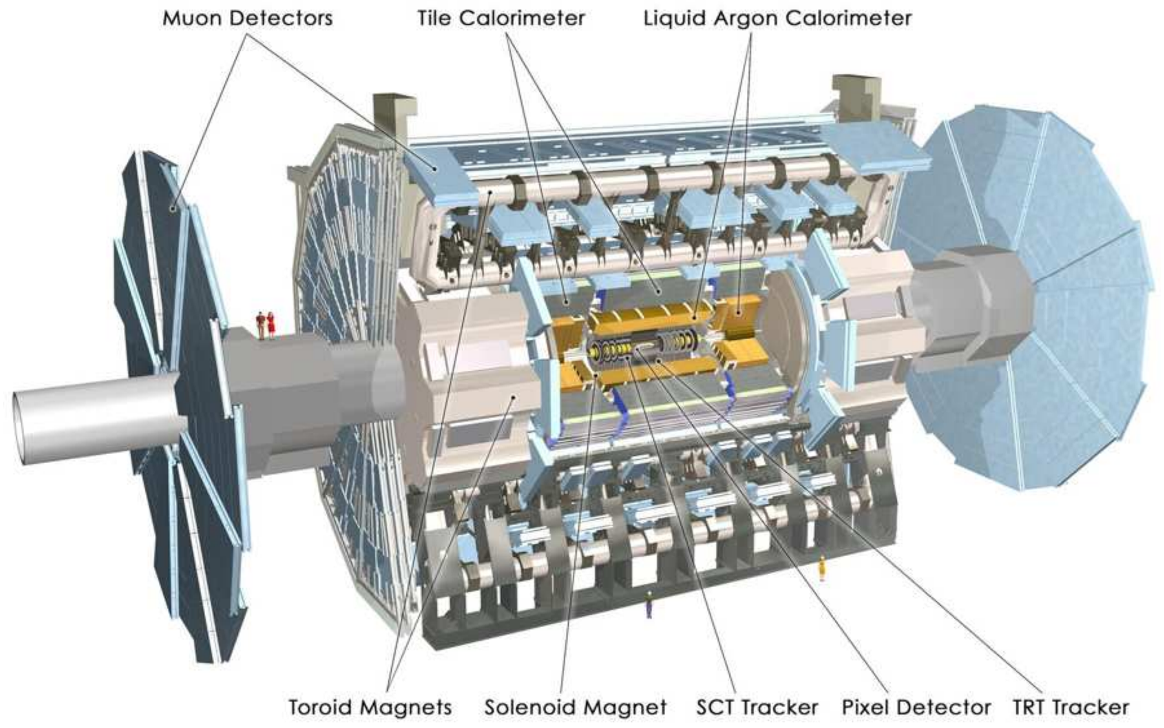

Fig. 3.5 A cut-away schematic diagram of the ATLAS detector, with some of the main detector subsystems highlighted. The components of the Inner Detector, the pixel detector, the semiconductor tracker, and the transition radiation tracker are shown at the centre of the detector. The liquid argon calorimeter (LAr) surrounds the Inner Detector and provides precise energy measurements of electrons and photons. The central air core toroid system surrounds the calorimeters; the two end cap toroids are visible at either end of the calorimeter. The distance scale between muon end caps corresponds to a length of 44 m, while the detector stands about 25 m tall. Figure from [107].

ponent of the three-momentum **p** that is directed radially outward, transverse to the global z-axis

$$p_{\mathrm{T}} = |\mathbf{p}| \sin\theta. \tag{3.3}$$

When expressed in Cartesian coordinates, it takes the familiar form

$$p_{\mathrm{T}} = \sqrt{(p_x^2 + p_y^2}. \tag{3.4}$$

This variable has the advantage that the rapidity of a particle in a new frame (say S') moving with velocity β along the same axis to the laboratory frame is given by

$$y' = \frac{1}{2} \ln\left(\frac{1+\beta}{1-\beta}\right). \tag{3.2}$$

Hence, rapidities are additive. Pseudorapidity converges to rapidity when the momentum of the particle is very large compared to the mass of the particle so that the mass may be ignored [15].

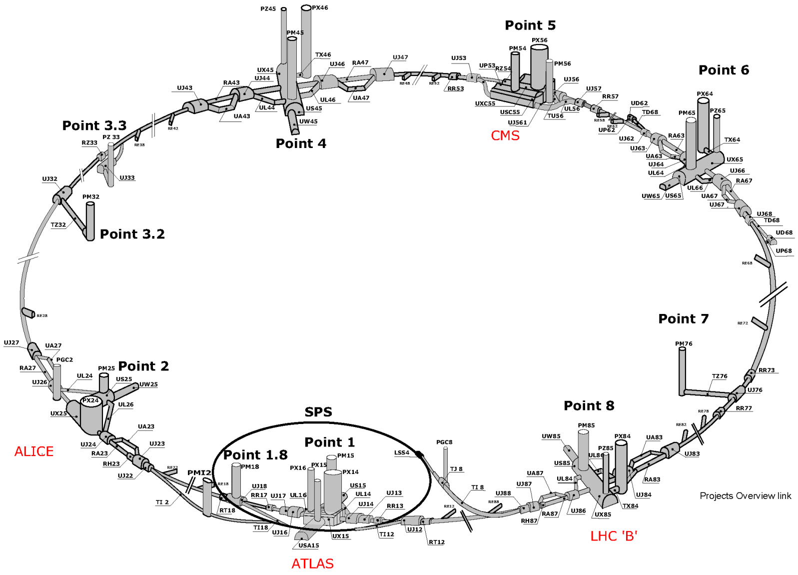

Fig. 3.6 The LHC ring with the various interaction points is shown above. ATLAS sits at Point 1, while CMS sits diametrically across at Point 5. LHCb sits at Point 8, and ALICE sits at Point 2.

The products of most collisions in ATLAS have most of their momentum along the beam axis (referred to as "forward" particles). High p_{T} electrons, muons, and hadrons are used as triggers for data acquisition, as they are often signatures of a high momentum-transfer process occurring in the proton collisions, such as the production of a massive boson. When the energy and longitudinal momentum are unable to be measured, but the polar angle can be, it is convenient to define the pseudorapidity variable η to characterize the particle. Pseudorapidity is defined as

$$\eta = -\ln\left(\tan\left(\frac{\theta}{2}\right)\right), \tag{3.5}$$

where θ is the polar angle [108]. Distances are often measured in the pseudorapidity-azimuthal angle space defined as

$$\Delta R = \sqrt{(\Delta\eta)^2 + (\Delta\phi)^2}. \tag{3.6}$$

3.2.2 The Inner Detector

The ATLAS Inner Detector (ID) is the subsystem closest to the beam pipe. The ID is a three-component tracking system consisting of silicon pixels, silicon microstrips, and a transition radiation tracker system which uses straw tube technology. Both barrel and end-cap systems exist for each component of the Inner Detector. A 5.3 m long, 15 m radius superconducting solenoid provides the 2 T field for the ID. A schematic of the detector is shown in Fig. 3.7.

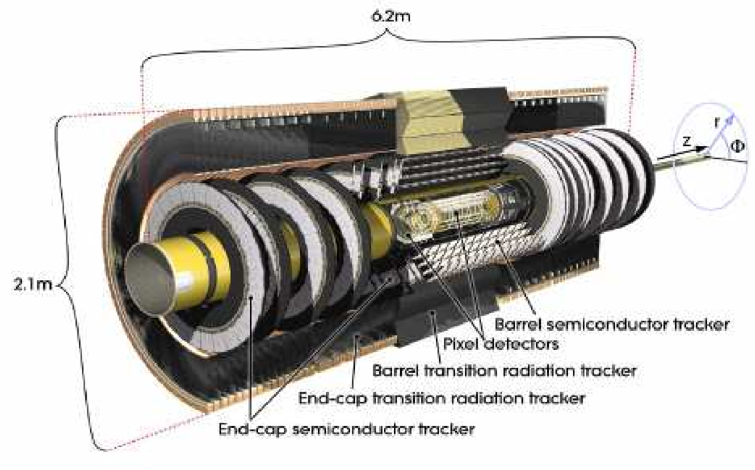

Fig. 3.7 A schematic of the ATLAS Inner Detector. The Inner Detector is composed of three different detector subsystems, namely the pixel detector, the semiconductor tracker (SCT), and the transition radiation tracker.

The pixel detector provides three precision points for tracks within the pseudo-rapidity range $|\eta| < 2.5$, and determines impact parameter resolution and the ability of the inner detector to find short-lived particles such as B-hadrons. It is made of three barrel layers[4] at radii of 50.5 mm, 88.5 mm, 122.5mm, with a total of 1456 modules, and three end-cap disks which are located at 7495 mm, 7580 mm and 7650 mm from the interaction point in the z direction, with a total of 288 modules. Each pixel module has an active region of $16.4 \times 60.8\,\mathrm{mm}^2$ and 250 μm thickness. The bulk n-type silicon sensors have an area of $50\times400\,\mu\mathrm{m}^2$. The modules are overlapped on the support structure to give hermetic coverage. The design resolution is approximately 10 μm in the r-ϕ direction and 115 μm in the z-r direction.

The semicondtructor tracker (SCT) is a detector which employs 4 layers of silicon microstrip detectors in the barrel section and 9 layers in the form of disks in the end-caps. Each layer is composed of two 285 mm thick p-in-n microstrip sensors glued back-to-back at a 40 mrad stereo angle. Each sensor has 768 strips AC-coupled to 6 ABCD3TA ASICs. For

---

[4] During the first long shutdown, as part of an upgrade to the ATLAS detector, a new fourth layer, named the insertable B-layer (IBL), was inserted into the pixel detector between the beam pipe and the layer 0 (also known as the B-layer), at an average radius of 33 mm. A new 25 mm radius beryllium beam pipe (4 mm smaller than used during Run 1) around the interaction region allows to accommodate the IBL.

the barrel modules, the pitch of the strips of 80 µm, while the strip width varies in the end-cap disks from 57 µm to 94 µm. The strip direction in the barrel modules is along the z-axis for axial modules, while for "stereo" modules, the strips are rotated 40 mrad with respect to the z-axis. The signal from each strip is shaped, amplified and compared to a threshold, nominally 1 fC. Binary output is then stored in a pipeline, sampled into three 25 ns bins (the middle synchronised with collisions) and read out if a trigger signal has arrived. Each module has two RX links for transmission of data to the Readout Driver Board (ROD) and one TX for receiving commands and trigger, both using VCSEL (Vertical-Cavity Surface-Emitting Laser) and PIN diode arrays. All 4088 modules combine for a total of 6.3 million readout channels.

Beyond the SCT sits the transition radiation tracker (TRT). The TRT covers the pseudorapidity region $|\eta| < 2.0$ and has continuous tracking to enhance the pattern recognition, to improve the momentum resolution. The TRT uses thin-walled straw tube technology to achieve momentum measurements. The tubes are filled with a $Xe/CO_2/O_2$ gas mixture as the active medium. The straws are interleaved with polypropylene to provide transition radiation to help identify electrons. Tracking information and transition radiation signals are obtained for each individual straw using separate low and high threshold discriminators in the front-end electronics. The barrel TRT is divided into 3 layers of modules in the radial direction and 32 sectors in ϕ. The straw tubes of the barrel TRT are 4 cm in diameter and have a length of 144 cm; they are oriented along the beam line. The TRT end-caps each consist of 2 types of independent wheels (referred to as "type-A" and "type-B") with straws oriented radially. The type-A wheels are closer to the interaction point and consist of 12 wheels, each with 8 successive layers spaced 8 mm apart. The type-B wheels are further from the interaction point starting after the last type-A wheel and consist of 8 wheels, also with 8 straw layers but spaced 15 mm apart. Each end-cap therefore has a total of 160 straw layers along the z-axis. For high p_T tracks originating from the interaction point, the design of the TRT ensures a large number of crossed straws (typically above 30) in the pseudorapidity range of $|\eta| < 2.0$.

3.2.3 ATLAS calorimetry

The calorimetry in ATLAS plays a key role of measuring showers initiated by photons, electrons, and hadrons. A superconducting solenoid magnet separates the ID from the calorimetry. The liquid-argon (LAr) calorimeter consists of the electromagnetic (EM) calorimeter, which sits inside the barrel crysostat, the hadronic end-cap (HEC) and the forward calorimeter (FCal). The active medium used for the collection of signal is liquid argon. The absorber consists of lead in the EM, copper in the HEC and the first layer of the

barrel EM	$\frac{\sigma_E}{E} = \frac{10\%}{\sqrt{E}} \oplus 0.7\%$
end-cap EM	$\frac{\sigma_E}{E} = \frac{10\%}{\sqrt{E}} \oplus 0.7\%$
HEC	$\frac{\sigma_E}{E} = \frac{50\%}{\sqrt{E}} \oplus 3\%$
FCAL	$\frac{\sigma_E}{E} = \frac{100\%}{\sqrt{E}} \oplus 10\%$

Table 3.1 Design energy resolutions of the different regions of the ATLAS LAr sub-system.

FCAL, and tungsten in the outer two layers of the FCAL. The lead absorbing material in the barrel EM covers a pseudorapidity range of $|\eta| < 1.475$, while the end-cap EM covers a range of $1.37 < |\eta| < 3.2$. The copper absorbing material of the HEC covers the range $1.5 < |\eta| < 3.2$, while the copper/tungsten absorber of the FCal covers the range $3.1 < |\eta| < 4.9$. The barrel EM and end-cap EM include a high-granularity accordion layer up to $|\eta| < 2.5$ and a presampler up to $|\eta| < 2.5$, which provides information to trigger on electron and photon objects. The LAr calorimeter system has 182468 readout channels in total. Ionisation electrons are produced by passage of charged particles in the material. They drift to electrodes and produce a triangular pulse shape, which is amplified, shaped and then sampled (at least 5 times) every 25 ns. The collected signal depends on the HV and the temperature and purity of the liquid argon. The design resolution of the Barrel, EM End-Cap, HEC, and FCAL are given in Table 3.1. The Tile Calorimeter (TileCal) is the barrel hadronic calorimeter covering the most central region of ATLAS. It is a key component for measurement of hadrons, jets, taus, and missing transverse energy. The TileCal is a sampling calorimeter which uses carbon steel (iron) plates as the absorber and plastic scintillating tiles as the active material. The particles produced in the interaction point travel through the calorimeter and light produced in the scintillating tiles is proportional to the energy deposited.

The TileCal consists of three cylinders, one long barrel (LB) split into two readout partitions, and two extended barrels that flank the long barrel on both sides, covering the most central region $|\eta| < 1.7$. Both the barrel and extended barrel cylinders are segmented into 64 modules in ϕ, corresponding to a $\Delta\phi$ granularity of 0.1 rad. The $\Delta\eta$ segmentation for each module is 0.1 in the first two radial layers and 0.2 in the third layer. The η, ϕ, and radial segmentation define the three dimensional TileCal cells. Each cell volume is made of dozens of iron plates and scintillating tiles. Wavelength shifting fibres coupled to the tiles on either edge of the cells collect the produced light and are read out via square light guides by two different photomultiplier tubes (PMTs), each linked to one readout channel. Analog pulses are received by digitizers where they are sampled every 25 ns. The pulses are shaped by passive circuits; the shaped pulse is amplified in separate high (HG) and low (LG) gain branches The HG and LG signals are sampled with the LHC bunch-crossing frequency of 40 MHz using a 10-bit ADC in the Tile Data Management Unit (DMU) chip which is located on the digitiser board.

The calibration system of the TileCal allows for adjustment of the energy on a channel-by-channel basis. A charge-injection system simulates physics signals in the TileCal channels by generating pulses from discharge capacitors in the read- out circuit and measuring the electronic response. A caesium system uses a movable radioactive source to equalise the response of all the cells and maintain a global response of the calorimeter. A laser calibration system tests the gain of each PMT. Finally, an integrator system integrates the response of the PMTs over time to measure the low-energy products of the majority of the proton-proton collisions in a given bunch crossing. This allows for a determination of the luminosity.

3.2.4 The muon system

Two different types of muon detectors are used in ATLAS, gaseous drift chambers for providing position measurement and “trigger” chambers such as resistive plate chambers (RPCs) and thin gap chambers (TGCs). Specifically, the ATLAS muon spectrometer consists of Monitored Drift Tubes (MDTs) for precision tracking in the spectrometer bending plane. The muon system also serves as a trigger to select events with high energy muons. This is accomplished via RPCs and TGCs for triggering in the barrel and end-cap, respectively. The chambers form three concentric cylindrical layers at radii of 5, 7.5, and 9.5 in the barrel region, and cover a pseudorapidity range of $|\eta| < 1.0$. In the forward region, the chambers are arranged in four vertical disks perpendicular to the beam axis at distances of 7, 11, 13.5, and 22m. The magnet system consists of 3 sets of air-core toroids, each with 8 coils, one for the barrel and one for each end-cap. The magnetic field provides a 1 T field at the centre of each coil. However, the magnetic field is non-uniform, especially in the barrel end-cap transition region. The design momentum resolution of the muon spectrometer is $\frac{\sigma_p}{p} = 3\%$ at 100 GeV and 10% at 1 TeV.

3.2.4.1 Muon tracking chambers

The basic component of the MDT chambers are aluminum tubes of 30 mm diameter and 400 µm thickness, with a central wire of 50 µm in diameter. The tubes are operated with a mixture of Ar/CO_2, and are arranged in multilayers consisting of three or four monolayers, respectively, on either side of a rigid support structure called a spacer frame. The nominal single wire resolution (per tube) is 80 µm.

The CSCs are the forward ($2.0 < |\eta| < 2.7$) precision muon system of ATLAS, located in the innermost layer of the muon end-caps. The chambers determine muon position by interpolating the charge on adjacent strips in four-layer chambers of multiwire proportional detectors with segmented cathode readout. There are 16 four-layer sets of CSCs on either side of the muon spectrometer system. The proportional chambers operate at a gas gain of 60 000 in an Ar/CO_2 gas mixture with two planes of cathode strips to measure the bending coordinate. The sensor wire pitch is 2.54 mm, and the pitch of the readout strip is 5.08 mm. The cambers are designed to handle higher background rates closer to the beam pipe. The nominal track resolution in the bending plane is 60 µm.

3.2.5 ATLAS trigger system

ATLAS employs a three-level trigger system; its first level (LVL1) is implemented in electronics and firmware (mostly ASICs and FPGAs), whereas the high-level triggers[5] are based on software algorithms which run at large computing farms [110]. The LVL1 decision is based on data from the calorimeters and muon trigger stations. It is capable of triggering on different types of objects such as inclusive high transverse momentum muons, taus, or jet clusters, forward jets, missing transverse energy, and total transverse energy sum [111]. The LVL1 system must reduce the rate of 1 GHz proton-proton interactions and 40 MHz beam-beam bunch crossings to 75 kHz within a maximum latency of 2.5 µs. The LVL2 trigger receives the results of the LVL1 trigger items and information on Regions of Interest (ROI) where LVL1 observed interesting objects. Execution of algorithms for LVL2 is controlled by the HLT steering software which runs the algorithm for each ROI [112]. The Event Filter is also controlled by the HLT steering. The trigger is designed to reduce the rate from an initial bunch-crossing rate of 40 MHz (interaction rate of 1×10^9 MHz at a luminosity of $10^{34}\,\mathrm{cm}^{-2}\cdot\mathrm{s}^{-1}$) by a factor of approximately 1×10^7 to around 200 Hz for permanent storage [113].

Events are written out into one or several "streams" depending on the Event Filter chains that were passed [112]. This allows one to reprocess events separately for each stream. There are several different physics streams. In addition to physics streams there are two special types of streams, the express stream and calibration stream. The express stream is processed within one to two hours after data taking and is designed for prompt reconstruction for use in monitoring and debugging before the bulk reconstruction. The calibration

---

[5] The LVL2 trigger and Event Filter are collectively referred to as the High Level Trigger, (HLT). A full description of the High-Level Trigger is given in [109].

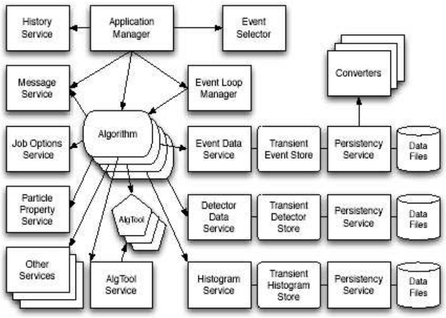

Fig. 3.8 A schematic of the component model of the Athena software framework.

stream is used to collect a large data sample for detector calibrations, whereas the express stream consists of only a portion of events from physics streams. For physics there are several inclusive data streams from the Trigger Physics Menu at an instantaneous luminosity of $10^{31}\mathrm{cm}^{-2}\cdot\mathrm{s}^{-1}$: egamma, jetTauEtMiss, muon, and minBias[111].

3.3 The Athena software framework

ATLAS uses an object-oriented software framework [114] written in C++ for reconstruction of events, simulation, and serialisation of physics objects into persistified data formats which follow the event data model (EDM). Athena builds on the Gaudi framework [115] developed for the LCHb collaboration. Athena follows the blackboard design where instances of abstractions called algorithms work as factories that read and write from a central transient event store. Algorithms exist as well-defined sequences of commands used to process data, each with an initialisation phase, a phase which loops over all events to be processed, and a final phase which performs and functions after all events are processed. Abstractions called tools and services carry most of the algorithmic workload. The properties of the algorithms, tools, and services are configurable [116] via python, which allows an individual algorithm to essentially plug in to the main framework and be configured properly and execute in the right sequence relative to other algorithms. A schematic of the Athena component model, showing the flow of data to various services and tools is in Fig. 3.8.

3.4 Event simulation in ATLAS

Simulation of the detector is critical to understanding detector behaviour and performance of the various subsystems as well as to understand detector acceptance for a wide range of physics processes. Simulation of collisions in ATLAS follows three general stages, handled almost entirely within the Athena framework: event generation of particles produced in the collision and their decays using a Monte Carlo (MC) generator, simulation of particles through the detector material, and digitisation of the readout from the detector subsystems/particle reconstruction. The output of the simulation chain can be presented in either an object-based format or in a format identical to the output of the ATLAS data acquisition system (DAQ). Thus, both the simulated and real data from the detector can then be run through the same ATLAS trigger and reconstruction packages.

3.4.1 Event generation

Event generation consists of the production of a set of particles that is passed through a model of the detector for simulation between the detector medium and the particles emerging from the collision. There are various generators employed by ATLAS for different physics processes, i.e., Higgs production, $t\bar{t}$ production, vector boson production in association with jets, as well as particle production in various BSM scenarios such as supersymmetric squarks, sleptons, and charginos, or black holes. Only the generators used for the ZZ analysis are presented here; a more comprehensive list is included in [117], while generators used in ATLAS are described in [118].

- POWHEGBOX [119] is a general framework for generation of events at NLO using the POWHEG [120] method to match matrix elements to parton showers (using only positive weights). Available processes include single vector boson production with decay, single top production in the s and t-channels, jet pair production, as well as vector boson pair production. The events produced by POWHEGBOX can be interfaced to PYTHIA or HERWIG for showering. POWHEGBOX is used to model the main process of $q\bar{q} \to ZZ$ at NLO. However, it does not include the contribution from gluons (Section 2.2), which is modelled using a separate generator gg2VV.

- MCFM is a parton-level Monte Carlo program which gives NLO predictions for various processes at hadron colliders. Matrix elements are calculated at NLO, incorporating full spin correlations. Processes include $W+$jets, $Z+$jets, $H \to WW$ and $H \to ZZ$, as well as diboson WW,ZZ and direct photon production. MCFM is not a full generator in the sense that it cannot produce unweighted events suitable for use in a physics analysis. It is a cross section calculator and serves as a very useful comparison to POWHEGBOX.

- gg2VV [121] represents the merging of the gg2ZZ and gg2WW [122] generators. It is a parton-level integrator and event generator for the $gg \to (H \to)\ WW$ and

$gg \rightarrow (H \rightarrow)\, ZZ$ processes. gg2VV accounts for the interference between the continuum $gg \rightarrow ZZ$ production and production which proceeds via a Higgs resonance [121]. However, the calculation is only available at the lowest-order treatment of the gluon-induced process, which is the same level as is done in MCFM.

- SHERPA [123] is a leading-order generator, which allows for additional jets in the matrix element. The list of physics processes that come with Sherpa covers particle production at tree level in the Standard Model and in models beyond the Standard Model, such as models with large extra dimensions, or an extended Higgs sector. SHERPA uses its own inbuilt matrix-element generators as well as its own phase-space generator, which automatically calculate and integrate tree-level amplitudes for the implemented models. This feature enables Sherpa to be used as a cross-section integrator and parton-level event generator as well.[6] SHERPA also implements its own parton showering algorithms, and it is not necessary to interface to a parton showering program such as JIMMY. Models with anomalous gauge couplings within the framework described in Section 2.4.1 have been implemented with SHERPA. The baseline samples used to model signal acceptance in a scenario with non-zero ZZV aTGCs are taken from SHERPA.

- MC@NLO [124] is an event generator which interfaces NLO calculations to parton showers using the MC@NLO technique [125]. The program is based on the HERWIG parton shower algorithm. MC@NLO may produce vector boson pairs, but in general is not used within ATLAS for modelling acceptance, as it uses the zero-width approximation in the case of ZZ production and does not include the Z lineshape. In addition to vector boson plus jet production it is typically used for modelling both single top and $t\bar{t}$ production as well as vector boson production in association with top.

- PYTHIA8 [126] is an event generator which implements a wide range of processes at leading order, including hard gluon scattering, direct photon production, charmonium and bottomium production, low-mass Drell-Yan pairs, as well as Higgs production. PYTHIA uses a p_{T}-ordered shower, as opposed to angular-ordering used by HERWIG [127], and this feature has remained unchanged since the older Fortran version of PYTHIA. Both the $q\bar{q}$ and gg signal samples for the $ZZ \rightarrow \ell^-\ell^+\nu\bar{\nu}$ analysis are showered using PYTHIA8.

---

[6] More recently, the processes $pp \rightarrow \ell^-\ell^+\nu\bar{\nu}$ and $pp \rightarrow \ell^-\ell^+\nu\bar{\nu} + 1$ jet have been implemented in SHERPA+OPENLOOPS including both the fully-gluonic states and also the quark-induced $qg \rightarrow \ell^-\ell^+\nu\bar{\nu} + q$, $\bar{q}g \rightarrow \ell^-\ell^+\nu\bar{\nu} + \bar{q}$ channels are taken into account, however this is not fully implemented within the ATLAS framework yet.

- HERWIG is a general-purpose LO MC generator which includes the simulation of hard lepton-lepton, lepton-hadron and hadron-hadron scattering and soft hadron-hadron collisions. It uses the parton shower approach for initial and final-state QCD radiation including colour-coherence effects and azimuthal correlations both within and between jets. Available processes include vector boson production in association with jets, WW and ZZ production as well as various $q\bar{q} \to H$. Herwig also uses a different hadronisation model compared to PYTHIA. The Fortran version of HERWIG is no longer developed and has been replaced by HERWIG++[128], which uses a general purpose C++ library (THEPEG) for implementing parton shower algorithms.

Most generators are written completely independently of the ATLAS software, so there must be an interface between them and the Athena software used for the generation. Many of the generators above output events in the Les Houches event file format [129], although some output events in different formats. The ATLAS simulation framework interfaces to all the generators to output HepMC GenEvents [130] format. Each generated event contains the particles from a single interaction with a vertex located at the geometric origin. Particles with a proper lifetime $c\tau > 10\,\mathrm{mm}$ are considered stable by the event generator, and can propagate far enough to interact with the detector material.

3.4.1.1 Simulation

The standard simulation relies on the Geant4 [131, 132] particle simulation kit. This is the most computationally intensive portion of the full simulation chain, and often determines how many events of a given process are generated to model a certain physics process. The geometric model (GeoModel) used by ATLAS is built up of basic solids and shapes into groupings called logical volumes, physical volumes and total volumes. The GeoModel is actually decoupled from the Athena software framework. A model of the detector typically has at least several hundred thousand physical volumes. The entire geometry is translated into a Geant4 equivalent. Many layouts are available corresponding to the previous revisions of the material. The material budget is constantly updated to accurately reflect the current detector geometry. It is also possible to apply detector “conditions” modifications to each chosen geometry layout; a misalignment can be configured by selecting misaligned layouts either for each subdetector or for the full detector. Also, while the generated events have their interaction at the detector origin, modifications to account for the beam properties are applied to the event before it is passed to the detector model. The simulation step outputs sequences of energy deposits and times in sensitive detector volumes (“HITS” files).

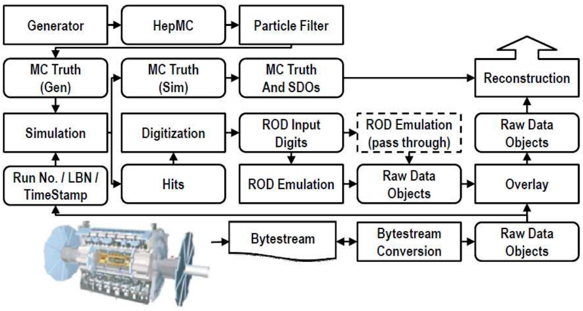

Fig. 3.9 A flow diagram showing the various stages of the ATLAS simulation process. Figure taken from [133].

3.4.1.2 Digitisation

The ATLAS digitisation software converts the hits produced by the simulation software into detector responses, referred to as “digits”. The input to the digitization is a specific “hits” file format. A digit is produced when the voltage or current on a particular readout channel rises above a pre-configured threshold within a particular time window. Each detector’s unique charge collection pattern are modelled in subdetector-specific digitization software. The various subdetector digitisation packages are steered by a top-level Python digitization package. Dead channels and noise rates are read from database tables to reproduce conditions previously seen over a sufficiently large enough period of data acquisition. The digits of each subdetector are written out as Raw Data Objects (RDO’s). The bunch profile of the beams and the luminosity of a given detector run to give an accurate reflection of the average number of collisions. Pileup is added at the digitisation stage by combining multiple minimum bias events spaced out over a sufficient period of time, and overlaying that with the main physics process being simulated. A flow diagram showing the various stages of the simulation is shown in Fig. 3.9.

Chapter 4

Physics object definitions and reconstruction in ATLAS

In *pp* collisions at the LHC, electrons, muons, photons and jets can be produced with a large range of energies, from a few GeV to several TeV. The following sections describe the methods by which objects are identified and reconstructed in ATLAS, and the challenges faced in trying to reconstruct such quantities.

4.1 Vertex and track reconstruction

4.1.1 Primary vertex reconstruction

The primary vertex reconstruction framework is implemented within the Athena software environment (Section 3.3), and allows the reconstruction of the primary vertices in both low and high luminosity regimes of the LHC. The reconstruction of primary vertices in ATLAS is generally subdivided into two stages [134]:

- **Primary vertex finding:** association of reconstructed tracks to a particular vertex candidate.
- **Vertex fitting:** reconstruction of the actual vertex position and its covariance matrix, estimate of the quality of the fit, refit of the incident tracks.

There are multiple ways of obtaining an unbiased estimator for the vertex. One may iteratively remove tracks incompatible with the actual vertex and fit again, or one may weight the track contribution to the χ^2 with the estimated “a priori” probability of that track to belong to the vertex to fit. In ATLAS, primary vertices are reconstructed using an iterative

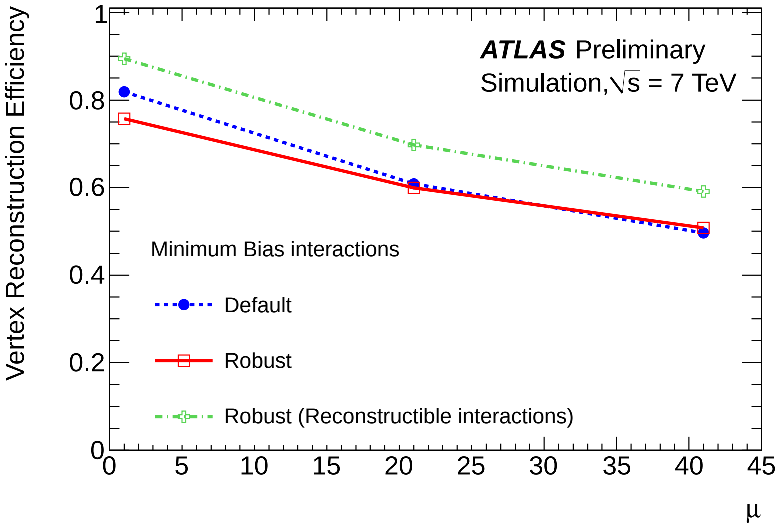

Fig. 4.1 The vertex reconstruction efficiency as a function of the average number of interactions in minimum bias Monte Carlo simulation. Figure taken from [137].

vertex finding algorithm [135]. Vertex seeds are obtained from the z-position at the beamline of the reconstructed tracks. An iterative χ^2 fit is then made using the seed and nearby tracks. Tracks displaced by more than 7σ are used to seed a new vertex and the procedure is repeated until no additional vertices can be found [136]. The beam spot position is used as a constraint [137]. Vertices are required to contain at least two tracks. The efficiency to reconstruct a vertex from a minimum bias interaction as a function of the average number of interactions per bunch crossing is shown in Fig. 4.1.

4.1.2 Track reconstruction

A track is a sequence of hits in subsystems which represent the trajectory of a charged particle. Each proton-proton collision gives rise to a large number of particles, which produces a large number of hits in the ATLAS inner detector subsystem. The track reconstruction software must distinguish hits from different charged particles to determine a trajectory that best matches a given set of measurements. Several different algorithms of track finding are used in ATLAS, but the primary track reconstruction strategy is the “inside-out” tracking method. The basic steps of the “inside-out” method involve pattern recognition [138], ambiguity solving, and TRT track extension. The measurements in the pixel detector and SCT form “silicon space-points”, which represent a three-dimensional point formed either from a cluster of silicon pixels, or from the intersection of the front and back sensors of a silicon module in the SCT. The pattern recognition starts by finding track seeds that are formed from all sets of three silicon space-points that are compatible within minimum cut of 500 MeV. The track seeds provide the necessary information to associate additional silicon hits to a track segment by using a fast Kalman filter [139] to follow the trajectory. Because many of the initial track candidates will share hits, or be incomplete, these ambiguities must be solved to form tracks. The ambiguity-solving process assigns a score to each track candidate to indicate the likelihood that the track candidate originated from a real particle trajectory. This score is evaluated via a global χ^2 fit, using a refined reconstruction geometry. In general, each hit associated with the track leads to a higher score, while holes, defined as the passage of the track through a detector element that was known to be active without producing a hit, will lower the track score. Ambiguities are resolved by choosing the track with the greater score. The fitted silicon track parameters at the outermost silicon measurement, closest to the TRT are used to define a "road" through the TRT, and any drift radius measurements that are within 10 mm of this road are assigned to the track. The track is then re-fitted with the additional TRT measurements and compared with the original silicon-only track using the scoring mechanism. If the quality of the fit to the track improves as a result of the association of information from the TRT, the track extension is kept.

4.1.3 Outside-in tracking

The inside-out sequence relies on a track seed to be found in the silicon detector. However, not all tracks can be found through an inside-out procedure. The track reconstruction sequence is complemented by an "outside-in" strategy, which starts from unassigned TRT segments and looks for matching hits in the pixel and SCT detectors. Track segments are identified using a standard Hough transform mechanism, while a dedicated association tool prevents hits that have already been assigned to tracks in the inside-out procedure to be used again, which saves a significant amount of CPU time.

The tracking efficiency as a function of p_{T} and η for samples with no pile-up ($\langle\mu\rangle = 1$) and significant pile-up are shown in Figs. 4.2(a) and 4.2(b).

4.2 Electron and photon reconstruction

4.2.1 Electron/photon trigger

The input to the electron/photon and tau/hadron trigger algorithms is a set of approximately 7200 trigger towers of granularity 0.1×0.1 formed by analogue summation of calorimeter cells. These triggers cover the region $|\eta| < 2.5$. The ATLAS electron/photon trigger algorithms are based on a window of 2×2 towers which overlap EM clusters (each summed)

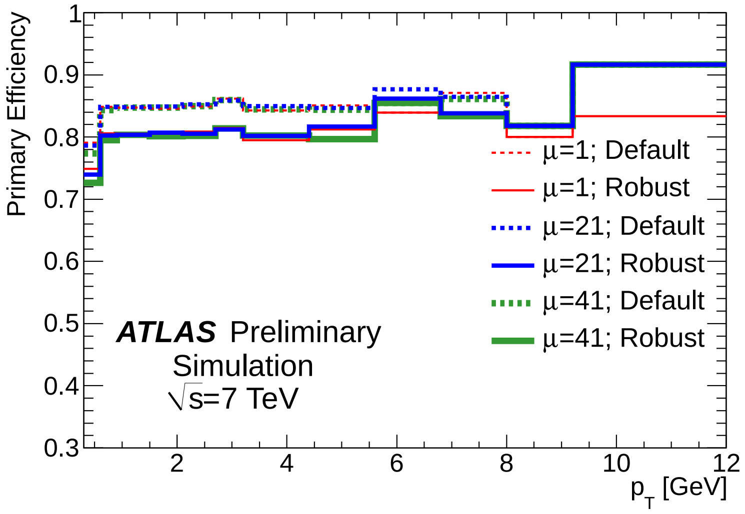

(a)

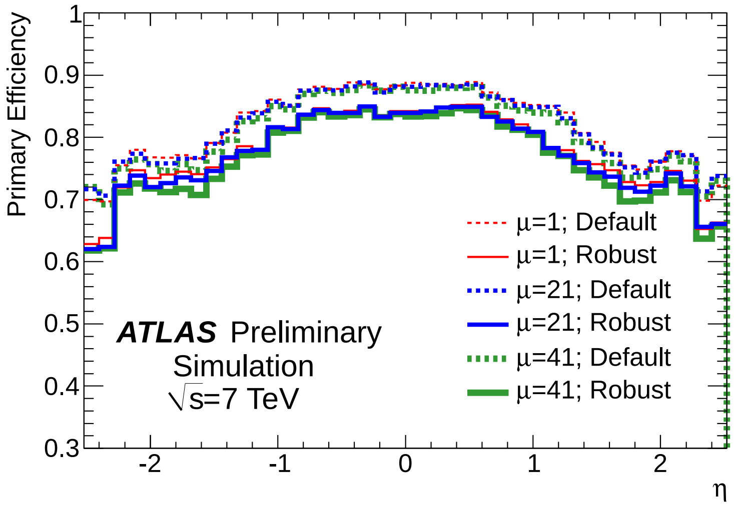

(b)

Fig. 4.2 The primary and secondary track reconstruction efficiency in minimum bias Monte Carlo samples as a function of (a) and (b) containing exactly one and on average 21 or 41 interactions per bunch crosssing at an energy of $\sqrt{s} = 7$ TeV. Figure taken from [136].

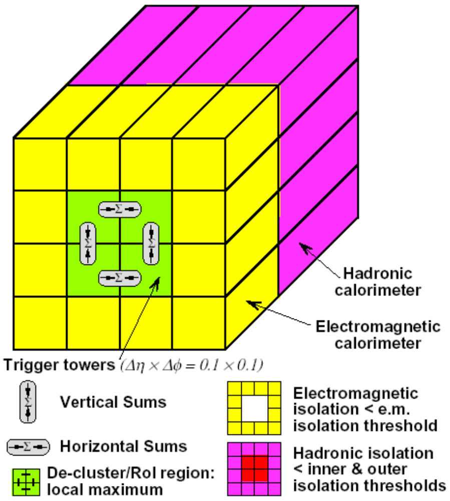

Fig. 4.3 A schematic of the L1 electron/photon calorimeter trigger algorithm. The algorithm is implemented in FPGAs, and identifies regions of interest from 2 ×2 EM tower that have E_{T}above threshold. EM isolation is achieved using surrounding 12 EM towers, and hadronic veto is done using the towers in the tile calorimeter. Figure taken from [140].

over two EM towers, shown schematically in Fig. 4.3. At L1, electromagnetic objects are selected if the total transverse energy deposited in the EM calorimeter in two adjacent towers is above a certain threshold. Electron triggers require that no energy is deposited in the hadronic calorimeter behind the energy cluster in the electromagnetic calorimeter associated with a trigger electron object. The algorithm itself is implemented in FPGAs. The L2 calorimeter reconstruction is very similar to the offline algorithm, except that clusters are seeded by the highest E_{T} cell in the middle calorimeter layer instead of applying the full online sliding-window algorithm. The Event Filter uses the offline reconstruction and identification described in the following sections, although it applies typically looser cuts in order to remain fully efficient.

4.2.2 Electron/photon reconstruction and identification

Electrons emerging from the collision point will pass through the inner detector and subsequently deposit their energy in the electromagnetic calorimeter (ECal). Electrons in the pseudorapidity range $|\eta| < 2.47$ are therefore reconstructed by matching an inner-detector track with an energy cluster in the ECal. This is referred to as the "standard" electron reconstruction. For electrons in the pseudorapidity range $2.47 < |\eta| < 4.9$, there is no corresponding track from the inner detector due to coverage of the ID, and electrons are reconstructed solely from calorimeter clusters, these are referred to as "forward" electrons. Only standard central electrons are used in the $ZZ \to \ell\ell\nu\bar{\nu}$ analysis, however, several AT-

LAS analyses, including the $ZZ \to \ell^-\ell^+\ell^-\ell^+$ analysis use forward electrons. Electrons are distinguished from other particles using several sets of identification criteria with varying levels of background rejection and signal efficiency.

To reconstruct EM clusters, seed clusters of longitudinal towers with total cluster transverse energy above 2.5 GeV are searched for by a "sliding-window" algorithm [141]. The window size is 3×5 in the $\eta - \phi$ space. A duplicate removal algorithm is applied on close-by seed clusters. For each seed EM cluster passing loose shower shape requirements of $R_\eta > 0.65$ and $R_{\text{had}} < 0.1$, a region-of-interest (RoI) with a cone-size of $\Delta R = 0.3$ around the seed cluster is formed. Track candidates are then fitted either with the pion hypothesis or the electron hypothesis using the ATLAS Global χ^2 Track Fitter. If a track candidate fails the pion hypothesis track fit, it is refitted with the electron hypothesis. Tracks are then considered loosely matched to an EM cluster by passing one of two criteria based on extrapolation of the track to the middle layer of the (accordion) ECal. The track parameters of the electron candidates are re-estimated using an optimised electron track fitter referred to as the Gaussian Sum Filter [142], which is a non-linear generalisation of the Kalman filter algorithm. An electron is reconstructed if at least one track is matched to the seed cluster. While all tracks assigned to a cluster are kept for further analysis, the best matched track is chosen as the primary track which is used to determine the kinematics and charge of the electron and to calculate the electron identification decision. The choice of the primary track is therefore a critical step in the electron reconstruction chain.

4.2.3 Electron identification

Not all objects built by electron reconstruction algorithms are signal electrons. Background objects include hadronic jets as well as background electrons from photon conversions, Dalitz decays and semi-leptonic heavy flavour hadronic decays. In order to reject as much of these backgrounds as possible while keeping the efficiency for signal electrons high, electron identification in ATLAS is based on discriminating variables, which are combined into a "menu" of selection criteria of increasing background rejection power. Both cut-based and multivariate (MVA) techniques are used.

The cut-based selections define the `isEM` menu, consisting of three different operating points: `loose`, `medium`, `tight`. A fourth operating point, `multilepton`, was introduced for 2012 data taking. These selections are optimised in 10 bins in $|\eta|$ and 11 bins in E_T. All tighter selections are strict subsets of looser selections, i.e. tight is a subset of medium, and medium is a subset of loose. The cut-based electron identification has been used in ATLAS since the first full run of the LHC in 2010. In 2011, as instantaneous luminosities increased to $\mathcal{O}(10^{33}\text{cm}^{-2}\text{s}^{-1})$ the background rejection provided by the re-optimised medium operating point was not enough to provide sustainable rates in the trigger, and that tightening the requirements for the isEM menu would lead to large efficiency losses to achieve more background rejection. Instead of increasing the number of variables to achieve a higher working point, i.e. from `loose` to `medium`, etc., it was decided to use the same set of variables at all levels and tighten the operating points by tightening the cut values used at subsequent levels. For the 2011 and 2012 menus, the working points are referred to as `loose++`, `medium++` and `tight++`, collectively referred to as the `isEM++` menu.

There are three general categories of discriminating variables for electron and photon identification. The first category considers the amount of energy deposited in different layers of the EM and the hadronic calorimeters relative to the total cluster energy. Real prompt photons should be isolated from hadronic activity, so the energy seen in the hardonic calorimeter should be small relative to the energy of the photon cluster. The two variables which quantify this are:

- R_{had}: the ratio of total transverse energy in the hadromic calorimeter to the transverse energy of the cluster,
- R_{had_1} the ratio of the transverse energy in the first sampling layer of the hadronic calorimeter to the transverse energy of the cluster.

The shower evolution in the second sampling layer is described by three variables:

- w_η: the lateral width of the shower in η over a region of 3×5 cells in $\eta \times \phi$ around the centre of the cluster,
- R_ϕ: The ratio in ϕ of cell energies in 3×3 and 3×7 cells,
- R_ϕ: The ratio in η of cell energies in 3×7 versus 7×7 cells.

There are five variables that characterise the shower profile in the strip layer:

- w_{s3}: The shower width for three strips around the strip with the maximum energy deposit,
- F_{side}: The energy outside the core of three central strips but within seven strips divided by the energy within three central strips,
- ΔE: The difference between the energy associated with the second maximum strip layer, and the energy reconstructed in the strip with the minimal value found between the first and second maxima,

- E_{ratio}: The ratio of the energy difference associated with the largest and second largest energy deposits over the sum of these energies.

The `medium++` working point for electrons in the $ZZ \to \ell^-\ell^+\nu\bar{\nu}$ analysis makes use of all of these variables. The full requirements are specified in [143].

4.2.4 Photon reconstruction

Reconstructed photons are seeded by clusters of energy in the electromagnetic calorimeter. Clusters are formed with the same sliding window algorithm used for electrons. The clusters have an E_{T} threshold of 2.5 GeV, and a size in layer 2 of the ECal of 3×5 cells in $\eta \times \phi$. They are distinguished from electrons by the absence of a track in the ID matching the candidate cluster. To distinguish between photons and electrons, a track-matching procedure follows cluster finding. Tracks are required to be within a rectangular window in $\Delta\eta \times \Delta\phi$ of 0.05×0.10 of the cluster barycentre, with a minimum track momentum of 10% of the cluster energy. If such a track is found, the candidate is assumed to be an electron candidate, and its position and energy are calibrated under that hypothesis. Clusters not matched to a track are classified as photons, and are stored in a photon container.

4.2.5 Photon identification

Prompt photons need to be separated from jets with significant electromagnetic components primarily coming from electromagnetic decays of light neutral mesons in hadronic jets. The ATLAS photon identification algorithm relies on a series of cuts using measurements of variables derived from energy deposits in the ECal cells. These variables represent different quantities as measured from shapes of electromagnetic shower profiles in the primary (second) layer and the “strip” layer of the ECal. A menu of two different photon qualities (`loose` or `tight`) was provided for photons in 2012 similar to the menu of operating points for electrons, where additional selections are placed to provide a tighter definition.

A photon coming from the hard scattering can “convert” to an electron-positron pair as it travels through the ID and material before the ECal.[1] The ID is used to reconstruct converted vertices up to a radius of less than 80 cm associated to a photon cluster. In this case, the photon candidate is referred to as a “converted” photon.

---

[1] Photon conversions are not covered in depth. For a more thorough description on photon conversions and cluster calibration, the reader is referred to [144].

4.2.6 Photon Isolation

An isolation requirement based on the transverse energy deposited in the calorimeters in a cone around the photon candidate can be used to differentiate between prompt photons from hard-scatter processes and photons from neutral hadrons (e.g π^0) which decay into two photons. The transverse isolation energy, $E_{\mathrm{T}}^{\mathrm{iso}}$, is computed using calorimeter cells from both the electromagnetic and hadronic calorimeters, in a cone of radius R in the $\eta - \phi$ space around the photon candidate. Correction for energy leakage outside of the cone and pileup effects is described in [144, 145]. ATLAS uses the variables `EtCone` for a measurement of the calorimeter isolation energy. The `EtCone` variables are the scalar sums of the transverse energy in all calorimeter cells within a cone of a given radius around the photon axis. The rectangular core of cells (5×7 in $\eta \times \phi$) closest to the photon is excluded from the sum.

4.3 Muon triggering

The muon trigger [146] selects events with muons in three steps. The first step uses fast-response trigger chambers and custom-built hardware to generate a L1 trigger based on hit coincidences. The second and third step make up the High Level Trigger (HLT), and are software-based. The L1 muon trigger identifies candidates by a coincidence of hits in two layers (“low p_{T}”) or three layers (“high p_{T}”) in the Resistive Plate Chambers (RPC) or the Thin Gap Chambers (TGCs) in the end-cap. The L1 trigger carries information as to which part of the detector the muon passed, the RoI. The momentum is estimated by looking at the degree of deviation of the hit pattern from a straight line. The p_{T} is classified according to a set of pre-defined thresholds indicated by labels like `mu15` (for $p_{\mathrm{T}} > 15$ GeV). `mu10` and lower are defined as “low p_{T}” triggers, while `mu11` and higher are defined to be “high p_{T}” triggers. The L2 and EF triggers start by reconstructing a muon track using only the data from the MS (trigger chambers and precision chambers), referred to as a “standalone track”. This track is combined with a track in the Inner Detector to form a “combined” muon. The muon EF uses the full off-line algorithms, running in RoIs determined by the L2 trigger. There are two reconstruction strategies used at EF level: outside-in and inside-out. In 2011, both strategies were run in parallel to maximise efficiency. In 2012, to reduce processing time, the outside-in algorithm was run first, and only if an event were to fail finding a muon candidate was the inside-out algorithm run.

To allow for a lower p_{T} threshold while keeping the trigger rate manageable, isolation criteria are added as an extra requirement to the muon candidate. The isolation algorithm sums the p_{T} of all ID tracks ($p_{\mathrm{T}} > 1$ GeV) in a cone with $\Delta R = 0.2$ centred around the muon candidate. The relative track isolation is obtained by subtracting the p_{T} of the muon from this sum, and dividing by the p_{T} of the muon itself. The isolation requirement was introduced in the main single-muon trigger in 2012. Primary muon triggers refer to general-purpose triggers that were not pre-scaled during the whole of 2012 running, and are listed below in Table 4.1.

4.4 Muon reconstruction

Muons are reconstructed from information obtained from hits in the muon spectrometer and tracks from the inner detector. ATLAS has four different types of muons used for analyses based on the detector subsystems used to identify the muon candidates: combined, segment-tagged, standalone, and calorimeter-tagged.

- **Combined muons:** Combined muons are the highest purity muon candidates. They are formed from the combination of an MS track with a track from the ID. The efficiency of their reconstruction is strongly affected by acceptance losses in the Muon Spectrometer subsystem. For instance, at $\eta \approx 0$, the MS is only partially equipped with muon chambers to provide spaces for services of the ID and the calorimeters.

- **Segment-Tagged muons**: Segment-tagged muons are formed from the combination of an MS track segment and an ID track.

- **Standalone:** Standalone muons are formed solely from hits in the MS and the tracks are extrapolated to the beamline

- **Calorimeter-tagged muons:** calorimeter-tagged muons are formed by matching ID tracks to calorimeter deposits consistent with a minimum ionising muon. No information from the MS is used.

There are two parallel muon reconstruction chains in use in ATLAS, `STACO` (chain 1) and `MUID` (chain 2). The `STACO` algorithm performs a *sta*tistical *co*mbination of independent track measurements from the ID and the MS using the parameters of the reconstructed tracks and their covariance matrices. The `STACO` chain begins the reconstruction of MS tracks with the MuonBoy algorithm. Next, straight track segments are formed by trying to combine each MDT hit of a multilayer with every MDT hit in the other multilayer of the same or adjacent station [147]. The hits are close enough in space at this stage for the straight line approximation to be valid locally. Magnetic field deflections are taken into account at the track fitting stage. At first pass, track segments are required to be associated with at least one second-coordinate hit. A second “loose” track segment search follows the

Trigger	L1	L2	Event Filter
`mu24i`	MU15	$p_{\mathrm{T}} > 22$ GeV	$p_{\mathrm{T}} > 24$ GeV, $\sum^{\Delta R<0.2} p_{\mathrm{T}}^{\mathrm{trk}}/p_{\mathrm{T}}^{\mu} < 0.12$
`mu36`	MU15	$p_{\mathrm{T}} > 22$ GeV	$p_{\mathrm{T}} > 36$ GeV
`mu40_SA_Barrel`	MU15	$p_{\mathrm{T}} > 40$ GeV, $\lvert\eta\rvert < 1.05$	$p_{\mathrm{T}} > 40$ GeV, $\lvert\eta\rvert < 1.05$
`2mu13`	2MU10	2μ with $p_{\mathrm{T}} > 13$ GeV	2μ with $p_{\mathrm{T}} > 13$ GeV
`mu18_mu8_FS`	2MU15	1μ with $p_{\mathrm{T}} > 18$ GeV	1μ with $p_{\mathrm{T}} > 18$ GeV

Table 4.1 Primary muon triggers in ATLAS for 2012 running with their L1, L2 and EF thresholds. The `mu24i` and `mu36` are used in the $ZZ \to \ell^-\ell^+\nu\bar{\nu}$ analysis (Section 5.5).

strict search, based on less stringent cuts. Tracks are first seeded from "strict" segments, with a first rough estimate of the momentum taken frmo the position and direction of the segment. Inner segments are extrapolated to outer stations and vice-versa using tracking in the magnetic field. Several trials are performed for different values of the momentum around the first estimate. This is referred to as a "momentum scan". If a match is found, the best match is included in the candidate track and a fit is performed leading to a second and more accurate estimate of the momentum. A second finer momentum scan around the improved momentum estimate is then performed. To obtain a global estimate of the likelihood of the candidate track, a global fit is performed using raw information, starting from the best result of previous fits. A final fit is then performed taking into account material traversed by the muon; this is done by adding additional fit parameters. This accounts for multiple scattering effects and energy loss of the muon as it traverses the detector. The corresponding scattering angles are free parameters in the fit using the small-angle approximation added as a constraint to the χ^2.

The muon reconstruction efficiency, the momentum scale and momentum resolution were studied in 2012 pp data covering a large phase space of $|\eta| < 2.7$ and $5 \lesssim p_\mathrm{T} \lesssim 100$ GeV using tag-and-probe methods in $Z \to \mu\mu$ events for various muon reconstruction types [148]. Plots of the reconstruction efficiency as a function of η for muons with $p_\mathrm{T} > 10$ GeV is given in Fig. 4.4.

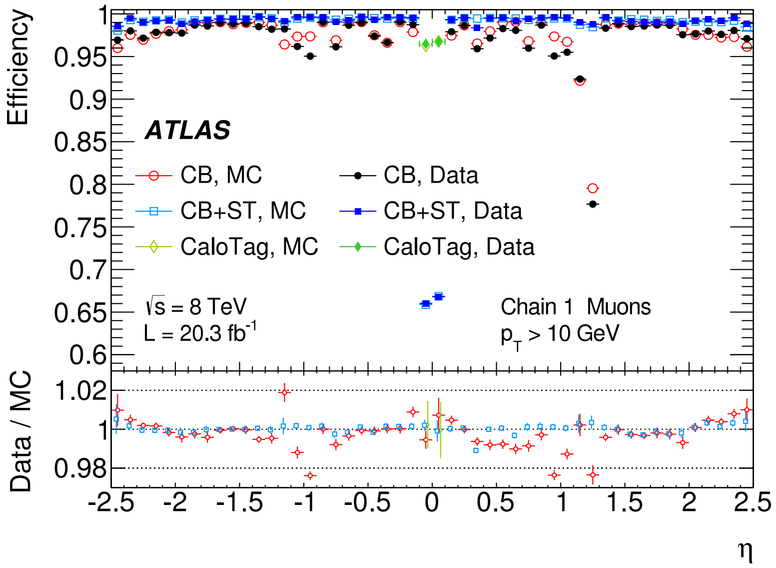

Fig. 4.4 Muon reconstruction efficiency as a function of $|\eta|$ measured in $Z \to \mu\mu$ events for muons with $p_\mathrm{T} > 10$ GeV and different muon reconstruction types. The error bars on the efficiencies indicate the statistical uncertainty. The panel at the bottom shows the ratio between the measured and predicted efficiencies. Figure taken from [148].

4.5 Jet reconstruction

Jets play a critical role in the physics measurements of any modern high energy hadron colliders, as both Standard Model processes and BSM processes can give rise to final states with high jet multiplicity. Jets are observed as groups of topologically-grouped energy deposits in the calorimeters associated with the tracks of charged particles measured in the inner detector. A jet algorithm is needed for jet reconstruction; the most commonly used jet algorithm is the anti-k_t algorithm implemented in the FastJet [149] package. The inputs to the jet collection are stable particles (particles with a lifetime longer than 10 ps) from generators, reconstructed tracks in the inner detector (track jets), or energy deposits in the calorimeter (calorimeter jets). Calorimeter jets are reconstructed from topologically connected clusters built from calorimeter cells that contain positive energy. Cell noise thresholds are set to account for increased contribution from overlaid minimum bias events (pile-up) fluctuations. Topo-clusters are reconstructed at the EM scale which measures energy deposited by particles produced in electromagnetic showers in the calorimeter. Clusters can then be calibrated using various different schemes such as the EM+JES scheme or the local cluster weighting (LCW) scheme. The EM+JES calibration applies corrections as a function of jet p_{T} and $|\eta|$ reconstructed at the electromagnetic scale. In the LCW scheme, each topo-cluster is first classified as electromagnetic or hadronic, using information primarily based on energy density and longitudinal shower depth. Various corrections are performed for dead material and different calorimeter response for electrons compared to pions. Jets are then clustered using the anti-k_t algorithm after calibration of topo-clusters giving EM or LCW jets. Further pileup corrections are applied at this stage. A jet-area-based correction is available for 2012 data. Calibrations for jet pseudorapidity and jet energy are applied by addition or multiplication of correction factors derived from MC simulation. A residual in-situ calibration is applied to data only. This corrects for jet p_{T} by multiplying by the ratio of responses between data and MC simulation with respect to a reference object:

$$\frac{\mathrm{Response}_{\mathrm{MC}}}{\mathrm{Response}_{\mathrm{Data}}} = \frac{\langle p_{\mathrm{T}}^{\mathrm{jet}} / p_{\mathrm{T}}^{\mathrm{ref}} \rangle_{\mathrm{MC}}}{\langle p_{\mathrm{T}}^{\mathrm{jet}} / p_{\mathrm{T}}^{\mathrm{ref}} \rangle_{\mathrm{Data}}}. \tag{4.1}$$

Several reference objects exist to cover a wide range of kinematic phase space, such as Z bosons (direct balance of the p_{T}^{Z} in the range $10-250$ GeV; photons (the photon E_{T} is balanced against the jet p_{T} or the hadronic recoil, or the highest p_{T} jet in an event. The jet energy scale uncertainty is estimated by systematic MC variations using in-situ measurements of single particle response.[2]

The jet energy scale uncertainty is composed of several different components, including the in-situ calibration uncertainty, uncertainty due to pileup, uncertainty due to flavour composition of the jet, and the response of the calorimeter to jets of a given flavour. The total jet energy scale uncertainty is the quadrature sum of the independent components.

4.6 Missing transverse momentum, $E_{\mathrm{T}}^{\mathrm{miss}}$

In collisions at a proton-proton collider such as the LHC, most strongly and weakly interacting particles will interact with the detector material, depositing their energies via electromagnetic or hadronic showers. However, neutrinos and other very weakly interacting particles will escape detection, and their energy/momenta cannot be reconstructed. It must be inferred indirectly using conservation of energy and momentum. The basic assumption is that prior to a collision, there is no net momentum in the transverse plane defined by the beams formed by the colliding particles. After the collision, any form of non-conservation of momentum would be attributed to particles which escaped detection. The vector quantity, "missing transverse momentum", (also referred to as "MET", or "ET-Miss") is defined as follows:

$$\mathbf{E}_{\mathrm{T}}^{\mathrm{miss}} = -\sum_{i=1}^{N_{\mathrm{object}}} \mathbf{p}_{\mathrm{T}}^{i}, \tag{4.2}$$

that is, the missing transverse energy is the vector that balances the summed transverse momenta of all objects in a given event. In practice, the $E_{\mathrm{T}}^{\mathrm{miss}}$ in an event is quite a difficult quantity to measure experimentally. For instance, one issue that arises is potential for double-counting due to overlapping measurements in the calorimeter and multiple measurements of individual muon momenta. Other detector-related effects such as calorimeter noise, detector defects and energy mismeasurement also provide contributions to the momentum sum [150].

Calorimeter cells and muons reconstructed in the muon spectrometer are the basic unit from which the $E_{\mathrm{T}}^{\mathrm{miss}}$ is constructed. The primary algorithm used by ATLAS, the "refined final algorithm", or `MET_RefFinal` [151] treats calorimeter cells as constituents of physics

---

[2] A more complete breakdown of the JES uncertainty consists of a set of nuisance parameters (NPs) resulting from in-situ absolute balance $Z+$jets $\gamma+$jets, and multi-jet balance, single-particle extrapolation above the multi-jet balance cutoff, η-intercalibration in-situ relative balance, pile-up and flavour uncertainties and punch-through corrections.

objects rather than fundamental elements. It is defined as the sum of a set of terms [152]:

$$\begin{aligned} E_{x(y)}^{\mathrm{miss}} = E_{x(y)}^{\mathrm{miss},e} + E_{x(y)}^{\mathrm{miss},\gamma} + E_{x(y)}^{\mathrm{miss},\tau} + E_{x(y)}^{\mathrm{miss,jets}} + \\ E_{x(y)}^{\mathrm{miss,SoftTerm}} + E_{x(y)}^{\mathrm{miss},\mu}, \end{aligned} \tag{4.3}$$

where each term is the negative sum of the momenta of all the calibrated reconstructed objects associated to that term projected onto the x and y directions. The "soft term" corresponds to clustered energy deposits in the calorimeter that are not associated with a jet or other reconstructed physics object. Calorimeter cells are associated to terms in the order in which they appear in Eq. (4.3), and shared cells are removed from terms lower in the hierarchy.

Electrons are calibrated with the standard ATLAS electron calibration, while photons are calibrated at the electromagnetic scale. The τ-jets are calibrated with local cluster weighting. Jets are reconstructed with the anti-k_t algorithm. The soft term is calculated from topoclusters and tracks not associated to high momentum objects; contributions both from jets with $p_{\mathrm{T}} < 20$ GeV and from unassociated topological clusters/tracks are included.

Sources of fake $E_{\mathrm{T}}^{\mathrm{miss}}$ generally fall into three categories: missed particles, Gaussian resolution from pile-up and the underlying event, and non-Gaussian tails. Missed particles are those which lie outside the detector acceptance, $|\eta| < 4.9$ for particles that stop in the calorimeter and $|\eta| < 2.7$ for muons. The effect of lost particles on the $E_{\mathrm{T}}^{\mathrm{miss}}$ resolution is small, with other sources dominating the $E_{\mathrm{T}}^{\mathrm{miss}}$ resolution. The resolution on these objects is not Gaussian and tends to have long tails where the object's momentum is measured to be lower than the true value.

Pile-up plays a large role in the resolution of the $E_{\mathrm{T}}^{\mathrm{miss}}$; when the average number of pile-up interactions per event increases, it can lead to a deterioration in the $E_{\mathrm{T}}^{\mathrm{miss}}$ performance. The dependence of the $E_{\mathrm{T}}^{\mathrm{miss}}$ on the number of primary vertices measured can be seen in Fig. 4.5. Methods to suppress pile-up are therefore needed which can restore the $E_{\mathrm{T}}^{\mathrm{miss}}$ resolution to values more like the ones observed at lower values of pileup. The major challenge in development of pile-up suppression methods for $E_{\mathrm{T}}^{\mathrm{miss}}$ reconstruction lies in the soft term correction of the soft event contributions. Several methods of correction have been studied for the soft term. One of them includes a multiplicative correction factor constructed from all the tracks in the event (the "soft-term vertex-fraction", or STVF). The STVF correction method uses the fraction of tracks from the primary vertex pointing to soft terms of the $E_{\mathrm{T}}^{\mathrm{miss}}$ to reweight the terms and recalculate the overall MET. The STVF is defined analogously to

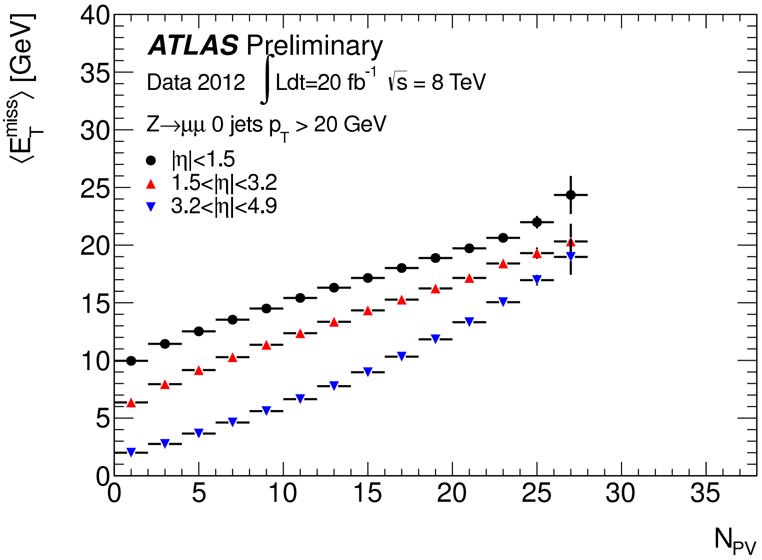

Fig. 4.5 The effect of pile-up on the average $\langle \sigma E_{\mathrm{T}} \rangle$ reconstructed in $Z \to \mu\mu$ events. In the range of $|\eta| < 1.5$, the $\langle \Sigma E_{\mathrm{T}} \rangle$ is linear in the number of vertices over a range of primary vertices out to 30. Figure taken from [153].

the jet vertex fraction (Section 5.6.3), and is formally expressed as

$$\mathrm{STVF}(\text{soft term}_i, \text{vertex}_j) = \frac{\sum_k p_{\mathrm{T}} \left(\text{track}_k^{\text{soft term}_i}, \text{vertex}_j \right)}{\sum_n \sum_l p_{\mathrm{T}} \left(\text{track}_l^{\text{soft term}_i}, \text{vertex}_n \right)}, \tag{4.4}$$

where the sum runs over all soft tracks, i.e., tracks not associated to hard object. Other methods based on jet area have been included as well. The level of agreement between data and simulation before and after correction for pileup with STVF is shown in Fig. 4.6.

The systematic uncertainties on the STVF variant of the $E_{\mathrm{T}}^{\mathrm{miss}}$ are comparable to the `MET_RefFinal` $E_{\mathrm{T}}^{\mathrm{miss}}$. One of the disadvantages of the STVF method is that it tends to overestimate the necessary pile-up suppression, which leads to a large underestimation of the soft $E_{\mathrm{T}}^{\mathrm{miss}}$ term. For analyses which place vetoes on high-p_{T} jets (Section 5.7), this will introduce spurious correlations between the lepton p_{T} and $E_{\mathrm{T}}^{\mathrm{miss}}$.

4.7 Conclusions

This chapter presented an overview of physics object reconstruction in ATLAS for electrons, photons, muons, jets, and missing energy. Extensive studies have been performed within ATLAS for all objects used in physics analyses in both 2011 and 2012 *pp* data. Reconstruction

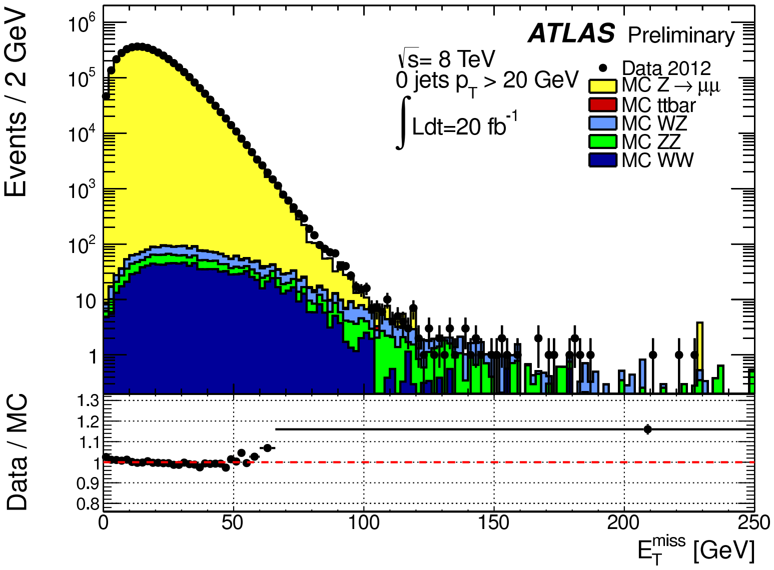

(a)

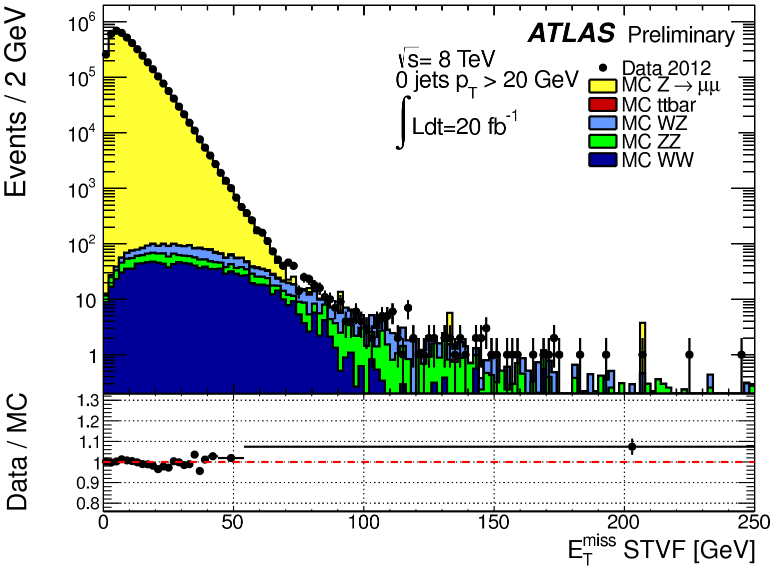

(b)

Fig. 4.6 The fully reconstructed $E_{\mathrm{T}}^{\mathrm{miss}}$ spectrum for above $p_{\mathrm{T}}^{\mathrm{jet}} > 20$ GeV (a) before and (b) after pile-up suppression with STVF [153].

efficiencies for central electrons and muons are shown to be over 95%, with performance dropping at higher pseudorapidities [143, 154]. Physics objects used throughout the *ZZ* analysis and the sources of uncertainties associated with reconstruction, identification, and energy/momentum resolution are discussed in Chapter 5.

Chapter 5

ZZ event selection

This chapter presents an overview of the physics objects described in Chapter 4 used in the $ZZ \to \ell^-\ell^+\nu\bar{\nu}$ analysis at 8 TeV. Object definitions for electrons, muons, photons, and jets as used in the analysis are given. The fiducial and total phase spaces in which cross sections are measured are defined, along with the objects used to obtain them. The performance of the simulation compared to data is given for a range of kinematic variables for the $ZZ \to \ell^-\ell^+\nu\bar{\nu}$ selection. Finally, experimental and theoretical systematics which affect the analysis are described in Section 5.8.

5.1 Analysis overview

The signal selection in the $ZZ \to \ell^-\ell^+\nu\bar{\nu}$ channel selects events with two opposite-sign, same-flavour isolated leptons (where a charged lepton $\ell^\pm = e^\pm, \mu^\pm$) with a large transverse momentum, a significant amount of $E_{\mathrm{T}}^{\mathrm{miss}}$ coming from the neutrinos, and no jets above a certain p_{T} threshold. With this selection, the signal has a manageable level of background over Standard Model processes. A cut-and-count-based approach is chosen for the 8 TeV analysis. Both the event selection and the choice of fiducial phase space closely follows the 7 TeV analysis [77], although some cut thresholds were changed relative to the 7 TeV analysis. The placement of cuts, in turn, loosely follows the selection of the $ZH \to \ell^-\ell^+ + E_{\mathrm{T}}^{\mathrm{miss}}$ analysis [155] for both the 7 and 8 TeV analyses. Measurement of the cross section requires several components:

- The number of observed events after all selections in each sub-channel $ZZ \to e^-e^+\nu\bar{\nu}$ or $ZZ \to \mu^-\mu^+\nu\bar{\nu}$.

- An estimate of the background events with uncertainties in each sub-channel. These are subtracted from the number of observed events in order to obtain the observed signal yield.
- A measurement of the signal acceptance, with uncertainties.
- The branching fraction of the ZZ system to the given final state. This is taken as a constant with the value provided by the Particle Data Group [15].
- The total integrated luminosity of the dataset used in order to convert the produced signal yield into a production cross section.

The signal acceptance and efficiency are calculated from simulated MC samples of $ZZ \rightarrow e^-e^+\nu\bar{\nu}$ and $ZZ \rightarrow \mu^-\mu^+\nu\bar{\nu}$ processes. The acceptance is factored into two components, denoted C_{ZZ} and A_{ZZ} that, when multiplied, give the ratio of the number of reconstructed events passing all selection in a given sample to the total number of events generated in a phase space where both Z bosons (invisibly and visibly decaying) in within the mass range $66 < m_{\ell^-\ell^+} < 116$ GeV, referred to as the "total phase space" or the "extrapolated phase space". Only C_{ZZ} is required to calculate a fiducial cross section, while the product of C_{ZZ} and A_{ZZ} and the branching ratio to a particular final state is required to calculate an extrapolated cross section, also referred to as a "total cross section". It is important to know the level of agreement between simulation and data for signal expectations and background estimates. Measurements performed by combined performance groups allow corrections to enhance the level of agreement between data and simulation. The main background contributions to selected events are discussed in Section 6.1. These backgrounds are estimated using a combination of simulation and data-driven techniques. The components listed above are used to measure a cross section in a fiducial volume which closely follows the ATLAS detector geometry and acceptance, and a more inclusive phase space defined by $66 < m_{\ell\bar{\ell}} < 116$ GeV. It is advantageous to measure the cross section in a fiducial volume, as it does not have the same level of theoretical uncertainties associated with extrapolating to a larger phase space that is not measured, while the total cross section is useful for event rate predictions in a more inclusive volume.

5.2 Data samples at 8 TeV

The analysis uses a data sample of proton-proton collisions recorded between February and December of 2012 during standard operation of the LHC at $\sqrt{s} = 8$ TeV. Bunch crossings were spaced by 50 ns with an average of approximately 1380 bunches per fill, with an average bunch intensity between 1.6 and 1.7×10^{11} protons per bunch [156, 157]. Events are selected based on data-quality flags per luminosity block which require all sub-detectors to be operational and above a predetermined efficiency. The calibration of the absolute luminosity scale is performed by the van der Meer method [158] for several independent luminosity detectors. Details of the luminosity calibration methodology in ATLAS can be found in [159]. The total integrated luminosity used for the analysis corresponds to approximately 20 300 pb^{-1}. The uncertainty in the luminosity as reported by the ATLAS luminosity working group (using methods described in [160, 161]) with a relative uncertainty, $\Delta\mathscr{L}/\mathscr{L}$, of approximately $\pm 2.8\,\%$ [162].

5.3 Simulated signal and background samples

The $q\bar{q}$ component of the $ZZ \rightarrow \ell^-\ell^+\nu\bar{\nu}$ signal is modelled with POWHEGBOX [163] at next-to-leading-order using the CT10 parton distribution function (PDF) set [164]. These events are subsequently showered with PYTHIA8 [126] within the Athena framework (Section 3.4.1) using the ATLAS AU2 tune [165]. This component is estimated to be approximately 94% of the total $ZZ \rightarrow \ell^-\ell^+\nu\bar{\nu}$ production cross section. POWHEGBOX does not use the zero-width approximation for the Z bosons, unlike other generators such as MC@NLO, which allows for modelling of off-shell boson production. Final-state QED radiation losses from Z resonances are modelled with PHOTOS [166]. The $gg \rightarrow ZZ$ component is modelled with gg2VV [121, 122], which is also showered with PYTHIA8. In contrast to gg2ZZ [122], which was used previously in the 7 TeV analysis, gg2VV includes interference terms from the $H \rightarrow ZZ$ terms, although the main interference effects occur beyond the Z pair threshold rather than the Higgs resonance [167]. The ZZ signal samples used for the $ZZ \rightarrow \ell^-\ell^+\ell^-\ell^+$ analysis are also generated with POWHEGBOX and showered with PYTHIA8, and the gg component is also generated with gg2VV and showered with PYTHIA8. The $ZZ \rightarrow \ell^-\ell^+\ell^-\ell^+$ processes are treated as backgrounds to the $ZZ \rightarrow \ell^-\ell^+\nu\bar{\nu}$ processes. All ZZ signal samples used in this analysis are shown Table 5.1, with the corresponding cross sections, and event generator filter efficiencies. All samples are produced with the default factorisation and renormalisation scales set to $\mu_F = \mu_R = m_{ZZ}$. For the $ZZ \rightarrow \ell^-\ell^+\ell^-\ell^+$ POWHEGBOX and gg2VV samples, a cut is applied at generator-level requiring the invariant mass of the charge lepton pairs to be larger than 4 GeV for both Z bosons, while for the $ZZ \rightarrow \ell^-\ell^+\nu\bar{\nu}$ samples, the cut applies to the charged lepton pair. In the case of the $ZZ \rightarrow \ell^-\ell^+\ell^-\ell^+$ POWHEGBOX samples, an additional filter is applied to the events requiring at least three charged leptons (e or μ) with $p_{\mathrm{T}} > 5$ GeV and $|\eta| < 10$. The filter mainly serves to reject τ events. Only 0.05% of $ZZ \to \ell^-\ell^+\ell^-\ell^+$ events are rejected for approximately on-shell ZZ production, where "on-shell" is defined to be both Z bosons produced in the mass range $66 < m_{\ell^-\ell^+} < 116$ GeV. The gg2VV samples have fiducial cuts of $|\eta| < 4.5$, $p_{\mathrm{T}}^{\ell} > 7$ GeV. Corresponding tables of background samples are listed in Chapter A.

5.4 Pile-up reweighting

Simulated Monte Carlo samples are often produced before or during a given data-taking period. It is to be expected, then, that the distribution of the average number of interactions per bunch crossing, denoted by $\langle\mu\rangle$, obtained in MC will not necessarily match that from data. Therefore, to obtain a more accurate representation of $\langle\mu\rangle$, an event weight is applied to fully reconstructed simulated events referred to as "pile-up reweighting". An official tool, `PileupReweighting`, is provided to obtain a corrected value of the average interactions per crossing, which applies a weight derived from the distribution in data and the $\langle\mu\rangle$ distribution for a given sample. Samples simulated during a given data taking period are are produced by choosing a run that is indicative of the average level of pileup experienced during that data-taking period (this is also to ensure correct detector conditions that are indicative of the data-taking period). A distribution of $\langle\mu\rangle$ values is simulated for each data-taking period. This is intended to cover the whole range of $\langle\mu\rangle$ values (roughly 0-40 interactions per bunch crossing) seen in the data for that period and allow the MC to be reweighted to the data.

5.5 Triggers and trigger matching

In agreement with other ATLAS Standard Model electroweak measurements, the analysis uses a logical OR of the lowest threshold unprescaled single-lepton triggers with isolation and a high p_{T} lepton trigger during all data taking periods. The triggers are given in Table 5.2. Both triggers have a lepton p_{T} threshold of 24 GeV. A track-based isolation cut is applied: the sum of the transverse momentum of tracks in a cone of size $\Delta R < 0.2$ around the lepton must be less than 10 % of the p_{T} for electrons, and 12 % of the p_{T} for muons. An `i` in the trigger name means the isolation requirement is placed on the triggering object. For electron triggers, `vh` means the trigger has both η-dependent p_{T} thresholds and a hadronic leakage cut at L1 [169].[1]

---

[1] The hadronic leakage requirement consists of a veto on hadronic energy of more than or equal to 1 GeV deposited in the hadronic layers of the calorimeter, within a region of 0.2×0.2 in $\eta \times \phi$ behind the EM cluster.

Process	Generator	Events	min. $m_{\ell^+\ell^-}$ at generator-level [GeV]	min. n_ℓ for multi-lepton filter	p_{T}^{ℓ} for multilepton filter [GeV]	max. $\lvert\eta^{\ell}\rvert$ for multilepton filter	$\varepsilon_{\mathrm{filter}}^{\mathrm{multilepton}}$	cross section [pb]
$ZZ \to e^-e^+e^-e^+$	PowhegBox	1099997	4	2	5	10	0.91	0.077
$ZZ \to e^-e^+\mu^-\mu^+$	PowhegBox	1599696	4	2	5	10	0.83	0.176
$ZZ \to e^-e^+\tau^-\tau^+$	PowhegBox	1099897	4	2	5	10	0.58	0.175
$ZZ \to \mu^-\mu^+\mu^-\mu^+$	PowhegBox	1099798	4	2	5	10	0.91	0.077
$ZZ \to \mu^-\mu^+\tau^-\tau^+$	PowhegBox	1098999	4	2	5	10	0.59	0.175
$ZZ \to \tau^-\tau^+\tau^-\tau^+$	PowhegBox	300000	4	2	5	10	0.11	0.077
$gg \to e^+e^-e^+e^-$	gg2VV	90000	4	-	-	-	-	0.00277
$gg \to \mu^+\mu^-\mu^+\mu^-$	gg2VV	90000	4	-	-	-	-	0.00277
$gg \to e^+e^-\mu^+\mu^-$	gg2VV	90000	4	-	-	-	-	0.01222
$ZZ \to e^-e^+\nu\bar{\nu}$	PowhegBox	300000	4	-	-	-	-	0.168
$ZZ \to \mu^-\mu^+\nu\bar{\nu}$	PowhegBox	300000	4	-	-	-	-	0.168
$ZZ \to \tau^-\tau^+\nu\bar{\nu}$	PowhegBox	300000	4	-	-	-	-	0.168
$gg \to e^+e^-\nu\bar{\nu}$	gg2VV	30000	4	-	-	-	-	0.00688
$gg \to \mu^+\mu^-\nu\bar{\nu}$	gg2VV	29999	4	-	-	-	-	0.00688

Table 5.1 The ZZ signal production process, cross section and number of fully simulated MC events. The MC generators used to produce the samples are included, as well as the minimum mass cut of lepton-antilepton pairs for each sample. A filter is applied in the Athena framework to the $ZZ \to \ell^-\ell^+\ell^-\ell^+$ samples, via the `Multilepton` filter from MC12 production [168], requiring a minimum number of leptons to be above a designated p_{T} threshold (5 GeV) and within a certain $|\eta|$ range. This filter is not applied to the gg2VV samples, nor is it applied to the $ZZ \to \ell\ell\nu\bar{\nu}$ samples. PowhegBox samples are produced at NLO in the $q\bar{q}$ process and have a k-factor of 1.

Period	e trigger	μ trigger

All	`EF_e24vhi_medium1`
	`OR`
	`EF_e60_medium1`
		`EF_mu24i_tight`
		`OR`
		`EF_mu36_tight`

Table 5.2 Electron and muon triggers used for the $ZZ \to \ell^-\ell^+\nu\bar{\nu}$ analysis. These triggers correspond to the lowest unprescaled single lepton triggers available for 2012 data taking. A logical OR is used between the triggers in a given sub-channel for a given data stream (`Egamma` stream, `Muons` stream). The notation `eXX/muXX` indicates the minimum p_{T} of the electron/muon in GeV at Event Filter (`EF`) level.

There is a chance that the same event could fire multiple triggers, for example, a muon could fire the electron trigger. To prevent duplicate events, a "trigger-overlap removal" is applied which requires that if an event fired both the electron and muon trigger, keep only the event in the electron stream and discard the event in the muon stream.

Events passing the preselection (Section 5.7) are required to have at least one "trigger-matched" lepton, that is, a muon within $\Delta R < 0.1$ of a muon which fires the trigger, or an electron within $\Delta R < 0.15$ of an electron which fires the trigger. To be matched, an online reconstructed lepton must have transverse momentum at least 1 GeV higher than the on-line threshold applied by the trigger hypothesis to ensure that the lepton is on the plateau of the efficiency curve. For example, an electron must have $p_{\mathrm{T}} > 25$ GeV to be matched to the `EF_e24vhi_medium1` trigger. Trigger matching for both electrons and muons is implemented by the package `TrigMuonEfficiency` [170].

5.5.1 Photon triggers

A photon reweighting method is used for the estimate of the $Z+X$ background, requiring events with one high E_{T} photon to be selected. In 2012 data taking, photon triggers were pre-scaled such that the trigger rate is approximately 1 Hz, with the prescale decreasing progressively in E_{T}^{γ} from 20 GeV to approximately 120 GeV. The first unprescaled trigger is `EF_g120_loose`.

In order to obtain a smooth photon spectrum, as shown in Fig. 5.2(b), photons within a given E_{T} bin is are scaled by the average prescale consistent with that E_{T} of that particular photon. Photons within a given trigger range bin are required to be 5 GeV over the lower threshold for their respective triggers with a maximum of 5 GeV over the lowest threshold for the next highest trigger, except in the case of photons above 125 GeV, as there is no higher trigger. For example, an event with a photon with E_{T}^{γ} of 50 GeV would be scaled by the value corresponding to `EF_g40_loose` as it is between 45 GeV < E_{T}^{γ} < 65 GeV. A summary of the high E_{T} single photon triggers, with their average prescales and E_{T}^{γ} thresholds is given in Table 5.3. Furthermore, in order to obtain a smooth photon spectrum, the dependence of the photon triggers on pile-up must be accounted for. Different triggers sample different pile-up conditions; selecting events with prescaled triggers introduces a bias that preferentially selects events with lower pile-up. This occurs because the trigger prescale is increased when the instantaneous luminosity is increased. This is correlated with the pile-up conditions. The resulting effect is that prescaled triggers sample the low pile-up data more than the high pile-up data. This has an effect on the $E_{\mathrm{T}}^{\mathrm{miss}}$ modelling and must be taken into account. To correct for this, a weight is also applied by taking the ratio of a given bin entry in the $\langle\mu\rangle$ distribution of the unprescaled trigger to the corresponding bin entry in the same distribution of a given prescaled trigger, to make the pile-up distributions appear like the unprescaled distribution. The $\langle\mu\rangle$ distributions are shown in Fig. 5.1.

Trigger	Average prescale	Photon E_{T} range [GeV]
`EF_g20_loose`	4415.781	$25 < E_{\mathrm{T}}^{\gamma} < 45$
`EF_g40_loose`	348.553	$45 < E_{\mathrm{T}}^{\gamma} < 65$
`EF_g60_loose`	80.942	$65 < E_{\mathrm{T}}^{\gamma} < 85$
`EF_g80_loose`	28.535	$85 < E_{\mathrm{T}}^{\gamma} < 105$
`EF_g100_loose`	13.037	$105 < E_{\mathrm{T}}^{\gamma} < 125$
`EF_g120_loose`	1.000	$E_{\mathrm{T}}^{\gamma} > 125$

Table 5.3 Single photon triggers used to select photons used to estimate the $Z+X$ background in the $ZZ \to \ell^{-}\ell^{+}\nu\bar{\nu}$ analysis. The lower value of the p_{T} range for a given trigger indicates that the minimum E_{T}^{γ} for selection is 5 GeV over the nominal E_{T}^{γ} threshold for a given trigger to ensure that the photon is on the efficiency plateau of the trigger.

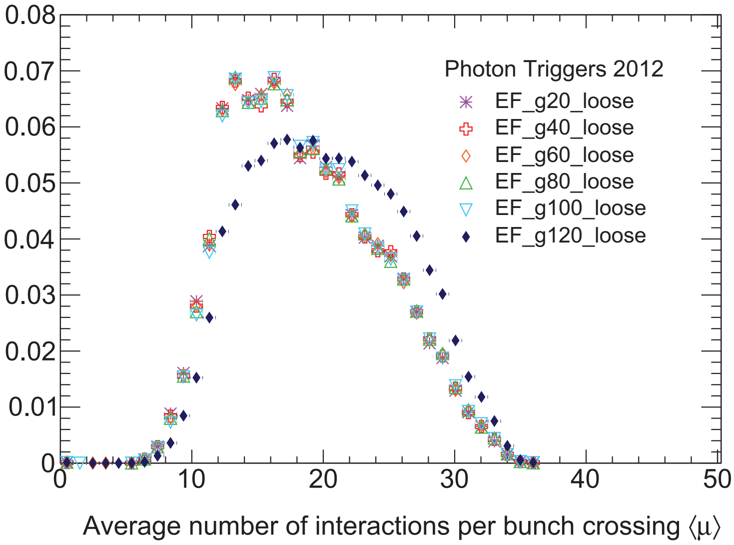

Fig. 5.1 Average number of interactions per bunch crossing for the single-photon triggers for 2012. The $\langle \mu \rangle$ distributions for each trigger are scaled to unit area.

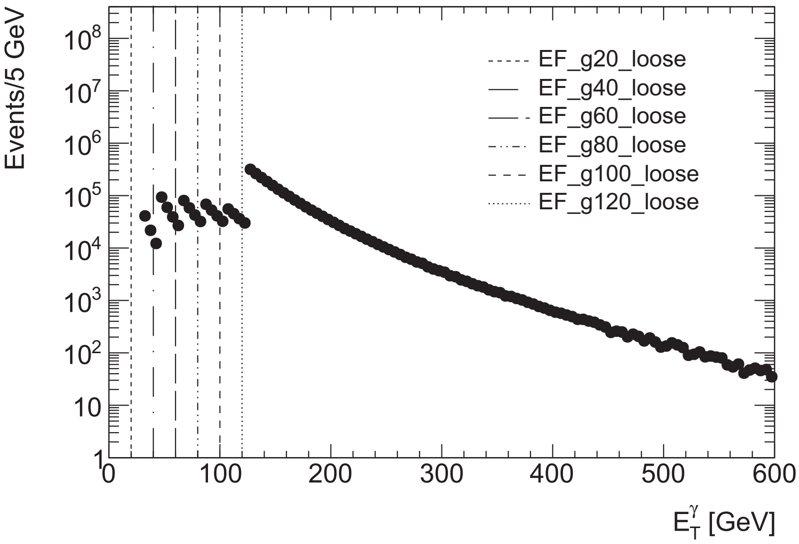

(a) The E_T spectrum of tight photons before events are multiplied by their corresponding trigger prescales and pile-up weights.

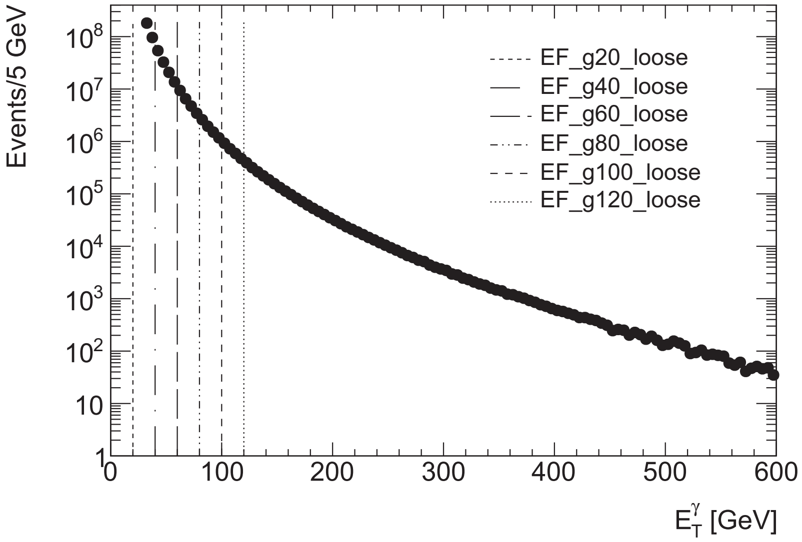

(b) The E_T spectrum of tight photons after events are multiplied by their corresponding trigger prescales and pile-up weights.

Fig. 5.2 The spectra of tight photons (a) before and (b) after events are multiplied by their corresponding trigger prescales, given in Table 5.3, and pile-up weights, obtained from Fig. 5.1. The dashed lines indicate the various E_T thresholds for single photon triggers used in 2012 data taking. The first unprescaled trigger is `EF_g120_loose`.

5.5.2 Lepton trigger scale factors

Trigger efficiencies for electrons and muons have been measured in $Z \rightarrow ee$ and $Z \rightarrow \mu\mu$ events in data using tag-and-probe studies [171]. To account for discrepancies in the modelling of the trigger efficiency in MC compared to data, a set of scale factors is derived to enhance the agreement. The statistical uncertainty on the trigger efficiency is derived from MC. The trigger scale factor is applied as an overall event-level weight after the requirement that at least one lepton is trigger matched. The trigger scale factors are calculated as the ratio

$$SF_\mathrm{trigger} = \frac{1 - \prod_{n=1}^{N_\ell}\left(1 - \varepsilon_{\mathrm{Data},\ell_n}\right)}{1 - \prod_{n=1}^{N_\ell}\left(1 - \varepsilon_{\mathrm{MC},\ell_n}\right)}, \tag{5.1}$$

where where N_ℓ is the number of leptons in a given event, $\varepsilon_\mathrm{Data}$ is the trigger efficiency determined from tag-and-probe studies from data for a single lepton flavour of lepton ℓ_n, and ε_MC is the trigger efficiency determined with tag-and-probe from MC.

5.5.3 Trigger efficiencies

The efficiencies of the single-lepton triggers are determined with the signal sample after all selection cuts. They are listed in below in Table 5.4.

Channel	MC efficiency [%]	MC efficiency with trigger scale factor applied [%]	Overall event scale factor
$e^-e^+\nu\bar{\nu}$	99.60	99.60	0.9989
$\mu^-\mu^+\nu\bar{\nu}$	94.51	94.51	1.0003
$\ell^-\ell^+\nu\bar{\nu}$	96.92	96.89	0.9997

Table 5.4 Efficiencies of the single lepton triggers in $ZZ \to e^-e^+\nu\bar{\nu}$ and $ZZ \to \mu^-\mu^+\nu\bar{\nu}$ events after all selection cuts. Leptons are required to be matched to a trigger, which reduces the efficiency by approximately 0.2% in the *ee* sub-channel and 0.1% in the $\mu\mu$ sub-channel compared to leptons that are not trigger-matched. The first column shows the trigger efficiency estimated from MC events without applying any correction factors. The second column shows the trigger efficiency after applying the trigger scale factor. The uncertainties on the efficiencies are between 0.5% and 1% in each sub-channel. The scale factors are applied on a per-event basis to reproduce the trigger efficiency measured in data in MC. The overall event level scale-factor represents the average value of the product of all scale factors for all events passing the full selection.

5.6 Analysis-level object definitions

This section briefly describes the criteria for analysis-level objects including electrons, muons, jets, $E_{\mathrm{T}}^{\mathrm{miss}}$, and photons.

5.6.1 Electrons

The analysis uses only “central” electrons in the pseudo-rapidity $|\eta| < 2.47$ that are reconstructed with the “standard” electron algorithm. In 2012 data taking, the standard electron algorithm included refitting electron tracks with the Gaussian-sum-filter. They are required to pass at least the `loose++` requirement. Electrons are required to have an author of 1 or 3, meaning that they can be reconstructed from the calorimeter-based algorithm (author 1) or both the calorimeter-based and track-based algorithms (author 3). An Object Quality (`OQ`) flag is placed which defines a “bad” electron or photon if its cluster is affected by the presence of a dead front-end-board in the first or second sampling layer or by the presence of a dead high-voltage region affecting the three samplings or by the presence of a masked cell. All electron candidates are required to pass the object quality cut (OQ AND `1446 == 0`). The bitmask `1446` defines a bad electron and indicates that its cluster is affected by at least one of the following three conditions: the presence of a dead front-end-board in the first or second sampling layer of the ECal, the presence of a dead region affecting the three samplings, or the presence of a masked cell in the core. To ensure that the candidates come from the primary vertex, the distance of closest approach of the electron's track in the $R-z$ plane with respect to the primary vertex $|z_0 \sin(\theta)|$, must be less than 0.5 mm and the d_0 significance is required to be less than 6.[2] The energy of electron candidates with 4 or more silicon (SCT and Pixel) hits taken from the calorimeter cluster measurement, and the η and ϕ are taken from the track. For electron candidates with fewer than 4 silicon hits, all electron parameters are taken directly from the cluster. In both cases, the cluster η and ϕ are used for the requirement and for overlap removal. Electron candidates are required to have $p_{\mathrm{T}} > 25$ GeV. Plots of the leading electron p_{T} and leading electron η are in events with two selected electrons is shown in Fig. 5.3(a), while plots of the sub-leading electron p_{T} and η are given in Fig. 5.3(c). Both track-based and calorimeter-based isolation requirements are placed on electrons; the track isolation requirement is set at `ptCone20`$/E_{\mathrm{T}} < 0.15$, while for the calorimeter isolation[3] the transverse energy in a cone of $\Delta R = 0.2$ around the electron candidate must be less than 15% of the electron E_{T}, `etcone20`$/p_{\mathrm{T}} < 0.15$.[4] Electrons used to build Z candidates will pass all requirements. The ZZ selection involves a veto on events with "third-leptons" to help reject WZ events. A "third-electron", also referred to as a "veto-type electron" is one which fails isolation, or, if it passes isolation requirements, fails a final requirement that the electron is `medium++`. These electrons are not used to construct Z candidates, but are carried through the selection specifically for the third-lepton veto.

5.6.2 Photons

Photons are required to have a minimum (calibrated) E_{T} of 30 GeV, and are required to pass the `tight` identification requirement using the `PhotonIDtool` [172] from the package `egammaAnalysisUtils` provided by the ATLAS Egamma group. The acceptance of photons is restricted to $|\eta| < 2.37$, and those falling in the crack region $1.37 < |\eta| < 1.52$ are

---

[2] Electrons which fall in the "crack" region defined by $1.37 < |\eta_{\mathrm{cluster}}| < 1.52$ are not removed as they as they have been in other ATLAS analyses.

[3] `etcone20` means the transverse energy $E_{\mathrm{T}} = E \sin\theta$ (ref) in the ECal deposited in a cone of half-opening angle 0.2 around electron minus transverse energy representing the electron (5×7 cells). This redundant transverse energy comes from either detector noise or jets if the electron is not isolated.

[4] In both cases, the energy in the isolation cone does not include the energy of the electron itself, and is corrected for the effects of pile-up.

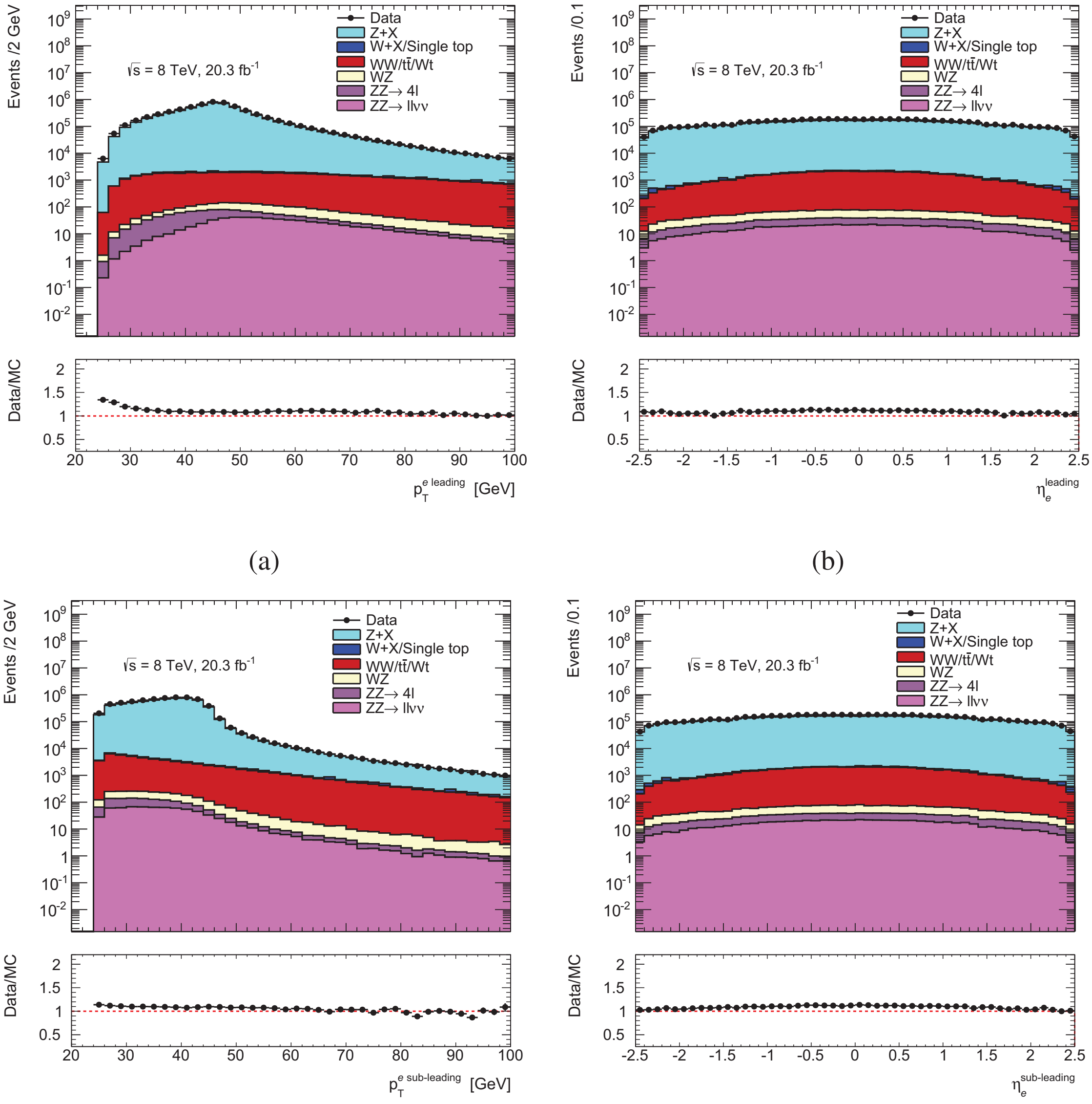

(a) (b)

(c) (d)

Fig. 5.3 (a) The p_T and (b) η of the leading and sub-leading (c),(d) electrons in events with two electrons which pass the selection criteria. Both leptons are required to be trigger-matched, no other cuts are applied at this stage. All major background contributions are given. Corrections/calibrations to simulation such as trigger scale factors are applied as well as lepton energy/momentum and identification scale factors and any event-level scale factors such as MC event weights, pile-up weights, and beamspot corrections.

excluded. In both electron and photon analyses, a selection must be applied to reject bad quality clusters or "fake" clusters which appear as a result of problems with the calorimeters during data taking. A 32-bit word is used to represent the object quality. The bitmask `&34214` is applied. Photon cleaning is performed as recommended by the ATLAS Egamma group [173]. A requirement is placed on the `EtCone` isolation variable (Section 4.2.6) with a cone size of 0.3 corrected for p_{T} leakage and ambient energy density calculated from topological clusters [174–176] that it be greater than 2 GeV. Finally, a requirement is placed that photons used for analysis are not converted [177]. Jets within a cone of $\Delta R < 0.3$ of photons are removed after jet overlap removal with electrons and muons.

5.6.3 Muons

As for electrons, muons are required to be central in that they are restricted to the pseudorapidity range $|\eta| < 2.5$. Only `STACO` muons are used for the analysis and are required to pass the "loose" identification requirement. Muons are required to be combined or segment-tagged. The recommendations from the Muon Combined Performance (MCP) group are applied. These recommendations place requirements on the track quality via the number of pixel hits and dead pixel sensors, the number of SCT hits, the number of pixel holes and SCT holes, and hits in the TRT. Muons must be isolated from energy deposits in the calorimeter with `etcone20`$/p_{\mathrm{T}} < 0.15$. The energy in the cone is corrected for contributions from pile-up events using the number of vertices reconstructed in the event. The inner detector track associated with a muon must be isolated from other tracks to reject secondary muons from hadronic jets. In order to reject muons from the decay of heavy quarks, the isolation requirement is `ptCone20`$/p_{\mathrm{T}} < 0.15$. Muons are required to have a p_{T} greater than 25 GeV. Finally, a requirement that the muon is a combined muon is placed. Veto-type muons are identified as muons which fail the calorimeter or track isolation, or, if they pass the calorimeter and track isolation, fail the combined requirement. Plots of the leading and sub-leading muon momenta and pseudorapidity are given in Fig. 5.4.

5.6.4 Jets

For this analysis, jets are reconstructed from topological clusters of energy in the calorimeter with the anti-k_t jet finder algorithm [178] with a radius parameter $R = 0.4$. The clusters are locally calibrated (LC) to include hadronic calibration, dead material correction and out-of-cluster corrections. Jets are required to have $p_{\mathrm{T}} > 25$ GeV and $|\eta| < 4.5$. Another requirement on the jets is added to reduce the pile-up using a discriminant called the "jet vertex fraction" (JVF) [177], which represents the probability that a jet came from a primary

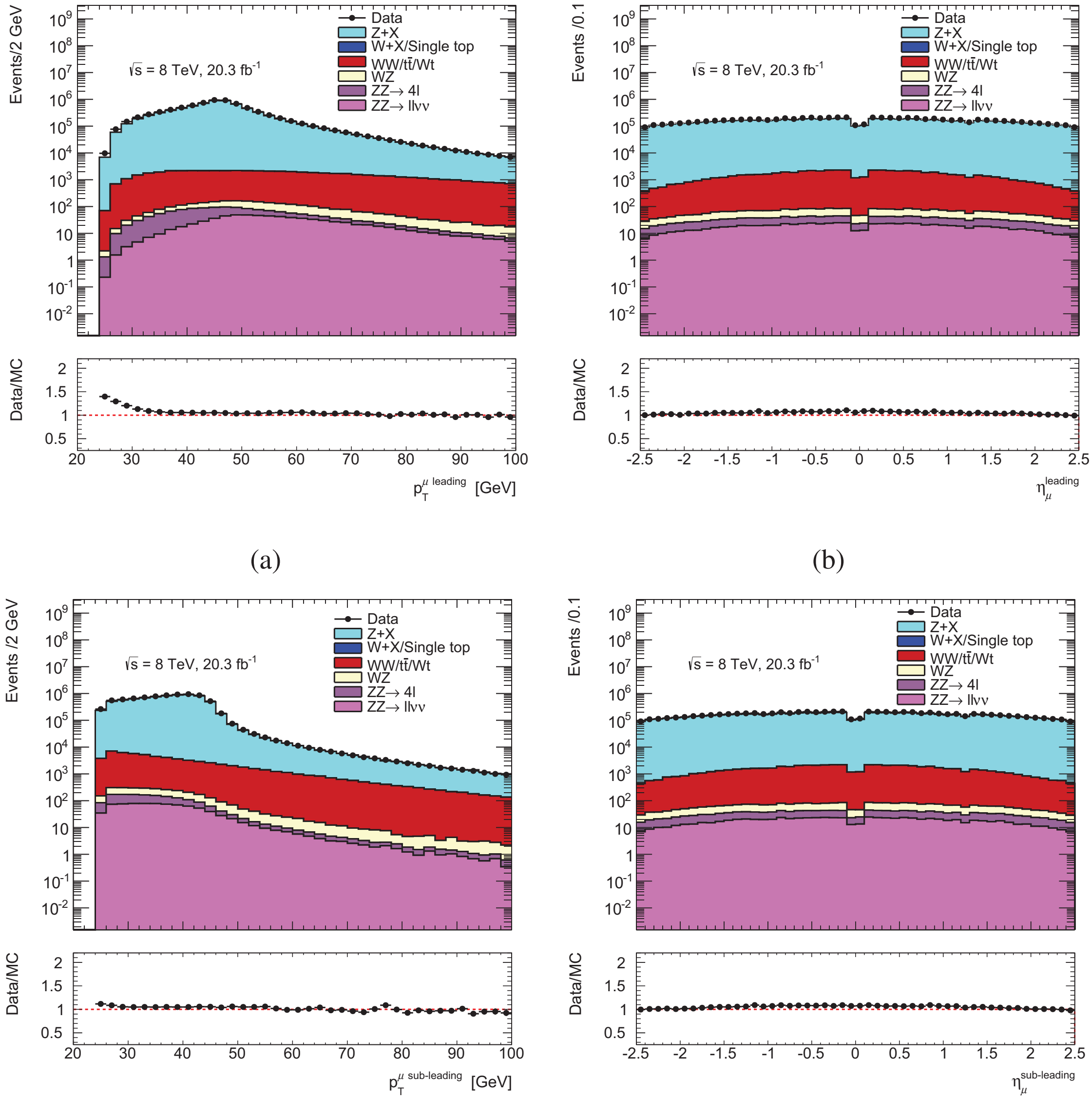

(a) (b)

(c) (d)

Fig. 5.4 (a) The p_{T} and (b) η of the leading and sub-leading (c), (d) electrons in events with two electrons which pass the selection criteria. Both leptons are required to be trigger-matched, no other cuts are applied at this stage. All major background contributions are given. Corrections/calibrations to simulation such as trigger scale factors are applied as well as lepton energy/momentum and identification scale factors and any event-level scale factors such as MC event weights, pile-up weights, and beamspot corrections.

vertex. The JVF is defined as the fraction of charged particle transverse momentum in each jet (in the form of tracks) originating in each identified primary vertex in a given event. More specifically, it is the sum of the transverse momenta of all matched tracks from a given vertex divided by the total jet-matched track momenta from all vertices. For a single jet, denoted by jet_i, the JVF with respect to the j^{th} vertex in a given event is:

$$\text{JVF}(\text{jet}_i, \text{vertex}_j) = \frac{\sum_k p_{\text{T}} \left(\text{track}_k^{\text{jet}_i}, \text{vertex}_j \right)}{\sum_n \sum_l p_{\text{T}} \left(\text{track}_l^{\text{jet}_i}, \text{vertex}_n \right)}. \tag{5.2}$$

Jets are required to have $|\text{JVF}| > 0.5$ if they have the kinematics of $p_{\text{T}} < 50$ GeV and $|\eta| < 2.4$. Jets are removed if they overlap with selected electrons within a cone size of 0.3. Jets which survive overlap removal with electrons are also removed if they overlap with selected muons within a cone size of 0.3. The recommendations to "clean", or remove events with bad jets, i.e., jets not associated to real energy deposits in the calorimeters are followed according to the recommendations from the ATLAS JET-ETMiss group [179, 180].

5.6.5 $E_{\text{T}}^{\text{miss}}$

The measurement of the $E_{\text{T}}^{\text{miss}}$ is performed by using the standard `MET_RefFinal` algorithm (Section 4.6) for both electron and muon channels. This algorithm classifies the calorimeter deposits corresponding to their identification with physics objects, e.g. electrons (RefEle), hard jets (RefJet), remaining softer jets (SoftJets) and further unclustered objects (CellOut Eflow). The performance of the CellOut Eflow term is optimised using the tracker information for low p_{T} tracks and avoiding double counting of tracker and calorimeter energies. Furthermore, measurements for different classes of isolated and non-isolated muons are added. The $E_{\text{T}}^{\text{miss}}$ distribution in events with a Z reconstructed from an opposite sign same-flavour pair after trigger matching requirements and the Zmass window requirement is shown in Fig. 5.5.

5.7 Event selection

The following describes the set of selection criteria in order to define a $ZZ \to \ell^-\ell^+\nu\bar{\nu}$ candidate event at reconstruction level, both for data and simulation.

1. $E_{\text{T}}^{\text{miss}}$ ***Cleaning*** Any event with a jet that has $p_{\text{T}} > 20$ GeV and passes the looser bad or ugly criteria is vetoed. A "bad" jet is one that is not associated to a real energy deposit in the calorimeter [180]. They are attributable to a wide range of sources

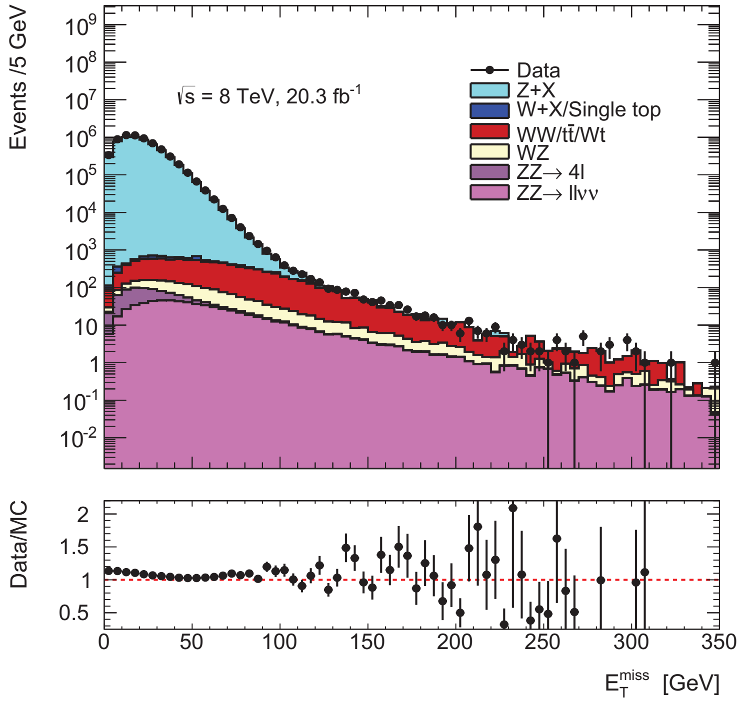

(a)

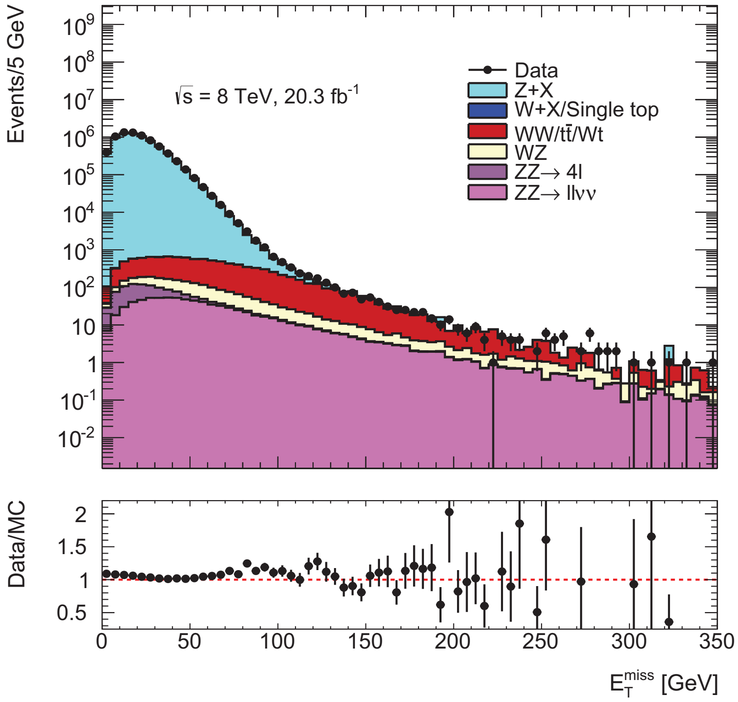

(b)

Fig. 5.5 The $E_{\mathrm{T}}^{\mathrm{miss}}$ spectrum after the Z mass window and lepton trigger matching requirements in (a) the ee and (b) $\mu\mu$ sub-channels. Before applying the ZZ selection, the dominant component of the $E_{\mathrm{T}}^{\mathrm{miss}}$ comes from the $Z+X$ background in which jets that are mismeasured give rise to significant missing energy. There are also significant contributions from events with real $E_{\mathrm{T}}^{\mathrm{miss}}$ such as WW, Wt, and $t\bar{t}$.

such as spikes in the hadronic end-cap, changes in LHC beam conditions, and cosmic-ray showers. "Ugly" jets correspond to real energy deposits in a region where the energy measurement is not accurate; this may happen in the transition region between barrel and end-cap and problematic calorimeter regions. Several variables are used to determine jet quality, such as the energy fraction in the electromagnetic calorimeter, the maximum energy fraction in one calorimeter layer, and the energy fraction in the hadronic end-cap [181].

2. ***LAr Hole Veto*** For events coming from the period where 6 FEBs of the LAr calorimeter were dead, events are vetoed when jets with p_{T} greater than 25 GeV threshold are found entering the dead region.

3. ***Two analysis-quality leptons*** Events are required to have two and only two same-flavour, opposite-sign leptons passing the selection criteria listed in Section 5.6, which come from the primary vertex. Veto-type leptons, or "third leptons" are not considered analysis-quality in that Z candidates are not constructed from them because they have failed either the identification or isolation cut (or both), rather they are only used to veto events if at least one remains after the remaining selection cuts.

4. ***Trigger matching*** At least one lepton with $p_{\mathrm{T}} > 20(25)$ GeV for muons (electrons), must match to a trigger object.

5. ***Z mass window*** The two leptons must satisfy $76 < m_{\ell^-\ell^+} < 106$ GeV. This helps to suppress the WW and $t\bar{t}$ backgrounds, which produce leptons which do not form a peak inside the mass window. A plot of the invariant mass of the two reconstructed leptons is shown in Fig. 5.8.

6. ***Lepton Separation*** $\Delta R\left(\ell^-,\ell^+\right) > 0.3$. The leptons which come from the Z decay are required to have track isolation, or in the case of electrons, calorimeter and track isolation. The isolation requirement places an implicit cut on the leptons such that they cannot be closer than $\Delta R\left(\ell^-,\ell^+\right) = 0.3$.

7. ***Missing transverse momentum*** The $E_{\mathrm{T}}^{\mathrm{miss,axial}}$, referred to as "axial MET" must exceed 90 GeV. Jets produced in association with a Z boson will give rise to a significant amount of $E_{\mathrm{T}}^{\mathrm{miss}}$ if the jets are mismeasured (fake $E_{\mathrm{T}}^{\mathrm{miss}}$). $ZZ \to \ell^-\ell^+\nu\bar{\nu}$ events should have a significant amount of real $E_{\mathrm{T}}^{\mathrm{miss}}$coming from the neutrinos. For on-shell diboson production, if the diboson system does not recoil off additional jets, the two bosons will tend to be well separated in the transverse plane. The $E_{\mathrm{T}}^{\mathrm{miss,axial}}$ is the negative of the projection of the $E_{\mathrm{T}}^{\mathrm{miss}}$ onto the Z bosons momentum vector. It is defined

as

$$\mathbf{E}_{\mathrm{T}}^{\mathrm{miss,axial}} = -\mathbf{E}_{\mathrm{T}}^{\mathrm{miss}} \cdot \cos\left(\Delta\phi(\mathbf{E}_{\mathrm{T}}^{\mathrm{miss}}, \mathbf{p}_{\mathrm{T}}^{Z})\right), \tag{5.3}$$

where $\Delta\phi$ is the azimuthal angle as explained in Section 3.2.1. A schematic diagram of $E_{\mathrm{T}}^{\mathrm{miss,axial}}$ in relation to $E_{\mathrm{T}}^{\mathrm{miss}}$ and p_{T}^{Z} is given in Fig. 5.6. Backgrounds to diboson processes have an $E_{\mathrm{T}}^{\mathrm{miss,axial}}$ spectrum peaked around zero, while the signal has a broad peak in the $E_{\mathrm{T}}^{\mathrm{miss,axial}}$ spectrum and is not centred about $E_{\mathrm{T}}^{\mathrm{miss,axial}}$ of zero. A large $E_{\mathrm{T}}^{\mathrm{miss,axial}}$ ensures that the two Z bosons have a large opening angle between them in the transverse plane. This cut serves to reduce the $Z+X$ background. The $E_{\mathrm{T}}^{\mathrm{miss,axial}}$ spectrum is plotted in Figs. 5.9 and 5.10.

8. ***Fractional difference*** $|E_{\mathrm{T}}^{\mathrm{miss}} - p_{\mathrm{T}}^{Z}|/p_{\mathrm{T}}^{Z} < 0.4$. This cut is also referred to as the "p_{T}-balance" cut. Events with two on-shell Z bosons and no high p_{T} jets should have the bosons produced with similar values of p_{T}. The requirement that the magnitude of the $E_{\mathrm{T}}^{\mathrm{miss}}$ be comparable to the p_{T}^{Z} further reduces the $Z/\gamma^{*}+X$ background. The p_{T}-balance spectrum in the ee and $\mu\mu$ selections are shown in Figs. 5.11 and 5.12.

9. ***Jet veto*** Events must contain no reconstructed jets which have $E_T > 25$ GeV. Vector bosons produced in association with jets, such as Wt will produce real $E_{\mathrm{T}}^{\mathrm{miss}}$ and high p_{T} leptons. However, the top decays will also produce additional jets. Requiring no high p_{T} jets in the event suppresses Wt and $t\bar{t}$ backgrounds. The jet multiplicity is shown in Figs. 5.13 and 5.14. The lack of a jet veto allows for more Wt and $t\bar{t}$ as well as additional $Z+X$ background in the signal region, and the size of the background becomes comparable to the WZ background, as shown in Fig. 5.15.

10. ***Third lepton veto*** Veto events with a third lepton passing all cuts and has a p_{T} >10 GeV. $ZZ \to \ell^{-}\ell^{+}\nu\bar{\nu}$ production will give rise to two opposite-sign, same-flavour leptons. However, WZ decays can mimic this signature if the p_{T} from the lepton is soft enough. This third lepton will not, in general, pass the isolation requirement. A veto on extra leptons in the event serves to reduce the contribution from WZ events.

A representation of the cutflow for the signal selection in the $e^{-}e^{+}\nu\bar{\nu}$ and $\mu^{-}\mu^{+}\nu\bar{\nu}$ sub-channels is shown in Figs. 5.19 and 5.20. The cutflow for $\tau^{-}\tau^{+}\nu\bar{\nu}$ is given in Fig. 5.21 to virtually no signal from τ's pass the full selection.

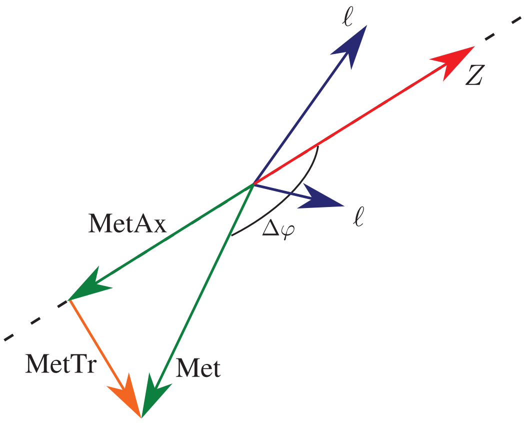

Fig. 5.6 A shematic diagram of $E_{\mathrm{T}}^{\mathrm{miss,axial}}$. The axial $E_{\mathrm{T}}^{\mathrm{miss}}$ is defined as the negative projection of the $E_{\mathrm{T}}^{\mathrm{miss}}$ onto the p_{T} of the Z boson Eq. (5.3).

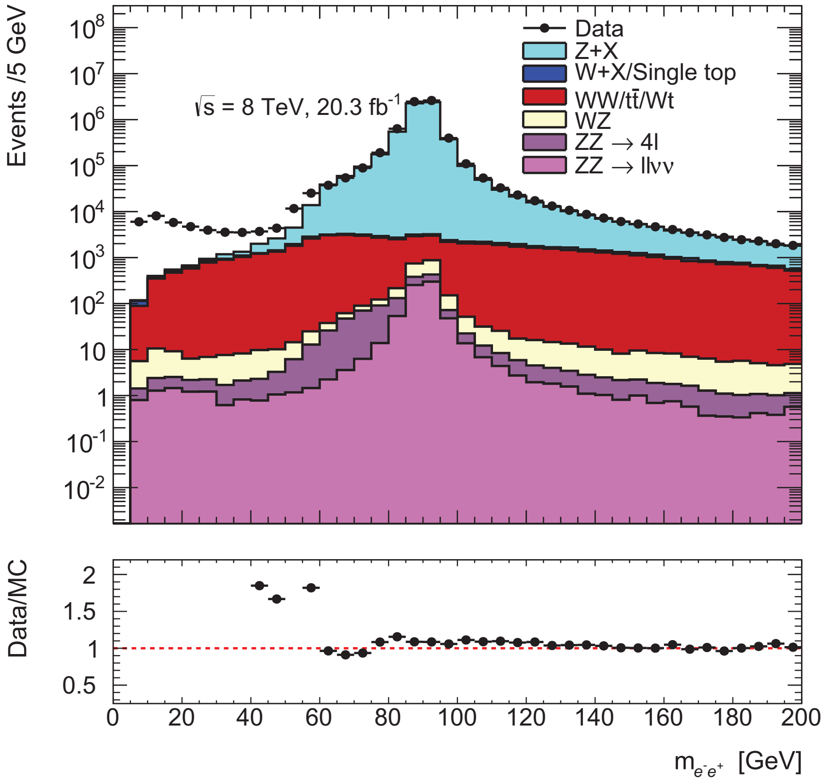

Fig. 5.7 The invariant mass of the lepton pair used to reconstruct the Z candidate after the dilepton requirement in the electron channel. No additional cuts are placed on the Z bosons. The leptons are required to be trigger-matched. The $ZZ \to e^{-}e^{+}\nu\bar{\nu}$ signal is the bottom-most contribution in the histogram stack. The excess at low mass is largely due to missing low-mass Drell-Yan samples with $m_{\ell^{-}\ell^{+}} < 60$ GeV, which model the $Z+X$ contribution.

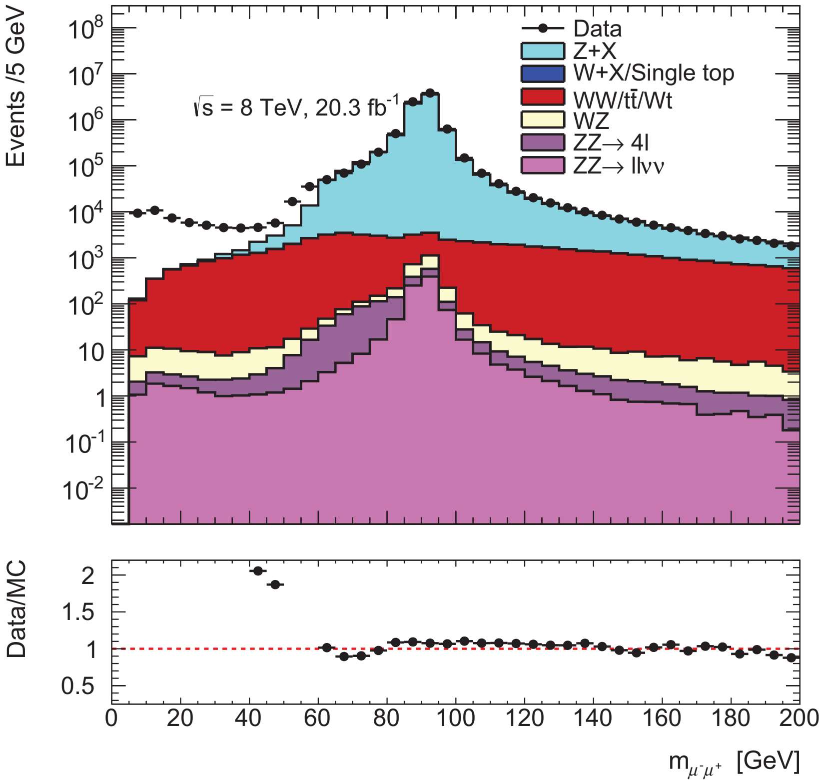

Fig. 5.8 The invariant mass of the lepton pair used to reconstruct the Z candidate after the dilepton requirement in the muon channel. No additional cuts are placed on the Z bosons. The leptons are required to be trigger-matched. The $ZZ \to \mu^-\mu^+\nu\bar{\nu}$ signal is the bottom-most contribution in the histogram stack. The excess at low mass is largely due to missing low-mass Drell-Yan samples with $m_{\ell^-\ell^+} < 60$ GeV, which model the $Z+X$ contribution.

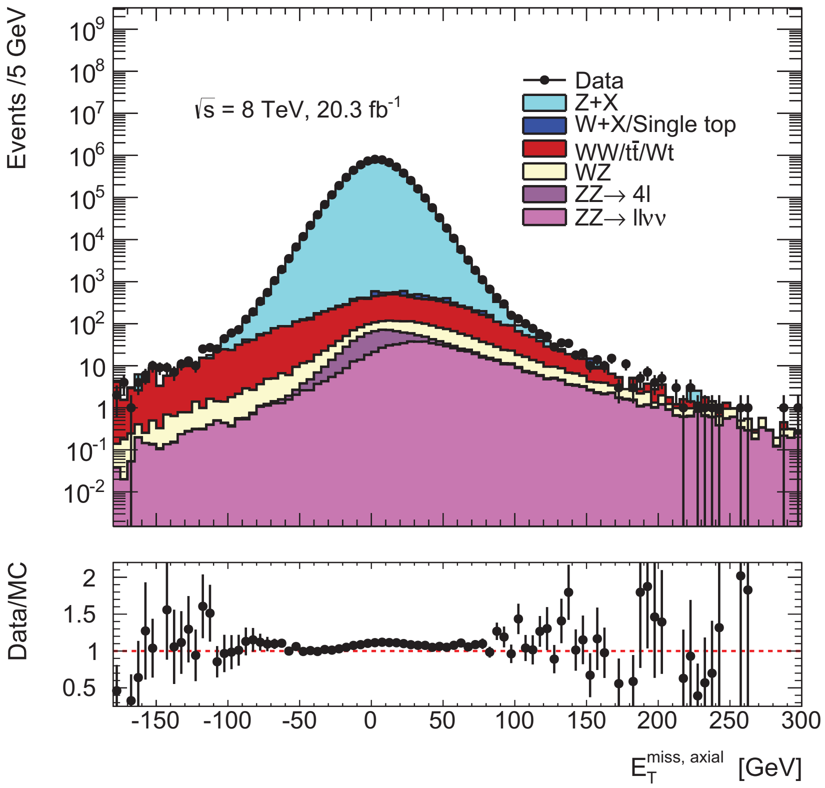

Fig. 5.9 The $E_{\mathrm{T}}^{\mathrm{miss,axial}}$ (Eq. (5.3)) spectrum after the lepton separation and Z mass window requirement in the *ee* sub-channel, before the signal region cuts are applied. Both electrons coming from the Z are required to be trigger-matched. Backgrounds to $ZZ \rightarrow \ell\ell\nu\bar{\nu}$ have their $E_{\mathrm{T}}^{\mathrm{miss,axial}}$ spectra centred about zero, while the signal is peaked away from zero and extends over the full range. The cut on $E_{\mathrm{T}}^{\mathrm{miss,axial}}$ at 90 GeV is useful for suppressing $Z+X$ background.

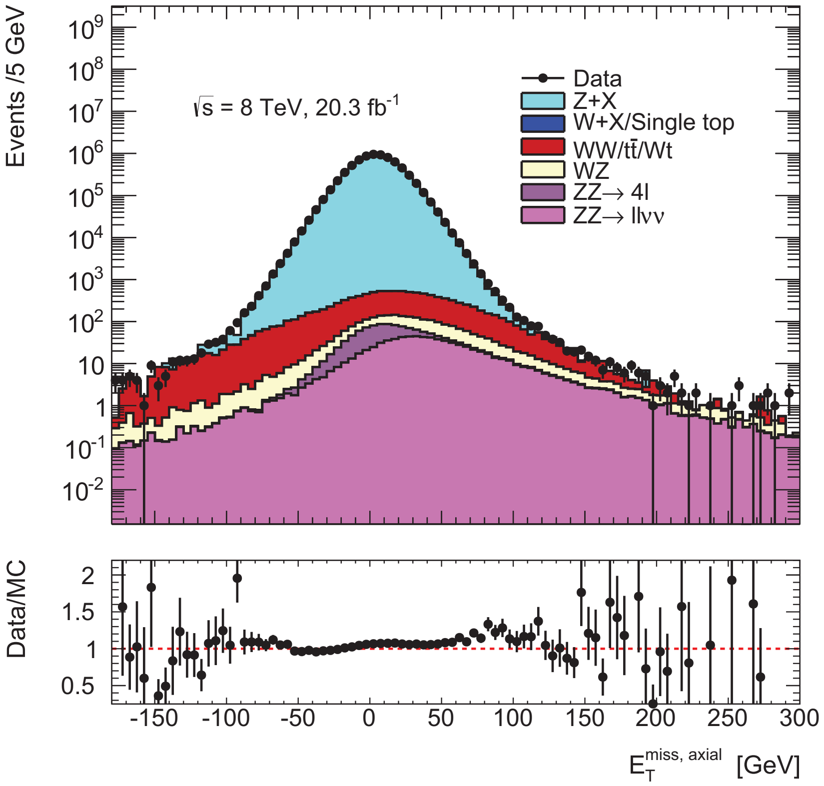

Fig. 5.10 The $E_{\mathrm{T}}^{\mathrm{miss,axial}}$ (Eq. (5.3)) spectrum after the lepton separation and *Z* mass window requirement in the $\mu\mu$ sub-channel, before the signal region cuts are applied.

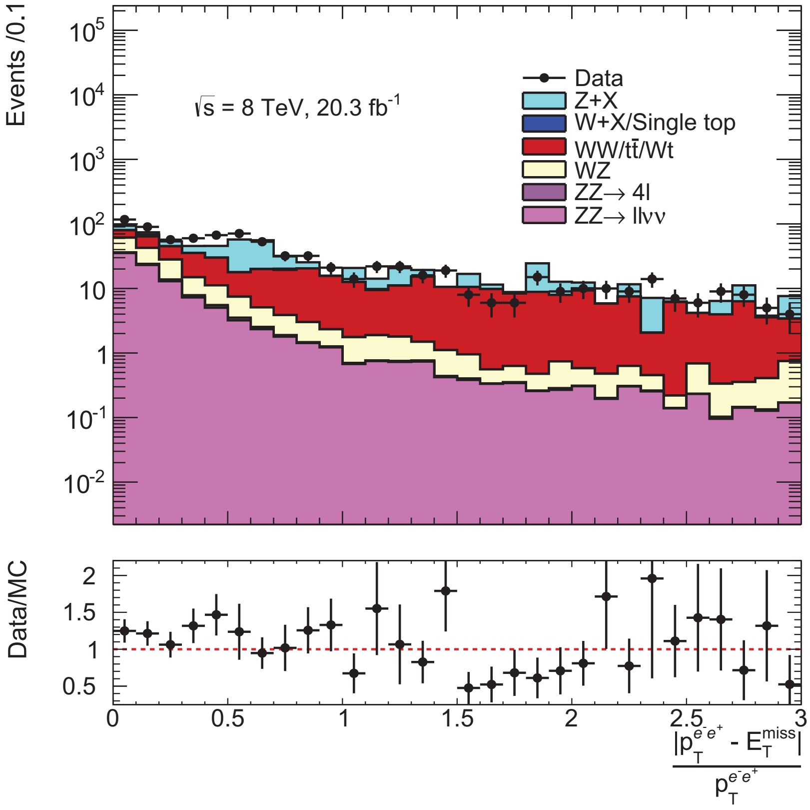

Fig. 5.11 The p_T-balance spectrum after the $E_\mathrm{T}^{\mathrm{miss,axial}}$ cut in the $ZZ \to e^- e^+ \nu \bar{\nu}$ selection.

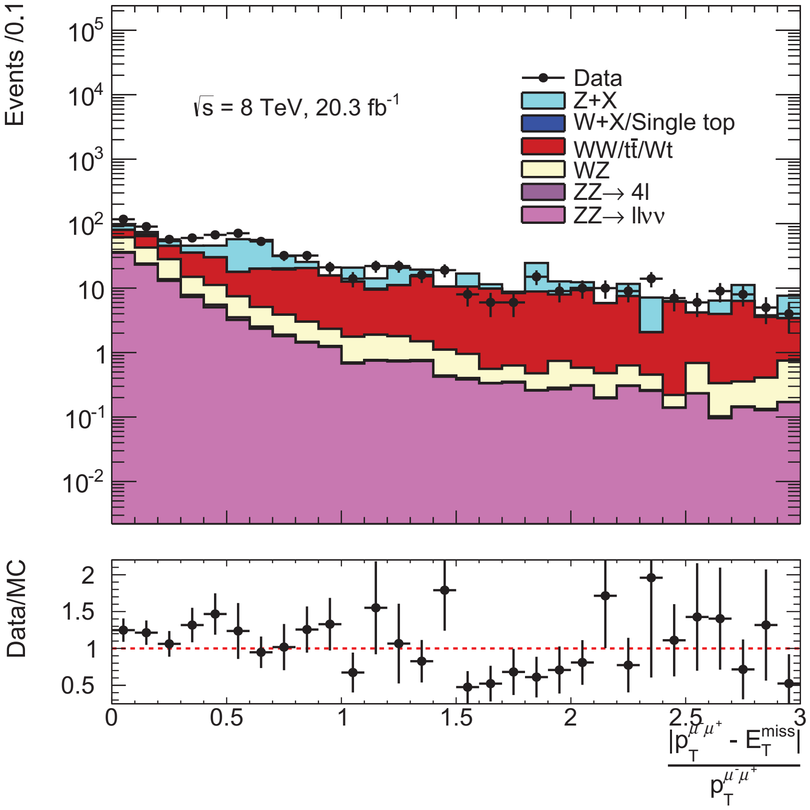

Fig. 5.12 The p_T-balance spectrum after the $E_T^{\text{miss,axial}}$ cut in the $ZZ \to \mu^-\mu^+\nu\bar{\nu}$ selection.

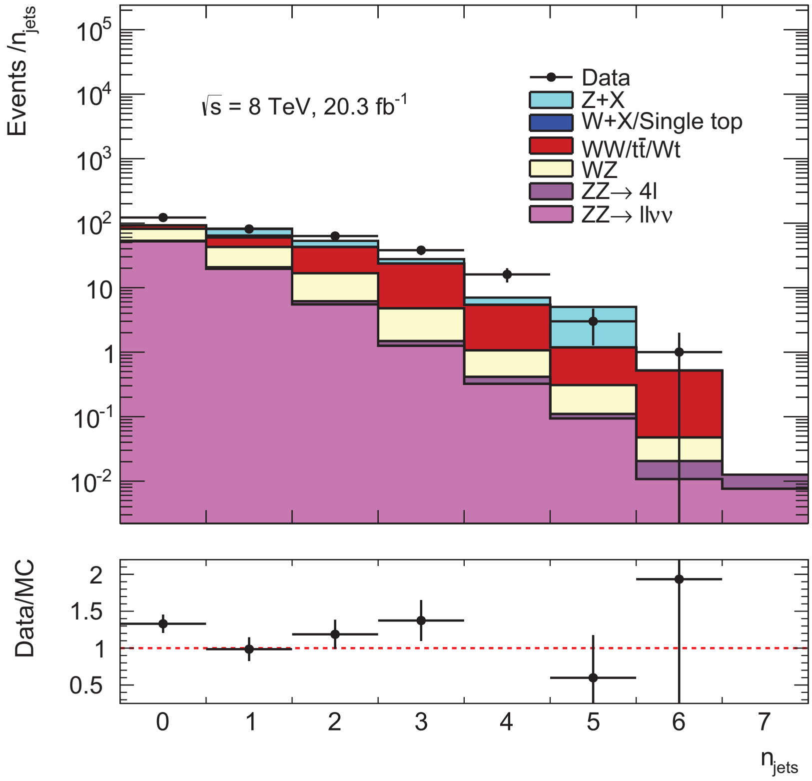

Fig. 5.13 The jet multiplicity after the $E_{\mathrm{T}}^{\mathrm{miss,axial}}$ and p_{T}-balance cuts in the in the $ZZ \rightarrow e^{-}e^{+}\nu\bar{\nu}$ selection.

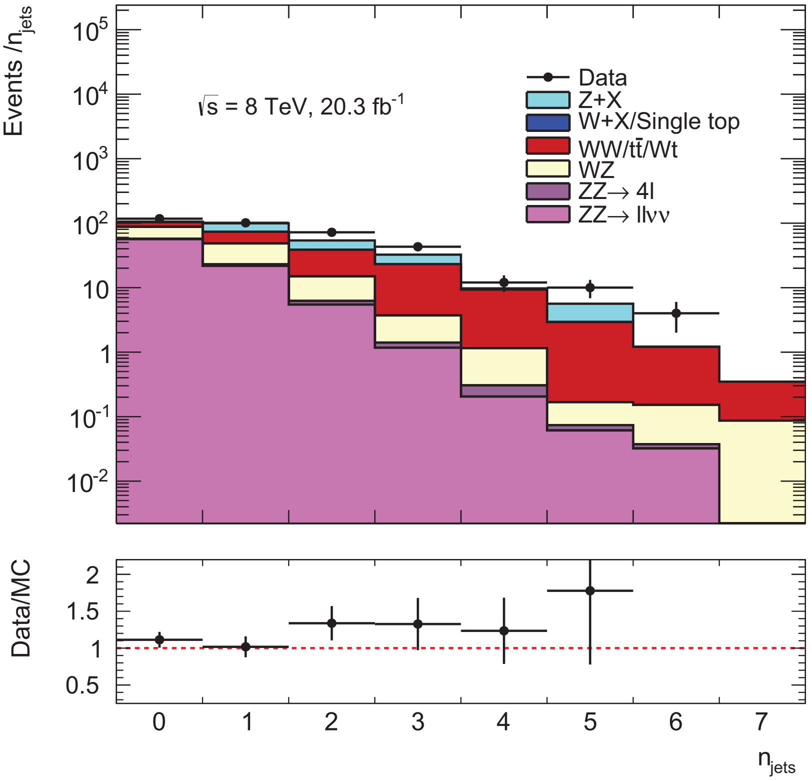

Fig. 5.14 The jet multiplicity after the $E_{\mathrm{T}}^{\mathrm{miss,axial}}$ and p_{T}-balance cuts in the in the $ZZ \to \mu^{-}\mu^{+}\nu\bar{\nu}$ selection.

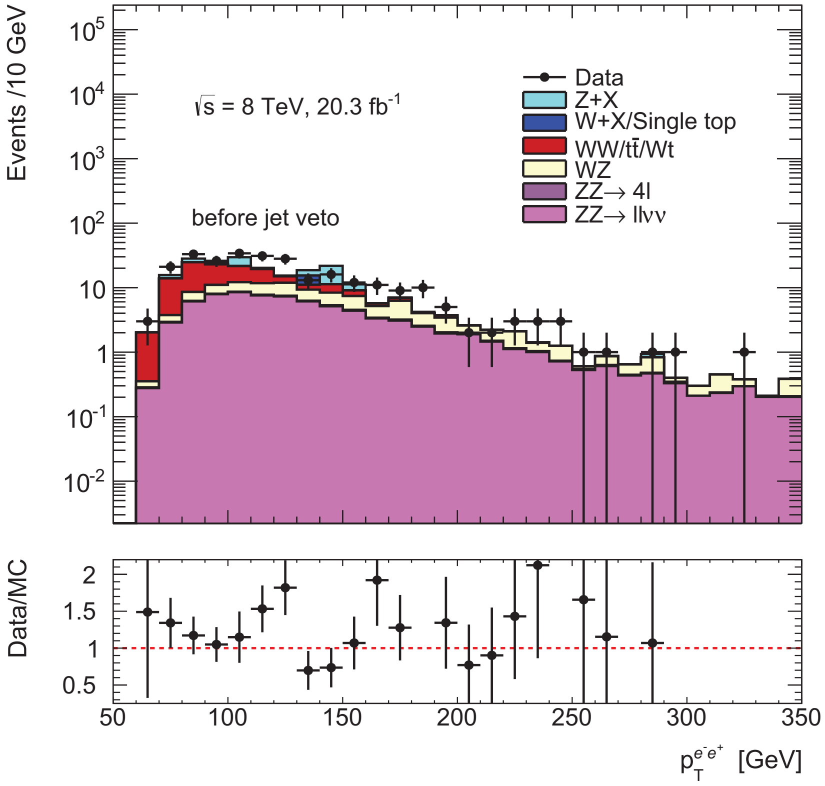

Fig. 5.15 The p_T^Z spectrum after the $E_T^{\text{miss,axial}}$ cut in the $ZZ \rightarrow e^- e^+ \nu \bar{\nu}$ selection without the jet veto applied. The dominant backgrounds at this stage are the WZ and the $WW, t\bar{t}, Wt$. The jet veto helps to suppress $WW, t\bar{t}, Wt$ as well as $Z+X$ not removed from the $E_T^{\text{miss,axial}}$ and p_T-balance.

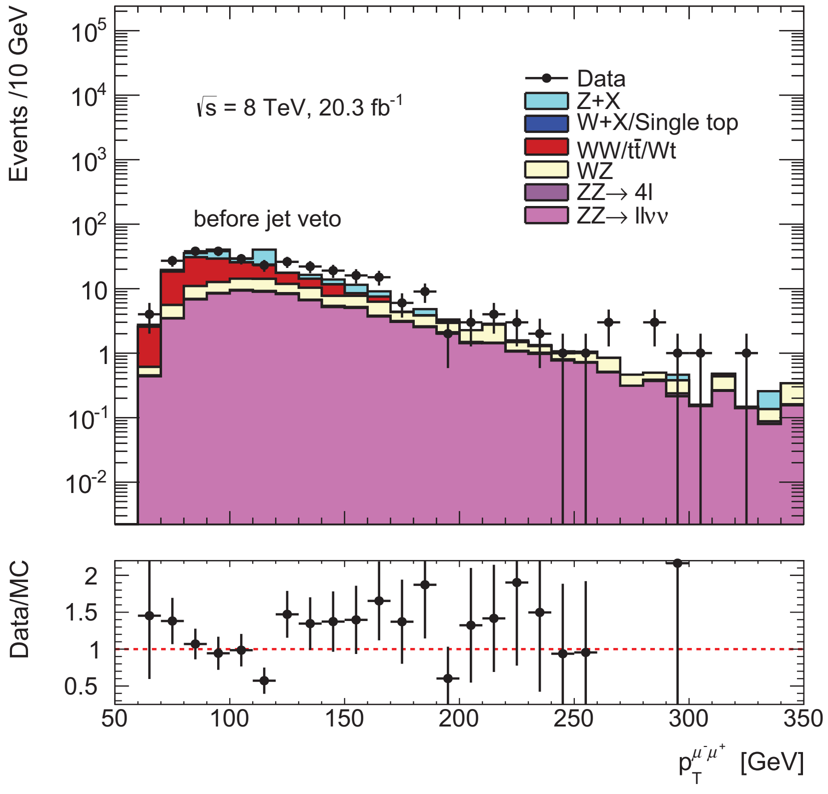

Fig. 5.16 The p_T^Z spectrum after the $E_T^{\text{miss,axial}}$ cut in the $ZZ \to \mu^- \mu^+ \nu \bar{\nu}$ selection without the jet veto applied.

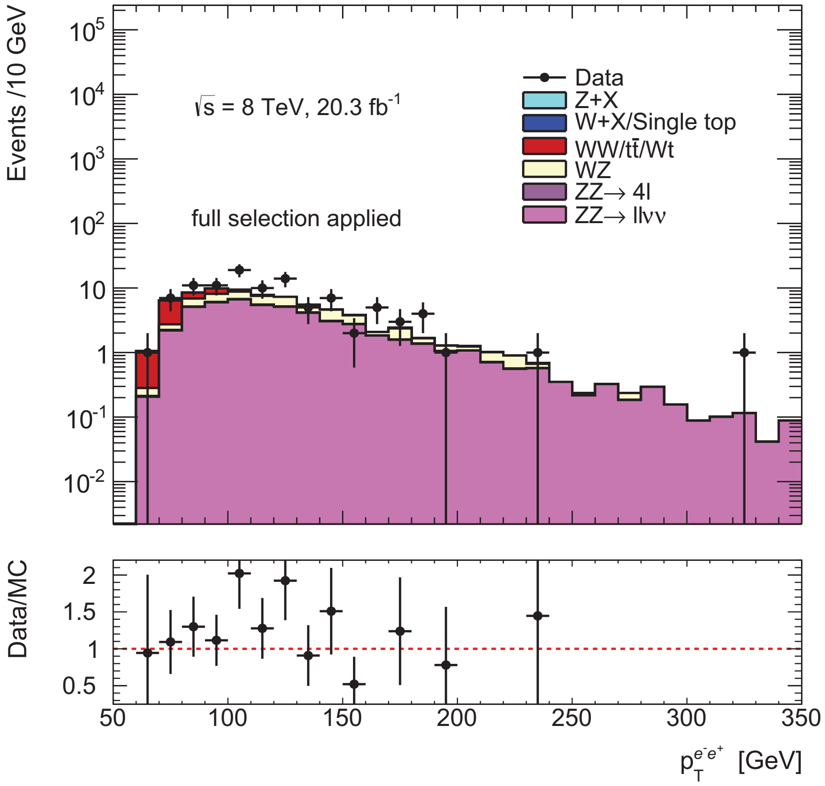

Fig. 5.17 The p_{T}^{Z} spectrum after all ZZ selection cuts in the $e^-e^+\nu\bar{\nu}$ sub-channel.

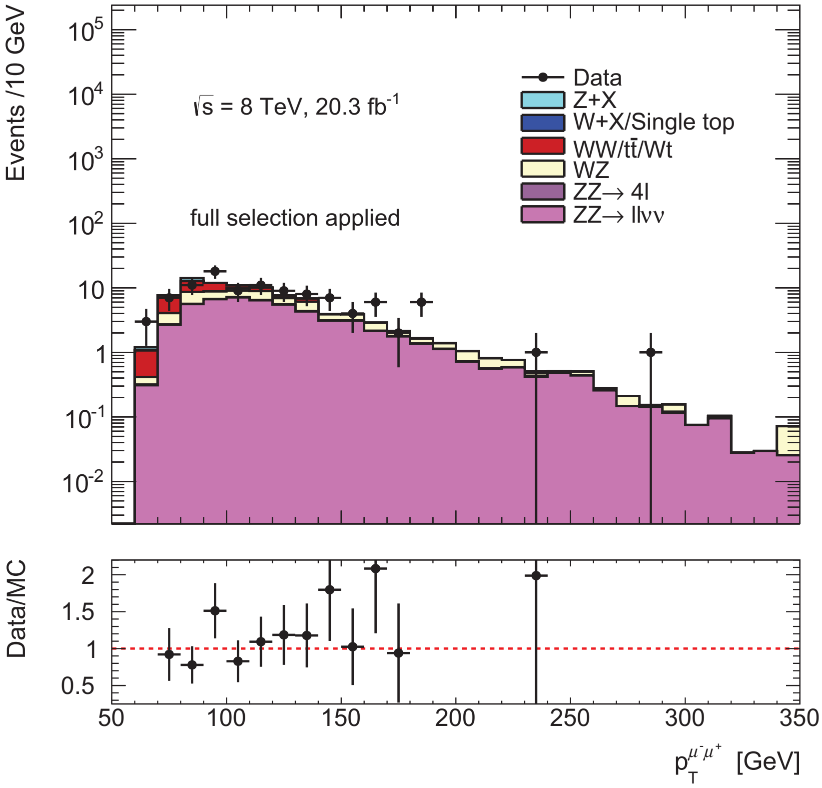

Fig. 5.18 The p_T^Z spectrum after all *ZZ* selection cuts in the $\mu^-\mu^+\nu\bar{\nu}$ sub-channel.

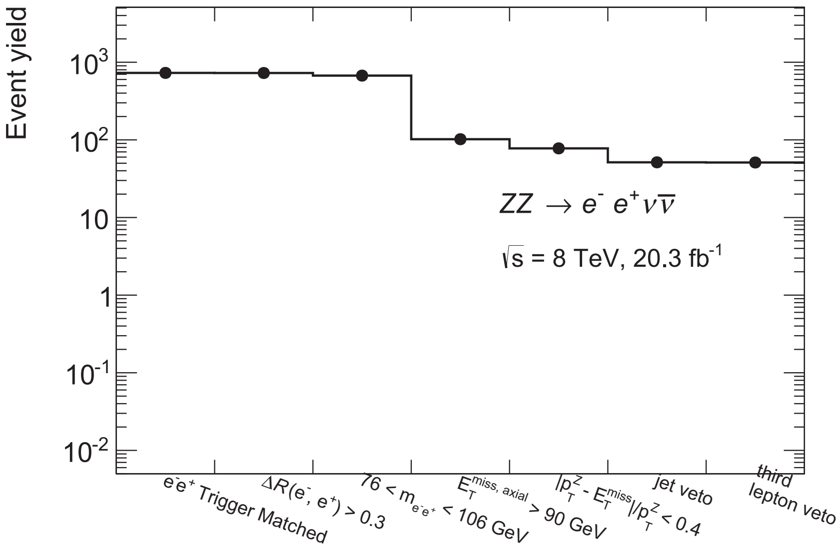

Fig. 5.19 A weighted cutflow of the selection on the $ZZ \to e^-e^+\nu\bar{\nu}$ signal.

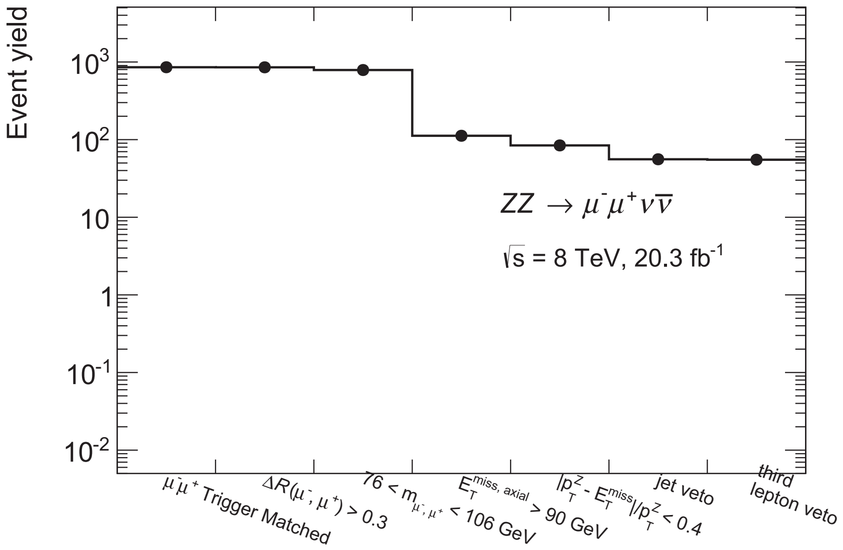

Fig. 5.20 A weighted cutflow of the selection on the $ZZ \rightarrow \mu^- \mu^+ \nu \bar{\nu}$ signal

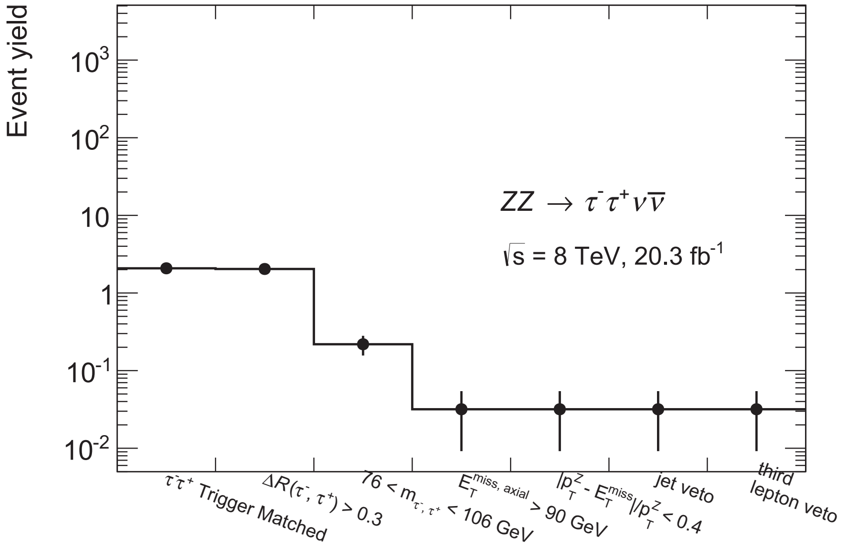

Fig. 5.21 A weighted cutflow of the selection on the $ZZ \rightarrow \tau^- \tau^+ \nu \bar{\nu}$ signal.

Table 5.5 summarises the observed and expected event counts in both sub-channels after all selection cuts. The first uncertainty is statistical and the second is systematic.

$ZZ \to \ell^-\ell^+\nu\bar{\nu}$	$e^-e^+ + E_{\mathrm{T}}^{\mathrm{miss}}$	$\mu^-\mu^+ + E_{\mathrm{T}}^{\mathrm{miss}}$
Observed	102	106
Expected Signal	$51.1 \pm 0.9^{+2.6}_{-2.5}$	$55.1 \pm 1.0^{+2.7}_{-2.9}$
Expected Total Background	$32.4^{+5.5}_{-4.6}{}^{+3.3}_{-3.2}$	$33.2^{+6.0}_{-5.0}{}^{+3.4}_{-3.3}$

Table 5.5 A summary of observed events and expected signal and background contributions in the individual $ZZ \to \ell^-\ell^+\nu\bar{\nu}$ sub-channels. The background estimations cover $Z+X$, single top, $t\bar{t}$ other diboson processes, and $W+X$. The first error is statistical while the second is systematic.

5.8 Reconstruction systematic uncertainties

This section lists the various experimental systematics associated with electron/muon/jet identification and reconstruction which affect the objects used for signal selection. As essentially all of the corrections come from the recommendations of one of the ATLAS working groups, references for the sources of any corrections used are provided where possible.

5.8.1 Electron systematics

The ratio, or efficiency, of a true single electron spectrum to one determined experimentally is subject to various individual efficiencies coming from the detector, such as the efficiency to reconstruct an electromagnetic cluster from deposits in the calorimeter, the efficiency to reconstruct an electron given a cluster, and the efficiency of an electron being identified based on the selection criteria used to classify electrons. The differences observed in the reconstruction and identification efficiencies between the data and simulation are taken into account by weighting the simulation with scale factors provided by the ATLAS Egamma group. The systematic uncertainties are then determined by varying the scale factors within their uncertainties. The electron identification efficiency scale factors and their uncertainties are determined from W and Z tag-and-probe measurements [182] and are given as a function of $|\eta|$, E_{T}, and electron algorithm (`loose`, `medium`, `tight`). The uncertainties of the η and E_{T}-dependent scale factors are added in quadrature to obtain the combined electron identification uncertainty.

Another source of uncertainty lies in the difference between the data and MC distributions for the modelling of isolation and impact parameter significance cut efficiencies in tag-and-probe studies. A set of scale factors to correct the modelling of isolation is obtained in bins of η and electron p_{T}. The uncertainty due to isolation and impact-parameter significance is obtained by varying the scale factors within their $\pm 1\sigma$ uncertainties and taking the difference with respect to the nominal selection.

Simulation generally does not reproduce the energy resolution observed in data for various reasons, such as the mapping of the detector material in the geometry database. Therefore, a smearing is applied to the energy resolution in MC. The systematic uncertainties associated with the smearing procedure are obtained from an official tool provided by the ATLAS Egamma group. Systematic uncertainties on the energy scale derived from the 2012 dataset are also implemented in an official tool.

5.8.2 Muon systematics

The nature of the systematic uncertainties associated with the muons is similar to that for electrons, i.e. the dominant contributions to the overall systematic are from reconstruction uncertainties and detector resolution uncertainties.

One of the primary uncertainties for combined muons is the resolution uncertainty associated with measurements in the inner detector and muon spectrometer (MS). The momentum resolution is expressed as quadrature sum of two terms, one of which is scaled by the momentum:

$$\frac{\sigma_{p_{\mathrm{T}}}}{p_{\mathrm{T}}} = a \oplus b p_{\mathrm{T}} , \tag{5.4}$$

where the momentum is parametrised by resolution parameters, and a scale parameter in the following form:

$$p_{\mathrm{T}}^{\mathrm{corr}} = p_{\mathrm{T}}^{MC} \cdot s \cdot (1 + \Delta p_1 G(0,1) + p_{\mathrm{T}} \cdot \Delta p_2 G(0,1)) , \tag{5.5}$$

where $p_{\mathrm{T}}^{\mathrm{corr}}$ is the scaled and corrected p_{T}, s is the scale parameter, p_1 and p_2 are the resolution parameters, and $G(0,1)$ is a Gaussian distribution centered on 0 with standard deviation 1. The scale and momentum resolution parameters are determined in different η regions of the detector using a maximum likelihood template fit to $Z \to \mu\mu$ events. Scale factors are derived to enhance the agreement. The uncertainty due to muon momentum smearing for ID and MS muons is obtained by varying the momentum resolution factors within their $\pm 1\sigma$ uncertainties and taking the difference with respect to the nominal selection.

Muon momentum resolution and scale are calibrated in a both a low p_{T} region using $J/\psi \rightarrow \mu\mu$ events and a higher p_{T} region using $Z \rightarrow \mu\mu$ events. A scale correction is added into the p_{T} term to adjust the difference between simulated events and those observed in data. These correction scale factors are applied to the muons during the selection. As with the momentum resolution uncertainty, the momentum scale uncertainty is obtained in a similar fashion using the momentum scale factors.

As with electrons, scale factors are obtained in bins of η and p_{T} for muons to provide corrections for the modelling of isolation and impact parameter significance. The uncertainty due to isolation and impact-parameter significance is obtained by varying the scale factors within their $\pm 1\sigma$ uncertainties and taking the difference with respect to the nominal selection.

Muon reconstruction efficiency is determined by using a tag-and-probe method at the J/ψ and Z resonances, which allows one to select an unbiased sample of muons by requiring an ID track (the probe) that, along with a well reconstructed muon (the tag), forms a system with invariant mass consistent with a dimuon resonance. This enables a sample of low-p_{T} probes and high-p_{T} probes to be selected independently of the MS and can be used to measure the efficiency for reconstructing a muon with MS measurement. The agreement between data and Monte Carlo simulation is evaluated by means of scale factors binned in p_{T} and η, which are the ratios of the efficiencies measured in experimental data and simulation data, i.e.

$$SF = \frac{\varepsilon_{\text{reco,Data}}}{\varepsilon_{\text{reco,MC}}}. \tag{5.6}$$

Scale factors are provided by the MCP group via the package `MuonEfficiencyCorrections`. The uncertainties provided by the classes are the statistical errors of the tag-and-probe efficiency measurement. The systematic error of the scale factors as a function of the muon momentum is provided by a separate method of the scale factor class, and is of the order of 0.2%. The efficiency scale factors are varied within their uncertainties and the selection is applied to muons, with the uncertainty taken as the difference with respect to the nominal selection.

5.8.3 Jet systematics

The fractional jet p_{T} resolution, $\sigma_{p_{\mathrm{T}}}/p_{\mathrm{T}}$, is estimated with two independent in-situ methods; the dijet balance method [183] and the bisector method [184]. At fixed rapidity, the fractional jet p_{T} resolution is equivalent to the fractional jet energy resolution $\sigma(E)/E$. An interface is provided to allow smearing of jets within the jet energy resolution in MC, via the tools `ApplyJetResolutionSmearing-00-01-02` and `JetResolution-02-00-02`. For

2012 data at 8 TeV, no smearing was applied to the nominal MC jets. The systematic uncertainty is obtained by applying smearing to jets within $\pm 1\sigma$ of the measured MC resolution and taking the difference with respect to the nominal selecton.

The jet vertex fraction allows for the identification of jets originating from the hard scatter (as opposed to those from pile-up) by defining a discriminant which measures the probability that a jet originated from a particular vertex. The jet vertex fraction algorithm requires for its input reconstructed tracks, jets, and primary vertices. Three different working points are provided (nominal, up variation and down variation) and the analysis is run accordingly using the nominal JVF cut, another with the JVF up cut variation and with the JVF down cut variation. The difference with respect to the nominal correspond to the systematic uncertainty associated to the use of JVF.

5.8.4 Missing transverse momentum systematics

An uncertainty is assigned to the soft terms scale and resolution, similarly to what is done for the jets with the JES and JER uncertainties. As with jets, the smearing is done using the official tool `MissingETUtility-01-02-08`, which propagates the object systematics as defined Section 5.6 to the hard object terms, and then separately provides scale and resolution systematics on the soft terms. The uncertainty due to the soft terms resolution/scale is taken with respect to the selection using the $E_{\mathrm{T}}^{\mathrm{miss}}$ calibrated using objects without smearing applied.

5.8.5 Trigger systematics

The uncertainty due to trigger matching of selected leptons and applying an event-by-event trigger weight. The selection requires reconstructed leptons to be matched to a specific trigger or a combination of triggers (Section 5.5). After the application of the trigger requirement, the event is weighted by a per-event trigger scale factor for the analysis, according to equation Eq. (5.1). The systematic uncertainty due to trigger efficiency is obtained by varying the scale factors within their $\pm 1\sigma$ systematic uncertainties and applying the full selection and taking the difference with respect to the nominal selection.

5.8.6 Theoretical uncertainties

There are several sources of theoretical uncertainty on the samples used for background estimates, as well as the signal samples. The dominant uncertainties are given below. The

MC samples used for the signal are generated using the CT10 PDF set, which provides 26 independent degrees of freedom (eigenvectors). For each of the 26 eigenvectors, an up and a down variation is calculated. An asymmetric total PDF uncertainty may be obtained as the quadrature sum of the up variations and correspondingly for the down variations. Typically, PDF systematics are also evaluated by generating signal samples with Some generators are parton-level only in that they produce a set of four-vectors which must be showered with QCD initial and final state radiation to turn them into a sample of fully-weighted events. This places a dependency on the particular model used to shower the events and the model of the underlying event and soft, non-diffractive physics in and event. The *ZZ* signal, composed of separate POWHEGBOX and gg2VV samples, are showered with PYTHIA8. To estimate the uncertainty due to parton shower, POWHEGBOX events were showered with HERWIG+JIMMY (v6.5) and the selection is applied, with the uncertainty taken as the difference with respect to the values obtained with the nominal selection. In addition to the parton shower uncertainty, there is also a dependence on the choice of factorisation and renormalisation scales used to produce the samples. The nominal signal samples are generated with the default factorisation and renormalisation scales set to $\mu_F = \mu_R = m_{ZZ}$. However, this is only one particular choice of scale. The uncertainty is evaluated by generating independent samples (at particle-level) of *ZZ* events with the factorisation and normalisation scales varied independently by a factor of 2. The value of the QCD scale uncertainty is taken as the combination of factorisation and normalisation scale (for a given variation) which gives the largest deviation with respect to the nominal in the event yield after the full selection is applied.

5.8.7 Luminosity uncertainty

The measurement of the cross section is inversely proportional to the integrated luminosity used for the data sample. Background estimates which use MC samples are also dependent upon the normalisation to the integrated luminosity. The uncertainty on the luminosity measurement as determined by the luminosity group to be 2.8% using the methods found in [161]. The impact of luminosity scaling on background estimates is discussed in Chapter 6.

Chapter 6

Background estimation

In order to measure the ZZ production cross section, the level of background contamination of events which mimic the signal but come from other processes must be known. The estimate of the total background contribution is subtracted from the observed events in data to give the number of signal events. Both data-driven techniques as well as simulation are used to estimate the various background contributions. This chapter presents the estimation techniques used to measure the backgrounds in the $ZZ \to \ell^-\ell^+\nu\bar{\nu}$ analysis, as well as the sources of uncertainty on the estimates.

6.1 Overview of background processes

For the $ZZ \to \ell^-\ell^+\nu\bar{\nu}$ analysis, the signal is defined as $pp \to ZZ \ \to \ell^+\ell^- + E_{\mathrm{T}}^{\mathrm{miss}}$, where $\ell^\pm = e^\pm, \mu^\pm$. However, there are many other known Standard Model processes which can give rise to two high p_{T} opposite-sign, same-flavour charged leptons and a significant amount of $E_{\mathrm{T}}^{\mathrm{miss}}$, producing events which pass the full selection. Backgrounds are generally categorised by the way in which they mimic the signal, allowing estimations of multiple sources of background at once. There are five different processes which provide major contributions to the background:

- WZ: This will mimic the signal if a lepton from the W is undetected. This is the largest background after all cuts, as shown in Figs. 5.17 and 5.18. This background is reduced by the veto on third leptons.

- $ZZ \to \ell^-\ell^+\ell^-\ell^+$: This is an irreducible background if two of the charged leptons go undetected. The contribution is estimated to be on the order of 1% of the total expectation, and is estimated using fully-simulated MC samples.

- $t\bar{t}$ and associated Wt production: This will give rise to high p_{T} leptons coming from decay of the $W^{\pm}$, jets, and $E_{\mathrm{T}}^{\mathrm{miss}}$. If the jets are mismeasured, this will cause additional (fake) $E_{\mathrm{T}}^{\mathrm{miss}}$. This background is suppressed by the jet veto.

- WW production: This gives rise to two leptons and large $E_{\mathrm{T}}^{\mathrm{miss}}$coming from leptonic decays of the W bosons. However, the two charged leptons will generally not form a resonance peaked about the Z pole, and the background is suppressed by the Z mass window requirement.

- $Z \to \tau\tau$, $ZZ \to \tau^-\tau^+\nu\bar{\nu}$: These final states can also give rise to two opposite-sign same flavour electrons or muons and real $E_{\mathrm{T}}^{\mathrm{miss}}$, but they constitute very small contributions to the overall background. The expected number of $ZZ \to \tau^-\tau^+\nu\bar{\nu}$ events which make it into the signal region is shown in Fig. 5.21 and is shown to be essentially negligible. The $t\bar{t}$, Wt, WW, $ZZ \to \tau^-\tau^+\nu\bar{\nu}$, $Z \to \tau\tau$ backgrounds are estimated together by using events in an opposite-flavour lepton pair control region.

- $W+X$ (X is jets or photons), multijet, single t production: If a jet is reconstructed as a lepton, the signature is the same as the signal. However, this will not have a peak in the $m_{\ell^-\ell^+}$ spectrum within the Z mass window. This background is estimated using the "matrix method" technique.

- $Z+X$, where X is a hadronic state or photon. An imbalance in the $E_{\mathrm{T}}^{\mathrm{miss}}$ will appear as the signal. This background is suppressed by the axial-$E_{\mathrm{T}}^{\mathrm{miss}}$ and the p_{T}-balance cuts. The contribution is estimated using single photon events that are reweighted to match Z boson kinematics.

Data-driven techniques are used where possible to estimate the backgrounds. This is done for the combined $t\bar{t}, WW, Wt, \tau\tau$ estimate and the estimates of $Z+X$ the $W+X$ backgrounds. The WZ is estimated using POWHEGBOX (interfaced to PYTHIA8), with the largest theoretical systematic uncertainties estimated with MCFM, while the $ZZ \to \ell^-\ell^+\ell^-\ell^+$ background is estimated using POWHEGBOX and gg2VV (both interfaced to PYTHIA8 for parton showering).

6.2 WZ background

The WZ background is the largest after all selection cuts are applied. The background is estimated by applying all ZZ signal selection cuts to the POWHEGBOX (interfaced to PYTHIA8) WZ samples. The MC prediction is validated in separate three-lepton control regions: eee, $ee\mu$, $\mu\mu e$, and $\mu\mu\mu$. For the $ee\mu$ and $\mu\mu e$ signatures, the same-flavour leptons are paired together to form a candidate Z boson, and for the eee and $\mu\mu\mu$ channels, the lepton pair which gives an invariant mass closest to the Z mass given by the PDG is used as the Z candidate, and the unpaired lepton is considered the third lepton. Comparisons to data are shown in Figs. 6.1(a) to 6.1(d) for the four control regions. The agreement

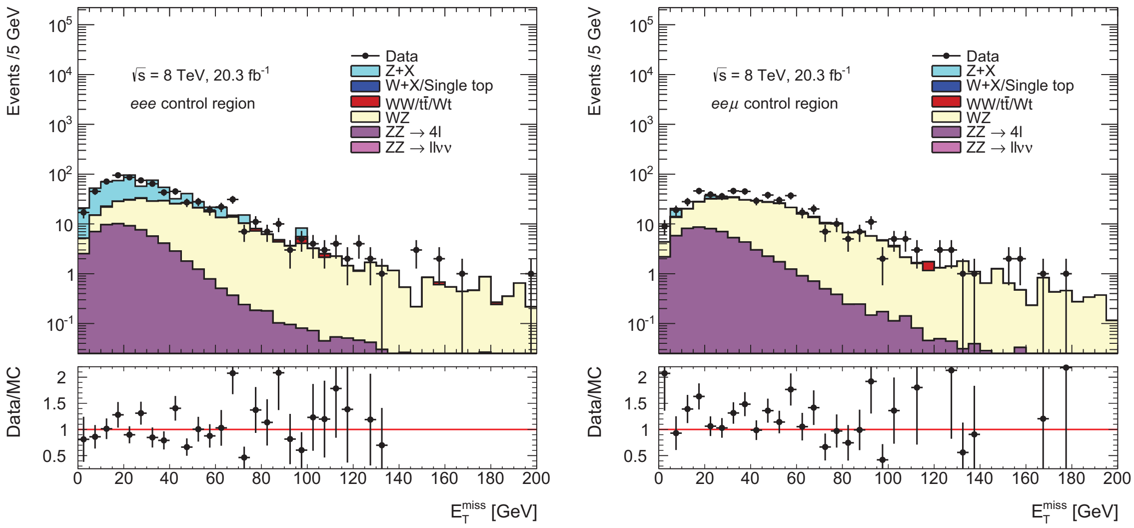

(a) eee (b) $ee\mu$

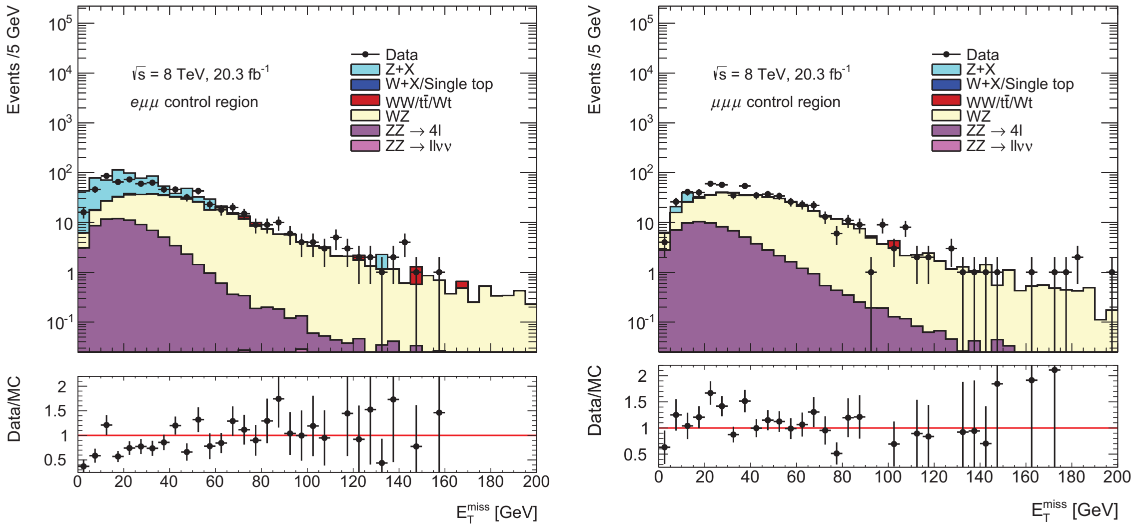

(c) $e\mu\mu$ (d) $\mu\mu\mu$

Fig. 6.1 $E_{\mathrm{T}}^{\mathrm{miss}}$ in the three-lepton validation regions used in the WZ background estimate. The leptons are required to be trigger matched. For the eee and $\mu\mu\mu$ control regions, the opposite-sign pairing which minimises the difference between the $m_{\ell^-\ell^+}$and the PDG Z mass is used to reconstruct the Z boson.

in the eee and $\mu\mu\mu$ control regions at low $E_{\mathrm{T}}^{\mathrm{miss}}$ is better compared to the $ee\mu$ and $e\mu\mu$ control regions. Previously, in the 7 TeV analysis, an additional systematic was assigned to cover any significant excess from the Z+jets component. As there is no significant excess in the Z+jets component, and the $WW, t\bar{t}, Wt$ contributions to the control regions is small, no additional systematic is assigned.

The nominal values of the WZ backgrounds in the ee and $\mu\mu$ sub-channels are given at the top of Table 6.1. Because the estimate is taken from simulation, it is subject to both experimental and theoretical uncertainties. Experimental uncertainties on lepton reconstruction and identification and triggering are accounted for, as well as uncertainties on jet energy scale and resolution and $E_{\mathrm{T}}^{\mathrm{miss}}$ resolution. All samples are normalized to the luminosity of the data sample (Section 5.8.7), making the estimate subject to a luminosity normalisation uncertainty. The dominant theoretical uncertainties come from the choice of QCD scale used to generate the WZ samples and the PDF uncertainty. Assessing the QCD scale uncertainty is typically done by varying the renormalisation and factorisation scales up and down independently[1] in the generator to produce a range of samples used to assess the magnitude of the resulting change on the background estimate. The WZ samples consist of all three flavours of leptonic decay for the W and Z (Chapter A), both for W^+ and W^-. Production of fully-simulated samples is computationally intensive, and production of fully-simulated variations for all WZ samples is not practical. To overcome this, particle-level WZ samples were produced with MCFM with the scales set to $\frac{1}{2}m_{WZ}$ for the nominal, m_{WZ} for the upward and $\frac{1}{4}m_{WZ}$ for the downward variation. The MCFM samples were then reweighted to provide a "scale weight" which was applied to the POWHEGBOX samples. The QCD scale weights as a function of p_{T}^{Z} are shown in Fig. 6.2. The PDF uncertainties are estimated using the eigenvectors provided by LHAPDF (Section 5.8.6) and applying the corresponding weights to the nominal POWHEGBOX samples. The nominal values of the the WZ background and the contributions to the background from systematic uncertainties are given in Table 6.1.

6.3 $ZZ \to \ell^-\ell^+\ell^-\ell^+$ background

The $ZZ \to \ell^-\ell^+\ell^-\ell^+$ background is also estimated using simulated samples. The samples used are listed in Table 5.1. This is the smallest background after all selection cuts are applied. Here the uncertainty due to PDF variation has not been included, as it is negligible. The nominal values of the background are given in Table 6.2.

---

[1] Generators such as POWHEGBOX allow for independent variation of the factorisation and normalisation scales, although many generators do not allow for this.

	ee channel	$\mu\mu$ channel
Expected events	16.9	18.7
statistical uncertainty	+6.5% −6.5%	+5.7% −5.7%
luminosity	+2.8% −2.8%	+2.8% −2.8%
electron energy scale	+4.0% −2.2%	−0.2% +0.2%
electron energy resolution	+0.4% +1.5%	0.0% −0.2%
electron reconstruction efficiency	+0.7% −0.7%	0.0% 0.0%
electron identification efficiency	+1.5% −1.5%	0.0% 0.0%
electron isolation	+0.3% −0.3%	0.0% 0.0%
muon reconstruction uncertainty	-	+0.6% −0.6%
muon identification efficiency	-	+0.1% −0.1%
muon momentum resolution	-	+1.7% −0.4%
muon momentum scale	-	+0.3% −0.8%
muon isolation	-	+2.8% −2.8%
jet energy scale	−6.0% +4.0%	−3.8% +3.9%
jet energy resolution	−6.1% +6.1%	−3.2% +3.2%
jet vertex fraction	+0.4% −0.3%	+0.4% −0.2%
$E_{\mathrm{T}}^{\mathrm{miss}}$ resolution (soft terms)	+2.2% −2.2%	−1.2% +1.2%
$E_{\mathrm{T}}^{\mathrm{miss}}$ scale (soft terms)	+0.9% +2.0%	−3.1% −0.1%
trigger	+0.1% −0.1%	+0.5% −0.5%
QCD scale	−6.0% +7.4%	−5.6% +6.9%
PDF	−3.2% +2.6%	−3.0% +2.6%

Table 6.1 The relative systematic uncertainties for the WZ background. The dominant uncertainties come from the contributions from limited statistics of the WZ samples and the QCD scale uncertainties. Uncertainties such as lepton reconstruction and identification and theoretical uncertainties are also included. A dash indicates an uncertainty of less than 0.1% .

	ee channel	$\mu\mu$ channel
Expected events	0.57	0.59
luminosity	$^{+2.8\%}_{-2.8\%}$	$^{+2.8\%}_{-2.8\%}$
statistical uncertainty	$^{+7.1\%}_{-7.1\%}$	$^{+7.7\%}_{-7.7\%}$
electron identification	$^{+1.6\%}_{-1.6\%}$	-
electron isolation	$^{+0.3\%}_{-0.3\%}$	-
electron reconstruction efficiency	$^{+0.7\%}_{-0.7\%}$	-
electron energy resolution	$^{-0.9\%}_{-0.8\%}$	-
electron energy scale	$^{+3.7\%}_{-5.4\%}$	-
muon momentum resolution	-	$^{-0.2\%}_{+0.7\%}$
muon momentum scale	-	$^{-0.2\%}_{0.0\%}$
muon reconstruction efficiency	-	$^{+0.3\%}_{-0.3\%}$
muon identificaton efficiency	-	$^{+0.5\%}_{+0.4\%}$
muon isolation	-	$^{+3.0\%}_{-3.0\%}$
jet energy scale	$^{-10.2\%}_{+3.2}$	$^{-5.3\%}_{+8.3\%}$
jet energy resolution	$^{-0.6\%}_{+0.6\%}$	$^{-8.4\%}_{+8.4\%}$
jet vertex fraction	$^{0.0\%}_{-1.6\%}$	-
$E_{\mathrm{T}}^{\mathrm{miss}}$resolution (soft terms)	$^{-0.9\%}_{+0.9\%}$	$^{-0.3\%}_{+0.3\%}$
$E_{\mathrm{T}}^{\mathrm{miss}}$scale (soft terms)	$^{-2.1\%}_{-0.4\%}$	$^{+0.4\%}_{+0.4\%}$
trigger	$^{+0.1\%}_{-0.1\%}$	$^{+0.5\%}_{-0.5\%}$

Table 6.2 The relative systematic uncertainties for the $ZZ \to \ell^-\ell^+\ell^-\ell^+$ background estimated from the POWHEGBOX and gg2VV samples in the *ee* and $\mu\mu$ sub-channels. The dominant contribution is from the statistical uncertainty on the samples used to estimate the background. In the *ee* sub-channel, electron reconstruction and identification systematics dominate, while in the $\mu\mu$ sub- channel, the muon reconstruction systematics and momentum scale systematics contribute.

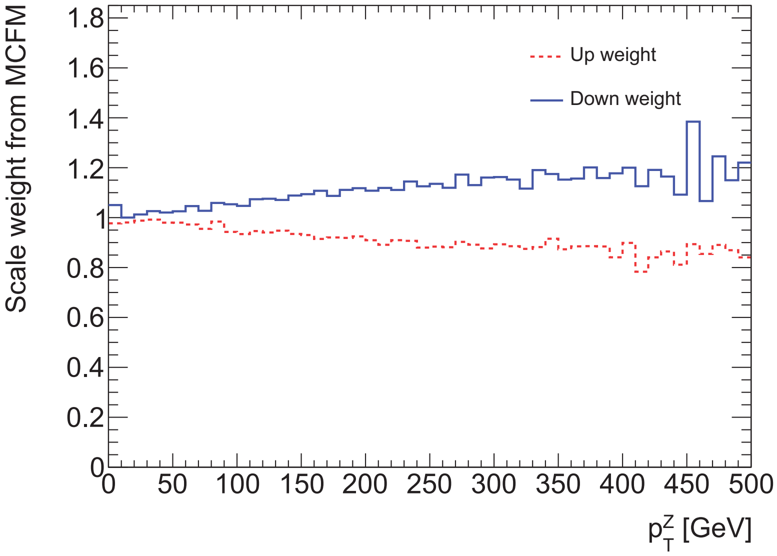

Fig. 6.2 Weights obtained by varying samples produced with MCFM at different factorisation and normalisation scales, which are then applied to POWHEGBOX WZ samples to assess the systematic uncertainty due to QCD scale.

6.4 $t\bar{t}$, Wt, WW, $ZZ \to \tau^-\tau^+\nu\bar{\nu}$, and $Z \to \tau\tau$ background

These events will give rise to two real high p_T leptons and real E_T^{miss} coming from boson decays to neutrinos. This background is estimated using a data-driven technique which exploits the fact that the leptonic decay branching ratios for the ee, $\mu\mu$ and $e\mu$ channels from $t\bar{t}$, Wt, WW and $Z \to \tau\tau$ are (1:1:2). The opposite-flavour region $e\mu$ contains no $ZZ \to e^-e^+\nu\bar{\nu}$ or $ZZ \to \mu^-\mu^+\nu\bar{\nu}$ signal. Events selected inside the Z-mass window can be used to estimate the background via an extrapolation to an opposite-sign same-flavour region.

Events are selected by applying the same cuts as for the $ZZ \to e^-e^+\nu\bar{\nu}$ and $ZZ \to \mu^-\mu^+\nu\bar{\nu}$ signal regions, however, instead of requiring the same flavour of lepton, opposite-flavour lepton pairs are selected. This region is referred to as the "$e\mu$ control region". Differences in lepton selection efficiencies between the two flavours must be accounted for. The number of dilepton events selected in the $\ell_1\ell_2$ channel (where $\ell_i = e, \mu$) proportional to the product of individual lepton efficiencies; this may be expressed as

$$N_{\ell_1\ell_2} = \varepsilon_{\ell_1}\varepsilon_{\ell_2}M_{\ell_1\ell_2}, \tag{6.1}$$

where $M_{\ell_1\ell_2}$ is the number of events produced in the $\ell_1\ell_2$ channel, and ε_{ℓ_1} and ε_{ℓ_2} are the corresponding selection efficiencies. These selection efficiencies are assumed to be independent of lepton kinematics. The number of same-flavour to opposite-flavour events is given in terms of the number of opposite-flavour events by

$$M_{ee} = M_{\mu\mu} = \frac{1}{2} M_{e\mu} = \frac{1}{2} \frac{N_{e\mu}}{\varepsilon_e \varepsilon_\mu}, \tag{6.2}$$

using Eq. (6.1). Here, $N_{e\mu}$ is the number number of opposite-flavour dilepton events in the $e\mu$ control region. Combining Eq. (6.1) (with $\ell_1 = \ell_2 = e$ or $\ell_1 = \ell_2 = \mu$) and Eq. (6.2) gives

$$\begin{aligned} N_{ee} &= \frac{N_{e\mu}}{2} \frac{\varepsilon_e}{\varepsilon_\mu}, \\ N_{\mu\mu} &= \frac{N_{e\mu}}{2} \frac{\varepsilon_\mu}{\varepsilon_e}. \end{aligned} \tag{6.3}$$

The ratio of selection efficiencies becomes

$$k_{ee} \equiv \frac{1}{2} \frac{\varepsilon_e}{\varepsilon_\mu} = \frac{1}{2} \frac{\sqrt{N'_{ee}/M'_{ee}}}{\sqrt{N'_{\mu\mu}/M'_{\mu\mu}}} = \frac{1}{2} \sqrt{\frac{N'_{ee}}{N'_{\mu\mu}}} \tag{6.4a}$$

$$k_{\mu\mu} \equiv \frac{1}{2} \frac{\varepsilon_\mu}{\varepsilon_e} = \frac{1}{2} \frac{\sqrt{N'_{\mu\mu}/M'_{\mu\mu}}}{\sqrt{N'_{ee}/M'_{ee}}} = \frac{1}{2} \sqrt{\frac{N'_{\mu\mu}}{N'_{ee}}} \tag{6.4b}$$

The quantities N'_{ee} and $N'_{\mu\mu}$ are estimated in a control region where $Z \to ee$ and $Z \to \mu\mu$ processes dominate. This control region consists of dilepton events passing the Z candidate cuts Section 5.7. As the contamination from non-$Z \to ee$ and non-$Z \to \mu\mu$ events is small, no background subtraction to the $Z \to ee$ and $Z \to \mu\mu$ processes is done in these regions. Ideally, N'_{ee} and $N'_{\mu\mu}$ would be measured in a separate ee and $\mu\mu$ control regions dominated by the processes being estimated in this data-driven method (WW, for example), but obtaining such a control region with sufficient statistics is challenging. Using these relations gives the expressions for the background estimates

$$N_{ee}^{t\bar{t},Wt,WW,ZZ\to\tau^-\tau^+\nu\bar{\nu},Z\to\tau\tau} = (N_{e\mu}^{\text{data}} - N_{e\mu}^{\text{bkgd}}) \times k_{ee} \tag{6.5a}$$

$$N_{\mu\mu}^{t\bar{t},Wt,WW,ZZ\to\tau^-\tau^+\nu\bar{\nu},Z\to\tau\tau} = (N_{e\mu}^{\text{data}} - N_{e\mu}^{\text{bkgd}}) \times k_{\mu\mu}, \tag{6.5b}$$

where $N_{e\mu}^{\text{bkgd}}$ is the contamination from other processes in the opposite-flavour control region coming from processes such as WZ, that are not part of this background estimate. The contamination $N_{e\mu}^{\text{bkgd}}$ is estimated from simulation. Fig. 6.3(a) shows the $E_{\text{T}}^{\text{miss}}$ spectrum in the opposite-flavour control region, and the p_{T} of the $e\mu$ pair is shown in Fig. 6.3(b).

The WW, Wt, and $t\bar{t}$ processes dominate and contribute more than 98% of the selected $e\mu$ events.

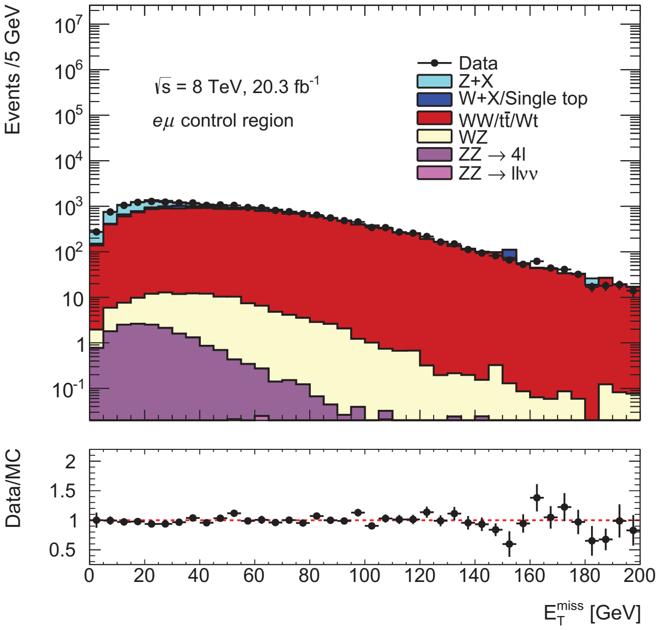

(a) The $E_{\mathrm{T}}^{\mathrm{miss}}$ spectrum in selected $e\mu$ events used for the $WW/t\bar{t}/Wt$ background.

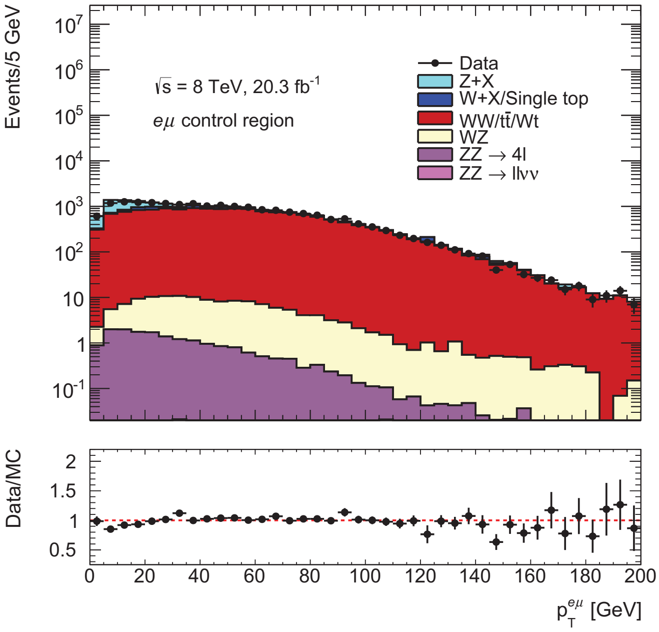

(b) The p_{T} of the dilepton pair in selected $e\mu$ events used for the $WW/t\bar{t}/Wt$ background.

Fig. 6.3 (a) The $E_{\mathrm{T}}^{\mathrm{miss}}$ spectrum and (b) the p_{T} of the dilepton pair in selected $e\mu$ events used for the $WW/t\bar{t}/Wt$ background. Within the mass window 76 GeV $< m_Z <$ 106 GeV, the dominant contributions are from $WW, t\bar{t}, Wt$. At this stage of the selection, contributions to the $e\mu$ control region from processes other than WW, $t\bar{t}$, Wt and $Z \to \tau\tau$, are between 2 and 3%. There are also non-negligible contributions from WZ, which are subtracted off to obtain the corrected number of $e\mu$ events in data using Eq. (6.5).

The dominant uncertainties for this background method fall into four general categories. They are:

- Statistical uncertainty in both the opposite-flavour $e\mu$ region, $N_{e\mu}$, and the control regions used to measure N'_{ee} and $N'_{\mu\mu}$. Correlation between sub-channels occurs since the same set of event counts is used for both sub-channels in each corresponding bin. Asymmetric Poisson uncertainties were used for the $N_{e\mu}$ event counts because this event count is close to zero for some of the bins.
- An additional uncertainty is placed on the quantities k_{ee} and $k_{\mu\mu}$, which is the difference between values obtained by calculating these quantities from $Z \to ee$ and $Z \to \mu\mu$ simulated samples and that obtained from the combined $t\bar{t}$, Wt, WW,$Z \to \tau\tau$ samples.

- Statistical uncertainty from the non-$e\mu$ background that is subtracted off in the actual background estimate. This uncertainty is correlated between channels, as it appears in the estimates for both sub-channels as shown in Eq. (6.5).
- Processes that are modelled with MC simulation to obtain $N_{e\mu}^{\text{bkgd}}$ are subject to luminosity, lepton reconstruction/identification and jet resolution and $E_{\text{T}}^{\text{miss}}$ uncertainties. Systematic variations which give changes less than 0.1% of the central value are neglected.

The nominal values of the background and systematic uncertainties are given in Table 6.3.

	ee	$\mu\mu$
Expected events	13.30	15.4
statistical uncertainty from estimation of $N_{e\mu}, N'_{ee}, N'_{\mu\mu}$	${}^{22.5\%}_{-19\%}$	${}^{24\%}_{-19\%}$
statistical uncertainty from estimation of $N_{e\mu}^{\text{bkgd}}$	$\pm 0.5\%$	$\pm 0.5\%$
uncertainty on calculation of $k_{ee}, k_{\mu\mu}$	$\pm 2.8\%$	$\pm 2.8\%$
luminosity	$\pm 0.04\%$	$\pm 0.04\%$
jet energy resolution	$\pm 0.25\%$	$\pm 0.25\%$
$E_{\text{T}}^{\text{miss}}$resolution and soft-terms scale	$\pm 0.3\%$	$\pm 0.3\%$
remaining reconstruction uncertainties (combined)	$\pm 0.4\%$	$\pm 0.4\%$
total uncertainty	${}^{23\%}_{-19\%}$	${}^{23.5\%}_{-19\%}$

Table 6.3 Data-driven estimates and for the collective $t\bar{t}$, Wt, WW, $ZZ \to \tau^+\tau^-\nu\nu$ and $Z \to \tau^+\tau^-$ background processes. Any reconstruction and luminosity uncertainty that is less than 0.1% of the nominal value in both directions has been neglected. The combined lepton reconstruction and identification uncertainties for summary purposes only.

6.5 $Z+X$ background

After selecting events with two leptons which pass the selection criteria within the Z-mass window, the most dominant background contribution is from $Z+X$, where X is a hadronic state or a photon and the Z boson decays leptonically, as shown in Section 5.7. The $E_{\text{T}}^{\text{miss,axial}}$ cut, the p_{T}-balance cut, and the jet veto all serve to suppress the $Z+X$ background. Simulation shows that the expected background from $Z+X$ is small relative to the overall signal.

However, as the cut on $E_{\mathrm{T}}^{\mathrm{miss,axial}}$ is at 90 GeV most of the Z+jets simulated samples tend to run out of statistics in the signal region, making background estimation subject to large systematic uncertainties due to the limited statistics of the samples. Furthermore, any estimate taken from simulation is heavily dependent upon the fake $E_{\mathrm{T}}^{\mathrm{miss}}$ modelling in MC simulation. This, in turn is dependent upon the contributions of jets, electrons, muons, and photons, in addition to the effects of pileup on the modelling of the $E_{\mathrm{T}}^{\mathrm{miss}}$. To reduce this dependency, a data-driven technique based on photon-reweighting is chosen. Using photons to model background contributions from invisibly decaying Z bosons was first developed in the context of calibrating the Standard Model background from $Z \to \nu\bar{\nu}$ decays to new physics processes [185]. This technique has been used in ATLAS SUSY searches to estimate the contribution from invisible Z decays in events with with jets, $E_{\mathrm{T}}^{\mathrm{miss}}$, and multiple leptons which could occur in a cascade decay of a squark or gluino [186]. Methods using $\gamma+$jets events to model $Z \to \ell^+\ell^- +$jets were developed in the context of the $ZZ \to \ell^-\ell^+\nu\bar{\nu}$ analyses at 7 TeV [77], although it can be extended to W^-W^+ and $H \to W^-W^+$ analyses [187]. Photon events are similar to Z boson events because they also have no true missing energy and they have a similar hadronic recoil. Furthermore, this method relies strongly on the data, which avoids mismodelling of the $E_{\mathrm{T}}^{\mathrm{miss}}$distribution in simulation. In general, it is difficult to find control regions based on lepton isolation and identification that are not contaminated with $Z+$jets processes, however photons allow a sufficiently high-statistics control region to model Z kinematics.

The details of photon selection and photon triggers used are described Section 5.6.2. The photon E_{T} spectrum and the $E_{\mathrm{T}}^{\mathrm{miss}}$ in single photon events are shown in Figs. 6.4 and 6.5.

At low $E_{\mathrm{T}}^{\mathrm{miss}}$ the dominant backgrounds to single photon plus jet production are quark and gluon-induced multijet processes which are not modelled. The excess in data at low E_{T}^{γ} in Fig. 6.4 is assumed to be primarily due to missing dijet and multijet samples. The tail of the $E_{\mathrm{T}}^{\mathrm{miss}}$ spectrum consists mainly of electroweak processes that have real missing energy, such as $W\gamma$, and $Z \to \nu\bar{\nu}+\gamma$. In addition to the photon E_{T} selection, a lepton veto is applied to reject leptonically decaying $W^{\pm}$ bosons produced with a photon. The veto requirement uses the same lepton definition as in the analysis.

In order for the $E_{\mathrm{T}}^{\mathrm{miss}}$ in photon events to model the $E_{\mathrm{T}}^{\mathrm{miss}}$ in Z events, a reweighting in a kinematic variable must be performed. In general, the reweighting is applied in a variable such as E_{T}^{γ} and $p_{\mathrm{T}}^{\mathrm{jet}}$. However, because of the jet veto used in the analaysis, only the photon E_{T} serves as a candidate for reweighting. A simple set of event weights is derived by taking the ratio of the p_{T}^{Z} sprectrum to the E_{T}^{γ} as shown in Fig. 6.8. The weight for a photon in a given range $E_{T,1} < E_{T}^{\gamma} < E_{T,2}$ is taken as the ratio of the total number of Z events within that p_{T} (E_{T}) range divided by the number of single photon events within that same p_{T} range,

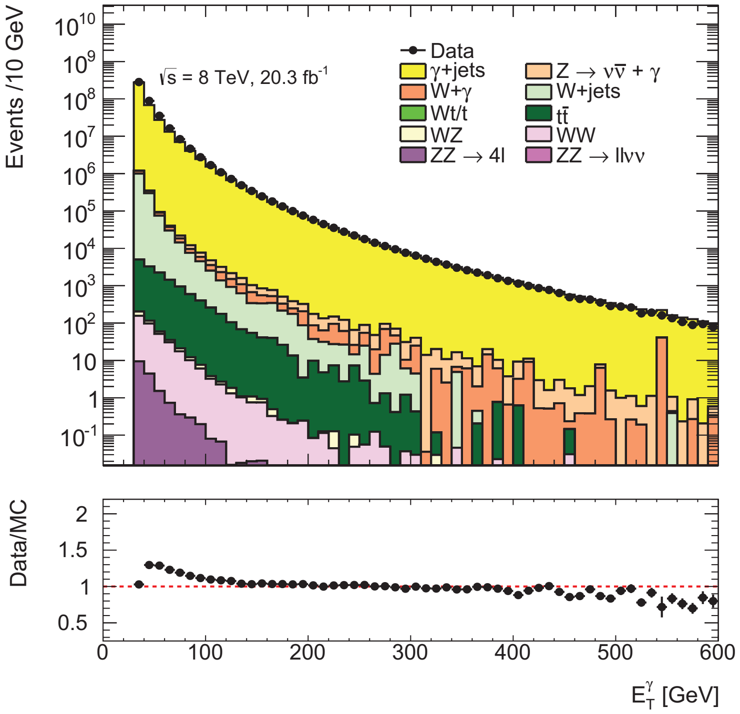

Fig. 6.4 The E_{T}^{γ} spectrum in single photon events produced in association with jets. Photons events in data within a particular E_{T}^{γ} range are multiplied by their respective prescales to obtain a smooth spectrum. This spectrum is used to derive weights which are used to model $Z+$jets events. The small excess at low E_{T}^{γ} is due primarily to missing QCD dijet and multijet samples.

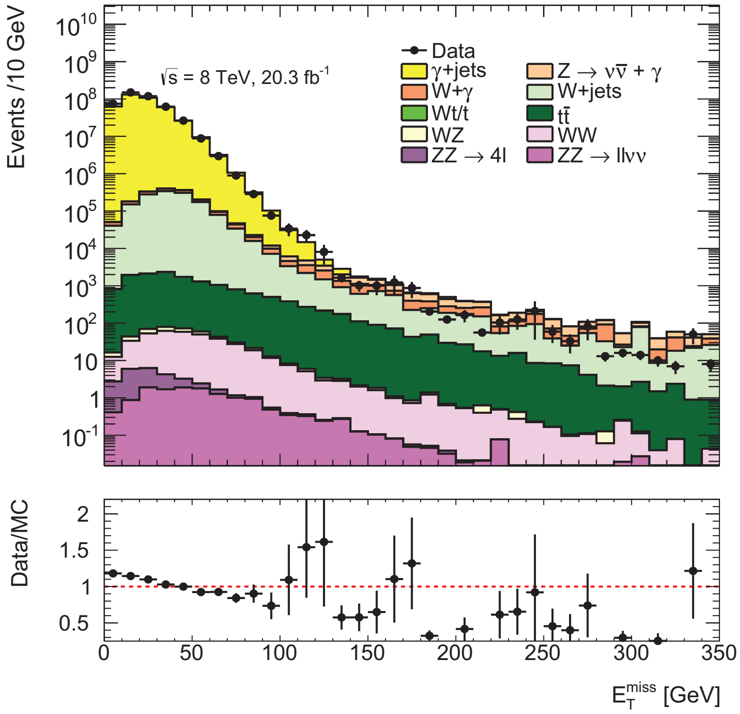

Fig. 6.5 The $E_{\mathrm{T}}^{\mathrm{miss}}$ spectrum in single photon events produced in association with jets.

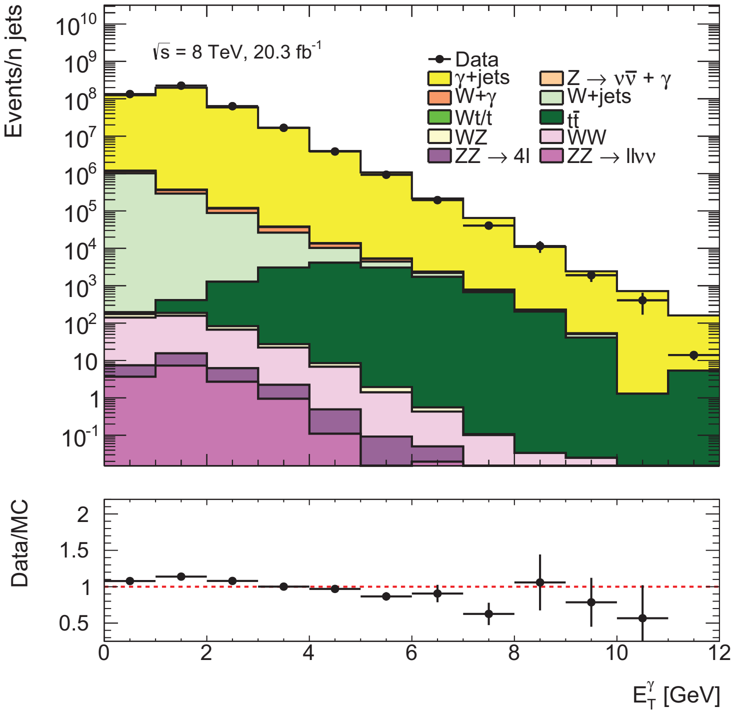

Fig. 6.6 The jet multiplicity spectrum in single photon events.

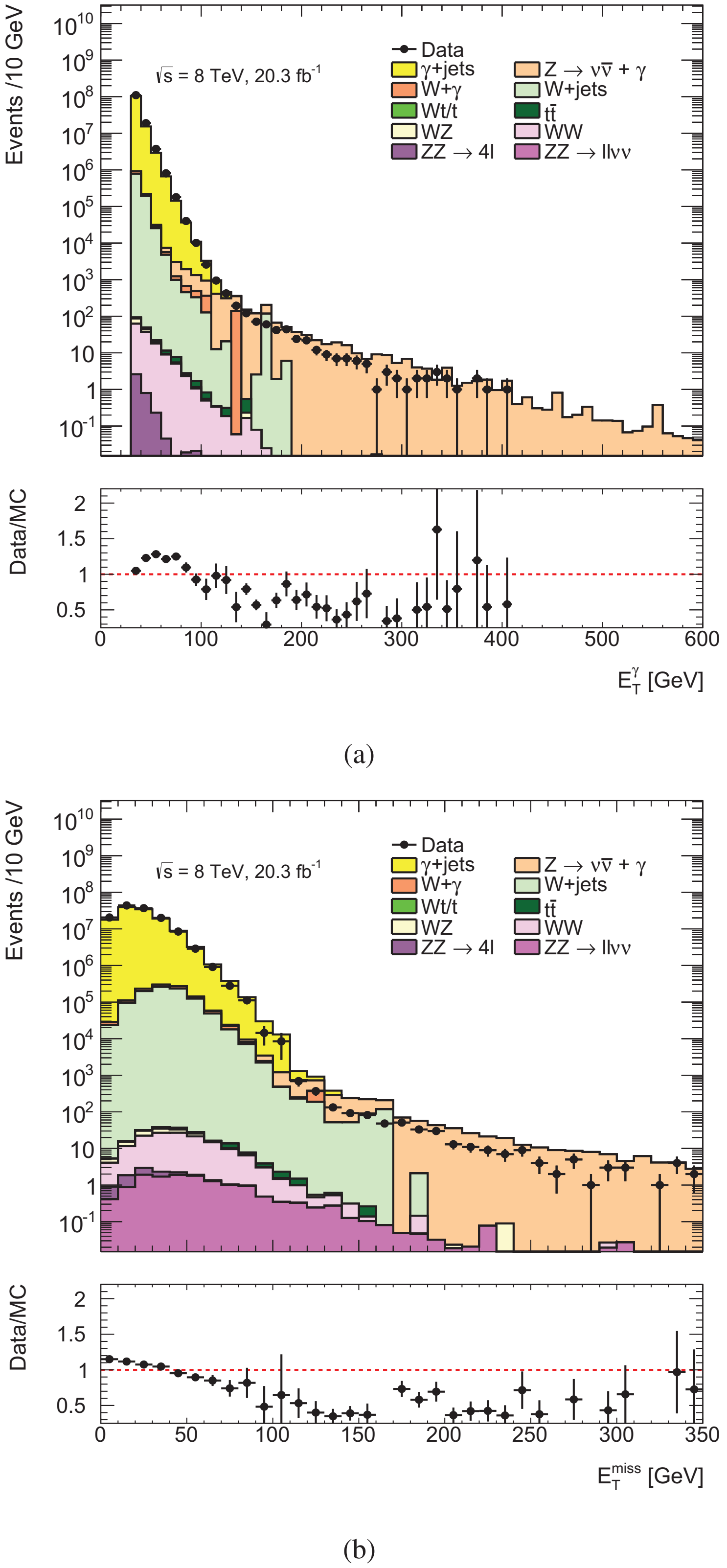

(a)

(b)

Fig. 6.7 The (a) E_{T}^{γ} and (b) $E_{\mathrm{T}}^{\mathrm{miss}}$ spectra in single photon events with a veto on additional jets. The E_{T}^{γ}spectrum is much more steeply falling compared to Fig. 6.4, and is used to derive a separate set of weights for the ZZ signal region once the jet veto is applied.

i.e.

$$w_\gamma\left(E_{\mathrm{T},1} < E_\mathrm{T}^\gamma < E_{\mathrm{T},2}\right) = \frac{N_\text{events}^Z\left(p_{\mathrm{T},1} < p_\mathrm{T}^Z < p_{\mathrm{T},2}\right)}{N_\text{events}^\text{single-photon}\left(E_{\mathrm{T},1} < E_\mathrm{T}^\gamma < E_{\mathrm{T},2}\right)}. \tag{6.6}$$

The spectra are derived from Z bosons using a low-E_T^miss control region of $E_\mathrm{T}^\text{miss} < 70$ GeV to ensure orthogonality to the signal region, but also to ensure sufficient statistics. Photon selection proceeds similarly to Z selection, although the lepton separation cut (Section 5.7) is not applied as the photon is not formed from a lepton pairing. The jet veto changes the p_T spectra and significantly reduces the statistics available for weighting. Because of the change in p_T shape, weights are derived using the same requirements with an additional requirement of the jet veto. Weights derived without the jet veto (Fig. 6.8(d)) are applied for modeling and shape comparison of the E_T^miss with data, while the full background estimate is obtained with the set of weights derived with the jet veto.

The modelling can be enhanced if the azimuthal angle between the photon and the E_T^miss is accounted for. The ZZ selection places a cut on $E_\mathrm{T}^\text{miss,axial}$, which uses the difference in azimuthal angle between the p_T^Z and the E_T^missas per Eq. (5.3). To enhance the modelling of the $E_\mathrm{T}^\text{miss,axial}$, weights are derived in both E_T^γ and $\Delta\phi(E_\mathrm{T}^\gamma, E_\mathrm{T}^\text{miss})$ analogously to the one-dimensional weights shown in Fig. 6.8. The two-dimensional weights are shown in Fig. 6.9. The binning in E_T^γ is coarser than that of $\Delta\phi(E_\mathrm{T}^\gamma, E_\mathrm{T}^\text{miss})$ due to the fact that the above distribution in E_T very strongly dependent upon E_T, with roughly a 10^6 variation from the lowest to highest bins. Ideally, the distribution would be folded around $\Delta\phi(E_\mathrm{T}^\gamma, E_\mathrm{T}^\text{miss}) = 0$, and the bins would be adjusted and optimised in both variables so there are not large deviations from bin-to-bin in $\Delta\phi(E_\mathrm{T}^\gamma, E_\mathrm{T}^\text{miss})$ resulting in a more uniform weighting procedure. However, this set of weights is acceptable, because the $E_\mathrm{T}^\text{miss,axial}$ cut is relatively high, so the weighting has a small effect in the signal region after all selection cuts are applied. To obtain the background, the weights are applied to events which require single photon events. The relevant ZZ selection cuts are applied except for the Z mass window and the fractional difference cut, as these are not defined for photons. The $E_\mathrm{T}^\text{miss,axial}$ spectrum with reweighted photons in place of $Z+$jets MC is shown in Fig. 6.10. Once the jet veto is applied, weights derived in the control regions using the jet veto are applied. Non-$\gamma+$jets background modelled with MC is also reweighted and subtracted off. The remaining events are taken as the nominal estimate of the background. The nominal values of the background estimate are given in Table 6.4. The dominant uncertainties in this background estimation technique come from several sources:

- The statistical uncertainty associated with the finite number of single photon events in data.

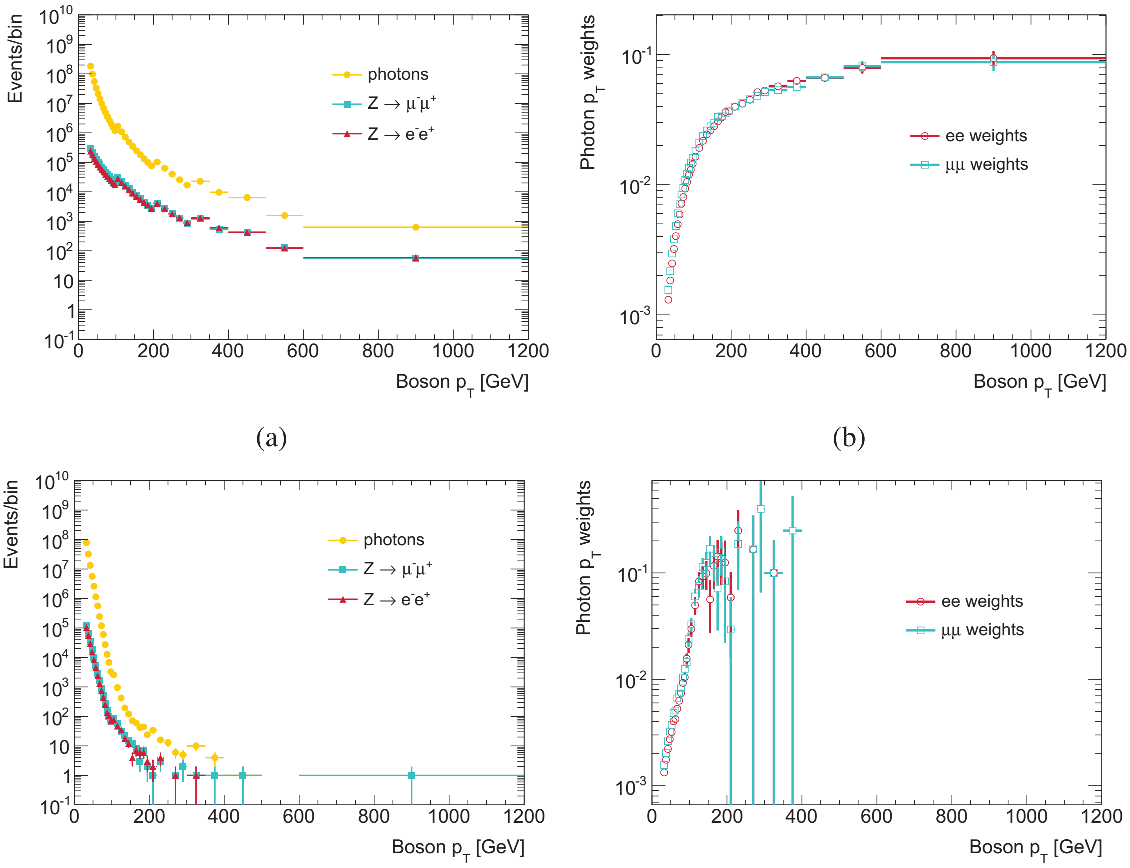

(a) (b)

(c) (d)

Fig. 6.8 An example of the photon E_T^{γ} spectrum and the p_T^Z spectrum for the $Z \to ee$ and $Z \to \mu\mu$ channels used to derive a set of kinematic weights applied to single photon events. Both photons and Z bosons are required to have a minimum of 30 GeV. The selection for the Z is the same as in the ZZ selection up to the Z mass window cut. A requirement of $E_T^{\mathrm{miss}} < 70$ GeV is placed to ensure orthogonality to the ZZ signal region. The boson p_T spectra with the jet veto are shown in (c), and the corresponding weights derived with the jet veto are shown in (d).

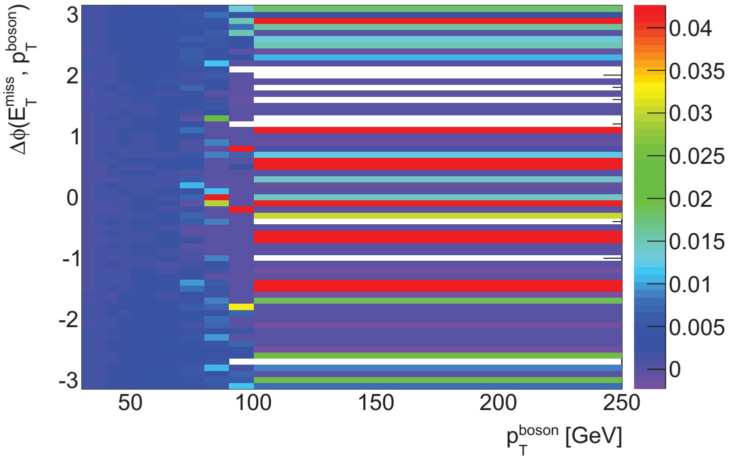

(a)

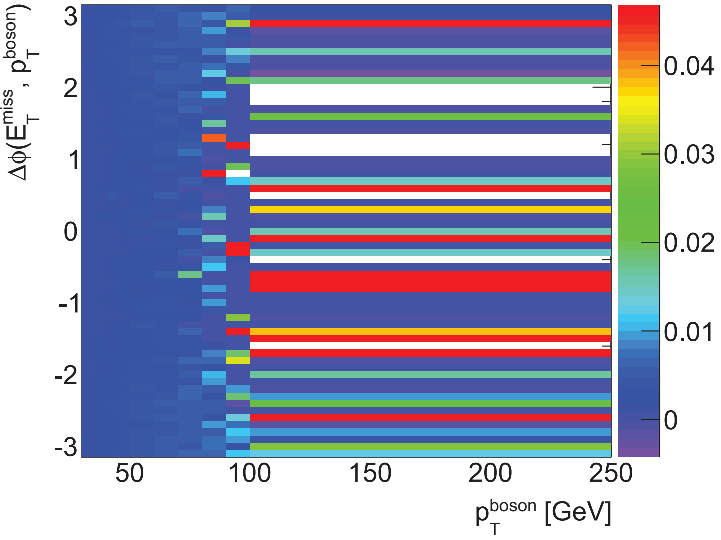

(b)

Fig. 6.9 Two-dimensional photon weights as a function of E_{T}^{γ} and $\Delta\phi(E_{\mathrm{T}}^{\gamma}, E_{\mathrm{T}}^{\mathrm{miss}})$ in the (a) *ee* channel and (b) the $\mu\mu$ channel. The weights shown are derived with the jet veto.

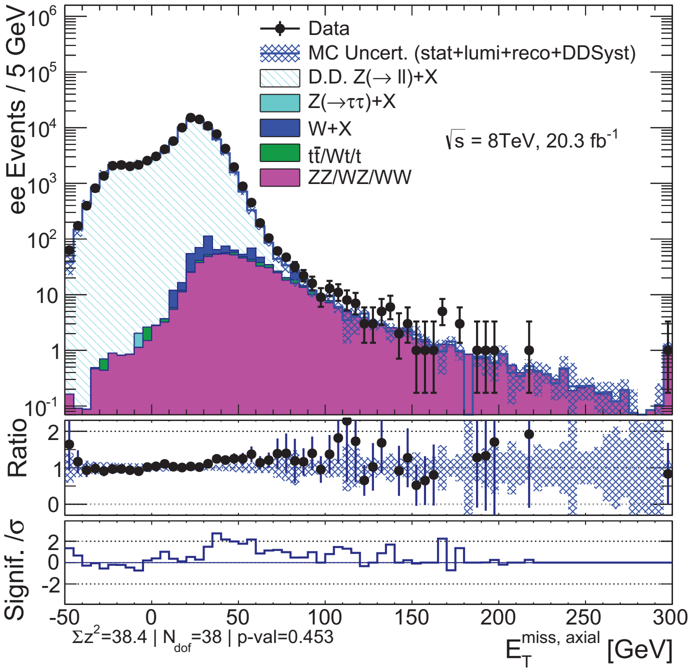

(a)

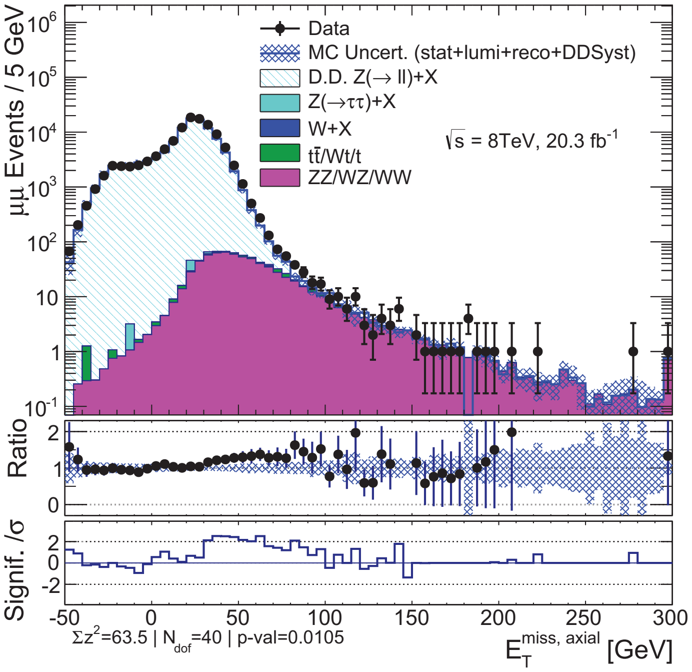

(b)

Fig. 6.10 The $E_{\mathrm{T}}^{\mathrm{miss,axial}}$ spectrum in the ee and $\mu\mu$ channel with all cuts applied except for the jet veto and the $E_{\mathrm{T}}^{\mathrm{miss,axial}}$ cut. The light blue contribution is single-photon events reweighted in both E_{T}^{γ} and $\Delta\phi(E_{\mathrm{T}}^{\gamma}, E_{\mathrm{T}}^{\mathrm{miss}})$ in place of $Z+$jets contribution taken from MC simulation. Non-$\gamma+$jets MC is weighted as well and subtracted off from the photon events in data. The nominal background consists of the remaining reweighted events after weighted non-$\gamma+$jets MC background subtraction.

uncertainty	ee channel	$\mu\mu$ channel
Expected events	-0.72	-0.46
photon events statistical uncertainty	$^{20.28\%}_{-20.28\%}$	$^{12.01\%}_{12.01\%}$
MC statistical/reconstruction uncertainty	$^{80.89\%}_{-80.89\%}$	$^{54.76\%}_{54.76\%}$
MC background subtraction	$^{105.88\%}_{-105.88\%}$	$^{74.19\%}_{74.19\%}$
weight variation	$^{64.28\%}_{64.28\%}$	$^{60.52\%}_{60.52\%}$

Table 6.4 Nominal values for the $Z+X$ background estimates in the ee and $\mu\mu$ channels obtained from the photon reweighting method.

- Luminosity uncertainty for MC background subtraction. The non-γ+jets MC is varied within the luminosity uncertainty and the background is recalculated. This luminosity uncertainty is correlated with other luminosity uncertainties used for acceptance and efficiency calculation and signal normalisation, as well as normalisation for backgrounds estimated by simulation.
- The statistical and reconstruction uncertainties associated with the non-γ+jets MC that is subtracted in the signal region. These samples are fluctuated within $\pm 1\sigma$ of these uncertainties and the background is recalculated, with the systematic uncertainty taken as the quadrature sum of the differences of each variation with respect to the nominal.
- The uncertainty associated with the photon weight values, as shown in Fig. 6.9. The photon weights are varied in both direction and the background is estimated for each variation.

The central value of the background estimates are negative for both the ee and $\mu\mu$ channel. This shows the limitations of the photon reweighting method. At high $E_{\mathrm{T}}^{\mathrm{miss,axial}}$, the contributions to photon events in the zero jet bin are predominantly $Z \to \nu\bar{\nu}+\gamma$ events as shown in Table 6.4. The MC subtraction therefore has a large effect on the value of the background estimate. The central value of the background estimate is consistent with zero, although it is covered with a conservative systematic uncertainty. As negative values of the background are unphysical, values representing event counts or values that can be strictly positive are restricted at zero in the model used for the cross section and the aTGC limit setting.

	Good (G)	Bad (B)
Electrons		Fail Good electron selection
	Track iso < 0.15	Track iso < 2
	Calo iso < 0.15	Calo iso < 2
	$\lvert z_0 * \sin\theta\rvert < 0.5$	$\lvert z_0 * \sin\theta\rvert < 5$
	$\lvert d_0/\sigma(d_0)\rvert < 6$	$\lvert d_0/\sigma(d_0)\rvert < 10$
	`Medium++`	`Loose++`
Muons		Fail Good muon selection
	Track iso < 0.15	Track iso < 2
	Calo iso < 0.15	Calo iso < 2
	$\lvert z_0 * \sin\theta\rvert < 0.5$	$\lvert z_0 * \sin\theta\rvert < 5$
	$\lvert d_0/\sigma(d_0)\rvert < 3$	$\lvert d_0/\sigma(d_0)\rvert < 10$

Table 6.5 Summary of requirements for good and bad leptons as used in the matrix method.

6.6 $W + X$, single-top, multijet background

This background is estimated using a technique which extrapolates the observed lepton type (tight or loose) based on isolation selection to the true nature of the lepton (real or fake), which allows a set of linear equations to solve for the lepton classification. This technique referred to as the “matrix-method” [188]. The matrix method has been used extensively in both ATLAS top measurements [189] and BSM searches [190] as well as corresponding measurements made by CMS and the Tevatron experiments. The basic premise behind the matrix method is to use a 4×4 matrix to map the observed lepton type (good-“G” or bad-“B”) to the true nature of the lepton type (real-“R” or fake-“F”). The lepton selections are relaxed from the full definitions given in Section 5.6.1 to define good and bad leptons according to the requirements listed in Table 6.5. The relaxed leptons are included in the overlap removal, where jets are removed within $\Delta R < 0.3$ of relaxed leptons. An opposite-sign same-flavour lepton pair passing basic Z candidate cuts (but not the full ZZ selection) is used to tag the event. An additional single relaxed lepton is also required, designated the probe lepton. The probe leptons are expected to be dominated by fakes due to jets from $Z+$jets events. The trigger-matching requirement of the Z candidate cuts must be satisfied by one of the leptons forming the Z candidate. No such trigger requirement is made for the probe leptons to avoid biasing the sample based on trigger. Events in the fake lepton selection are required to have $E_{\mathrm{T}}^{\mathrm{miss}} < 90$ GeV to ensure that no events appear in the ZZ signal region.

The real lepton selection selects events according to basic Z candidate cuts with an additional requirement that $|m_{\ell^-\ell^+} - m_Z| < 5$ GeV and $E_{\mathrm{T}}^{\mathrm{miss}} < 90$ GeV. One of the two leptons, taken to be the tag lepton, is required to be a good lepton. The tag lepton is also require to be trigger matched. The other lepton is treated as the probe lepton. The p_{T} distributions of the probe electrons in both the real and fake-dominated regions are given in Fig. 6.11. A fake rate is defined as a function of lepton p_{T} to be

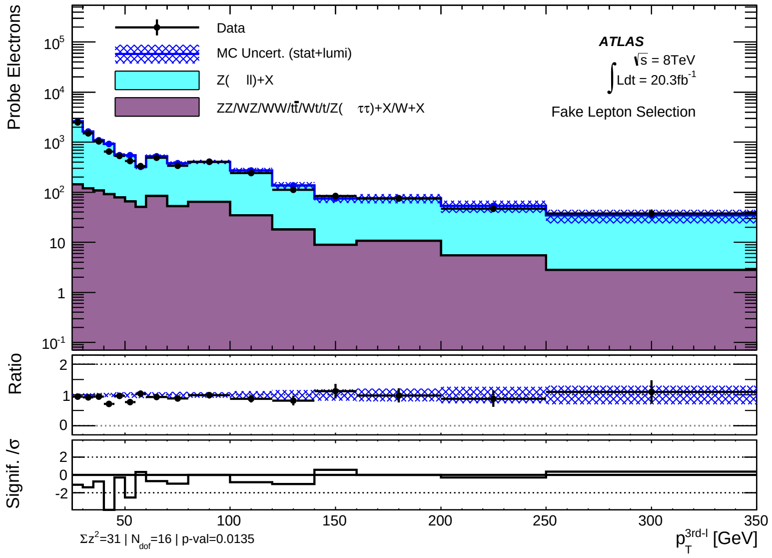

(a)

$$f = \frac{N_{\mathrm{good}} - N_{\mathrm{good}}^{\text{non-}Z+\text{jets MC}}}{N - N^{\text{non-}Z+\text{jets MC}}}, \tag{6.7}$$

where N is the number of probe leptons in the fake lepton selection region, N_{good} is the number of good probe leptons in the fake control region, $N_{\mathrm{good}}^{\text{non-}Z+XMC}$ is the predicted number of non-$Z+X$ probe leptons in the region, and $N_{\mathrm{good}}^{\mathrm{non}-Z+XMC}$ is the predicted number of good non $Z+X$ leptons in the region. The efficiency is calculated as a function of p_{T} to be

$$r = \frac{M_{\mathrm{good}} - M_{\mathrm{good}}^{\text{non-}Z+XMC}}{M - M^{\mathrm{non}Z+XMC}}, \tag{6.8}$$

where M is the number of probe leptons in the real lepton selection region, M_{good} is the number of good probe leptons in this region, $M^{\text{non-}Z+XMC}$ is the predicted number of $Z+X$ probe leptons in the region, and $M_{\mathrm{good}}^{\text{non-}Z+XMC}$ is the predicted number of good non-$Z+X$ leptons in this region. The efficiencies and fake rates are shown in Fig. 6.12. The relaxed lepton signal region is defined with the same set of cuts as the ZZ signal regions except using relaxed leptons in place of analysis quality leptons. Relaxed leptons are removed from the set of leptons used in the third lepton veto. Each event in the relaxed lepton signal regions is

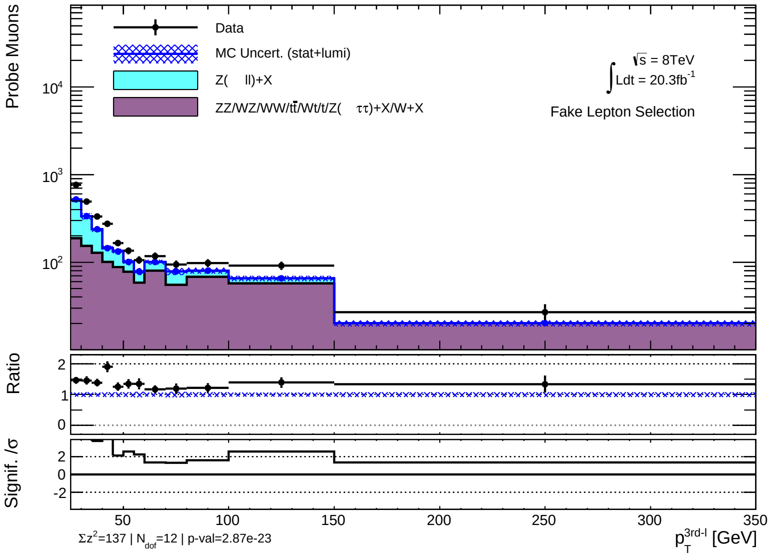
Probe Muons
Data
MC Uncert. (stat+lumi)
Z(ll)+X
ZZ/WZ/WW/tt̄/Wt/t/Z(ττ)+X/W+X
√s = 8TeV
∫Ldt = 20.3fb⁻¹
Fake Lepton Selection
10⁴
10³
10²
Ratio
2
1
0
Signif. /σ
2
0
-2
50
100
150
200
250
300
350
Σz²=137 | N_dof=12 | p-val=2.87e-23
p_T^3rd-l [GeV]

(b)

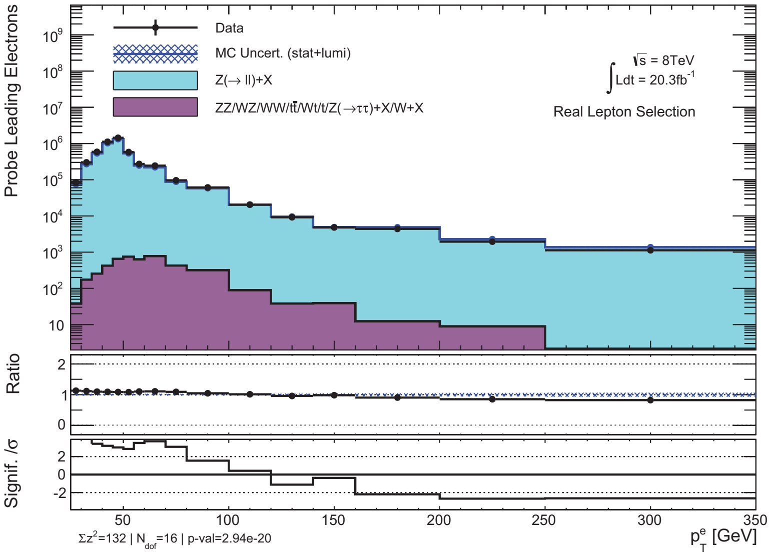
Probe Leading Electrons
Data
MC Uncert. (stat+lumi)
Z(→ ll)+X
ZZ/WZ/WW/tt̄/Wt/t/Z(→ττ)+X/W+X
√s = 8TeV
∫Ldt = 20.3fb⁻¹
Real Lepton Selection
10⁹
10⁸
10⁷
10⁶
10⁵
10⁴
10³
10²
10
Ratio
2
1
0
Signif. /σ
2
0
-2
50
100
150
200
250
300
350
Σz²=132 | N_dof=16 | p-val=2.94e-20
p_T^e [GeV]

(c)

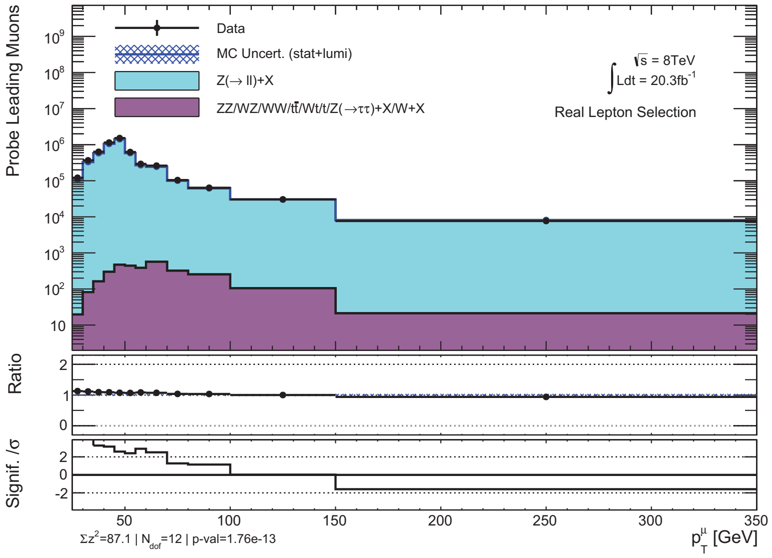

(d)

Fig. 6.11 Real and fake lepton-dominated control regions where leptons are selected to measure the fake rate and efficiency respectively. Figures (a) and (b) show the p_T spectrum of the third lepton (designated the probe electron) in the fake-dominated region. Figures (c) and (d) show the p_T distribution of the probe leptons in the real-dominated region. Only probes that are leading leptons are plotted in the real-dominated region.

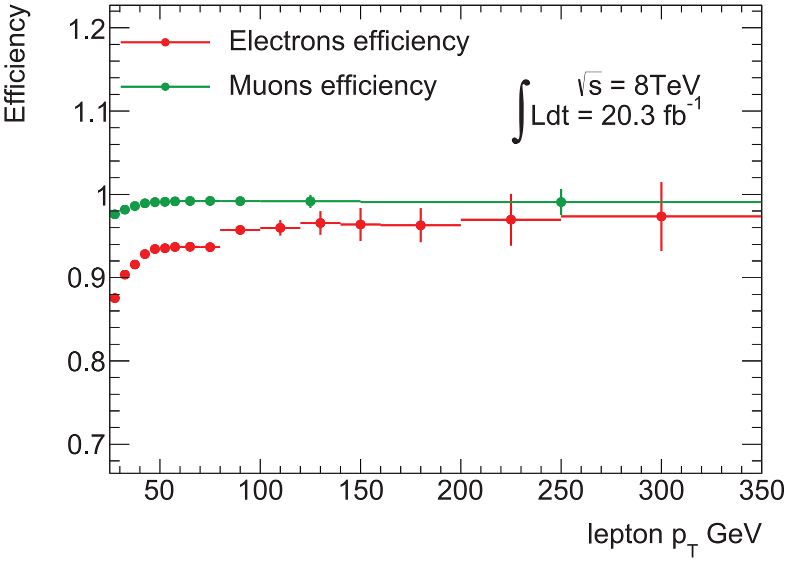

(a)

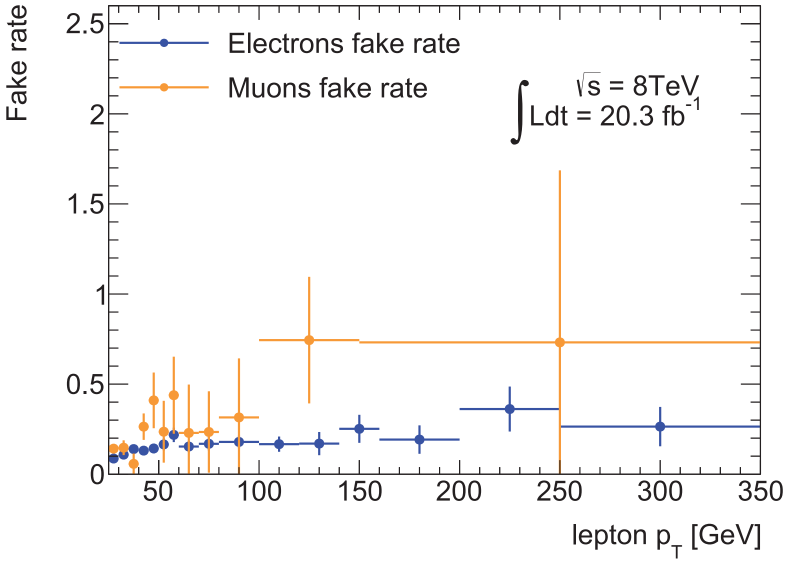

(b)

Fig. 6.12 Efficiencies (a) and fake rates (b) corresponding to the real and fake lepton selections used in the matrix method. The efficiencies are calculated according to Eqs. (6.7) and (6.8).

classified based on the number of good and bad leptons in the event, i.e. GG, *GB*, *BG*, *BB*. Here *GG* indicates two good leptons in the event, while *GB* and *BG* indicate one good and one bad lepton in the event (the leptons are ordered by p_{T} such that *GB* means the higher p_{T} lepton is good and the lower p_{T} lepton is bad), and BB means two bad leptons in the event. The event classification can be arranged into column-vector form, with a weight of 1 given to an event of a certain type and a weight of 0 for all other types of events, i.e.

$$\begin{bmatrix} N_{GG} \\ N_{GB} \\ N_{BG} \\ N_{BB} \end{bmatrix}, \tag{6.9}$$

This vector is related to the true, but unknown, nature of the leptons (real or fake) through their matrix efficiencies r, and fake rates f according to

$$\begin{bmatrix} N_{GG} \\ N_{GB} \\ N_{BG} \\ N_{BB} \end{bmatrix} = \begin{bmatrix} r_1 r_2 & r_1 f_2 & f_1 r_2 & f_1 f_2 \\ r_1(1-r_2) & r_1(1-f_2) & f_1(1-r_2) & f_1(1-f_2) \\ (1-r_1)r_2 & (1-r_1)f_2 & (1-f_1)r_2 & (1-f_1)f_2 \\ (1-r_1)(1-r_2) & (1-r_1)(1-f_2) & (1-f_1)(1-r_2) & (1-f_1)(1-f_2) \end{bmatrix} \times \begin{bmatrix} N_{RR} \\ N_{RF} \\ N_{FR} \\ N_{FF} \end{bmatrix}, \tag{6.10}$$

Variation	ee channel	$\mu\mu$ channel
Expected events	2.62	-0.90
statistical uncertainty	$^{41\%}_{-41\%}$	$^{82\%}_{-82\%}$
systematic uncertainty	$^{20\%}_{-20\%}$	$^{82\%}_{-82\%}$

Table 6.6 Data-driven estimates of the $W+X$, single-top, and multijet background. The systematic uncertainty comes from the uncertainties in the fake rates and efficiencies, which are subject to MC background uncertainty and limited statistics in the fake and real-lepton-dominated control regions.

where r_1 and f_1 are the measured efficiency and fake rate for the first lepton, and r_2 and f_2 the efficiency and fake rate for the second lepton. Here N_{RR}, N_{RF}, N_{FR}, and N_{FF} are event classifications with two real, one real and one fake, one fake one real, and two fake leptons. The matrix method allows for the $W+X/Wt$ and multijet components to be expressed separately in terms of the fake rates and numbers of events with at least one fake lepton according to the following expressions:

$$\begin{aligned} N_{GG}^{W+X/Wt} &= \sum_{i=1}^{n_{events}} r_1^i f_2^i N_{RF}^i + f_1^i r_2^i N_{FR}^i, \\ N_{GG}^{\text{multijet}} &= \sum_{i=1}^{n_{events}} f_1 f_2 N_{FF}. \end{aligned} \tag{6.11}$$

As this is a data-driven background, the dominant uncertainties do not come from experimental uncertainties such as lepton reconstruction and identification efficiencies compared to a simulation-based background like the WZ background estimate, but rather the limited number of events in the relaxed lepton signal regions. Furthermore, there can be large statistical uncertainties due to the available statistics in the regions where the fake rates and efficiencies are derived. The systematic uncertainty due to the fake rate and efficiency is determined by varying the fake rate and efficiency independently and taking the biggest deviation in each bin as the systematic. This systematic is treated as correlated between the $ZZ \to e^-e^+\nu\bar{\nu}$ and $ZZ \to \mu^-\mu^+\nu\bar{\nu}$ sub-channels. The nominal data-driven estimates of the $W+X/Wt/$multijet background contribution to ZZ and the systematic uncertainties are given in Table 6.6.

6.7 Conclusions

This chapter presented the methods of background estimation in the $ZZ \to \ell\ell\nu\bar{\nu}$ analysis. Backgrounds were measured with a combination of simulation and data-driven techniques. The data driven techniques often involve extrapolations from dedicated control regions back to the signal region, and the factors that are used for those extrapolations are not always completely dependent on data. Background subtraction in control regions can also result in poor statistics used for the background estimate in the signal region, which may give negative central values. This is the case for the $W+X$ background technique via the matrix-method and the single photon reweighting technique. These uncertainties are subject to rather large uncertainties to cover deficiencies in the method. These background estimates are used directly as input to the statistical model used to calculate the fiducial and extrapolated cross sections (Chapter 7), and correlation between parameters which share the same underlying systematic uncertainties is accounted for in the cross section model.

Chapter 7

Measurement of the ZZ cross section

Precision measurements of diboson processes, including ZZ production, have been important not only as tests of the Standard Model, but also because they constitute irreducible backgrounds for $pp \to H \to ZZ$ production and BSM processes in phenomenological models like the pMSSM [191, 192]. Several extensions to the SM, such as warped extra dimensions [193–195], grand unified theories [196], and technicolour models [197–199], predict the existence of heavy resonances that are able to decay to pairs of vector bosons. For example, recent versions of models with large extra dimensions where all Standard Model fields propagate in these new dimensions predict enhanced coupling of resonances such as gravitons to the ZZ final state and suppressed decay rates to light fermion and diphoton states [200]. Accurate measurements of both the $ZZ \to \ell^-\ell^+\nu\bar{\nu}$ and $ZZ \to \ell^-\ell^+\ell^-\ell^+$ production also provide stringent tests of SM predictions and another another way to look for potential sources of new physics via aTGCs.

This chapter presents measurement of the ZZ production cross section at 8 TeV using the full ATLAS dataset corresponding to an integrated luminosity of $20.3\,\mathrm{fb}^{-1}$ collected during 2012 operation. Here, the $ZZ \to \ell^-\ell^+\ell^-\ell^+$ decay channel is also analysed with the $ZZ \to \ell^-\ell^+\nu\bar{\nu}$ decay channel to calculate a combined total cross section for $pp \to ZZ$ in the mass range $66 < m_{\ell^-\ell^+} < 116$ GeV. Fiducial and total cross sections are presented for both the $ZZ \to \ell^-\ell^+\nu\bar{\nu}$ and $ZZ \to \ell^-\ell^+\ell^-\ell^+$ channels.[1] A baseline comparison is made to a prediction calculated with POWHEGBOX and gg2VV. The fiducial phase space is described in detail, and the theoretical cross sections are presented. The reconstruction efficiency correction C_{ZZ}, and acceptance A_{ZZ} are presented along with the major contributions to systematic uncertainties for each. The measured fiducial and extrapolated cross sections

---

[1] The details of the $ZZ \to \ell^-\ell^+\ell^-\ell^+$ analysis are not given in this thesis. However, the channel has been extensively studied, and details of the method of selection, background estimation and acceptance calculation can be found in [78].

sections for the $ZZ \to \ell^-\ell^+\nu\bar{\nu}$ and $ZZ \to \ell^-\ell^+\ell^-\ell^+$ sub-channels are given. A combined extrapolated cross section combining all sub-channels in both decay modes is also given. Finally a brief study into the application of a correction factor to the jet veto acceptance and its effect on the cross section is presented.

7.1 Fiducial phase space definition

The cross sections presented are measured in both a fiducial phase space (also referred to as a "fiducial volume") and a larger, more inclusive phase space restricting the *Z* bosons to be on mass-shell in the mass range $66 < m_{\ell^-\ell^+} < 116$ GeV (also referred to as the "total volume"). The full selection of candidate $ZZ \to \ell^-\ell^+\nu\bar{\nu}$ events is given in Section 5.7. The fiducial phase space is constructed to closely follow detector acceptance and constitutes a restricted phase space defined at particle-level that is not subject to same level of theoretical uncertainties associated with extrapolating to a larger phase space that is not directly measured. The definition of the fiducial phase space in the $ZZ \to \ell^-\ell^+\nu\bar{\nu}$ decay channel is as follows:

1. ***Lepton*** p_{T} ***requirement:*** $p_{\mathrm{T}}^{\ell^\pm} > 20$ GeV.
2. ***One pair of opposite-sign, same flavour leptons:*** $\ell^\pm = e^\pm, \mu^\pm$. Leptons are required to have a *Z* parent which can be found via iteration through the HEPMC event record [130].
3. ***Mass-window:*** Both *Z* bosons (invisibly and visibly decaying) are required to satisfy $76 < m_{\ell^-\ell^+} < 106$ GeV or $76 < \mathrm{m}_{\nu\bar{\nu}} < 106$ GeV for invisibly decaying *Z* bosons.
4. ***Axial-***$E_{\mathrm{T}}^{\mathrm{miss}}$***requirement:***$E_{\mathrm{T}}^{\mathrm{miss,axial}} = -p_{\mathrm{T}}^{\nu+\bar{\nu}} \cos\left(\Delta(\phi p_{\mathrm{T}}^{\nu+\bar{\nu}}, p_{\mathrm{T}}^{Z})\right) > 90$ GeV, where p_{T}^{Z} is the p_{T} of the charged-lepton pair.
5. p_{T}***-Balance requirement:*** $\frac{p_{\mathrm{T}}^{\nu+\bar{\nu}} - p_{\mathrm{T}}^{Z}}{p_{\mathrm{T}}^{Z}} < 0.4$.
6. ***Jet veto:*** No particle-level jets with $p_{\mathrm{T}} > 25$ GeV and $|\eta| < 4.5$. The jets must not be closer than $\Delta R < 0.3$ to an electron.
7. ***Lepton separation:*** $\Delta R\,(\ell^-, \ell^+) > 0.3$.

To account for radiative losses when reconstructing momenta of particle-level leptons, final-state[2] particle-level leptons are "dressed" with momenta of final-state photons within a cone

---

[2] This corresponds to status 1 photons for PYTHIA and PYTHIA8, although different generators/parton-showers will generally treat particles at various stages using different status schemes.

of $\Delta R = 0.1$. Photons that are used to dress leptons are required to not originate from a hadronic decay (i.e. the photons are not allowed to have a parent with a PDG ID code [15] corresponding to a hadron).

The $ZZ \to \ell^- \ell^+ \ell^- \ell^+$ analysis defines three different fiducial volumes depending on the decay sub-channel $ZZ \to e^- e^+ e^- e^+$, $ZZ \to e^- e^+ \mu^- \mu^+$, or $ZZ \to \mu^- \mu^+ \mu^- \mu^+$. The definitions are:

- ***Two pairs of opposite-sign, same flavour leptons:*** $(Z/\gamma^*)(Z/\gamma^*) \to \ell^+ \ell^- \ell^+ \ell^-$, $\ell = e, \mu$, where each Z decays to a particle-antiparticle pair of a given lepton flavour, i.e. $Z \to e^- e^+$ or $Z \to \mu^- \mu^+$.

- ***Mass window requirement:*** $66 < m_{12}(Z/\gamma^*) < 116$ GeV, where $m_{12}(Z/\gamma^*)$ is the mass of the Z reconstructed from the first and second leptons. The opposite-sign, same-flavour lepton pairings are done such that the mass of the reconstructed Z bosons is closest to the PDG value of the Z mass.

- ***Mass window requirement:*** $66 < m_{34}(Z/\gamma^*) < 116$ GeV, where $m_{34}(Z/\gamma^*)$ is the mass of the Z reconstructed from the third and fourth leptons, and the lepton pairing is done as mentioned above.

- ***Lepton p_{T} requirement:*** $p_{\mathrm{T}}^{\ell^\pm} > 7$ GeV.

- ***Lepton η requirement:***
  - 4μ : $|\eta^\mu| < 2.7$;
  - $4e$: $|\eta^e| < 2.5$ for all electrons OR $|\eta^e| < 2.5$ for three electrons and $|\eta^{e_4}| < 4.9$ for the fourth electron;
  - $2e2\mu$: $|\eta^\mu| < 2.7$ AND ($|\eta^e| < 2.5$ (both electrons) OR ($|\eta^{e_1}| < 2.5$ and $|\eta^{e_2}| < 4.9$)) .

- ***Lepton separation:*** $\min(\Delta R(\ell, \ell)) > 0.2$

Reconstruction-level and particle-level quantities are obtained from the same POWHEGBOX and gg2VV samples used to model the signal. Particle-level quantities are obtained from the HEPMC event record in each of the samples. These quantities are used for calculation of the reconstruction efficiency factor C_{ZZ} (Section 7.3) and acceptance factor A_{ZZ} (Section 7.4).

7.2 Prediction of the theoretical cross section

Diboson processes have been implemented in several generators, such as MC@NLO [124], HERWIG [201], HERWIG++ [128], and SHERPA [123] and POWHEGBOX. It is sometimes possible in these generators to turn off the contribution of γ^* which decays to charged leptons, however, this contribution does not appear in the case of decays to neutrinos. ZZ production is implemented in POWHEGBOX at lowest order in the electroweak coupling and next-to-leading order in QCD. POWHEGBOX was chosen to model the $ZZ \to \ell^-\ell^+\nu\bar{\nu}$ channel at 7 TeV [77] and has been used in other ATLAS electroweak analyses either to model the signal process and calculate cross sections [202], or to calculate acceptance [203, 204]. ZZ production induced by the gluon-gluon initial state is implemented in generators such as gg2VV or MCFM 6.2 onward, but is only available at lowest order in QCD for the gluon-induced process.

7.2.1 Higher-order corrections to the cross section

7.2.1.1 NNLO QCD corrections

The first calculation of next-to-next-to-leading order (NNLO) QCD corrections to the inclusive production of $pp \to ZZ$ for on-shell Z bosons can be found in [205]. The NNLO computation requires the evaluation of the tree-level scattering amplitudes with two additional partons, evaluation of the one-loop amplitudes with one additional parton, and evaluation of the one-loop-squared and two-loop corrections to the Born subprocess $q\bar{q} \to ZZ$. The impact of NNLO corrections with respect to the NLO result was found to range from approximately 11% at $\sqrt{s} = 7$ TeV to 17% at $\sqrt{s} = 14$ TeV. Using NNLO PDFs [206], the gluon fusion contribution provides between 58% and 62% of the full NNLO correction. Corrections were provided for the ATLAS off-shell Higgs signal strength measurement in the $pp \to H \to ZZ \to \ell^-\ell^+\ell^-\ell^+$ channel [207], and were translated as a set of NNLO k-factors that could be applied specifically to specific kinematic distributions such as m_{ZZ}. However, these weights are not applied to the event yield here because aTGC limits in the $ZZ \to \ell^-\ell^+\ell^-\ell^+$ analysis are set using p_{T}^{Z}, not m_{ZZ}. Furthermore, the fact that an NNLO PDF was used would involve additional weighting to be applicable for use with a PDF such as CT10.

7.2.1.2 NLO electroweak corrections

A set of higher-order electroweak effects was calculated for on-shell outgoing vector bosons [208, 209]. These corrections are becoming increasingly relevant at current LHC energies (8

TeV and higher), contributing approximately 4% to the total production cross section. These effects have been included in HERWIG++ using a reweighting procedure [210]. However, HERWIG++ does not include contributions from off-shell Z bosons, which does not make it a suitable choice to model the ZZ kinematics given that the size of the γ^* interference is of the order of the contributions when both bosons are on-shell. Thus, a comparable reweighting procedure was implemented and validated for the ATLAS event data model which allows one to apply the effects directly to POWHEGBOX [211]. The k-factors are provided as a function of the Mandelstam variables $\hat{s}$ and t. With this procedure, all differential distributions of interest can be reweighted. The corrections are only valid for the leading-order process above the corresponding diboson production threshold and with both Z bosons on-shell. To account for this, a condition is placed on the bosons which require $\sqrt{\hat{s}} > 2m_Z^{\mathrm{PDG}}$ to be satisfied in the centre-of-mass frame of the diboson system, where m_Z^{PDG} is the value of the Z mass taken from the PDG. The systematic uncertainty due to the reweighting procedure is estimated by varying the k-factors within their statistical uncertainty and applying the corresponding weights to the $q\bar{q}$ component of the calculations of A_{ZZ} and C_{ZZ}. Reweighted kinematic distributions compared to the leading-order prediction in the $ZZ \to \mu^-\mu^+\nu\bar{\nu}$ and $ZZ \to e^-e^+\mu^-\mu^+$ sub-channels are given in Fig. 7.1.

7.2.2 Theoretical fiducial cross section

The theoretical fiducial cross sections are obtained from POWHEGBOX and gg2VV by scaling the cross section of a particular signal sample (Section 5.3) by the fraction of events that fall into the fiducial phase space. This is given by the expression

$$\sigma^{\text{derived}} = \sum_{i=\text{Powheg, gg2VV}} \left(\sigma^{\text{signal sample}} \cdot \varepsilon_{\text{filter}} \frac{N_{\text{phase space}}}{N_{\text{signal sample}}} \right)_i , \tag{7.1}$$

where $\sigma^{\text{signal sample}}$ is the cross section prediction provided by POWHEGBOX or gg2VV, $N_{\text{phase space}}$ is the number of events in the corresponding fiducial phase space (Section 7.1) depending on whether calculation is performed for a given $ZZ \to \ell^-\ell^+\nu\bar{\nu}$ or $ZZ \to \ell^-\ell^+\ell^-\ell^+$ sub-channel, and $N_{\text{signal sample}}$ is the total number of events contained in the sample. The filter efficiency $\varepsilon_{\text{filter}}$ is that for multilepton filter running within the Athena framework and is applied after event generation. This is only applied for $ZZ \to \ell^-\ell^+\ell^-\ell^+$ samples and is not applied for $ZZ \to \ell\ell\nu\bar{\nu}$ samples. Here, $N_{\text{signal sample}}$ is the resulting number of events of the signal sample available in the dataset after applying the filter. The theoretical prediction is obtained including the higher-order electroweak effects by using the correspondingly weighted events for $N_{\text{phase space}}$. The theoretical fiducial cross sections in the

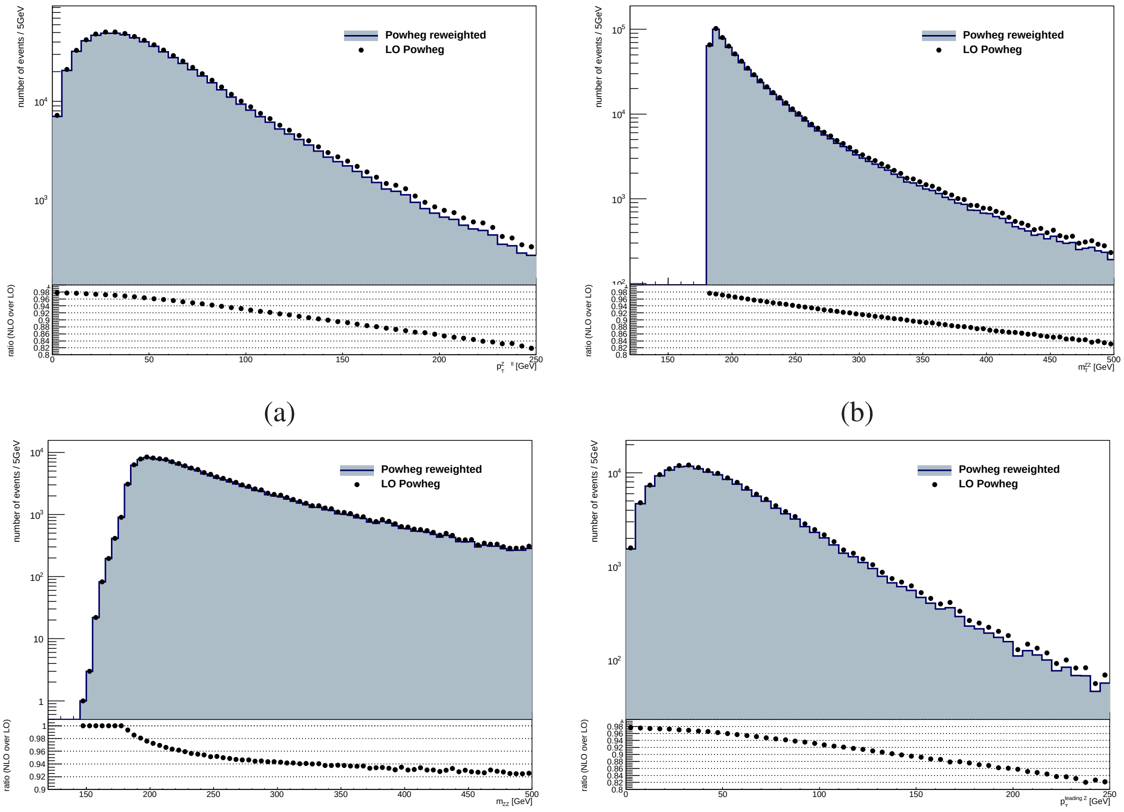

(a) (b)

(c) (d)

Fig. 7.1 Spectra of the reweighted Z bosons by applying the higher-order electroweak corrections compared to the leading-order in electroweak (LO) prediction from POWHEGBOX. (a) the p_T of the visible Z boson and (b) the transverse mass of the ZZ system, m_T^{ZZ} in the $ZZ \to \mu^-\mu^+\nu\bar{\nu}$ sub-channel. (c) the invariant mass of the four-lepton system, m_{ZZ}, and (d) the p_T of the leading Z boson in the $ZZ \to e^-e^+\mu^-\mu^+$ sub-channel. The higher-order corrections are calculated as a function of the Mandelstam variables $\sqrt{\hat{s}}$ and t. The relation between the invariant mass of the outgoing particles and the Mandelstam variables allows for full specification of the event kinematics, allowing essentially any kinematic variable to be reweighted. The ratios in the histograms are not the k-factors themselves, but rather show the effect of the reweighting on the kinematic variables. No access to the original plotting routines, so scales and axes could not be altered or enlarged. Figures taken from [211].

$ZZ \to \ell^- \ell^+ \nu \bar{\nu}$ sub-channels are given in Table 7.2, and the corresponding cross sections for the $ZZ \to \ell^- \ell^+ \ell^- \ell^+$ sub-channels are given in Table 7.3, using the numbers directly from Table 7.1. The corresponding calculations for total cross sections with and without electroweak corrections is given in Table 7.4, and the corresponding predicted total cross sections corrected for branching ratios are given in Table 7.5.

7.3 The fiducial efficiency correction, C_{ZZ}

In order to make a measurement of the total ZZ production cross section, an extrapolation must be made from the measurement which is performed within the detector acceptance to a more inclusive phase space. The fiducial volume is chosen to closely reflect the detector acceptance. A cross section measured within the fiducial phase space is free from the theoretical uncertainties which arise as a result of this extrapolation. It is therefore useful to calculate a cross section in the fiducial phase space without the full extrapolation. To do so requires a knowledge of object reconstruction efficiency, and efficiency of selection cuts. This quantity is referred to by several names, such as the fiducial correction factor, or fiducial efficiency correction, and is denoted by C_{ZZ}. It is used to model the reconstruction efficiency given a fiducial volume and particular signal selection, and is defined as

$$C_{ZZ} = \varepsilon_{\text{trig}} \times \varepsilon_{\text{event}} \times \varepsilon_{\text{lep}} \times \varepsilon_{\text{reco}}, \tag{7.2}$$

where $\varepsilon_{\text{trig}}$ is the trigger efficiency, $\varepsilon_{\text{event}}$ is the efficiency of the event-level cuts (like the primary vertex cut, etc.), $\varepsilon_{\text{lep}} = \varepsilon_{\ell}\varepsilon_{\ell}$ is the product of the individual efficiencies for the two leptons to pass the lepton object selection cuts, and $\varepsilon_{\text{reco}}$ is the reconstruction to generator-level fiducial volume correction which also includes smearing corrections and resolutions. As simulated samples from two different generators are used, C_{ZZ} is calculated from both the POWHEGBOX and gg2VV signal samples, with each sample weighted by its contribution to the total cross section. The calculation is done for each channel separately by taking the ratio of the number of reconstructed events which pass all cuts to the number of events at generator level which fall in the fiducial volume Eq. (7.3). Full weights are applied to the reconstructed events, such as lepton reconstruction scale factors, lepton identification scale factors, trigger scale factors, pileup weights, etc. Furthermore, theoretical corrections such as NLO electroweak corrections are applied. The fiducial efficiency is calculated according to the expression

$$C_{ZZ} = \frac{N^{\text{MC pass all cuts}}_{\text{Reconstructed } ZZ}}{N^{\text{MC Fiducial Volume}}_{\text{Generated } ZZ}}, \tag{7.3}$$

Generator	Process	$\sigma^{\text{signal sample}}$ [fb]	$\varepsilon_{\text{filter}}$	$N_{\text{signal sample}}$	N_{total}	$N_{\text{total}}^{\text{EW}}$	N_{fid}	$N_{\text{fid}}^{\text{EW}}$
POWHEGBOX	$ZZ \to e^-e^+\nu\bar{\nu}$	168	1	299400	162302	154970.5	7225	6534.75
gg2VV	$ZZ \to e^-e^+\nu\bar{\nu}$	6.8827	1	30000	18908	18908	438	438
POWHEGBOX	$ZZ \to \mu^-\mu^+\nu\bar{\nu}$	168	1	300000	162334	154977.7	7006	6341.25
gg2VV	$ZZ \to \mu^-\mu^+\nu\bar{\nu}$	6.8827	1	29999	18825	18825	418	418
POWHEGBOX	$ZZ \to e^-e^+e^-e^+$	76.9	0.9077	1099997	118716	113278	96590	92154.3
gg2VV	$ZZ \to e^-e^+e^-e^+$	2.7723	1	90000	11628	11628	10342	10342
POWHEGBOX	$ZZ \to e^-e^+\mu^-\mu^+$	175.6	0.8279	1599696	163441	155984	117863	112428
gg2VV	$ZZ \to e^-e^+\mu^-\mu^+$	12.2216	1	90000	5395	5395	4361	4361
POWHEGBOX	$ZZ \to \mu^-\mu^+\mu^-\mu^+$	76.8	0.91241	1099798	117811	112431	75401	71914.1
gg2VV	$ZZ \to \mu^-\mu^+\mu^-\mu^+$	2.7723	1	90000	11748	11748	8916	8916

Table 7.1 Cross sections, filter efficiencites, total numbers of events, and events in the corresponding total and fiducial phase spaces for each of the $ZZ \to \ell^-\ell^+\nu\bar{\nu}$ and $ZZ \to \ell^-\ell^+\ell^-\ell^+$ samples. The numbers are inserted into Eq. (7.1) to calculate theoretical cross sections. Here N_{total} is the number of events in the more inclusive phase space $66 < m_{\ell^-\ell^+} < 116$ GeV, N_{fid} is the number of events in the fiducial phase space, and $N_{\text{total}}^{\text{EW}}$ is this number weighted by higher order electroweak corrections on an event-by-event basis.

Generator	Process	σ^{fid} [fb]	statistical error [fb]	theoretical error [fb]	$\sigma^{\text{fid}}_{\text{EW}}$ [fb]	statistical error [fb]	theoretical error [fb]
POWHEGBOX	$ZZ \to e^- e^+ \nu\bar{\nu}$	4.05	± 0.05	$^{+0.30}_{-0.23}$	3.67	± 0.05	$^{+0.27}_{-0.21}$
gg2VV	$ZZ \to e^- e^+ \nu\bar{\nu}$	0.10	± 0.00	$^{+0.06}_{-0.06}$	0.10	± 0.00	$^{+0.06}_{-0.06}$
summed $ZZ \to e^- e^+ \nu\bar{\nu}$		4.15	± 0.05	$^{+0.36}_{-0.29}$	3.77	± 0.05	$^{+0.33}_{-0.27}$
POWHEGBOX	$ZZ \to \mu^- \mu^+ \nu\bar{\nu}$	3.92	± 0.05	$^{+0.29}_{-0.22}$	3.55	± 0.04	$^{+0.26}_{-0.20}$
gg2VV	$ZZ \to \mu^- \mu^+ \nu\bar{\nu}$	0.10	± 0.00	$^{+0.06}_{-0.06}$	0.10	± 0.00	$^{+0.06}_{-0.06}$
summed $ZZ \to \mu^- \mu^+ \nu\bar{\nu}$		4.02	± 0.05	$^{+0.35}_{-0.28}$	3.65	± 0.04	$^{+0.32}_{-0.26}$

Table 7.2 Calculated fiducial cross section predictions for the $ZZ \to e^- e^+ \nu\bar{\nu}$ and $ZZ \to \mu^- \mu^+ \nu\bar{\nu}$ sub-channels. The theoretical prediction is taken as the sum of the contributions from POWHEGBOX and gg2VV samples. The cross sections $\sigma^{\text{fid}}_{\text{EW}}$ indicate cross sections calculated with events weighted by higher-order electroweak corrections. Cross sections without electroweak corrections are given for comparison. The gg contribution is seen to be approximately 2.7% for both sub-channels.

Generator	Process	σ^{fid} [fb]	statistical error [fb]	theoretical error [fb]	$\sigma^{\text{fid}}_{\text{EW}}$ [fb]	statistical error [fb]	theoretical error [fb]
POWHEGBOX	$ZZ \to e^-e^+e^-e^+$	6.13	$\pm$ 0.02	$^{+0.45}_{-0.34}$	5.85	$\pm$ 0.02	$^{+0.43}_{-0.33}$
gg2VV	$ZZ \to e^-e^+e^-e^+$	0.32	$\pm$ 0.00	$^{+0.20}_{-0.20}$	0.32	$\pm$ 0.00	$^{+0.20}_{-0.20}$
summed $ZZ \to e^-e^+e^-e^+$		6.45	$\pm$ 0.02	$^{+0.65}_{-0.54}$	6.17	$\pm$ 0.02	$^{+0.63}_{-0.53}$
POWHEGBOX	$ZZ \to e^-e^+\mu^-\mu^+$	10.71	$\pm$ 0.03	$^{+0.78}_{-0.60}$	10.22	$\pm$ 0.03	$^{+0.75}_{-0.57}$
gg2VV	$ZZ \to e^-e^+\mu^-\mu^+$	0.59	$\pm$ 0.01	$^{+0.38}_{-0.37}$	0.59	$\pm$ 0.01	$^{+0.38}_{-0.37}$
summed $ZZ \to e^-e^+\mu^-\mu^+$		11.30	$\pm$ 0.04	$^{+1.16}_{-0.97}$	10.81	$\pm$ 0.04	$^{+1.13}_{-0.95}$
POWHEGBOX	$ZZ \to \mu^-\mu^+\mu^-\mu^+$	4.80	$\pm$ 0.02	$^{+0.35}_{-0.27}$	4.58	$\pm$ 0.02	$^{+0.33}_{-0.26}$
gg2VV	$ZZ \to \mu^-\mu^+\mu^-\mu^+$	0.27	$\pm$ 0.00	$^{+0.18}_{-0.17}$	0.27	$\pm$ 0.00	$^{+0.18}_{-0.17}$
summed $ZZ \to \mu^-\mu^+\mu^-\mu^+$		5.08	$\pm$ 0.02	$^{+0.53}_{-0.44}$	4.86	$\pm$ 0.02	$^{+0.51}_{-0.43}$

Table 7.3 Calculated fiducial cross section predictions for the $ZZ \to e^-e^+e^-e^+$, $ZZ \to e^-e^+\mu^-\mu^+$, and $ZZ \to \mu^-\mu^+\mu^-\mu^+$ subchannels. The theoretical prediction is taken as the sum of the contributions from POWHEGBOX and gg2VV samples. The cross sections $\sigma^{\text{fid}}_{\text{EW}}$ indicate cross sections calculated with events weighted by higher-order electroweak corrections. Cross sections without electroweak corrections are given for comparison.

Generator	Process	σ^{total} [fb]	statistical error [fb]	theoretical error [fb]	$\sigma^{\text{total}}_{\text{EW}}$ [fb]	statistical error [fb]	theoretical error [fb]
POWHEGBOX	$ZZ \to e^-e^+\nu\bar{\nu}$	91.07	$\pm$ 0.23	$^{+6.65}_{-5.10}$	86.96	$\pm$ 0.22	$^{+6.35}_{-4.87}$
gg2VV	$ZZ \to e^-e^+\nu\bar{\nu}$	4.34	$\pm$ 0.03	$^{+2.78}_{-2.75}$	4.34	$\pm$ 0.03	$^{+2.78}_{-2.75}$
summed $ZZ \to e^-e^+\nu\bar{\nu}$		95.41	$\pm$ 0.26	$^{+9.43}_{-7.85}$	91.30	$\pm$ 0.25	$^{+9.13}_{-7.62}$
POWHEGBOX	$ZZ \to \mu^-\mu^+\nu\bar{\nu}$	90.91	$\pm$ 0.23	$^{+6.64}_{-5.09}$	86.79	$\pm$ 0.22	$^{+6.34}_{-4.86}$
gg2VV	$ZZ \to \mu^-\mu^+\nu\bar{\nu}$	4.32	$\pm$ 0.03	$^{+2.77}_{-2.73}$	4.32	$\pm$ 0.03	$^{+2.77}_{-2.73}$
summed $ZZ \to \mu^-\mu^+\nu\bar{\nu}$		95.23	$\pm$ 0.23	$^{+9.41}_{-7.82}$	91.11	$\pm$ 0.22	$^{+9.11}_{-7.59}$
POWHEGBOX	$ZZ \to e^-e^+e^-e^+$	7.53	$\pm$ 0.02	$^{+0.55}_{-0.42}$	7.19	$\pm$ 0.02	$^{+0.52}_{-0.40}$
gg2VV	$ZZ \to e^-e^+e^-e^+$	0.36	$\pm$ 0.00	$^{+0.23}_{-0.23}$	0.36	$\pm$ 0.00	$^{+0.23}_{-0.23}$
summed $ZZ \to e^-e^+e^-e^+$		7.89	$\pm$ 0.03	$^{+0.78}_{-0.65}$	7.55	$\pm$ 0.02	$^{+0.75}_{-0.63}$
POWHEGBOX	$ZZ \to e^-e^+\mu^-\mu^+$	14.85	$\pm$ 0.04	$^{+1.08}_{-0.83}$	14.18	$\pm$ 0.04	$^{+1.03}_{-0.79}$
gg2VV	$ZZ \to e^-e^+\mu^-\mu^+$	0.73	$\pm$ 0.01	$^{+0.47}_{-0.46}$	0.73	$\pm$ 0.01	$^{+0.47}_{-0.46}$
summed $ZZ \to e^-e^+\mu^-\mu^+$		15.59	$\pm$ 0.05	$^{+1.55}_{-1.30}$	14.91	$\pm$ 0.05	$^{+1.51}_{-1.26}$
POWHEGBOX	$ZZ \to \mu^-\mu^+\mu^-\mu^+$	7.51	$\pm$ 0.02	$^{+0.55}_{-0.42}$	7.16	$\pm$ 0.02	$^{+0.52}_{-0.40}$
gg2VV	$ZZ \to \mu^-\mu^+\mu^-\mu^+$	0.36	$\pm$ 0.00	$^{+0.23}_{-0.23}$	0.36	$\pm$ 0.00	$^{+0.23}_{-0.23}$
summed $ZZ \to \mu^-\mu^+\mu^-\mu^+$		7.87	$\pm$ 0.03	$^{+0.78}_{-0.65}$	7.53	$\pm$ 0.02	$^{+0.76}_{-0.63}$

Table 7.4 The calculated extrapolated ("total") cross section predictions for the $ZZ \to e^-e^+\nu\bar{\nu}$, $ZZ \to \mu^-\mu^+\nu\bar{\nu}$, $ZZ \to e^-e^+\nu\bar{\nu}$, $ZZ \to \mu^-\mu^+\nu\bar{\nu}$, and $ZZ \to \mu^-\mu^+\mu^-\mu^+$ sub-channels. The predictions are obtained by scaling the cross section of a sample generated for a particular final state by the fraction of events which fall into the inclusive phase space $66 < m_{\ell^-\ell^+} < 116$ GeV relative to the total number of events in the sample as in Eq. (7.1). The total cross sections in this table are not corrected for branching ratio to a particular final state.

sub-channel	$\sigma^{\text{tot}}(ZZ)$ [pb]	statistical error [pb]	theoretical err. [pb]	branching ratio
$ZZ \to e^- e^+ \nu\bar{\nu}$	6.79	0.02	$^{+0.68}_{-0.57}$	0.013452
$ZZ \to \mu^- \mu^+ \nu\bar{\nu}$	6.77	0.02	$^{+0.68}_{-0.56}$	0.013464
average $ZZ \to \ell^- \ell^+ \nu\bar{\nu}$	6.78	0.01	$^{+0.68}_{-0.57}$	
$ZZ \to e^- e^+ e^- e^+$	6.67	0.02	$^{+0.67}_{-0.56}$	0.00113098
$ZZ \to e^- e^+ \mu^- \mu^+$	6.59	0.02	$^{+0.66}_{-0.56}$	0.00226397
$ZZ \to \mu^- \mu^+ \mu^- \mu^+$	6.64	0.02	$^{+0.67}_{-0.56}$	0.001133
average $ZZ \to \ell^- \ell^+ \ell^- \ell^+$	6.63	0.01	$^{+0.67}_{-0.56}$	
combined average	6.69	0.01	$^{+0.67}_{-0.56}$	

Table 7.5 The calculated extrapolated cross sections in the $ZZ \to e^- e^+ \nu\bar{\nu}$, $ZZ \to \mu^- \mu^+ \nu\bar{\nu}$, $ZZ \to e^- e^+ \nu\bar{\nu}$, $ZZ \to \mu^- \mu^+ \nu\bar{\nu}$, and $ZZ \to \mu^- \mu^+ \mu^- \mu^+$ sub-channels corrected for branching ratio. Cross sections shown include higher-order electroweak corrections. The two $ZZ \to \ell^- \ell^+ \nu\bar{\nu}$ sub-channels are combined to give an average extrapolated cross section as are the three $ZZ \to \ell^- \ell^+ \ell^- \ell^+$ channels. A combined $pp \to ZZ$ cross section using an average of all sub-channels is reported at the bottom of the table. This average is compared to the combined measured cross section in Section 7.5.2.

where $N^{\text{MC pass all cuts}}_{\text{Reconstructed } ZZ}$ is the number of signal ZZ MC events which pass all selection at reconstruction level, with all scale factors, event weights, and corrections applied, and $N^{\text{MC Fiducial Volume}}_{\text{Generated } ZZ}$ is the number of generated signal ZZ events which fall in the fiducial volume, with appropriate truth-level weights applied. The numerator includes contributions from $ZZ \to \tau^-\tau^+\nu\bar{\nu}$ where the taus decay leptonically. However, it was found that the contribution from the $\tau^-\tau^+$ samples passing the full event selection is essentially zero, making the contamination from those events negligible (Fig. 5.21). The numerator also includes a contribution from events which are generated outside the fiducial volume, but pass all of the cuts at reconstruction-level. This could be the case for an event with a generated lepton with p_{T} just lower than the lepton p_{T} threshold for event selection which is reconstructed with p_{T} slightly above the threshold. Since the numerator is not a strict subset of the denominator due to these two contaminations, C_{ZZ} is not a true efficiency. As the denominator is a quantity measured at particle-level, the only weight that is applied are theoretical corrections, discussed further below.

Because two different generators are chosen to model the signal process, the reconstruction acceptance is broken into its respective $q\bar{q}$ and gg components such that the resulting C_{ZZ} may be taken as the sum of two terms $C_{q\bar{q}\to ZZ}$ and $C_{gg\to ZZ}$, which may be calculated as

$$C_{q\bar{q}\to ZZ} = \frac{N^{\text{MC Pass All Cuts}}_{\text{Reconstructed } q\bar{q} \to ZZ}}{N^{\text{MC Fiducial Volume}}_{\text{Generated } ZZ}}, \tag{7.4}$$

and

$$C_{gg\to ZZ} = \frac{N^{\text{MC Pass All Cuts}}_{\text{Reconstructed } gg \to ZZ}}{N^{\text{MC Fiducial Volume}}_{\text{Generated } ZZ}}, \tag{7.5}$$

which allows for the total C_{ZZ} to be expressed as

$$C_{ZZ} = C_{q\bar{q}\to ZZ} + C_{gg\to ZZ}. \tag{7.6}$$

This form makes it convenient to apply any corrections or scale factors to any particular component of C_{ZZ} as is the case of a scale factor to correct the efficiency of the jet veto in simulation (the jet veto scale factor,). As the various ZZ signal MC samples are used to estimate C_{ZZ}, the uncertainties in the measured quantity include both theoretical (Section 5.8.6) and experimental uncertainties (Section 5.8). To estimate the various sources of uncertainty on C_{ZZ}, weights and scale factors are independently varied within their 1σ limits and the resulting C_{ZZ} is calculated. A summary of C_{ZZ} in the $ZZ \to e^-e^+\nu\bar{\nu}$ and $ZZ \to \mu^-\mu^+\nu\bar{\nu}$ sub-channels is given in Table 7.6, and the corresponding values in the

$ZZ \to e^-e^+e^-e^+$,$ZZ \to e^-e^+\mu^-\mu^+$, and $ZZ \to \mu^-\mu^+\mu^-\mu^+$ sub-channels are given in Table 7.7.

7.4 Acceptance, A_{ZZ}

In going from the calculation of a fiducial cross section to a “total” cross section measured in a larger, more inclusive phase space, an extrapolation must be made to correct the reconstruction-level cross section to a more inclusive phase space. This is done by applying a correction from the particle-level fiducial volume to the phase space defined by $66 < m_{\ell^-\ell^+} < 116$ GeV. This correction is denoted as the acceptance, or A_{ZZ} and is calculated as

$$A_{ZZ} = \frac{N^{\text{MC fiducial phase space}}_{\text{Generated}ZZ}}{N^{\text{MC total phase space}}_{\text{Generated }ZZ}}. \tag{7.7}$$

The denominator of A_{ZZ} is the number of events which fall in the extrapolated phase space $66 < m_{\ell^-\ell^+} < 116$ GeV, and the numerator is the number of events in the fiducial phase space; this is the same as the denominator in the calculation of C_{ZZ} in Eq. (7.3), and the same weighting is applied in both cases. It is convenient to separate out the acceptance from the reconstruction efficiency terms, as the factorisation separates out the term that is sensitive to theoretical uncertainties (A_{ZZ}) from the term representing primarily detector efficiency (C_{ZZ}). A_{ZZ} is calculated independently for each $ZZ \to \ell^-\ell^+\nu\bar{\nu}$ and $ZZ \to \ell^-\ell^+\ell^-\ell^+$sub-channel. The acceptance in the $ZZ \to e^-e^+\nu\bar{\nu}$ and $ZZ \to \mu^-\mu^+\nu\bar{\nu}$ sub-channels is given in Table 7.8, and the corresponding acceptances in the $ZZ \to e^-e^+e^-e^+$, $ZZ \to e^-e^+\mu^-\mu^+$, and $ZZ \to \mu^-\mu^+\mu^-\mu^+$ sub-channels are given in Table 7.9.

C_{ZZ} may be used to perform a check on the theoretical fiducial cross section calculated by using a simple formula relating the expected number of events passing all selection to the product of the luminosity, the cross section and C_{ZZ}, according to:

$$N^{\text{xsec}}_{\text{expected}} = \sigma^{\text{EW}}_{\text{fid}} \cdot C_{ZZ} \cdot \mathscr{L}. \tag{7.8}$$

	$C^{ee}_{q\bar{q}\to ZZ}$	$C^{ee}_{gg\to ZZ}$	$C^{\mu\mu}_{q\bar{q}\to ZZ}$	$C^{\mu\mu}_{gg\to ZZ}$	C^{ee}_{ZZ}	$C^{\mu\mu}_{ZZ}$
C_{ZZ} Nominal Value	0.6579	0.0196	0.7340	0.0183	0.6775	0.7523
statistical uncertainty	$^{+2.2\%}_{-2.2\%}$	$^{+7.1\%}_{-7.1\%}$	$^{+2.1\%}_{-2.1\%}$	$^{+7.4\%}_{-7.4\%}$	$\pm 2.1\%$	$\pm 2.1\%$
electron identification	$^{+1.6\%}_{-1.6\%}$	$^{+1.5\%}_{-1.5\%}$	-	-	$\pm 1.6\%$	-
electron isolation	$^{+0.3\%}_{-0.3\%}$	$^{+0.3\%}_{-0.3\%}$	-	-	$\pm 0.3\%$	-
electron reconstruction	$^{+0.7\%}_{-0.7\%}$	$^{+0.6\%}_{-0.6\%}$	-	-	$\pm 0.7\%$	-
electron energy resolution	$^{+0.2\%}_{-0.0\%}$	$^{-0.7\%}_{-0.1\%}$	-	-	$^{+0.2\%}_{-0.0\%}$	-
electron energy scale	$^{+1.65\%}_{-1.82\%}$	$^{+1.0\%}_{-2.2\%}$	$^{+0.1\%}_{-0.1\%}$	-	$^{+1.6\%}_{-1.8\%}$	-
muon momentum resolution	-	-	$^{-0.3\%}_{-0.1\%}$	$^{+0.4\%}_{-0.0\%}$	-	$^{-0.3\%}_{+0.1\%}$
muon momentum scale	-	-	$^{+0.1\%}_{-0.2\%}$	-	-	$^{+0.1\%}_{-0.2\%}$
muon reconstruction efficiency	-	-	$^{+0.7\%}_{-0.7\%}$	$^{+0.7\%}_{-0.7\%}$	-	$^{+0.7\%}_{-0.7\%}$
muon identification efficiency	-	-	$^{-0.1\%}_{-0.2\%}$	$^{+1.0\%}_{+0.0\%}$	-	$^{+0.1\%}_{-0.2\%}$
muon isolation	-	-	$^{+3.0\%}_{-3.0\%}$	$^{+3.0\%}_{-3.0\%}$	-	$^{+3.0\%}_{-3.0\%}$
jet energy scale	$^{+4.1\%}_{-3.1\%}$	$^{+8.4\%}_{-6.7\%}$	$^{+3.4\%}_{-3.8\%}$	$^{+4.1\%}_{-6.8\%}$	$^{+4.2\%}_{-3.2\%}$	$^{+3.4\%}_{-3.9\%}$
jet energy resolution	$^{-1.4\%}_{+1.4\%}$	$^{-2.9\%}_{+2.9\%}$	$^{-2.7\%}_{+2.7\%}$	$^{-1.7\%}_{+1.7\%}$	$^{-1.4\%}_{+1.4\%}$	$^{-2.7\%}_{+2.7\%}$
jet vertex fraction	$^{+0.3\%}_{-0.2\%}$	$^{0.0\%}_{-1.7\%}$	$^{+0.3\%}_{-0.1\%}$	$^{+0.6\%}_{-0.5\%}$	$^{+0.3\%}_{-0.2\%}$	$^{+0.3\%}_{-0.1\%}$
$E_{\mathrm{T}}^{\mathrm{miss}}$ resolution (soft terms)	$^{+0.1\%}_{-0.1\%}$	$^{-0.1\%}_{+0.1\%}$	$^{-0.5\%}_{+0.5\%}$	$^{+4.7\%}_{-4.7\%}$	$^{+0.1\%}_{-0.1\%}$	$^{-0.4\%}_{+0.4\%}$
$E_{\mathrm{T}}^{\mathrm{miss}}$ scale (soft terms)	$^{-0.8\%}_{+1.6\%}$	$^{+0.2\%}_{+0.6\%}$	$^{-1.1\%}_{+0.4\%}$	$^{-1.1\%}_{+2.3\%}$	$^{-0.8\%}_{+1.6\%}$	$^{-1.1\%}_{+0.5\%}$
trigger	$\pm 0.1\%$	$\pm 0.1\%$	$\pm 0.5\%$	$\pm 0.5\%$	$\pm 0.1\%$	$\pm 0.5\%$
electroweak corrections	$\pm 0.3\%$	$\mp 0.1\%$	$\pm 0.4\%$	-	$\pm 0.3\%$	$\pm 0.4\%$
MC generator difference	$\mp 0.4\%$	$\mp 18.4\%$	$\mp 1.7\%$	$\mp 21.0\%$	$\mp 0.9\%$	$\mp 2.2\%$
PDF	$^{+0.3\%}_{-0.3\%}$	$^{+7.7\%}_{-6.7\%}$	$^{+0.3\%}_{-0.3\%}$	$^{+7.7\%}_{-6.6\%}$	$\pm 0.1\%$	$^{+0.2\%}_{-0.3\%}$
$\Delta C_{ZZ}/C_{ZZ}$	$^{+5.63\%}_{-4.87\%}$	$^{+23.1\%}_{-22.3\%}$	$^{+6.08\%}_{-6.39\%}$	$^{+24.8\%}_{-25.0\%}$	$^{+5.75\%}_{-4.99\%}$	$^{+6.20\%}_{-6.54\%}$

Table 7.6 Calculated C_{ZZ} in the $ZZ \to e^- e^+ \nu\bar{\nu}$ and $ZZ \to \mu^- \mu^+ \nu\bar{\nu}$ channels, with relative uncertainties given. A dash indicates a relative uncertainty smaller than 0.05%. The relative uncertainty given at the bottom of the table and is the quadrature sum of all the uncertainties.

	$e^-e^+e^-e^+$	$e^-e^+\mu^-\mu^+$	$\mu^-\mu^+\mu^-\mu^+$
C_{ZZ} nominal value	0.495	0.643	0.846
statistical uncertainty	$\pm 0.61\%$	$\pm 0.47\%$	$\pm 0.31\%$
electron energy resolution	$\pm 0.07\%$	$\pm 0.01\%$	$-\%$
electron energy scale	$\pm 0.41\%$	$\pm 0.15\%$	$\pm 0.01\%$
electron identification efficiency	$\pm 3.60\%$	$\pm 1.79\%$	$-\%$
electron isolation	$\pm 1.37\%$	$\pm 0.66\%$	$-\%$
electron reconstruction efficiency	$\pm 1.70\%$	$\pm 0.82\%$	$-\%$
muon momentum resolution	–	$\pm 0.03\%$	$\pm 0.02\%$
muon momentum scale	–	$\pm 0.02\%$	$\pm 0.02\%$
muon reconstruction	–	$\pm 0.88\%$	$\pm 1.75\%$
muon isolation	–	$\pm 1.69\%$	$\pm 3.39\%$
trigger	$\pm 0.04\%$	$\pm 0.10\%$	$\pm 0.20\%$
electroweak corrections	–	–	–
MC generator difference	$\pm 1.82\%$	$\pm 1.71\%$	$\pm 1.18\%$
QCD Scale ($q\bar{q}$ only)	$\pm 0.16\%$	$\pm 0.19\%$	$\pm 0.22\%$
PDF	$\pm 0.16\%$	$\pm 0.13\%$	$\pm 0.02\%$
$\Delta C_{ZZ}/C_{ZZ}$	$\pm 4.65\%$	$\pm 3.34\%$	$\pm 4.01\%$

Table 7.7 Efficiency correction C_{ZZ} in the $ZZ \rightarrow e^-e^+e^-e^+$ and $ZZ \rightarrow e^-e^+\mu^-\mu^+$ and $ZZ \rightarrow \mu^-\mu^+\mu^-\mu^+$ sub-channels and the systematic uncertainties. The total relative uncertainty in each $ZZ \rightarrow \ell^-\ell^+\ell^-\ell^+$ sub-channel is given at the bottom of the table.

	ee	$\mu\mu$
A_{ZZ} nominal value	0.04126	0.03999
statistical uncertainty	$\pm1.1\%$	±1.2
electroweak corrections	$\mp0.9\%$	$\mp1.0\%$
QCD scale (qqbar only)	$^{+2.2\%}_{-0.6\%}$	$^{+1.1\%}_{-1.6\%}$
parton shower	$\mp4.2\%$	$\mp3.5\%$
PDF	$^{+1.0\%}_{-1.5\%}$	$^{+1.1\%}_{-1.4\%}$
$\Delta A_{ZZ}/A_{ZZ}$	$^{+5.09\%}_{-4.73\%}$	$^{+4.16\%}_{-4.40\%}$

Table 7.8 Calculated A_{ZZ} in the $ZZ \to \mu^-\mu^+\nu\bar{\nu}$ and $ZZ \to \mu^-\mu^+\nu\bar{\nu}$ channels, with relative uncertainties given. The sum at the bottom of the table is also a quadrature sum of all the terms.

	$e^-e^+e^-e^+$	$\mu^-\mu^+\mu^-\mu^+$	$e^-e^+\mu^-\mu^+$
A_{ZZ} nominal value	0.817	0.645	0.725
statistical uncertainty	$\pm0.36\%$	$\pm0.46\%$	$\pm0.41\%$
electroweak corrections	-	-	-
QCD scale (qqbar only)	$\pm0.17\%$	$\pm0.27\%$	$\pm0.23\%$
PDF	$\pm0.64\%$	$\pm0.89\%$	$\pm0.71\%$
generator difference	$\pm1.97\%$	$\pm2.97\%$	$\pm2.24\%$
$\Delta A_{ZZ}/A_{ZZ}$	$\pm2.11\%$	$\pm3.14\%$	$\pm2.39\%$

Table 7.9 Acceptance A_{ZZ} in the $ZZ \to e^-e^+e^-e^+$, $ZZ \to e^-e^+\mu^-\mu^+$, and $ZZ \to \mu^-\mu^+\mu^-\mu^+$ sub-channels and the theoretical systematic uncertainties including QCD scale and PDF uncertainties. To account for the lack of the parton shower/underlying event uncertainty, the comparison to SHERPA is given. The total relative uncertainty in each $ZZ \to \ell\ell\ell'\ell'$ sub-channel is given at the bottom of the table.

sub-channel	$\sigma^{\text{fid}}_{\text{theory}}$ (with EW effects)	C_{ZZ}	$N^{\text{xsec}}_{\text{expected}}$	N_{expected}	difference [%]
$ZZ \rightarrow e^- e^+ \nu\bar{\nu}$	3.77	0.669	51.2	51.1	0.12%
$ZZ \rightarrow \mu^- \mu^+ \nu\bar{\nu}$	3.65	0.746	55.2	55.1	0.25%
$ZZ \rightarrow e^- e^+ e^- e^+$	6.17	0.495	62.0	62.2	-0.38%
$ZZ \rightarrow e^- e^+ \mu^- \mu^+$	10.81	0.643	141.1	141.6	-0.36%
$ZZ \rightarrow \mu^- \mu^+ \mu^- \mu^+$	4.86	0.846	83.4	83.7	-0.35%

Table 7.10 A check of the calculated theory cross sections and the number of expected signal events from the underlaying samples reported in Table 7.1. The values for C_{ZZ} used here are given in Table 7.6 and Table 7.7. The expected number of events is calculated from the cross sections according to Eq. (7.8) with the integrated luminosity $\mathscr{L} = 20.3\text{fb}^{-1}$. The values for $\sigma^{\text{EW}}_{\text{fid}}$ are taken from Table 7.2 and Table 7.3. The differences in each of the sub-channels is less than one half of one percent.

7.5 Cross section extraction

For a given sub-channel in the $ZZ \to \ell^-\ell^+\nu\bar{\nu}$ analysis, the fiducial cross section can be calculated as

$$\sigma^{\text{fid}}_{ZZ\to\ell^-\ell^+\nu\bar{\nu}} = \frac{N^{\text{obs}}_{ZZ\to\ell^-\ell^+\nu\bar{\nu}} - N^{\text{bkg}}_{ZZ\to\ell^-\ell^+\nu\bar{\nu}}}{\mathscr{L} \times C_{ZZ\to\ell\ell\nu\bar{\nu}}}, (\ell = e, \mu), \tag{7.9}$$

while for the four charged lepton channels it becomes

$$\sigma^{\text{fid}}_{ZZ\to\ell^-\ell^+\ell^-\ell^+} = \frac{N^{\text{obs}}_{ZZ\to\ell^-\ell^+\ell^-\ell^+} - N^{\text{bkg}}_{ZZ\to\ell^-\ell^+\ell^-\ell^+}}{\mathscr{L} \times C_{ZZ\to\ell^-\ell^+\ell^-\ell^+}}. \tag{7.10}$$

Here, N^{observed} and N^{bkg} denote the number of observed and total background events in a given sub-channel respectively, $\mathscr{L}$ is the integrated luminosity of the data sample used, and $C_{ZZ\to\ell\ell\nu\bar{\nu}}$ is the fiducial correction factor. In addition to the fiducial cross section, an extrapolation is made from the fiducial phase space to a larger, more inclusive phase space, defined by $66 < m_Z < 116$ GeV, and is referred to as the “total” cross section, or “extrapolated” cross section. The total cross section for the $\ell^-\ell^+\nu\bar{\nu}$ channels is calculated as:

$$\begin{aligned}\sigma^{\text{tot}}_{ZZ\to\ell^-\ell^+\nu\bar{\nu}} &= \frac{N^{\text{obs}}_{\ell^-\ell^+\nu\bar{\nu}} - N^{\text{bkg}}_{\ell^-\ell^+\nu\bar{\nu}}}{\mathscr{L} \times \text{BR}\{ZZ \to \ell^-\ell^+\nu\bar{\nu}\} \times A_{ZZ\to\ell^-\ell^+\nu\bar{\nu}} \times C_{ZZ\to\ell^-\ell^+\nu\bar{\nu}}}, \\ &= \frac{\sigma^{\text{fid}}_{ZZ\to\ell^-\ell^+\nu\bar{\nu}}}{\text{BR}\{ZZ \to \ell^-\ell^+\nu\bar{\nu}\} \times A_{ZZ\to\ell^-\ell^+\nu\bar{\nu}}},\end{aligned} \tag{7.11}$$

where $A_{ZZ\to\ell^-\ell^+\nu\bar{\nu}}$ is the detector acceptance, $\text{BR}\{ZZ \to \ell^-\ell^+\nu\bar{\nu}\}$ is the branching ratio for one Z to decay to an $\ell^+\ell^-$ final state and the other Z to decay to a $\nu\bar{\nu}$ final state. Analogously, the total cross section for the $ZZ \to \ell^-\ell^+\ell^-\ell^+$ channels is

$$\sigma^{\text{tot}}_{ZZ\to\ell^-\ell^+\ell^-\ell^+} = \frac{\sigma^{\text{fid}}_{ZZ\to\ell^-\ell^+\ell^-\ell^+}}{\text{BR}\{ZZ \to \ell^-\ell^+\ell^-\ell^+\} \times A_{ZZ\to\ell^-\ell^+\ell^-\ell^+}}. \tag{7.12}$$

The cross section could be calculated using Eqs. (7.9) to (7.12), but this would not take into account the Poisson nature of the observed and expected events. Furthermore, it would be difficult to propagate the systematic uncertainties and handle correlations between different systematic uncertainties. In practice, the extraction method is based on maximising a profile-likelihood function with respect to the cross section σ as the parameter of interest (POI), using a model with a single bin for each sub-channel. However, Eqs. (7.9) to (7.12) provide a useful means to check the central values of cross sections in the individual channels, as well as estimating bounds on uncertainties for the various parameters of interest.

7.5.1 Statistical model for cross section extraction

The cross section σ is obtained by maximising the profile-likelihood with respect to the parameter σ. As it is easier to work with numerical minimisation routines, the maximisation is carried out by minimising the negative log-likelihood function, $-\ln(L)$. This is performed using a model based on ROOFIT [212] classes which interface to the MINUIT function minimiser [213]. A likelihood function is constructed for each channel corresponding to the decay modes $ZZ \to e^-e^+\nu\bar{\nu}$, $ZZ \to \mu^-\mu^+\nu\bar{\nu}$, in the case of the $ZZ \to \ell^-\ell^+\nu\bar{\nu}$ channels and for the case of the four charged lepton final states, a separate likelihoods are constructed for the $ZZ \to e^-e^+e^-e^+$, $ZZ \to \mu^-\mu^+\mu^-\mu^+$, and $ZZ \to e^-e^+\mu^-\mu^+$ channels before minimisation. A single-bin model is used in each sub-channel; no information on the differential behaviour of the various kinematic distributions is incorporated into the model. The likelihoods for similar final states (e.g. $e^-e^+\nu\bar{\nu}$ and $\mu^-\mu^+\nu\bar{\nu}$) are multiplied before performing the minimisation, and a simultaneous fit to the parameters of interest is made.

The likelihood is constructed as a product of Poisson terms, with the mean taken as the expected number of events and the exponent being the observed number of events. Each Poisson term is interpreted as the probability of observing N_{observed} events given an expectation of N_{bkgd} plus N_{signal} (parameterised in terms of the cross section σ and reconstruction correction factor C_{ZZ}), and may be expressed as

$$P(\sigma, C_{ZZ}, \mathscr{L}, N_{\text{signal}}, N_{\text{bkgd}}; N_{\text{observed}}) = \frac{e^{-(N_{\text{sig}}(\sigma, C_{ZZ}, \mathscr{L}) + N_{\text{bkgd}})} \cdot (N_{\text{sig}}(\sigma, C_{ZZ}, \mathscr{L}) + N_{\text{bkgd}})^{N_{\text{observed}}}}{N_{\text{observed}}!}. \quad (7.13)$$

For the fiducial cross sections the expected number of signal events, (N_{signal} in Eq. (7.13)), in channel i is taken as a product of the input parameters

$$N_{\text{sig},i}\left(\sigma_{\text{fid},i}, \mathscr{L}, C_{ZZ,i}\right) = \sigma_{\text{fid}} \cdot \mathscr{L} \cdot C_{ZZ,i}, \quad (7.14)$$

where the index i runs over the range of sub-channels $ZZ \to e^+e^-\nu\bar{\nu}$, $ZZ \to \mu^+\mu^-\nu\bar{\nu}$ for the $ZZ \to \ell^-\ell^+\nu\bar{\nu}$ cross sections, and $ZZ \to e^-e^+e^-e^+$, $ZZ \to e^-e^+\mu^-\mu^+$, $ZZ \to \mu^-\mu^+\mu^-\mu^+$, for the $ZZ \to \ell^-\ell^+\ell^-\ell^+$cross sections. When measuring a total cross section, the signal expectation is modified to account for the acceptance factor A_{ZZ}, and the branching ratio to go to a given final state:

$$N_{\text{sig},i}\left(\sigma_{\text{tot},i}, \mathscr{L}, C_{ZZ,i}\right) = \sigma_{\text{tot}} \cdot \mathscr{L} \cdot C_{ZZ,i} \cdot A_{ZZ,i} \cdot \text{BR}_i. \quad (7.15)$$

The background term in each sub-channel is a sum of the individual backgrounds. For the $ZZ \to e^{+}e^{-}\nu\bar{\nu}$ and and $ZZ \to \mu^{+}\mu^{-}\nu\bar{\nu}$ sub-channels, the backgrounds in the i^{th} sub-channel are expressed as the sums

$$N_{\text{bkg},i} = N_{W+X,i} + N_{WW/t\bar{t}/Z\to\tau\tau,i} + N_{Z+X,i} + N_{WZ,i} + N_{ZZ\to 4\ell,i}, \tag{7.16}$$

where the index i runs over the same indices before. In the case of the $ZZ \to e^{-}e^{+}e^{-}e^{+}$, $ZZ \to e^{-}e^{+}\mu^{-}\mu^{+}$, $ZZ \to \mu^{-}\mu^{+}\mu^{-}\mu^{+}$ sub-channels, the background is taken as the sum of data-driven and irreducible contributions:

$$N_{\text{bkg},i} = N_{\text{Data-driven},i} + N_{\text{irreducible},i}. \tag{7.17}$$

The basic inputs to the cross section model include the numbers of observed events, backgrounds ($W+X$, $WW/t\bar{t}/Z \to \tau\tau$, $Z+X$,WZ, $ZZ \to 4\ell$), integrated luminosity, correction factors C_{ZZ}, and in the case of total cross section, the acceptance, and the branching ratio for a given final state. Each input variable is an implicit function of the underlying nuisance parameters, which model the systematic uncertainties. The nuisance parameters are modelled by either a Gaussian probability distribution function, or a Poisson probability distribution function. The Gaussian terms each have a mean μ of 0 and a standard deviation of 1 (Gaussian nuisance parameters are referred to by α). A shift away from the centre of the Gaussian would indicate a constraint on the nuisance parameter. Thus after the fit, each nuisance parameter should be consistent with zero within uncertainties. The Poisson constraint terms are applied for purely statistical uncertainties obtained from counting a sum of event weights, as in the WZ and $ZZ \to \ell^{-}\ell^{+}\ell^{-}\ell^{+}$ backgrounds to the $ZZ \to \ell^{-}\ell^{+}\nu\bar{\nu}$ channels. These constraint terms are constructed as to have a mean of 1 and a standard deviation equal to the statistical uncertainty of the input parameter (i.e. the MC statistical uncertainty). The non-Gaussian constraint terms are represented by (γ). After multiplication with the constraint terms, for j Gaussian uncertainties, and for n Poisson uncertainties the likelihood becomes

$$\begin{aligned} &L(\sigma, C_{ZZ}, \mathscr{L}, N_{\text{signal}}, N_{\text{bkgd}}; N_{\text{observed}}) = \\ &\frac{e^{-(N_{\text{signal}}(\sigma, C_{ZZ}, \mathscr{L}) + N_{\text{bkgd}})} \cdot (N_{\text{sig}}(\sigma, C_{ZZ}, \mathscr{L}) + N_{\text{bkgd}})^{N_{\text{observed}}}}{N_{\text{observed}}!} \times \prod_{k=1}^{j} \alpha_i\,(0|1) \times \prod_{q=1}^{n} \gamma_q. \end{aligned} \tag{7.18}$$

The minimised likelihood functions for the $ZZ \to e^{-}e^{+}\nu\bar{\nu}$ and $ZZ \to \mu^{-}\mu^{+}\nu\bar{\nu}$ fiducial cross sections are given are in Figs. 7.2 and 7.3, and the minimised likelihood functions for the fiducial cross sections in the $ZZ \to e^{-}e^{+}e^{-}e^{+}$, $ZZ \to e^{-}e^{+}\mu^{-}\mu^{+}$, and $ZZ \to \mu^{-}\mu^{+}\mu^{-}\mu^{+}$

sub-channels are given in Figs. 7.4 to 7.6. The corresponding likelihood functions for the total cross sections are given in Figs. 7.7 to 7.9.

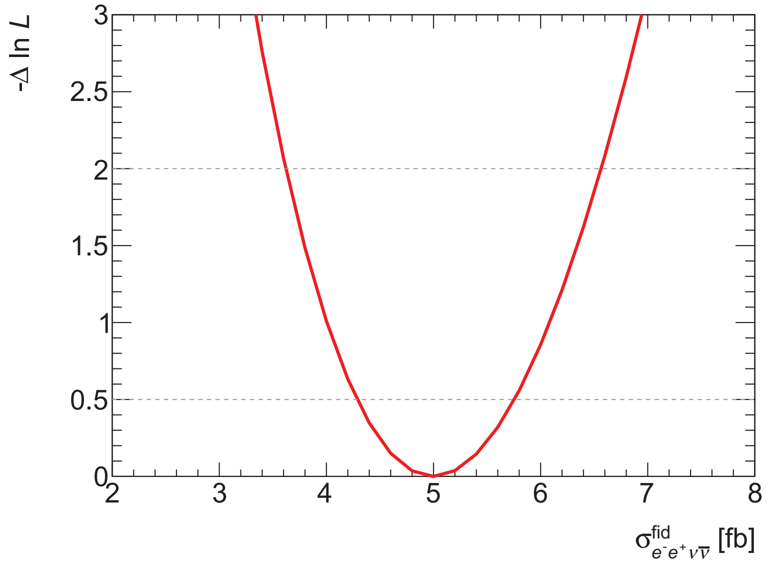

Fig. 7.2 The minimised likelihood function L for the fiducial cross section in the $ZZ \to e^-e^+\nu\bar{\nu}$ channel. The dashed lines indicate the values by which the likelihood changes by 1/2 and 2 from its minimum value indicating the 1σ and 2σ confidence levels on the parameter of interest.

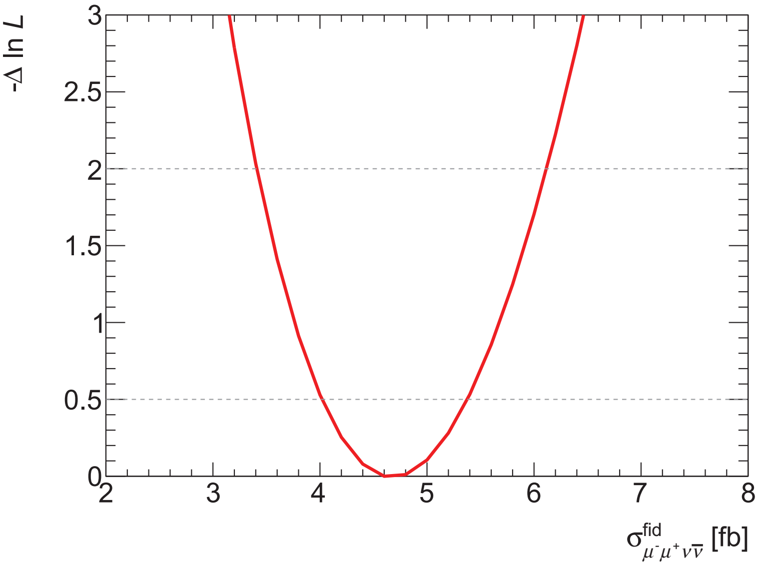

Fig. 7.3 The minimised likelihood function L for the fiducial cross section in the $ZZ \to \mu^-\mu^+\nu\bar{\nu}$ channel. The dashed lines indicate the values by which the likelihood changes by 1/2 and 2 from its minimum value indicating the 1σ and 2σ confidence levels on the parameter of interest.

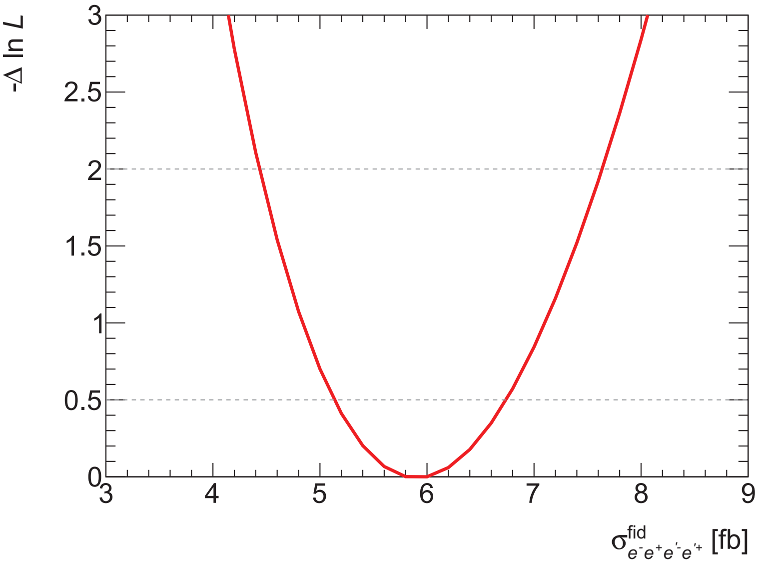

Fig. 7.4 The minimised likelihood function L for the fiducial cross section in the $ZZ \to e^-e^+e^-e^+$ channel. The dashed lines indicate the values by which the likelihood changes by 1/2 and 2 from its minimum value indicating the 1σ and 2σ confidence levels on the parameter of interest.

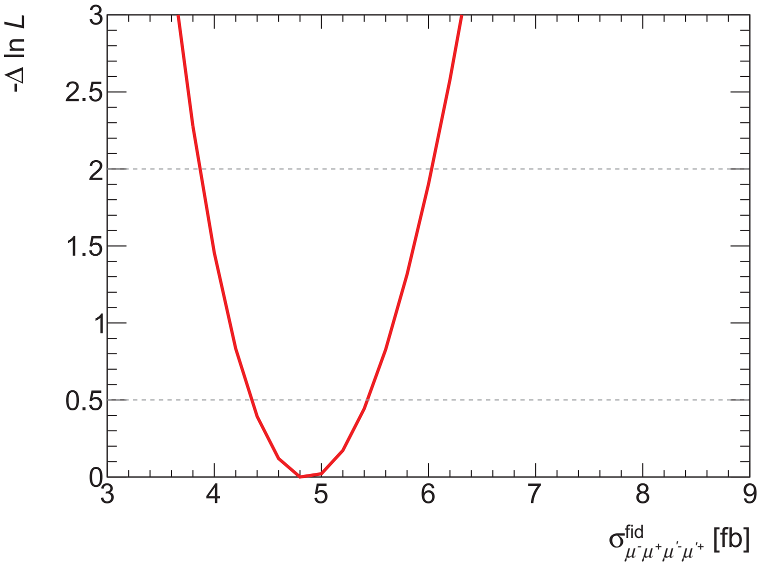

Fig. 7.5 The minimised likelihood function L for the fiducial cross section in the $ZZ \rightarrow \mu^-\mu^+\mu^-\mu^+$ channel.

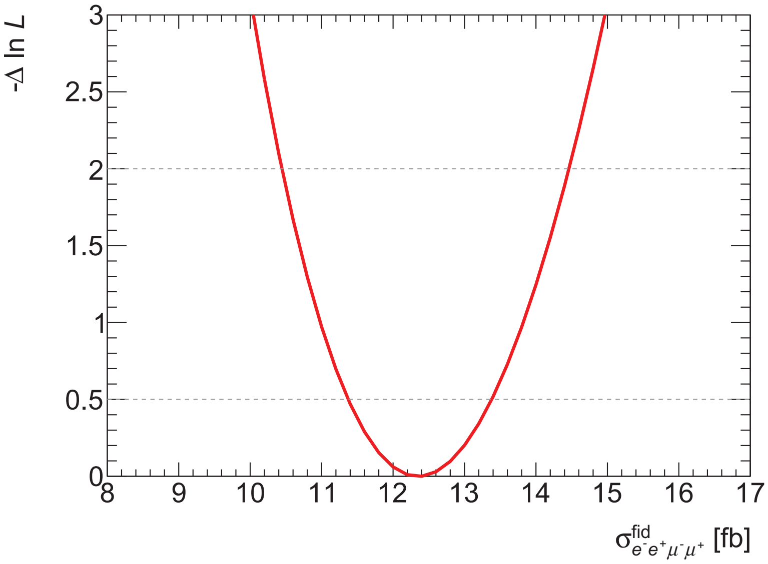

Fig. 7.6 The minimised likelihood function L for the fiducial cross section in the $ZZ \rightarrow e^-e^+\mu^-\mu^+$ channel.

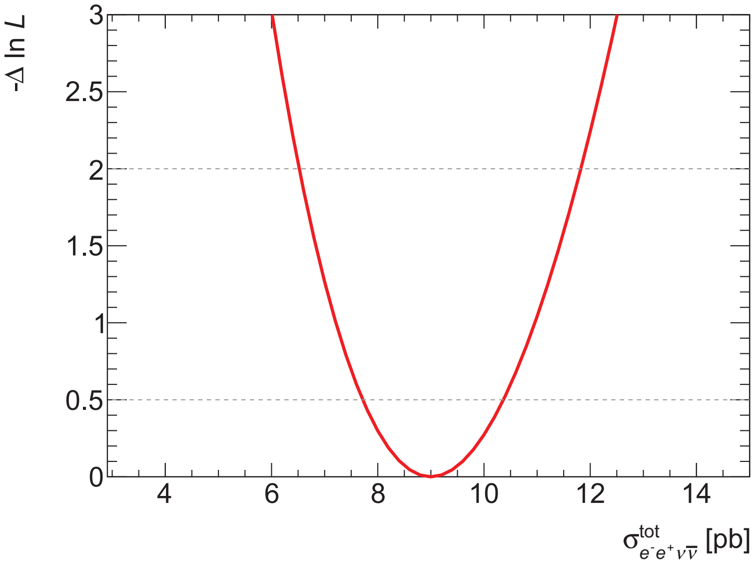

Fig. 7.7 The minimised likelihood function L for the total cross section in the $ZZ \rightarrow e^-e^+\nu\bar{\nu}$ channel. The dashed lines indicate the values by which the likelihood changes by 1/2 and 2 from its minimum value indicating the 1σ and 2σ confidence levels on the parameter of interest.

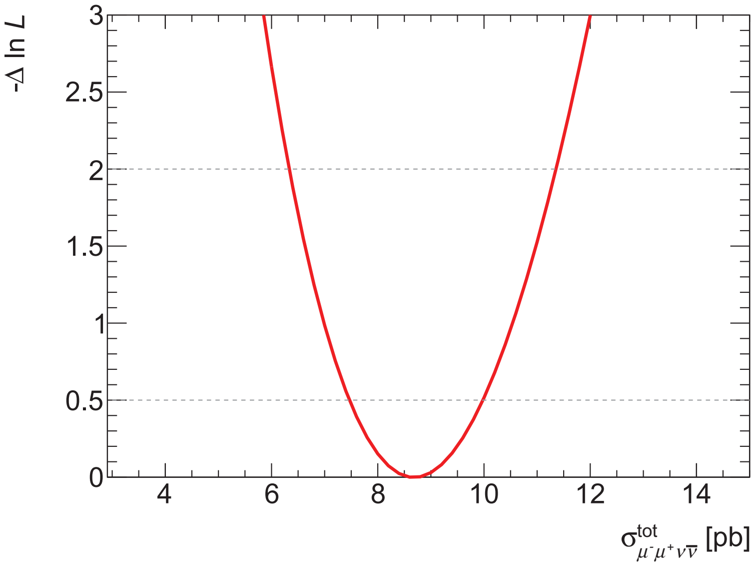

Fig. 7.8 The minimised likelihood function L for the total cross section in the $ZZ \rightarrow \mu^-\mu^+\nu\bar{\nu}$ channel.

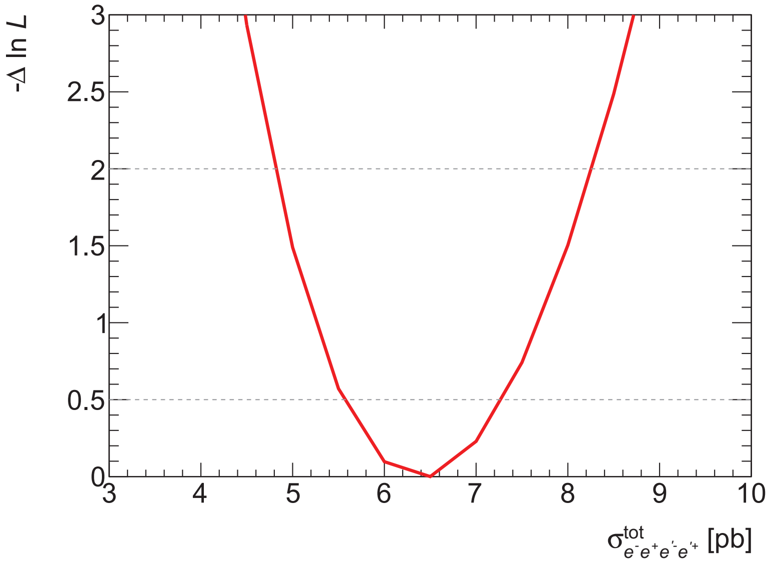

Fig. 7.9 The minimised likelihood function *L* for the total cross section in the $ZZ \to e^- e^+ e^- e^+$ channel.

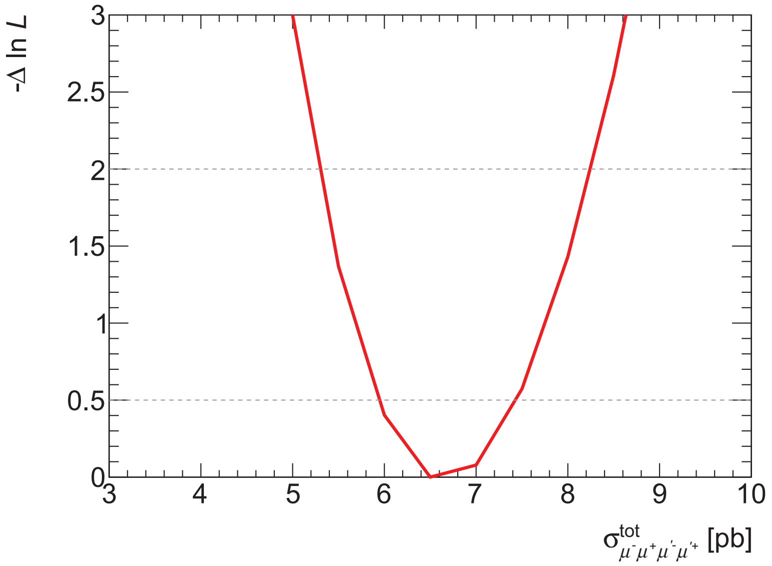

Fig. 7.10 The minimised likelihood function *L* for the total cross section in the $ZZ \to \mu^- \mu^+ \mu^- \mu^+$ channel.

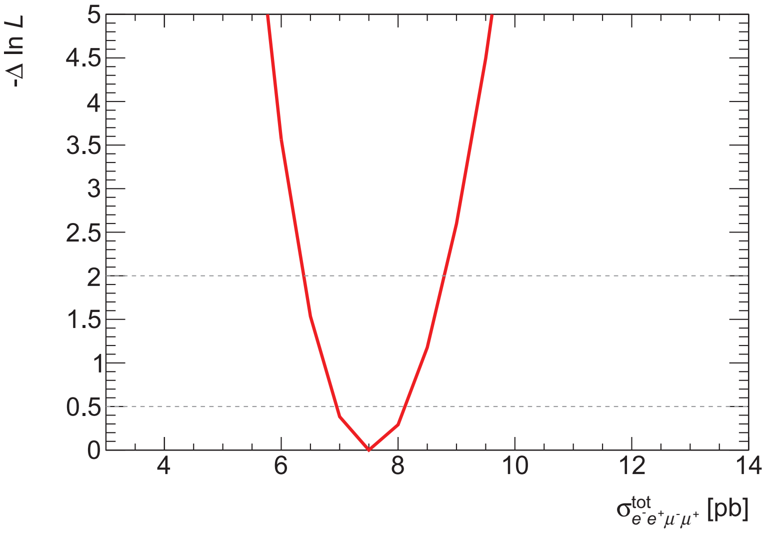

Fig. 7.11 The minimised likelihood function L for the total cross section in the $ZZ \to e^-e^+\mu^-\mu^+$ channel.

7.5.2 Measured cross sections

The measured fiducial cross sections in the $ZZ \to e^-e^+\nu\bar{\nu}$ and $ZZ \to \mu^-\mu^+\nu\bar{\nu}$ sub-channels are given in Table 7.11 and for the $ZZ \to e^-e^+e^-e^+$, $ZZ \to e^-e^+\mu^-\mu^+$, and $ZZ \to \mu^-\mu^+\mu^-\mu^+$ sub-channels in Table 7.12. Total cross sections are given in Tables 7.13 and 7.14. The systematic uncertainties include all sources except luminosity, which is listed separately.

Channel	Fiducial cross section [fb]
$ee\nu\nu$	$4.99\,^{+0.76}_{-0.71}$ (stat) $^{+0.45}_{-0.38}$ (syst) $^{+0.20}_{-0.15}$ (lumi)
$\mu\mu\nu\nu$	$4.67\,^{+0.70}_{-0.65}$ (stat) $^{+0.45}_{-0.35}$ (syst) $^{+0.19}_{-0.15}$ (lumi)

Table 7.11 Measured fiducial cross sections for the $ZZ \to e^-e^+\nu\bar{\nu}$ and $ZZ \to \mu^-\mu^+\nu\bar{\nu}$ sub-channels. The corresponding theory prediction is given in Table 7.2.

Channel	Fiducial cross section [fb]
$eeee$	$5.90\,^{+0.83}_{-0.76}$ (stat) $^{+0.29}_{-0.23}$ (syst) $^{+0.19}_{-0.15}$ (lumi)
$ee\mu\mu$	$12.35\,^{+1.03}_{-0.98}$ (stat) $^{+0.38}_{-0.33}$ (syst) $^{+0.37}_{-0.32}$ (lumi)
$\mu\mu\mu\mu$	$4.87\,^{+0.56}_{-0.52}$ (stat) $^{+0.21}_{-0.17}$ (syst) $^{+0.15}_{-0.12}$ (lumi)

Table 7.12 Measured fiducial cross sections for each $ZZ \to \ell^-\ell^+\ell^-\ell^+$ sub-channels. The corresponding theory prediction is given in Table 7.3.

Channel	Total cross section [pb]
$ee\nu\nu$	$8.99\,^{+1.37}_{-1.28}$ (stat) $^{+0.95}_{-0.78}$ (syst) $^{+0.36}_{-0.28}$ (lumi)
$\mu\mu\nu\nu$	$8.68\,^{+1.29}_{-1.21}$ (stat) $^{+0.94}_{-0.73}$ (syst) $^{+0.35}_{-0.27}$ (lumi)

Table 7.13 Measured total cross sections for the $ZZ \to e^-e^+\nu\bar{\nu}$ and $ZZ \to \mu^-\mu^+\nu\bar{\nu}$ sub-channels. Cross sections are corrected for branching ratio to a given final state using the values in given in Table 7.5. The corresponding theory prediction may be found in Table 7.5.

Channel	Total cross section [pb]
$eeee$	$6.38\ ^{+0.90}_{-0.83}$ (stat) $^{+0.32}_{-0.25}$ (syst) $^{+0.20}_{-0.16}$ (lumi)
$ee\mu\mu$	$7.52\ ^{+0.63}_{-0.60}$ (stat) $^{+0.25}_{-0.21}$ (syst) $^{+0.23}_{-0.20}$ (lumi)
$\mu\mu\mu\mu$	$6.66\ ^{+0.77}_{-0.71}$ (stat) $^{+0.30}_{-0.24}$ (syst) $^{+0.21}_{-0.17}$ (lumi)

Table 7.14 Measured total cross sections for each $ZZ \to \ell^-\ell^+\ell^-\ell^+$ sub-channel. The corresponding theory prediction is given in table 7.5.

Finally, a combined cross section is presented in which the two $ZZ \to \ell^-\ell^+\nu\bar{\nu}$ sub-channels and the three $ZZ \to \ell^-\ell^+\ell^-\ell^+$ channels are combined. Likelihood functions are constructed for each channel, and the product of the likelihoods is taken and the product is minimised with respect to the total combined cross section, σ_{tot}. A weighted average for the combined cross section would favour the total cross section towards the values with the smaller uncertainties, thus one would expect the result to be weighted towards the values obtained for the $ZZ \to \ell^-\ell^+\ell^-\ell^+$ channels. Taking only statistical uncertainties on the values from Table 7.13 and Table 7.14 would give a measurement on the order of approximately 7.25 pb. The value of the combined cross section is given in Table 7.15.

channel	Total cross section [pb]
All channels	$7.30\ ^{+0.38}_{-0.37}$ (stat) $^{+0.28}_{-0.25}$ (syst) $^{+0.23}_{-0.20}$ (lumi)

Table 7.15 The total cross section for all ZZ channels combined. The corresponding theory prediction is given in table 7.5.

The $\ell^-\ell^+\nu\bar{\nu}$ fiducial cross sections are consistently higher than the theoretical prediction. The agreement is better in the $\ell^-\ell^+\ell'^-\ell'^+$ sub-channels. The excess remains in the $\ell^-\ell^+\nu\bar{\nu}$ sub-channels for the total cross sections. The agreement between prediction and measurement is again for the $\ell^-\ell^+\ell'^-\ell'^+$ final states for total cross sections. As the combined cross section represents the statistical combination of both the $\ell^-\ell^+\nu\bar{\nu}$ and $\ell^-\ell^+\ell'^-\ell'^+$ channels, the pull of the $\ell^-\ell^+\nu\bar{\nu}$ channels causes the combined cross section to be high with respect to the prediction. An excess with respect to the theoretical prediction was also observed in the 7 TeV analysis, and is seen in other diboson analysis by both the ATLAS and CMS collaborations.

Contour plots showing the 1 and 2-σ confidence levels on the various measured cross sections are shown in Figs. 7.12 to 7.19 The measured cross sections in the $\ell^-\ell^+\nu\bar{\nu}$ sub-channels is high with respect to the theoretical prediction, but the discrepancy is within 1.3 to 1.5 standard deviations when considering the difference in the central values divided by the quadrature sum of the uncertainties for prediction and measurement.

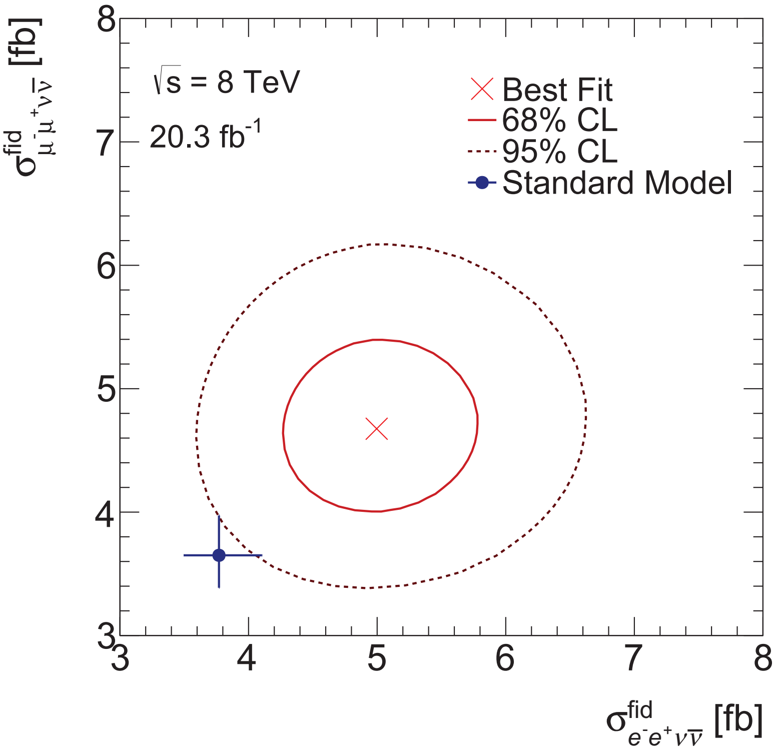

Fig. 7.12 The 1 and 2σ contours as a result of the simultaneous fit to both the $ZZ \to e^-e^+\nu\bar{\nu}$ and $ZZ \to \mu^-\mu^+\nu\bar{\nu}$ sub-channels, and theoretical prediction for the fiducial cross section. The Standard Model prediction is taken from POWHEGBOX and gg2VV with electroweak corrections applied. The errors are taken from Table 7.2.

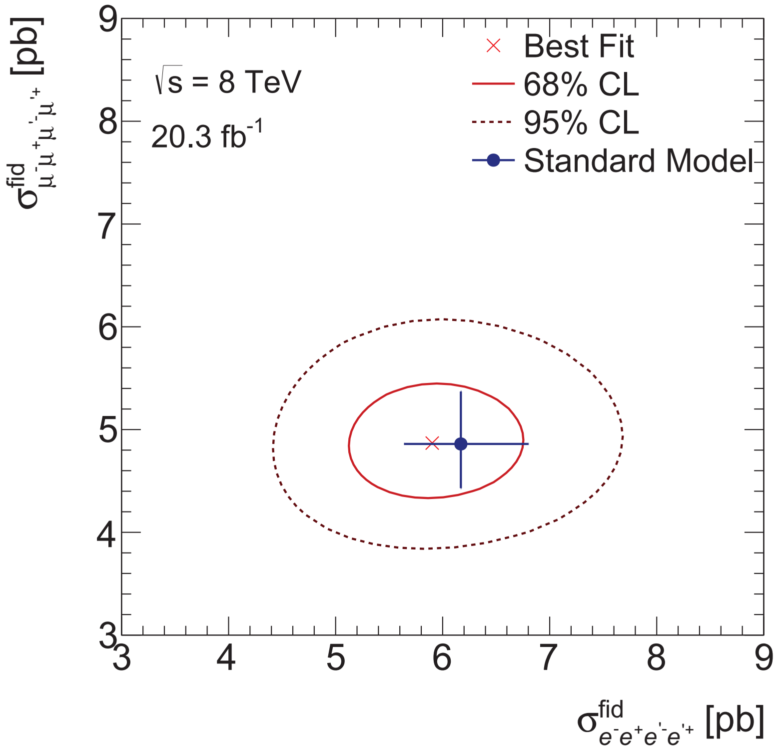

Fig. 7.13 The 1 and 2σ contours and theoretical prediction for the fiducial cross seciton in the $ZZ \rightarrow e^-e^+e^-e^+$and $ZZ \rightarrow \mu^-\mu^+\mu^-\mu^+$sub-channels. The Standard Model prediction is taken from POWHEGBOX and gg2VV with electroweak corrections applied (Table 7.3).

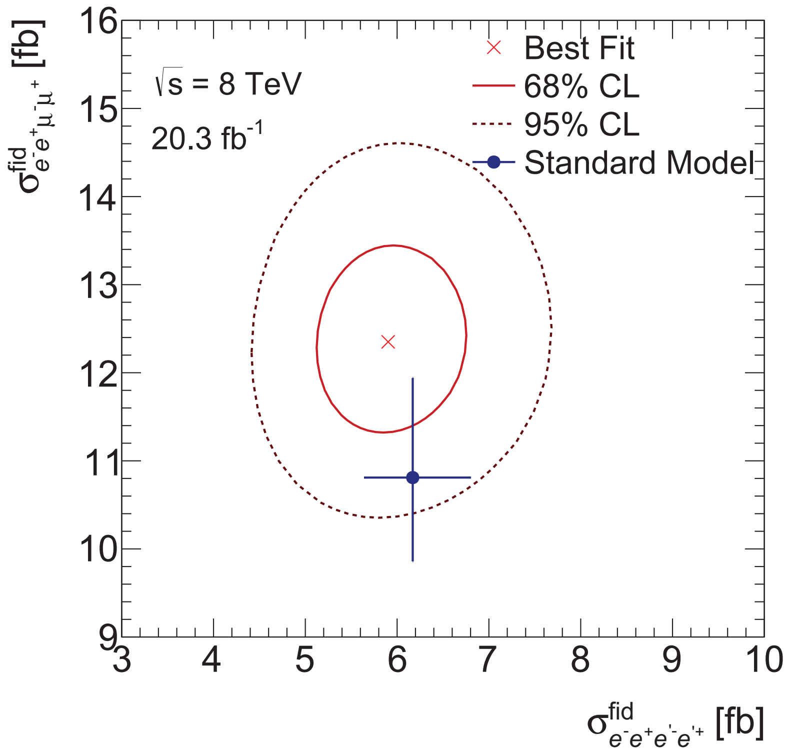

Fig. 7.14 The 1 and 2σ contours and theoretical prediction for the fiducial cross seciton in the $ZZ \to e^-e^+e^-e^+$ and $ZZ \to e^-e^+\mu^-\mu^+$ sub-channels. The Standard Model prediction is taken from POWHEGBOX and gg2VV with electroweak corrections applied.

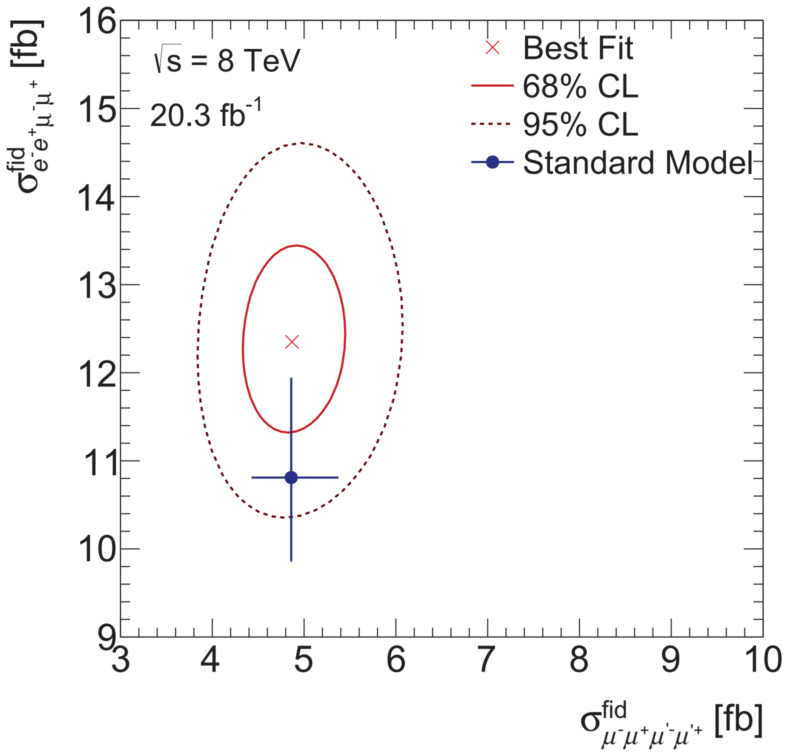

Fig. 7.15 The 1 and 2σ contours and theoretical prediction for the fiducial cross section in the $ZZ \to \mu^-\mu^+\mu^-\mu^+$and $ZZ \to e^-e^+\mu^-\mu^+$sub-channel. The Standard Model prediction is taken from POWHEGBOX and gg2VV with electroweak corrections applied.

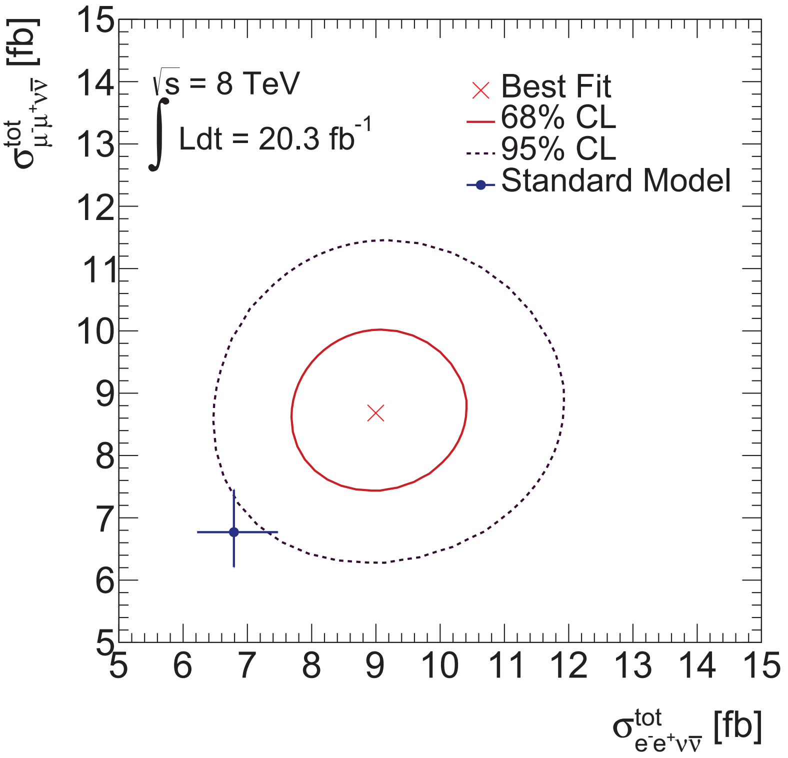

Fig. 7.16 The 1 and 2σ contours and theoretical prediction for the total cross section in the $ZZ \rightarrow e^-e^+\nu\bar{\nu}$ and $ZZ \rightarrow \mu^-\mu^+\nu\bar{\nu}$ sub-channels. The Standard Model prediction is taken from POWHEGBOX and gg2VV with electroweak corrections applied (Table 7.5).

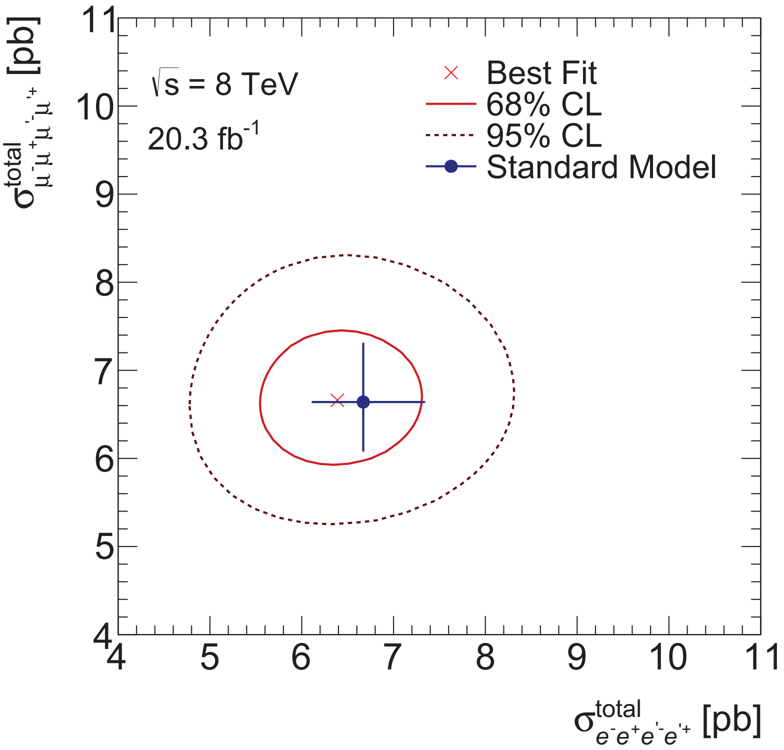

Fig. 7.17 The 1 and 2σ contours and theoretical prediction for the total cross section in the $ZZ \to e^-e^+e^-e^+$ and $ZZ \to \mu^-\mu^+\mu^-\mu^+$ sub-channels. The Standard Model prediction is taken from POWHEGBOX and gg2VV with electroweak corrections applied (Table 7.5).

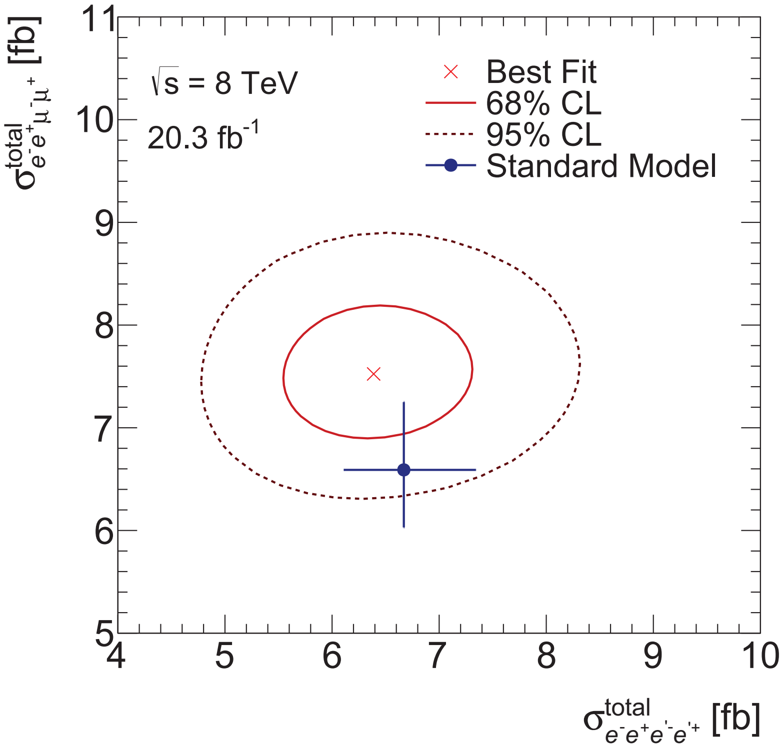

Fig. 7.18 The 1 and 2σ contours and theoretical prediction for the total cross section in the $ZZ \to e^-e^+e^-e^+$ and $ZZ \to e^-e^+\mu^-\mu^+$ sub-channels. The Standard Model prediction is taken from POWHEGBOX and gg2VV with electroweak corrections applied (Table 7.5).

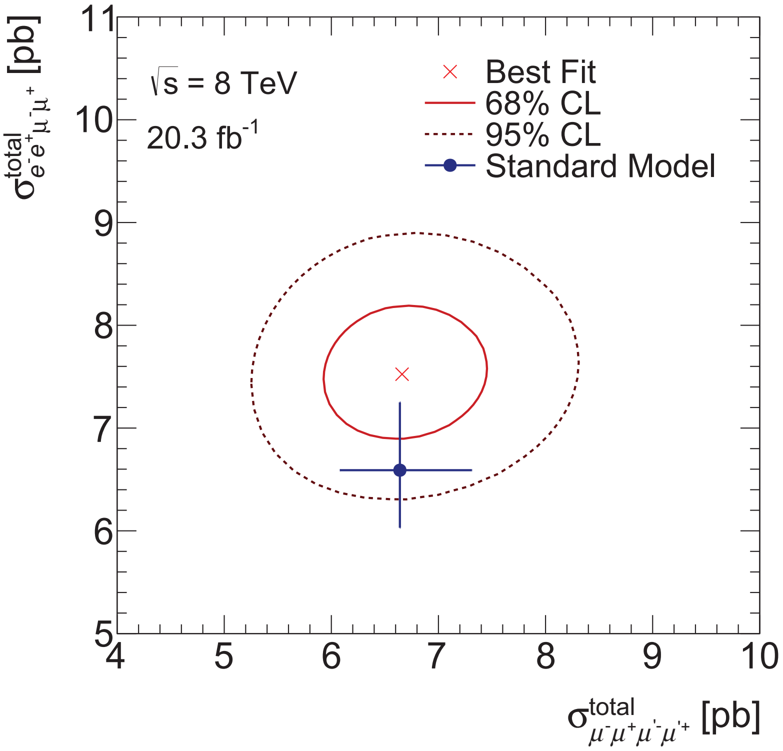

Fig. 7.19 The 1 and 2σ contours and theoretical prediction for the total cross section in the $ZZ \to \mu^-\mu^+\mu^-\mu^+$and $ZZ \to e^-e^+\mu^-\mu^+$sub-channels. The Standard Model prediction is taken from POWHEGBOX and gg2VV with electroweak corrections applied (Table 7.5).

7.6 A scale factor correction to the jet veto efficiency

In the ATLAS Standard Model WW [204] and ZZ [77] analyses at 7 TeV an overall factor was applied to the efficiency of the jet veto requirement to enhance the agreement between data and simulation, and to reduce experimental uncertainties associated with jets such as jet energy scale and jet energy resolution. However, the impact on the cross section and the resulting reduction in systematic uncertainties were not thoroughly studied. This section presents a study on the impact of applying such a scale factor on the jet veto to the fiducial efficiency correction C_{ZZ} in the $ZZ \to \ell^-\ell^+\nu\bar{\nu}$ sub-channels.

This scale factor, referred to as the "jet veto scale factor", is applied to C_{ZZ} after all selection cuts, and is derived by using single Z-boson data and single Z simulated MC samples. The correction is measured as the ratio of the jet veto efficiency in data with respect to the jet veto efficiency in simulation, $\varepsilon_{Data}/\varepsilon_{MC}$. Each efficiency is calculated as the ratio of the number of events with zero jets to the number of events with zero or more jets,

$$\varepsilon = \frac{N_{0\ \mathrm{jet}}}{N_{\geq\ 0\ \mathrm{jet}}}\,. \tag{7.19}$$

Event selection begins similarly to the ZZ selection, by pairing opposite-sign, same-flavour, trigger-matched leptons to form Z bosons separately in the electron muon channels. The Z bosons are required to have a mass within 15 GeV of the PDG value of the Z -boson mass. The cuts are applied in the same manner as the ZZ selection, except the axial-$E_{\mathrm{T}}^{\mathrm{miss}}$, p_{T}-balance cut, and third-lepton veto, are not applied so as to not select ZZ events. No background subtraction is performed to the selected Z events, as contamination was found to be less than 1%.

Table 7.16 shows the relative fractions of events before and after the jet veto is applied in data and in the nominal (inclusive) single Z sample. The nominal jet veto scale factors in the ee and $\mu\mu$ channels are shown with their statistical uncertainty in Table 7.16.

Channel	Sample	$\varepsilon = N_{0\ \mathrm{jet}}/N_{\geq 0\ \mathrm{jet}}$	Scale Factor = $\varepsilon_{\mathrm{Data}}/\varepsilon_{\mathrm{MC}}$
ee	Data	0.7701 ± 0.0001	0.9874 ± 0.0010
	MC	0.7799 ± 0.0008	
$\mu\mu$	Data	0.7686 ± 0.0002	0.9916 ± 0.0003
	MC	0.7751 ± 0.0002	

Table 7.16 The jet veto acceptances for Z data and MC samples, and the corresponding scale factors for the ee and $\mu\mu$ channels. The uncertainties shown are statistical only.

The Z boson data provides an effective calibration of the jet energy scale, and its veto acceptance receives only small uncertainties from statistics and potential background. As single Z data and MC are used to calculate a correction, both theoretical and experimental uncertainties appear in the jet veto scale factor, several of which are correlated with the theoretical uncertainties that appear in the acceptance and correction factors A_{ZZ} and C_{ZZ} for ZZ events. The purpose of the correction factor for the jet veto is to correct a particular generator (in this case POWHEGBOX) to data, therefore the theoretical uncertainties in the jet veto scale factor were evaluated using the Z events produced by the same generator.

To determine the uncertainty due to lepton reconstruction and identification, jet resolution and scale, as well as other sources of reconstruction-level uncertainty, the jet veto efficiencies are calculated by increasing or decreasing by $\pm 1\sigma$ the various components of the reconstruction systematics individually. The effects on the jet veto efficiencies and scale factors, as well as the differences with respect to the nominal jet veto scale factor (Table 7.16) are shown in Table 7.17. The reconstruction and identification systematics for the jet veto scale factor are on the percent-level in both the ee and $\mu\mu$ channels. Electron-reconstruction and identification systematics do not have a large effect on the jet veto scale factor in the $\mu\mu$ channel and conversely, muon reconstruction and identification related systematics do not affect the scale factor in the ee channel.

Theoretical uncertainties arise from the fact that a fixed-order perturbation series is used for the cross section calculation. While measuring cross sections in exclusive jet bins is done with the goal of enhancing signal significance, the application of jet vetoes introduces theoretical uncertainties; the uncertainty in the exclusive cross section is larger than that in the corresponding inclusive one due to the more complicated structure of the perturbative series which describes the exclusive cross section. Varying the factorisation and renormalisation scales allows one to get a handle on the size of the missing higher-order terms caused by the imposition of a cut on a kinematic variable which is used to separate jet bin boundaries provided the contribution of the higher order terms is not large (50% or greater) relative to the lower order terms. If the uncertainties in inclusive jet-binned cross sections are assumed to be uncorrelated, the theoretical scale uncertainty due to QCD scale choice in jet veto acceptance may be obtained using the Stewart-Tackmann (ST) method [214]. The jet veto acceptance can be written in terms of its inclusive 0 and 1-jet components as

$$\varepsilon = 1 - \frac{\sigma_{\geq 1\mathrm{jet}}}{\sigma_{\geq 0\mathrm{jet}}}. \tag{7.20}$$

Uncertainty on jet veto scale factor	*ee*	$\mu\mu$
electron energy resolution	$\pm 0.01\%$	-
electron energy scale	$^{-0.03\%}_{+0.03\%}$	-
electron identification efficiency	-	-
electron isolation	$^{+0.05\%}_{-0.05\%}$	-
electron reconstruction efficiency	$^{+0.02\%}_{-0.02\%}$	-
muon momentum resolution	-	-
muon momentum scale	-	-
muon reconstruction	-	-
muon identification	-	-
muon isolation	-	$^{+0.14\%}_{-0.14\%}$
jet energy scale	$^{-2.7\%}_{+2.4\%}$	$^{-3.19\%}_{-2.66\%}$
jet energy resolution	± 1.9 %	$^{+2.34\%}_{-2.35\%}$
jet vertex fraction	$^{+0.2\%}_{-0.15\%}$	$^{+0.19\%}_{-0.19\%}$
$E_{\mathrm{T}}^{\mathrm{miss}}$ scale soft terms	-	-
$E_{\mathrm{T}}^{\mathrm{miss}}$ resolution soft terms	-	-
trigger	-	-

Table 7.17 Reconstruction, identification, and jet uncertainties on the jet veto scale factor in the *ee* and $\mu\mu$ channels as calculated from single *Z* simulated samples. The differences are with respect to the nominal jet veto scale factor. Dashes indicate less than 0.01% change for a particular uncertainty.

By simple error propagation, the uncertainty in the jet veto acceptance due to QCD scale should be calculated according to

$$\left(\frac{\delta\varepsilon}{\varepsilon}\right)^2 = \left(\frac{1-\varepsilon}{\varepsilon}\right)^2 \left(\frac{\delta^2\sigma_{\geq 0 jet}}{\sigma^2_{\geq 0 jet}} + \frac{\delta^2\sigma_{\geq 1 jet}}{\sigma^2_{\geq 1 jet}}\right). \tag{7.21}$$

The effect of the varied renormalisation and factorisation scales was studied using truth samples. Both inclusive Z and ZZ samples were generated with POWHEGBOX and showered with PYTHIA for nine different configurations (including the nominal[3]) within the limits[4]

$$\frac{1}{4} \leq \frac{\mu_F}{\mu_R} \leq 4.$$

The relevant selection was applied to the Z and ZZ samples at particle-level and the inclusive 0 and 1-jet cross sections as well as the jet veto efficiencies were calculated.

In order to measure the uncertainty in the jet veto scale factor due to choice of PDF, the nominal MC samples samples (the default PDF set for the POWHEGBOX single Z samples is CT10) were varied within their uncertainties. The results are given in Table 7.22.

	ee	$\mu\mu$
PDF uncertainty on jet veto SF	$^{+0.14\%}_{-0.11\%}$	$^{+0.14\%}_{-0.10\%}$

Table 7.22 The changes in the jet veto acceptances and corresponding scale factors obtained by varying the CT10 PDF set within its uncertainties. The differences are with respect to the nominal jet veto scale factor in the respective channels.

The scale factor associated with the jet veto is motivated by using single Z events to reduce the reconstruction and theoretical uncertainties on derived quantities such as the correction C_{ZZ}. This can be seen as a cancellation effect in the product of the efficiency correction factor C_{ZZ} and the jet-veto scale factor. The uncertainty on the efficiency correction is generally reduced when multiplied by the jet veto scale factor. Table 7.23 shows the value of C_{ZZ} in the ee and $\mu\mu$ sub-channels. For the statistical model used to extract the cross

---

[3] For POWHEGBOX, the default renormalisation and factorisation scale are set to a dynamic scale, m_{ZZ} for ZZ production, while a fixed scale of m_Z is used for single Z production.

[4] If the higher-order corrections to the $q\bar{q}$ contribution to the cross section are small, the variations in the factorisation and renormalisation scale should be sufficient to cover the theoretical uncertainty due to QCD scale when using a fixed-order calculation as the baseline. The choice to vary the scales individually and simultaneously by a factor two is conventional, and is generally accepted between theorists and experimentalists as a way to obtain a sensible estimate of the QCD scale uncertainty.

Variation							
μ_R	μ_F	$\sigma^Z_{\geq 0 jet}$ [pb]	$\delta\sigma^Z_{\geq 0 jet}$ [%]	$\sigma^Z_{\geq 1 jet}$ [pb]	$\delta\sigma^Z_{\geq 1 jet}$ [%]	ε^Z	$\delta\varepsilon^Z$ [%]
$\mu_0 = m_Z$	$\mu_0 = m_Z$	451.90	-	74.95	-	0.8341	-
μ_0	$\frac{\mu_0}{2}$	435.87	-3.54	71.91	-4.06	0.8350	1.06
μ_0	$2\mu_0$	446.44	-1.20	73.95	-1.33	0.8343	0.35
$\frac{\mu_0}{2}$	μ_0	426.89	-5.53	70.34	-6.15	0.8352	1.63
μ_0	$2\mu_0$	462.38	2.31	76.62	2.23	0.8343	0.63
$2\mu_0$	$2\mu_0$	468.52	3.67	77.61	3.55	0.8343	1.01
$\frac{\mu_0}{2}$	$\frac{\mu_0}{2}$	459.14	1.60	76.23	1.71	0.8340	0.46
$2\mu_0$	$\frac{\mu_0}{2}$	459.82	1.75	75.85	1.19	0.8350	0.41
$\frac{\mu_0}{2}$	$2\mu_0$	445.08	-1.51	73.54	-1.87	0.8348	0.47

Table 7.18 The effect of variations in the renormalisation and factorisation scale in the inclusive jet cross sections in $Z \rightarrow ee$ events generated with POWHEGBOX at particle-level. The variation in jet veto efficiency is calculated according to equation Eq. (7.21).

Variation							
μ_R	μ_F	$\sigma^Z_{\geq 0\text{jet}}$ [pb]	$\delta\sigma^Z_{\geq 0\text{jet}}$ [%]	$\sigma^Z_{\geq 1\text{jet}}$ [pb]	$\delta\sigma^Z_{\geq 1\text{jet}}$ [%]	ε^Z	$\delta\varepsilon^Z$ [%]
$\mu_0 = m_Z$	$\mu_0 = m_Z$	452.30	-	78.559		0.8263	
μ_0	$\frac{\mu_0}{2}$	435.84	-3.63	75.259	-4.201	0.8273	1.16
μ_0	$2\mu_0$	446.40	-1.30	77.504	-1.343	0.8264	0.39
$\frac{\mu_0}{2}$	μ_0	427.24	-5.53	74.026	-5.770	0.8267	1.67
μ_0	$2\mu_0$	462.87	2.33	80.176	2.058	0.8268	0.65
$2\mu_0$	$2\mu_0$	468.60	3.60	81.267	3.447	0.8266	1.04
$\frac{\mu_0}{2}$	$\frac{\mu_0}{2}$	458.95	1.47	79.800	1.579	0.8261	0.45
$2\mu_0$	$\frac{\mu_0}{2}$	460.20	1.74	79.554	1.267	0.8271	0.45
$\frac{\mu_0}{2}$	$2\mu_0$	445.86	-1.42	77.139	-1.807	0.8270	0.48

Table 7.19 The effect of variations in the renormalisation and factorisation scale in the inclusive jet cross sections in $Z \to \mu\mu$ events generated with POWHEGBOX at particle-level. The variation in jet veto efficiency is calculated according to equation 7.21.

section, uncertainties which appear in both the correction factor and the jet veto scale factor are taken as fully correlated or anti-correlated depending upon the direction of change under a given variation.

Table 7.23 shows approximately a 1% reduction in the central value for both the *ee* and $\mu\mu$ channels. While the jet veto scale factor is only applied to the $q\bar{q}$ component, the gluon-gluon contribution is small enough such that a scale factor of 98 to 99 % translates directly to a 1% shift in the overall value. A reduction in the jet related uncertainties (jet energy scale, jet energy resolution and jet vertex fraction) is observed on applying the scale factor when comparing the values from Table 7.6. As the jet veto scale factor introduces a shift on the central value of C_{ZZ} by about 1%, this translates directly to a shift in the central value of the cross sections measured in the $ZZ \to e^-e^+\nu\bar{\nu}$ and $ZZ \to \mu^-\mu^+\nu\bar{\nu}$ sub-channels. The resulting reduction in uncertainties also translates to a reduction in the uncertainties in the cross section. When using the jet veto scale factor, the method is essentially the same as given in Section 7.5.1, only C_{ZZ} for a given sub-channel in section model is modified to

$$C_{ZZ} = SF_{\text{jet veto}} \cdot C_{q\bar{q}\to ZZ} + C_{gg\to ZZ} \,. \tag{7.22}$$

Cross section measurements with the jet veto scale factor applied to C_{ZZ} in the $e^-e^+\nu\bar{\nu}$ and $\mu^-\mu^+\nu\bar{\nu}$ sub-channels are given in Tables 7.24 to 7.26. The systematic uncertainties for the fiducial cross sections are reduced by up to 30% in both channels, although because the value of C_{ZZ} is reduced, the central values of the cross sections are increased as expected (Eq. (7.9)). The corresponding shift in central value from the nominal value is comparable to the reduction in systematic uncertainties obtained by applying the jet veto scale factor to C_{ZZ}. Full breakdowns of systematic uncertainties are given in Chapter B.

Channel	Fiducial cross section [fb]
$e^-e^+\nu\bar{\nu}$	$5.07\,^{+0.77}_{-0.72}$ (stat) $^{+0.32}_{-0.28}$ (syst) $^{+0.20}_{-0.16}$ (lumi)
$\mu^-\mu^+\nu\bar{\nu}$	$4.72\,^{+0.70}_{-0.66}$ (stat) $^{+0.32}_{-0.26}$ (syst) $^{+0.19}_{-0.15}$ (lumi)

Table 7.24 Measured fiducial cross sections for the $ZZ \to e^-e^+\nu\bar{\nu}$ and $ZZ \to \mu^-\mu^+\nu\bar{\nu}$ sub-channels with the $q\bar{q}$ component of C_{ZZ} multiplied by the jet veto scale factor.

	C^{ee}_{ZZ} with jet veto SF	$C^{\mu\mu}_{ZZ}$ with jet veto SF
C_{ZZ}	0.6693	0.7461
statistical uncertainty	$\pm 2.1\%$	$\pm 2.1\%$
electron identification	$\pm 1.6\%$	-
electron isolation	$\pm 0.3\%$	-
electron reconstruction	$\pm 0.7\%$	-
electron energy resolution	$^{+0.1\%}_{-0.0\%}$	-
electron energy scale	$^{+1.62\%}_{-1.93\%}$	-
muon momentum resolution	-	$^{-0.2\%}_{-0.1\%}$
muon momentum scale	-	$^{+0.1\%}_{-0.2\%}$
muon reconstruction efficiency	-	$^{+0.7\%}_{-0.7\%}$
muon identification effieicney	-	$^{-0.1\%}_{-0.2\%}$
muon isolation	-	$^{+3.2\%}_{-3.2\%}$
jet energy scale	$^{+2.0\%}_{-1.0\%}$	$^{+1.1\%}_{-1.3\%}$
jet energy resolution	$^{+0.4\%}_{-0.4\%}$	$^{-0.4\%}_{+0.4\%}$
jet vertex fraction	$^{+0.1\%}_{-0.1\%}$	$^{+0.2\%}_{+0.1\%}$
$E_{\mathrm{T}}^{\mathrm{miss}}$ resolution (soft terms)	$^{+0.1\%}_{-0.1\%}$	$^{-0.4\%}_{+0.4\%}$
$E_{\mathrm{T}}^{\mathrm{miss}}$ scale (soft terms)	$^{-0.8\%}_{+1.6\%}$	$^{-1.1\%}_{+0.5\%}$
trigger	$\pm 0.1\%$	$\pm 0.5\%$
electroweak corrections	$\pm 0.3\%$	± 0.4
MC generator difference	$\mp 0.9\%$	$\mp 2.2\%$
PDF	$\pm 0.2\%$	$\pm 0.3\%$
$\Delta C_{ZZ}/C_{ZZ}$	$^{+4.15\%}_{-3.67\%}$	$^{+4.35\%}_{-4.54\%}$

Table 7.23 Calculated values for C_{ZZ} and the resulting uncertainties with the $q\bar{q}$ component multiplied by the jet veto scale factor.

Channel	Total cross section [pb]
$e^-e^+\nu\bar{\nu}$	$9.14\ ^{+1.39}_{-1.30}$ (stat) $^{+0.77}_{-0.64}$ (syst) $^{+0.36}_{-0.28}$ (lumi)
$\mu^-\mu^+\nu\bar{\nu}$	$8.77\ ^{+1.31}_{-1.22}$ (stat) $^{+0.74}_{-0.58}$ (syst) $^{+0.35}_{-0.28}$ (lumi)

Table 7.25 Measured total cross sections for the $ZZ \rightarrow e^-e^+\nu\bar{\nu}$ and $ZZ \rightarrow \mu^-\mu^+\nu\bar{\nu}$ sub-channels with the $q\bar{q}$ component of C_{ZZ} multiplied by the jet veto scale factor.

channel	Total cross section [pb]
All channels	$7.36\ ^{+0.39}_{-0.38}$ (stat) $^{+0.27}_{-0.25}$ (syst) $^{+0.23}_{-0.21}$ (lumi)

Table 7.26 The total cross section for all *ZZ* channels combined with the jet veto scale factor applied to the respective $q\bar{q}$ components of C_{ZZ} for the $e^-e^+\nu\bar{\nu}$ and $\mu^-\mu^+\nu\bar{\nu}$ sub-channels.

7.7 Conclusions and discussion

This chapter presented theoretical predictions of the *ZZ* cross section in the fiducial volume defined in Section 7.1 and the extrapolated cross section in the mass range $66 < m_{\ell^-\ell^+} < 116$ GeV. The efficiency correction C_{ZZ} necessary for measurement of a fiducial cross section and the acceptance A_{ZZ} were defined and calculated with full systematic uncertainties for both the $ZZ \rightarrow \ell^-\ell^+\nu\bar{\nu}$ and $ZZ \rightarrow \ell^-\ell^+\ell^-\ell^+$ decay channels. The statistical model used for the cross section based on the maximum likelihood method was also discussed and the combination method for the combined cross section was explained. The cross sections stand in reasonable agreement compared with the Standard Model prediction, although the cross sections in the $ZZ \rightarrow \ell^-\ell^+\nu\bar{\nu}$ sub-channels are consistently high with respect to the theoretical prediction. The $ZZ \rightarrow \ell^-\ell^+\ell^-\ell^+$ cross sections show better agreement with the NLO $q\bar{q}$+ LO gg prediction. The application of a correction to model the jet veto efficiency in simulation and reduce theoretical systematic uncertainties was explored. It was shown that the correction factor introduces roughly 1% reduction the value of C_{ZZ} which translates directly into a higher measured cross section. The reduction of jet-related uncertainties is on the order of the shift introduced to the central value compared to the nominal value of the cross section with no such correction applied.

The measured cross sections given in Section 7.5.2 are high compared to the Standard Model prediction taken from POWHEGBOX and gg2VV. Both ATLAS and CMS have measured ZZ cross sections that are higher than the Standard Model prediction. It is worth noting that the agreement in the $ZZ \to \ell^-\ell^+\ell^-\ell^+$ channels is better than that in the $ZZ \to \ell^-\ell^+\nu\bar{\nu}$ sub-channels. This could be due to the selection placed in the $ZZ \to \ell^-\ell^+\nu\bar{\nu}$ analysis, in particular the requirement of the jet veto. Another explanation is that the contributions from higher order corrections to both the $q\bar{q}$ and gg processes would serve to increase the theoretical prediction. In the case of the Higgs production, the NLO gg contributions are very large. The higher-order electroweak corrections serve to systematically drive down the expected yield, but it is has been shown that higher-order QCD corrections would serve to enhance the cross section [207, 215]. The observation of excess has not gone unnoticed; several explanations for the source of the excess [216, 217] in the WW channel have already been proposed. The imposition of jet vetoes to enhance signal-to-background also poses a difficulty, as many of the calculations for higher order QCD corrections are for inclusive cross sections, not exclusive jet-binned cross sections. While the excess has caused some in the particle physics community to view diboson physics as one possible source for potential of observation of beyond Standard Model physics, theoretical calculations at NNLO and higher orders must be completed for more accurate predictions. As the LHC continues to collect large amounts of integrated luminosity during its second run, the ZZ measurement will at some point no longer be dominated by statistical uncertainties, allowing more precise measurements to be made. The Standard Model has done a phenomenal job of holding up to very stringent tests, it remains to be seen if it will continue to hold up through the next few decades, or if some new physics will be discovered.

Chapter 8

Limits on anomalous triple gauge couplings

The lack of large excesses in the measured cross sections of recent measurements by ATLAS and CMS, combined with previous limits on anomalous triple gauge couplings indicate that new physics effects, if indeed present, would have to be small, with couplings at most at the per-mille level. Limit setting is important to be able to rule out models which allow neutral ZZV couplings. This chapter discusses the limit setting procedure on neutral ZZV anomalous triple gauge couplings, including parametrisation of the signal yield, matrix element reweighting, and the statistical procedure used to set 95% confidence limits on the values of the couplings, and presents the results derived from the $ZZ \to \ell^- \ell^+ \nu \bar{\nu}$ data.

8.1 Parametrisation of the signal yield

One of the signatures of anomalous triple gauge couplings is an enhanced event yield at higher energies and at large scattering angles. Variables that are related to the invariant mass of the ZZ system provide sensitivity to the couplings. Kinematic variables that are particularly sensitive to neutral ZZV aTGCs are p_{T}^{Z} and $\Delta\phi\,(\ell^-, \ell^+)$. Limits from the first measurement of the ZZ production cross section by ATLAS [76] relied only on the cross section to set limits on anomalous couplings due to lack of statistics. However, a direct parametrisation of the signal yield in one or more variables allows a binned probability model in a particular kinematic variable to be used where the contributions in high p_{T} bins have higher statistical power for discovering or constraining new physics contributions. For the ATLAS analyses at 7 and 8 TeV kinematic spectra are parameterised in p_{T}^{Z} for the $ZZ \to \ell^- \ell^+ \nu \bar{\nu}$ channel. Standard Model and anomalous ZZ couplings are modelled using

SHERPA which has an implementation of the generic ZZV couplings [123] as described in Section 2.4.1. While additional anomalous couplings can contribute when the Z bosons are off-shell [67], these couplings are highly suppressed near the Z pole, and are not currently implemented in SHERPA. Simulated p_{T}^{Z} and $\Delta\phi\,(\ell^-,\ell^+)$ spectra for ZZ production with various combinations of anomalous aTGCs are shown in Fig. 8.1.

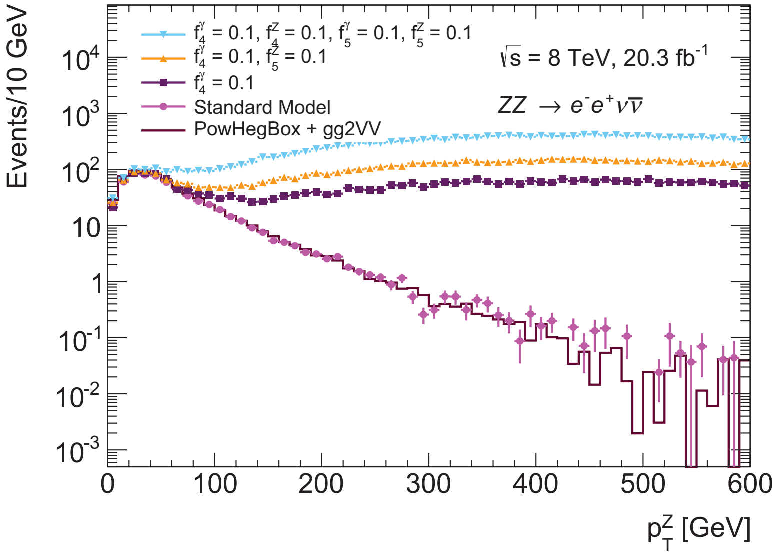

(a) The simulated p_{T}^{Z} spectrum in the $e^-e^+\nu\bar{\nu}$ sub-channel for ZZ production with various combinations of anomalous ZZV triple gauge couplings. The Standard Model prediction taken from the baseline POWHEGBOX +gg2VV samples is given in the solid line, and is compared to the SHERPA sample without contributions from anomalous couplings ($f_4^V = 0$ and $f_5^V = 0$). The other dotted are the spectra spectra with three different choices of anomalous coplings.

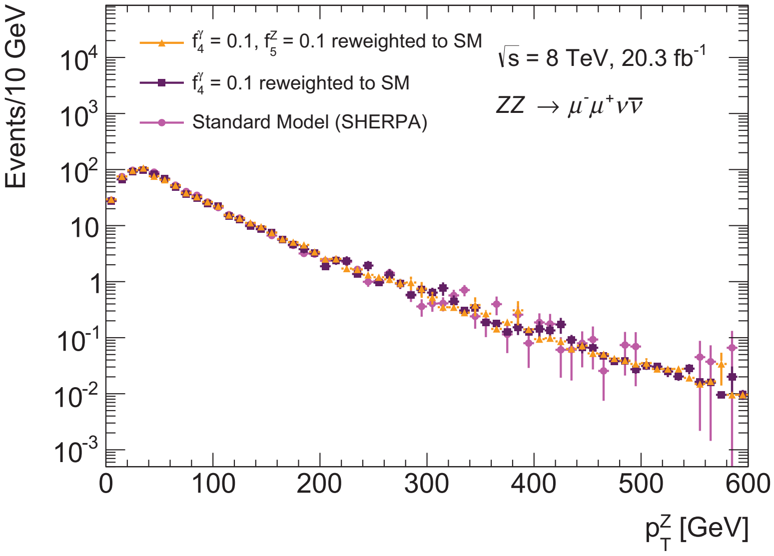

(b) The simulated $\Delta\phi\,(\ell^-,\ell^+)$ spectrum in the $e^-e^+\nu\bar{\nu}$ sub-channel for *ZZ* production with various combinations of anomalous *ZZV* triple gauge couplings. The Standard Model prediction taken from the baseline POWHEGBOX +gg2VV samples is given in the solid line, and is compared to the SHERPA sample without contributions from anomalous couplings ($f_4^V = 0$ and $f_5^V = 0$). The other dotted are the spectra spectra with three different choices of anomalous coplings.

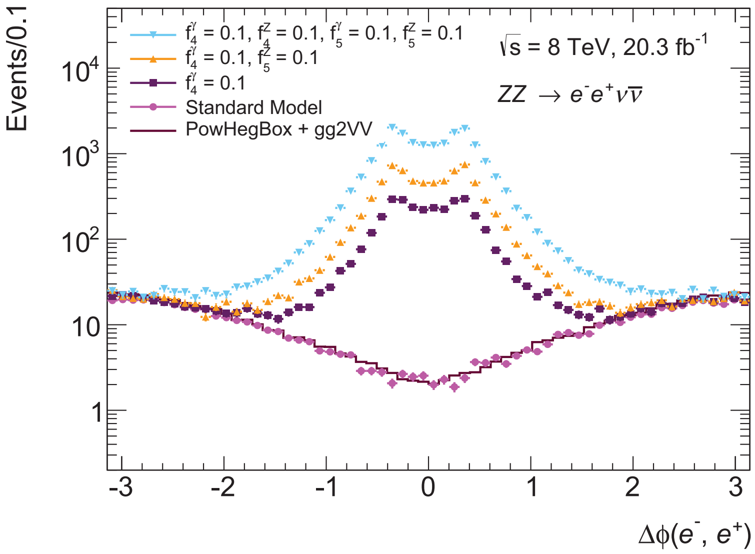

(c) The simulated $\Delta\phi\,(\ell^-,\ell^+)$ spectrum in the $\mu^-\mu^+\nu\bar{\nu}$ sub-channel for *ZZ* production with various combinations of anomalous *ZZV* triple gauge couplings. The Standard Model prediction taken from the baseline POWHEGBOX +gg2VV samples is given in the solid line, and is compared to the SHERPA sample without contributions from anomalous couplings ($f_4^V = 0$ and $f_5^V = 0$). The other dotted are the spectra spectra with three different choices of anomalous coplings.

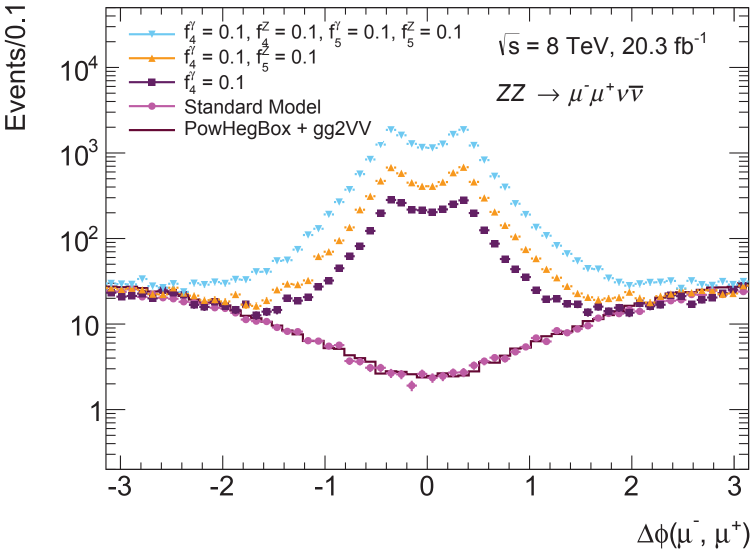

(d)

Fig. 8.1 The simulated p_{T}^{Z} and $\Delta\phi\,(\ell^-,\ell^+)$ spectra for ZZ production with various combinations of anomalous ZZV triple gauge couplings. The couplings are set to the values used to produce the SHERPA samples used to model ZZ production with anomalous couplings, which are larger than both the ATLAS and CMS limits at 7 TeV by roughly a factor of 10, but are shown here for effect. Spectra are compared to the baseline ZZ signal from POWHEGBOX and gg2VV used for the cross section prediction and signal modelling. The anomalous couplings enhance the event yield at high p_{T}^{Z} and enhance the spectrum at low values of $\Delta\phi\,(\ell^-,\ell^+)$.

8.1.1 Choice of unitarisation scheme

The issue of maintaining unitarity at high values of $\sqrt{s}$ within effective field theory was discussed in Section 2.4.1. One way to remedy this is to multiply the bare couplings by a form factor (Eq. (2.3)), which introduces scale dependence on the values of the couplings such that the scale of the new physics occurs at Λ_{FF} and at high partonic centre-of mass energies $\sqrt{\hat{s}}$, the values of the anomalous couplings approached zero such that the S-matrix is unitary. Previous limits on anomalous couplings set by the DØ collaboration (Section 2.4.1) were set in an effective field theory where the scale of new physics is set to $\Lambda_{\mathrm{FF}} = 3$ TeV. The limits presented in the ATLAS ZZ analysis at 7 TeV [77] were calculated in the case of a form factor scale of $\Lambda_{\mathrm{FF}} = 3$ TeV and with an infinite form factor scale $\Lambda_{\mathrm{FF}} = \infty$. The values obtained with the scale set to $\Lambda_{\mathrm{FF}} = 3$ TeV were about 1.5 times higher than those set with an infinite scale. The effects of the form factor scale serve to decrease sensitivity with respect to limit setting. A study done in the $ZZ \rightarrow \ell^-\ell^+\ell'^-\ell'^+$ decay channel showing ZZ aTGC limits as a function of the scale Λ_{FF} with 8 TeV data from ATLAS is described in [218].

The role of the unitarisation scheme has been a topic of active discussion among collaborations exploring new physics via aTGCs as to how to set the best limit that has a consistent physical interpretation. The effective lagrangian approach should be considered as a way to parametrize deviations from the Standard Model in a model independent expansion that complements direct searches. The issue of unitarisation concerns the validity of this expansion and it is relevant only in the case of non-observation (i.e. limit-setting) how far can this be extrapolated. The introduction of a regularization scheme such as form-factor or a cut, corresponds in effect to a limitation in the allowed range where one can parametrize deviations. This implies that experimental searches could potentially not use the full sensitivity of the data, including "non-observation" in high-p_{T} bins, rather a restriction is placed such that sensitivity exists in a specific range. Furthermore, the choice of form-factor reflects prior information put into the model and to a certain extent defies the "model-independent" effective lagrangian approach.

The results presented in the following sections use a form-factor scale of $\Lambda_{\mathrm{FF}} = \infty$ for aTGC sample generation, matrix element reweighting scheme and limit setting procedure. By using bare couplings, the analysis is free of (arbitrary) form factor assumptions, and therefore can provide the most stringent limits.

8.1.2 Matrix element reweighting

In order to set limits on anomalous triple-gauge couplings, the expected number of events after all selection must be parameterised as a function of the strength of the aTGC couplings. There are a few methods for obtaining these yields. One method would be to generate a grid of fully-simulated samples over a range of coupling values. However, generating enough fully-simulated events at each value of the coupling to apply a full event selection and still have sufficient statistics in the tails of the distributions proves to be very computationally intensive, and is highly impractical, given that there are four couplings to be tested. Another method involves a matrix element reweighting procedure to reweight (or rescale) a sample generated with one set of couplings to another based on a recalculation of the matrix element from the kinematics of the hard interaction on an event-by-event basis. In this way the full phase space dependence of the yield is accounted for. In order to perform reweighting in this way, one must have access to the matrix elements which produced the hard-scatter process which will give rise to the relevant events. The obvious advantage of this procedure is the ability to describe each point in phase space without the need for further interpolation between points. Using a fully-simulated sample as input to obtain the parametrisation allows the effects of detector reconstruction and identification efficiencies and detector acceptance to be modelled as well.

In the effective Lagrangian approach, new triple gauge-boson vertex operators are added linearly to the Standard Model and the strength of each new term is parameterised with a new TGC, f_i^V. As the terms are added linearly, the squared amplitude is a bilinear form that is a quadratic function of the f_i^V parameters. Once the coefficients of the second order polynomial are known, the dependence of the observable on the couplings is specified. In the case of two anomalous couplings, for instance, f_1 and f_2, an observable $\mathscr{O}$ that is proportional to the amplitude may be written as:

$$\begin{aligned}\mathscr{O} &= |M_0 + f_1 M_1 + f_2 M_2|^2 \\ &= M_0^2 + 2 f_1 M_0 M_1 + 2 f_2 M_0 M_2 + f_1^2 M_1^2 + 2 f_1 f_2 M_1 M_2 + f_2^2 M_2^2 \\ &= [1\ f_1\ f_2] \begin{bmatrix} M_0^2 & M_0 M_1 & M_0 M_2 \\ M_0 M_1 & M_1^2 & M_1 M_2 \\ M_0 M_2 & M_1 M_2 & M_2^2 \end{bmatrix} \begin{bmatrix} 1 \\ f_1 \\ f_2 \end{bmatrix} .\end{aligned} \tag{8.1}$$

Due to the quadratic dependence of the yield on the coupling and symmetric nature of the matrix element ($f_{ij} = f_{ji}$), one can write the square of the amplitude in an upper triangular form, as

$$\mathcal{O} = [1\ f_1\ f_2] \begin{bmatrix} F_{00} & F_{01} & F_{02} \\ 0 & F_{11} & F_{12} \\ 0 & 0 & F_{22} \end{bmatrix} \begin{bmatrix} 1 \\ f_1 \\ f_2 \end{bmatrix}, \tag{8.2}$$

where the factors of 2 have been absorbed into the F_{ij}. The F_{00} term is the SM contribution while the anomalous terms are represented by the higher-order F_{ij}.

To derive event weights, consider a simplified case with one non-zero anomalous coupling. In this case, there are three coefficients to be determined as can be seen from the expression for the differential cross section,

$$\mathrm{d}\sigma_{\mathrm{SM+aTGC}} = F_{00} + fF_{01} + f^2 F_{11}\,. \tag{8.3}$$

Using three different values of f, for instance $f_k = \{0, 1-1\}$, and three different values of the differential cross section, $d\sigma_k$, three independent equations can be established to solve for the values of F_i in matrix form:

$$\begin{pmatrix} \mathrm{d}\sigma_1 \\ \mathrm{d}\sigma_2 \\ \mathrm{d}\sigma_3 \end{pmatrix} = \begin{pmatrix} 1 & 0 & 0 \\ 1 & 1 & 1 \\ 1 & -1 & 1 \end{pmatrix} \begin{pmatrix} F_{00} \\ F_{01} \\ F_{11} \end{pmatrix}. \tag{8.4}$$

This expression can be simplified if the expression is expressed as

$$\mathbf{d}\boldsymbol{\sigma} = A\mathbf{F}, \tag{8.5}$$

where A is a matrix. The system of equations may be solved to give the F_{ij} coefficients provided that A is invertible. This is true if the coupling parameters are chosen such that the three equations are independent. Thus, for n aTGC's, there will be $(n+2)(n+1)/2$ independent coefficients to fully describe the bilinear form. The solution of Eq. (8.5) starts by using the event kinematics (the four-vectors of the final-state leptons) provided from the original generator that is used to produce the events (SHERPA in this instance). The four-vectors are put into the extracted matrix element and the cross section is evaluated $(n+2)(n+1)/2$ times for each event using different combinations of anomalous couplings to obtain the vector of differential cross sections $\mathbf{d}\boldsymbol{\sigma}$ each event. Once the matrix A is inverted and the cross sections are evaluated via the matrix elements, the coefficients F_{ij} are obtained by taking the matrix product of A^{-1} and $\mathbf{d}\boldsymbol{\sigma}$. When considering all four couplings f_i^V, the matrix A is 15×15, and both $\mathbf{d}\boldsymbol{\sigma}$ and $\mathbf{F}$ are column-vectors with 15 entries. In the case of four anomalous couplings, the differential cross section for a particular event given a particular choice of couplings can be expressed as

$$\begin{aligned}
\mathrm{d}\sigma_{\mathrm{SM+aTGC}}(f_4^\gamma, f_4^Z, f_5^\gamma, f_5^Z) = F_{00} &+ f_4^\gamma F_{01} + f_4^Z F_{02} + f_5^\gamma F_{03} + f_5^Z F_{04} \\
&+ \left(f_4^\gamma\right)^2 F_{11} + f_4^\gamma f_4^Z F_{12} + f_4^\gamma f_5^\gamma F_{13} + f_4^\gamma f_5^Z F_{14} \\
&+ \left(f_4^Z\right)^2 F_{22} + f_4^Z f_5^\gamma F_{23} + f_4^Z f_5^Z F_{24} \\
&+ \left(f_5^\gamma\right)^2 F_{33} + f_5^\gamma f_5^Z F_{34} \\
&+ \left(f_5^Z\right)^2 F_{44},
\end{aligned} \tag{8.6}$$

or in the matrix notation as

$$\mathrm{d}\sigma_{\mathrm{SM+aTGC}} = [1 f_4^\gamma \ f_4^Z \ f_5^\gamma \ f_5^Z] \begin{bmatrix} F_{00} & F_{01} & F_{02} & F_{03} & F_{04} \\ 0 & F_{11} & F_{12} & F_{13} & F_{14} \\ 0 & 0 & F_{22} & F_{23} & F_{24} \\ 0 & 0 & 0 & F_{33} & F_{34} \\ 0 & 0 & 0 & 0 & F_{44} \end{bmatrix} \begin{bmatrix} 1 \\ f_4^\gamma \\ f_4^Z \\ f_5^\gamma \\ f_5^Z \end{bmatrix}, \tag{8.7}$$

where again factors of two have been absorbed into the off-diagonal elements of F_{ij}. Using this expression, an event originating from one sample can be reweighted to an arbitrary aTGC point by assigning the weight

$$\begin{aligned}
w_{\mathrm{sm+aTGC}} &= \frac{\mathrm{d}\sigma_{\mathrm{SM+aTGC}}(f_4^\gamma, f_4^Z, f_5^\gamma, f_5^Z)}{\mathrm{d}\sigma_{\mathrm{ref}}}, \\
&= \frac{\sum_{i=0}^{n_{\mathrm{TGC}}} \sum_{j=0}^{n_{\mathrm{TGC}}} f_i f_j F_{ij}}{\mathrm{d}\sigma_{\mathrm{ref}}}.
\end{aligned} \tag{8.8}$$

where $\mathrm{d}\sigma_{\mathrm{ref}}$ is a “reference cross section” and denotes the differential cross section for the event at the point in aTGC space where it was originally generated under a set choice of couplings. This is essentially a normalisation constant ensuring that the leading-order term F_{00} is the Standard Model coefficient.

The framework used for the reweighting procedure is named “the AfterBurner” [219, 220]. As the name suggests, it allows derivation of aTGC weights since the weights are not evaluated during the event generation. The implementation of the reweighting is discussed in [221]. The Afterburner uses an extraction of matrix elements from the BHO (Baur, Han and Ohnemus) generator [222–224]. While the BHO generator produces events at NLO in QCD, the extraction only includes the leading-order and the QCD real emission diagrams, i.e. Born-level 2 → 2, and 2 → 5 processes (up to 1 jet), and does not include the QCD loop contributions. The original BHO code does not include aTGCs for ZZ production. ZZ

aTGCs were added to the AfterBurner through an extraction of the leading-order matrix elements from the Baur-Rainwater generator [69] which was interfaced with the existing BHO extraction.

The reweighting procedure can be easily extended to reweight a sample generated with a given set of aTGCs to any other set of aTGCs. The aTGC coefficients F_{ij} are completely specified by the kinematics of the ingoing and outgoing particles and therefore are unaffected by a change of anomalous coupling of the sample used to derive the weights. A recalculation of the coefficients F_{ij} for different anomalous couplings is therefore redundant; in principle, only one simulated sample is needed to fully describe all the aTGC dependence at every point in phase space, however, for purposes of validation of the matrix element reweighting technique, a small number of samples at different aTGC points is used for the signal yield parametrisation. A plot of samples generated with non-zero values of the aTGC couplings reweighted to the Standard Model is given in Fig. 8.2. As an event yield parametrisation in terms of the number of events is needed for the statistical model, the weights must be translated into an event yield of the expected number of events. The ZZ production cross section within a defined region of phase space is given in terms of the aTGC couplings by

$$\sigma_{\mathrm{SM+aTGC}}^{\mathrm{selected}} = \sigma_{\mathrm{ref}} \frac{\sum_{k=1}^{N_{\mathrm{selected}}} w_{\mathrm{SM+aTGC},\,k}}{N_{\mathrm{ref}}}, \tag{8.9}$$

where the sum of event weights is for events in the reference sample which pass all standard selection cuts. The expected number of events is obtained by scaling by the particular integrated luminosity, L, according to

$$N_{ZZ,\mathrm{SM+aTGC}} = L\sigma_{\mathrm{ref}} \frac{\sum_{k=1}^{N_{\mathrm{selected}}} w_{\mathrm{SM+aTGC},k}}{N_{\mathrm{ref}}}. \tag{8.10}$$

The selected events are weighted by all reconstruction/identification, trigger and event weights as with all other simulated samples used for signal and background modelling. One may define scaled yield coefficients N_{ij}, which express the contribution from a particular coupling in terms of events scaled to a particular reference cross section and luminosity as

$$N_{ij} = \frac{L\sigma_{\mathrm{ref}}}{N_{\mathrm{ref}}} \left(\frac{\sum_{k=1}^{N_{\mathrm{selected}}} F_{ij,k}}{\mathrm{d}\sigma_{\mathrm{ref}}} \right). \tag{8.11}$$

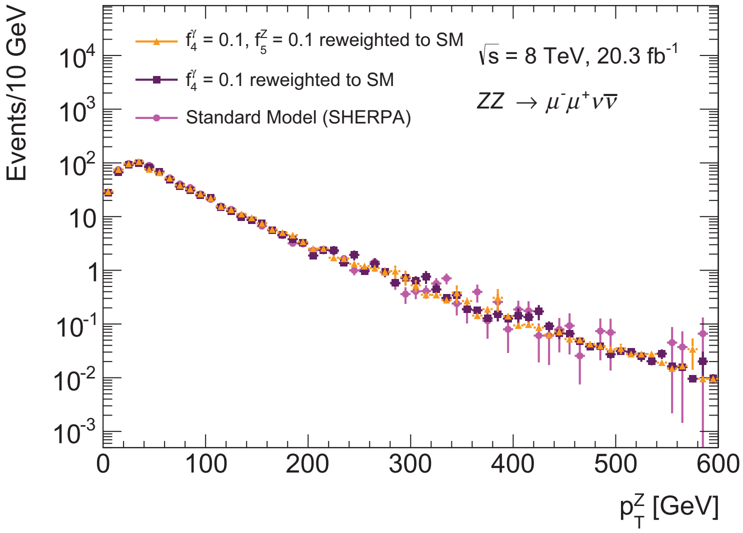

(a) The simulated p_{T}^{Z} spectrum in the $\mu^-\mu^+\nu\bar{\nu}$ sub-channel reweighted from a sample simulated with non-zero aTGC back to the Standard Model.

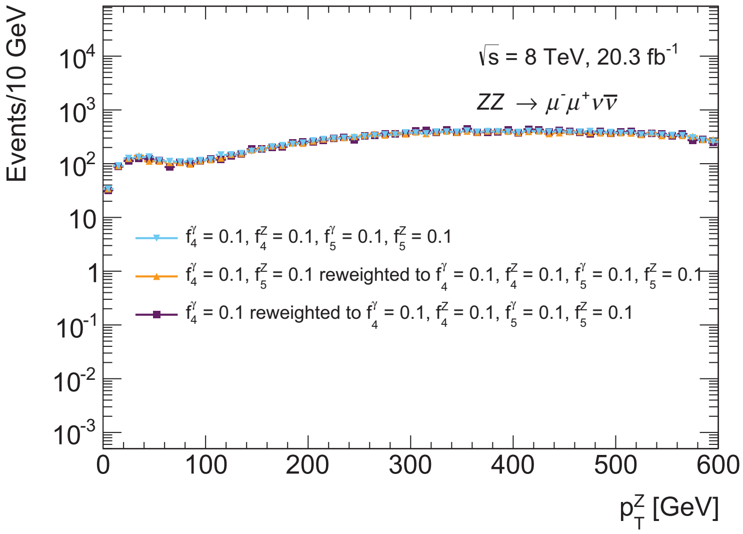

(b) The simulated p_{T}^{Z} spectrum in the $\mu^-\mu^+\nu\bar{\nu}$ sub-channel reweighted from one set of aTGC values to another.

Fig. 8.2 The simulated p_{T}^{Z} spectrum in the $\mu^-\mu^+\nu\bar{\nu}$ sub-channel reweighted between aTGC points. The Afterburner framework allows event weights to be determined after sample generation. In principle, only two different samples need to be generated to obtain weights necessary for a full signal yield parametrisation as a function of coupling strength, one Standard Model sample and one sample with one or more couplings with non-zero values. To validate the procedure, sample generated with a given configuration of aTGC parameters are reweighted (a) the Standard Model, and (b) another aTGC points.

One can then define an expected event yield as a function of the couplings analogously to the differential cross section given in Eq. (8.6) as

$$\begin{aligned} N_{ZZ,\mathrm{expected}}(f_4^\gamma, f_4^Z, f_5^\gamma, f_5^Z) = N_{00} &+ f_4^\gamma N_{01} + f_4^Z N_{02} + f_5^\gamma N_{03} + f_5^Z N_{04} \\ &+ \left(f_4^\gamma\right)^2 N_{11} + f_4^\gamma f_4^Z N_{12} + f_4^\gamma f_5^\gamma N_{13} + f_4^\gamma f_5^Z N_{14} \\ &+ \left(f_4^Z\right)^2 N_{22} + f_4^Z f_5^\gamma N_{23} + f_4^Z f_5^Z N_{24} \\ &+ \left(f_5^\gamma\right)^2 N_{33} + f_5^\gamma f_5^Z N_{34} \\ &\quad \left(f_5^Z\right)^2 N_{44} \,. \end{aligned} \tag{8.12}$$

The normalised yield coefficients are given as a function of the p_{T}^{Z} binning used for limit setting in Table 8.1.

Figures 8.3 and 8.4 shows total event yields as a function of coupling over a wide range of coupling values. Each curve assumes one coupling is non-zero while all other couplings are set to zero. The yield curves are symmetric with respect to the Standard Model values of zero due to the quadratic dependence of the yield on the couplings.

	p_{T}^{Z} Bin					
	60 – 100 GeV	100 – 150 GeV	150 – 210 GeV	210 – 270 GeV	270 – 350 GeV	> 350 GeV
N_{00}	$17.2 \pm 1.6^{+1.2}_{-0.8}$	$27.5 \pm 1.8^{+2.2}_{-1.4}$	$12.7 \pm 1.0^{+0.8}_{-0.8}$	$3.7 \pm 0.3^{+0.2}_{-0.2}$	$1.5 \pm 0.1^{+0.1}_{-0.1}$	$0.7 \pm 0.0^{+0.1}_{-0.1}$
N_{01}	$0.1 \pm 0.2^{+0.2}_{-0.5}$	$0.1 \pm 0.4^{+0.3}_{-0.3}$	$0.6 \pm 0.3^{+0.1}_{-0.3}$	$0.3 \pm 0.2^{+0.1}_{-0.2}$	$0.3 \pm 0.1^{+0.1}_{-0.0}$	$0.1 \pm 0.0^{+0.0}_{-0.0}$
N_{02}	$-0.2 \pm 0.4^{+0.5}_{-0.5}$	$-0.1 \pm 0.7^{+0.9}_{-1.0}$	$1.0 \pm 0.6^{+0.3}_{-0.8}$	$0.1 \pm 0.3^{+0.2}_{-0.2}$	$0.4 \pm 0.2^{+0.1}_{-0.1}$	$-0.0 \pm 0.1^{+0.0}_{-0.1}$
N_{03}	$-0.1 \pm 0.1^{+0.2}_{-0.1}$	$-0.2 \pm 0.2^{+0.3}_{-0.3}$	$-0.2 \pm 0.2^{+0.1}_{-0.0}$	$0.1 \pm 0.0^{+0.0}_{-0.0}$	$0.0 \pm 0.0^{+0.0}_{-0.0}$	$0.0 \pm 0.0^{+0.0}_{-0.0}$
N_{04}	$0.0 \pm 0.2^{+0.2}_{-0.1}$	$-0.4 \pm 0.4^{+0.6}_{-0.6}$	$-0.7 \pm 0.4^{+0.3}_{-0.1}$	$0.1 \pm 0.1^{+0.1}_{-0.1}$	$0.1 \pm 0.1^{+0.0}_{-0.1}$	$0.0 \pm 0.0^{+0.0}_{-0.0}$
N_{11}	$620 \pm 80^{+66}_{-70}$	$4460 \pm 250^{+300}_{-300}$	$9600 \pm 400^{+600}_{-700}$	$14000 \pm 500^{+800}_{-800}$	$24000 \pm 600^{+1500}_{-1400}$	$105000 \pm 1400^{+6700}_{-6000}$
N_{12}	$700 \pm 100^{+120}_{-140}$	$4300 \pm 300^{+300}_{-200}$	$9200 \pm 400^{+600}_{-600}$	$13000 \pm 500^{+650.0}_{-760}$	$22000 \pm 700^{+1500}_{-1400}$	$93000 \pm 1400^{+5900}_{-6000}$
N_{13}	$-0.0 \pm 0.0^{+0.0}_{-0.0}$	$0.0 \pm 0.2^{+0.0}_{-0.1}$	$0.1 \pm 0.2^{+0.1}_{-0.1}$	$-0.0 \pm 0.2^{+0.1}_{-0.1}$	$0.4 \pm 0.2^{+0.1}_{-0.2}$	$0.7 \pm 0.6^{+0.4}_{-0.4}$
N_{14}	$0.0 \pm 0.0^{+0.0}_{-0.0}$	$0.0 \pm 0.1^{+0.0}_{-0.0}$	$-0.0 \pm 0.1^{+0.1}_{-0.1}$	$-0.1 \pm 0.1^{+0.1}_{-0.1}$	$0.2 \pm 0.1^{+0.1}_{-0.2}$	$0.6 \pm 0.4^{+0.3}_{-0.3}$
N_{22}	$1150 \pm 180^{+220}_{-270}$	$6700 \pm 500^{+400}_{-300}$	$14400 \pm 740^{1000}_{-900}$	$19800 \pm 900^{+970}_{-1200}$	$33000.0 \pm 1200^{+2400}_{-2100}$	$141000 \pm 2400^{+8800}_{-9000}$
N_{23}	$-0.0 \pm 0.0^{+0.1}_{-0.0}$	$0.0 \pm 0.1^{+0.0}_{-0.1}$	$0.1 \pm 0.1^{+0.1}_{-0.1}$	$-0.2 \pm 0.1^{+0.1}_{-0.1}$	$0.2 \pm 0.1^{+0.1}_{-0.2}$	$0.6 \pm 0.4^{+0.3}_{-0.3}$
N_{24}	$0.0 \pm 0.0^{+0.1}_{-0.0}$	$0.1 \pm 0.2^{+0.1}_{-0.1}$	$0.2 \pm 0.3^{+0.2}_{-0.2}$	$-0.7 \pm 0.5^{+0.2}_{-0.2}$	$0.7 \pm 0.5^{+0.3}_{-0.8}$	$2.2 \pm 1.3^{+1.0}_{-0.9}$
N_{33}	$525 \pm 76^{+60}_{-67}$	$3900 \pm 230^{+280}_{-270}$	$8800 \pm 360^{+570}_{-610}$	$13100 \pm 460^{+750}_{-760}$	$23000 \pm 600^{+1500}_{-1400}$	$103000 \pm 1300^{+6600}_{-6800}$
N_{34}	$600 \pm 90^{+110}_{-130}$	$3800 \pm 250^{+250}_{-200}$	$8460 \pm 400^{+570}_{-540}$	$12100 \pm 490^{+620}_{-730}$	$20800 \pm 660^{+1480}_{-1300}$	$91600 \pm 1400^{+5800}_{-5900}$
N_{44}	$980 \pm 160^{+205}_{-250}$	$5900 \pm 440^{+380}_{-310}$	$13100 \pm 680^{+890}_{-820}$	$18600 \pm 850^{+900}_{-1100}$	$31600 \pm 1100^{+2350}_{-2000}$	$138000 \pm 2000^{+9000}_{-9000}$

Table 8.1 Yield coefficients for $ZZ \rightarrow e^{-}e^{+}\nu\bar{\nu}$ channel binned in p_{T}^{Z}. The first uncertainty is statistical, while the second is the quadrature sum of the luminosity uncertainty and all reconstruction uncertainties.

$\mu\mu$ channel	p_{T}^{Z} Bin					
	60 – 100 GeV	100 – 150 GeV	150 – 210 GeV	210 – 270 GeV	270 – 350 GeV	> 350 GeV
N_{00}	$18.6 \pm 1.7^{+1.4}_{-1.8}$	$30.7 \pm 1.9^{+1.8}_{-1.5}$	$12.2 \pm 0.9^{+1.5}_{-0.6}$	$3.5 \pm 0.3^{+0.2}_{-0.2}$	$1.5 \pm 0.1^{+0.1}_{-0.1}$	$0.7 \pm 0.0^{+0.1}_{-0.1}$
N_{01}	$0.6 \pm 0.3^{+0.1}_{-0.2}$	$0.9 \pm 0.7^{+0.3}_{-0.1}$	$0.5 \pm 0.4^{+0.1}_{-0.1}$	$0.1 \pm 0.2^{+0.1}_{-0.1}$	$0.2 \pm 0.1^{+0.0}_{-0.0}$	$0.1 \pm 0.1^{+0.0}_{-0.1}$
N_{02}	$0.7 \pm 0.4^{+0.2}_{-0.4}$	$-0.4 \pm 1.6^{+0.6}_{-0.6}$	$0.4 \pm 0.7^{+0.2}_{-0.1}$	$-0.1 \pm 0.6^{+0.1}_{-0.1}$	$0.1 \pm 0.1^{+0.1}_{-0.1}$	$-0.0 \pm 0.1^{+0.0}_{-0.1}$
N_{03}	$-0.1 \pm 0.1^{+0.1}_{-0.1}$	$0.1 \pm 0.2^{+0.1}_{-0.1}$	$0.1 \pm 0.2^{+0.1}_{-0.1}$	$-0.1 \pm 0.1^{+0.0}_{-0.0}$	$-0.0 \pm 0.0^{+0.0}_{-0.0}$	$0.0 \pm 0.0^{+0.0}_{-0.0}$
N_{04}	$0.1 \pm 0.2^{+0.1}_{-0.2}$	$0.4 \pm 0.5^{+0.5}_{-0.5}$	$0.3 \pm 0.3^{+0.2}_{-0.2}$	$-0.3 \pm 0.2^{+0.1}_{-0.1}$	$-0.0 \pm 0.1^{+0.0}_{-0.1}$	$0.0 \pm 0.0^{+0.0}_{-0.0}$
N_{11}	$980 \pm 113^{+67}_{-75}$	$5200 \pm 270^{+390}_{-280}$	$11200 \pm 430^{+930}_{-670}$	$14400 \pm 490^{+940}_{-900}$	$23500 \pm 640^{+1690}_{-1870}$	$93400 \pm 1300^{+7500}_{-7200}$
N_{12}	$820 \pm 95^{+40}_{-45}$	$4800 \pm 260^{+330}_{-300}$	$10400 \pm 450^{+980}_{-560}$	$13100 \pm 500^{+800}_{-800}$	$21400 \pm 680^{+1540}_{-1600}$	$85000 \pm 1400^{+6800}_{-6600}$
N_{13}	$-0.0 \pm 0.0^{+0.0}_{-0.0}$	$-0.0 \pm 0.0^{+0.0}_{-0.0}$	$-0.2 \pm 0.1^{+0.1}_{-0.0}$	$-0.5 \pm 0.2^{+0.3}_{-0.4}$	$-0.0 \pm 0.2^{+0.1}_{-0.2}$	$0.4 \pm 0.4^{+0.3}_{-0.3}$
N_{14}	$0.0 \pm 0.0^{+0.0}_{-0.0}$	$0.0 \pm 0.0^{+0.0}_{-0.0}$	$-0.2 \pm 0.1^{+0.1}_{-0.1}$	$-0.2 \pm 0.1^{+0.1}_{-0.1}$	$0.1 \pm 0.1^{+0.0}_{-0.1}$	$0.2 \pm 0.2^{+0.1}_{-0.2}$
N_{22}	$1200 \pm 150^{+60}_{-60}$	$7300 \pm 440^{+500}_{-460}$	$15900 \pm 770^{+1590}_{-850}$	$19800 \pm 880^{+1230}_{-1170}$	$32500 \pm 1200^{+2300}_{-2400}$	$129000 \pm 2000^{+10000}_{-10000}$
N_{23}	$-0.0 \pm 0.0^{+0.0}_{-0.0}$	$-0.1 \pm 0.0^{+0.0}_{-0.0}$	$-0.1 \pm 0.1^{+0.1}_{-0.0}$	$-0.2 \pm 0.1^{+0.1}_{-0.1}$	$0.1 \pm 0.1^{+0.0}_{-0.0}$	$0.2 \pm 0.3^{+0.1}_{-0.2}$
N_{24}	$0.0 \pm 0.0^{+0.0}_{-0.0}$	$-0.1 \pm 0.1^{+0.1}_{-0.1}$	$-0.4 \pm 0.3^{+0.3}_{-0.1}$	$-0.6 \pm 0.3^{+0.4}_{-0.4}$	$0.4 \pm 0.5^{+0.1}_{-0.2}$	$0.5 \pm 0.9^{+0.3}_{-0.5}$
N_{33}	$840 \pm 100^{+60}_{-70}$	$4540 \pm 240^{+350}_{-240}$	$10300 \pm 400^{+860}_{-620}$	$13560 \pm 460^{+890}_{-850}$	$22500 \pm 600^{+1600}_{-1800}$	$91600 \pm 1200^{+7300}_{-7100}$
N_{34}	$695 \pm 85^{+35}_{-40}$	$4200 \pm 240^{+300}_{-250}$	$9500 \pm 400^{+900}_{-500}$	$12280 \pm 480^{+770}_{-740}$	$20500 \pm 700^{+1500}_{-1500}$	$83000 \pm 1300^{+6600}_{-6500}$
N_{44}	$1020 \pm 130^{+50}_{-60}$	$6400 \pm 400^{+440}_{-400}$	$14600 \pm 720^{+1450}_{-790}$	$18600 \pm 830^{+1150}_{-1100}$	$31100 \pm 1100^{+2200}_{-2300}$	$126000 \pm 2000^{+10000}_{-10000}$

Table 8.2 Yield coefficients for $ZZ \to \mu^- \mu^+ \nu \bar{\nu}$ channel binned in p_{T}^{Z}. The first uncertainty is statistical, while the second is the quadrature sum of the luminosity uncertainty and all reconstruction uncertainties.

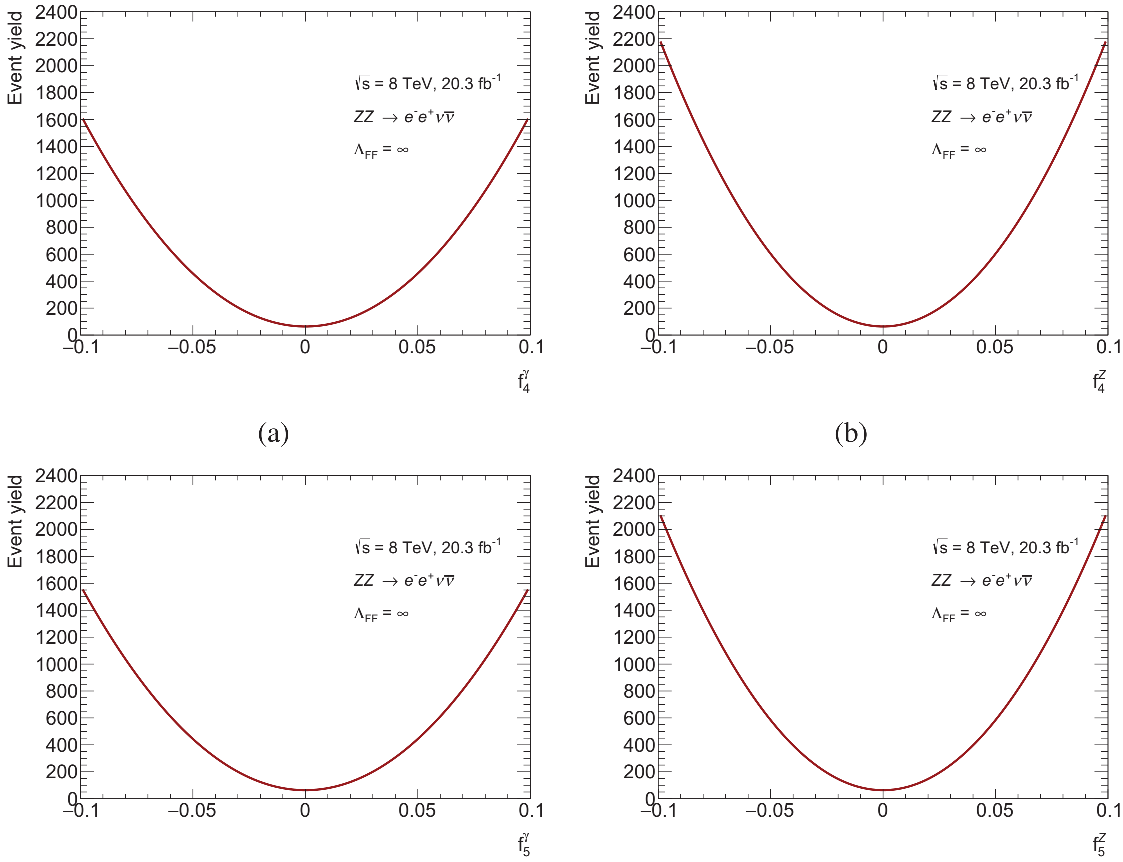

(a) (b)

(c) (d)

Fig. 8.3 Total event yields (inclusive over all bins) parameterised as a function of a single anomalous triple gauge coupling. The yield curves are obtained by expressing the yield according to Eq. (8.12) and using the normalised yield coefficients from Table 8.1 for only one coupling, making the cross terms and terms proportional to the remaining three couplings 0. The top two curves show the yields for (a) f_4^γ only and (b) f_4^Z only, while the bottom two curves show the yields for (c) f_5^γ only, and (d) f_5^Z only.

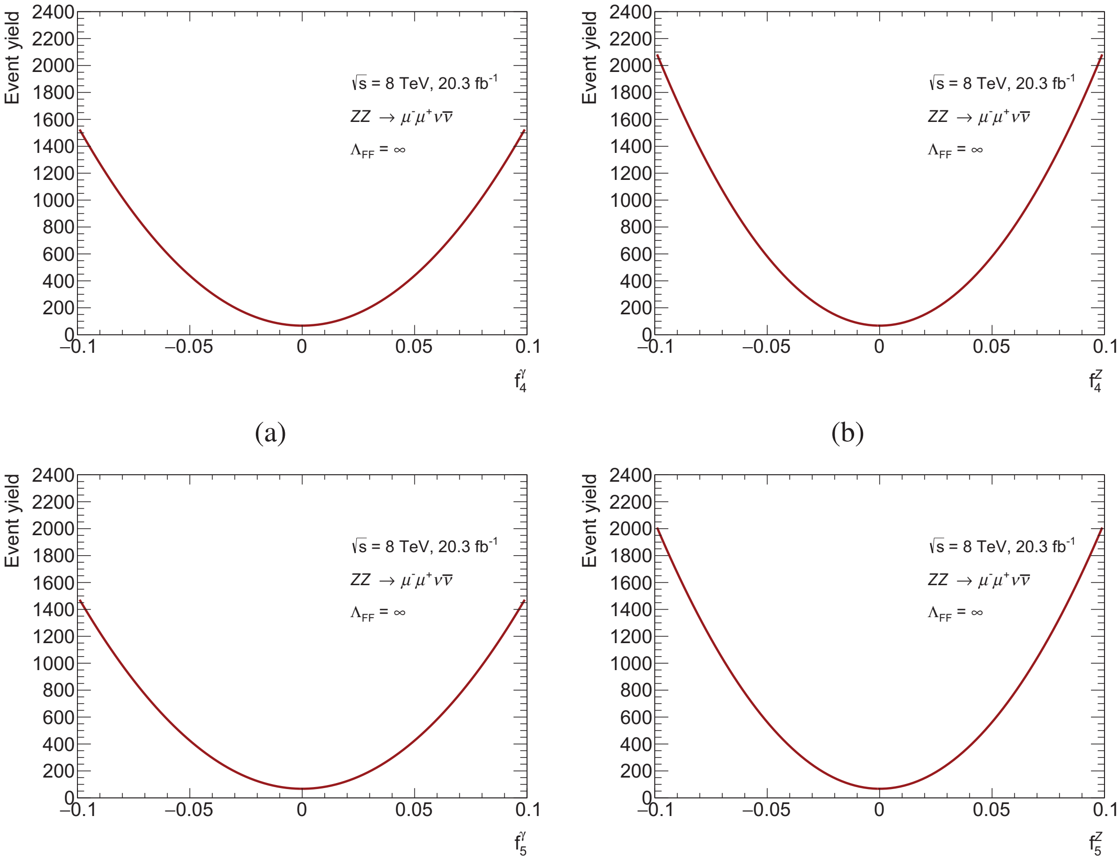

(a) (b)

(c) (d)

Fig. 8.4 Total event yields (inclusive over all bins) parameterised as a function of a single anomalous triple gauge coupling parameter in the $ZZ \to \mu^-\mu^+\nu\bar{\nu}$ sub-channel.

8.2 Limit setting procedure

8.2.1 Statistical model for limit setting

The statistical model used for determining the limits on aTGC parameters is very similar to that used to derive the ZZ cross section. The probability of observing N^j_{observed} events in data given N^j_{signal} signal and N^j_{bkgd} background events given a distribution in n bins is expressed as a Poisson distribution in the number of signal and background events, i.e.

$$P = \prod_{j=1}^{n} \text{Pois}\left(N^j_{\text{observed}} | N^j_{\text{expected}}\right) . \tag{8.13}$$

Here, the number of expected events in bin j at a given test point is a function of the aTGC couplings defined as the sum of the Standard Model and anomalous contributions, and the backgrounds in the j^{th} bin:

$$\begin{aligned} N^j_{\text{expected}} &= N^j_{\text{signal}}\left(\boldsymbol{\mu}_{\text{test}}\right) + N^j_{\text{bkgd}} , & (8.14) \\ &= N^j_{\text{SM}} + N^j_{\text{aTGC}}\left(\boldsymbol{\mu}_{\text{test}}\right) + N^j_{\text{bkgd}} . & (8.15) \end{aligned}$$

The backgrounds in a particular bin are the same as those used as input to the cross section model:

$$N^j_{\text{bkgd}} = N^j_{W+X} + N^j_{Z+X} + N^j_{WW,t\bar{t},Wt,Z\to\tau\tau} + N^j_{WZ} + N^j_{ZZ\to 4\ell} . \tag{8.16}$$

Here the set $\boldsymbol{\mu}$ is given by the set of four anomalous couplings $\{f_4^\gamma, f_4^Z, f_5^\gamma, f_5^Z\}$. The model is essentially the same as the cross section model, however, the parameters of interest in the fit become the aTGC couplings instead of the cross section. Limits may be set in several different scenarios in which one or more couplings are allowed to take on values other than zero. This section presents the procedure for one-dimensional limit setting, although it can be extended and generalised to multiple dimensions (i.e. more than one coupling at a time). In a one-dimensional limit-setting scenario, only one coupling is fitted at a time and all other anomalous couplings are set to zero. Analogously, for a two-dimensional limit-setting scenario, two parameters of interest are fitted at a time, while the other two are set to zero.

Searches in ATLAS typically have a prescription for conduction the statistical tests used for both discovery and exclusion of new physics [225]. Most of these methods involve a frequentist approach using likelihood-based test statistics [226], with the choice of test statistic depending on whether the goal is to optimise with respect to exclusion or sensitivity for discovery. For this analysis, the test statistic that is used is based on the profile-likelihood ratio, Λ, which is calculated as [15]

$$\Lambda(N_{\text{observed}}, \boldsymbol{\theta}_0; \boldsymbol{\mu}_{\text{test}}) = \frac{\max_{\hat{\hat{\boldsymbol{\theta}}}} L(N_{\text{observed}} | N_{\text{expected}}(\boldsymbol{\mu}_{\text{test}}, \boldsymbol{\theta}_0); \boldsymbol{\mu}_{\text{test}}, \hat{\hat{\boldsymbol{\theta}}})}{\max_{\hat{\boldsymbol{\mu}}, \hat{\boldsymbol{\theta}}} L(N_{\text{observed}} | N_{\text{expected}}(\boldsymbol{\mu}_{\text{test}}, \boldsymbol{\theta}_0); \hat{\boldsymbol{\mu}}, \hat{\boldsymbol{\theta}})}, \tag{8.17}$$

where L is the likelihood function, $\hat{\hat{\boldsymbol{\theta}}}\,(\boldsymbol{\mu}_{\text{test}})$ represents the conditional maximum likelihood estimators for the nuisance parameters, $\boldsymbol{\theta}_0$ are the nuisance parameters under a particular configuration of expected events and $\boldsymbol{\mu}_{\text{test}}$ is the value of the couplings fixed at a given test point. The choice of test statistic is motivated by the Neyman-Pearson lemma [227]. [1] The profile-likelihood ratio is a function of the couplings being tested, and is restricted to the range

$$0 < \Lambda\,(N_{\text{observed}}, \boldsymbol{\theta}_0; \boldsymbol{\mu}_{\text{test}}) \leq 1. \tag{8.19}$$

The maximum value of 1 that the profile likelihood ratio can take is obtained when $\boldsymbol{\mu}_{\text{test}} = \hat{\boldsymbol{\mu}}$, i.e. at the best-fit value of $\boldsymbol{\mu}$. The numerator of Eq. (8.17) indicates that the likelihood is maximised with respect to the nuisance parameters and the parameters of interest $\boldsymbol{\mu}$ are held constant. The set of nuisance parameters $\hat{\hat{\boldsymbol{\theta}}}\,(\boldsymbol{\mu}_{\text{test}})$ represents the conditional maximum likelihood estimators for the nuisance parameters, that is, the the values of the nuisance parameters at the maximum value of the likelihood achieved while holding the parameters of interest constant. The denominator is maximised with respect to both the nuisance parameters and the parameters of interest (i.e., all parameters, the couplings and the systematics, are allowed to float), giving the best fit to the data (or pseudodata, where appropriate). The sets $\hat{\boldsymbol{\mu}}$ and $\hat{\boldsymbol{\theta}}$ represent the values of the parameters of interest and the nuisance parameters when the likelihood is maximised achieving a best fit.

As with the cross section, the profile-likelihood calculation is implemented as a minimisation of the profile-log-likelihood (Eq. (8.21)) using MINUIT via a set of ROOFIT classes rather than maximising the likelihood function. The profile-log-likelihood, pll, is defined as the input negative-log-likelihood (nll) minimised with respect to all nuisance parameters

---

[1] The Neyman-Pearson lemma states that for a test between two hypotheses $H_0 : \theta = \theta_0$ (the null hypothesis) and $H_1 : \theta = \theta_1$ (the alternative hypothesis), given some probability of wrongly rejecting the null hypothesis, $\alpha = P(x \notin \omega | H_0)$, the region ω which minimises the probability of wrongly accepting the null hypothesis $\beta = P(x \in \omega | H_1)$ is a contour given by the likelihood ratio

$$\frac{P(x|H_1)}{P(x|H_0)} > k_\alpha, \tag{8.18}$$

for some threshold α, called the significance of the test. Any other region can be shown to have less statistical power.

minus the nll of the best fit [228]:

$$\begin{aligned} \mathrm{pll} &= -\ln(\Lambda)\,, && (8.20) \\ &= \min_{\hat{\hat{\boldsymbol{\theta}}}} \left(-\ln L(N_{\text{observed}}, \boldsymbol{\theta}_0; \boldsymbol{\mu}_{\text{test}}, \hat{\hat{\boldsymbol{\theta}}}) \right) - \min_{\hat{\boldsymbol{\mu}}, \hat{\boldsymbol{\theta}}} \left(-\ln L(N_{\text{observed}}, \boldsymbol{\theta}_0; \hat{\boldsymbol{\mu}}, \hat{\boldsymbol{\theta}}) \right) . && (8.21) \end{aligned}$$

Thus the test statistic used, q, is given by twice the profile 2pll, or

$$q = -2\ln(\Lambda)\,. \tag{8.22}$$

8.2.2 Pseudo-experiments and the probability distribution of the test statistic

Observed limits using data are calculated at 95% confidence-level by measuring the region of the one-dimensional coupling space where the p-value is greater than 5%. The p-value under the signal-plus-background hypothesis is defined as the probability, under the assumption of this hypothesis, to find a value of the test statistic q with equal or lesser compatibility with the signal-plus-background model compared to that found with the test statistic evaluated with observed data q_{observed}. Put another way, the p-value can be expressed as the probability to find a value of the test statistic q more extreme (greater than or equal to) than that observed in data, q_{observed}. The p-value is calculated as:

$$p_{s+b} = P(q \geq q_{\text{observed}|s+b}) = \int_{q_{\text{observed}}}^{\infty} f\left(q_\mu | s+b, \mu\right) \mathrm{d}q_\mu\,, \tag{8.23}$$

where the function that is integrated, $f\left(q_\mu | s+b, \mu\right)$ is the sampling distribution of the test statistic. The value of the parameter being tested is excluded at a confidence level of $1-\alpha = 0.95$ if, at that test point, $p_{s+b} < 0.05$. For sufficiently large datasets, one may use asymptotic properties of the test statistic [229]. The justification lies in Wilks' theorem [230], which states that for a sufficiently large data sample (where $1/\sqrt{N}$ is neglibible), the probability distribution function of the quantity $q = -2\ln(\Lambda)$ approaches a $\chi^2(n)$ distribution with n degrees of freedom, that is, $f\left(q_\mu | H_\mu\right) \approx \chi^2_n$, for n parameters of interest. Thus the sampling distribution of the test statistic should be distributed as χ^2_1 when testing one anomalous coupling. For this to be applicable, the likelihood must be sufficiently parabolic about the minimum such that the higher order terms can be neglected. In general, in the case of low statistics, the likelihood does not meet these criteria and the sampling distribution of the test statistic must be built up from toy Monte-Carlo, also referred to as pseudo-experiments. A pseudo-experiment is a set of random numbers which take the place of N_{observed} for use in a statistical test. Here, the pseudo-data in a given bin are drawn from a Poisson distribution with the mean given by the sum of the signal expectation and the background contribution for that bin. The pseudo-data are treated in the same manner as data when calculating the profile-likelihood ratio and the test statistic.

Once the distribution of the test statistic under the signal-plus-background null hypothesis and the value of the test statistic in data at a given point $\mu = \boldsymbol{\mu}_{\text{test}}$ are known, the p-value is evaluated. Instead of integrating the distribution of the test statistic, the p-value may alternatively be calculated as:

$$p\text{-value} = \frac{\text{number of pseudo-experiments with test statistic } q_{\text{pseudo}} > q_{\text{observed}}}{\text{total number of pseudo-experiments}} \quad . \tag{8.24}$$

The distribution of p-values is built up by performing a raster scan at several points along the one-dimensional parameter space for each anomalous coupling. Here, the p-value is determined by performing ten thousand pseudo-experiments at each scanned point. Due to the quadratic nature of the normalised event yield with respect to the couplings, different pseudo-experiments can give quite different results in terms of the profile-log-likelihood and whether a unique minimum or a double-minimum is found. Therefore, no restriction on the value of the coupling is imposed during the fitting procedure. The profile-log-likelihood evaluated as a function of one coupling at the Standard Model point in two pseudo-experiments and at the test point 0.004 in one pseudo-experiment f_4^γ are shown in Fig. 8.5. The sampling distributions of the test statistic in 10,000 pseudo-experiments and the corresponding test statistic observed in data at selected scanned points for f_4^γ and f_5^Z is given in Figs. 8.6 and 8.7.

From the distributions (Table 8.3), it is possible to see that the test statistic is distributed approximately as a χ^2 with one degree of freedom at points sufficiently far away from the limit. At points inside the observed limit, the test statistic distribution has local peaks. Using asymptotic formulae to evaluate the test statistic distribution would not fully take this structure into account, hence the motivation to build up the distributions from pseudo-experiments.

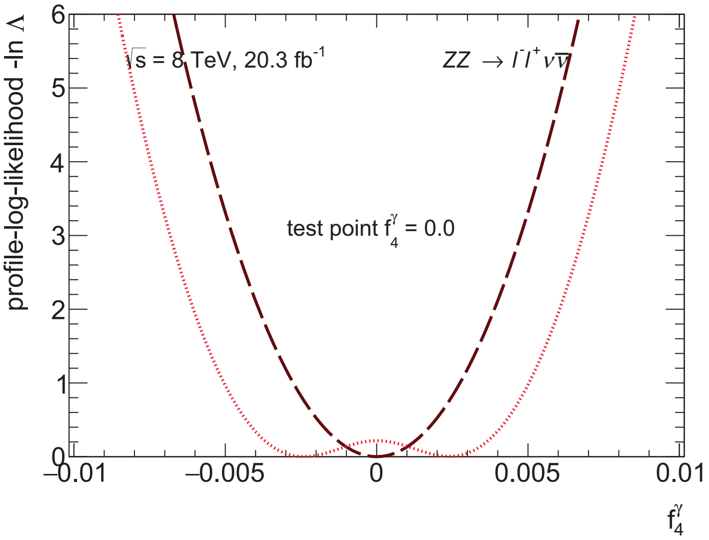

(a)

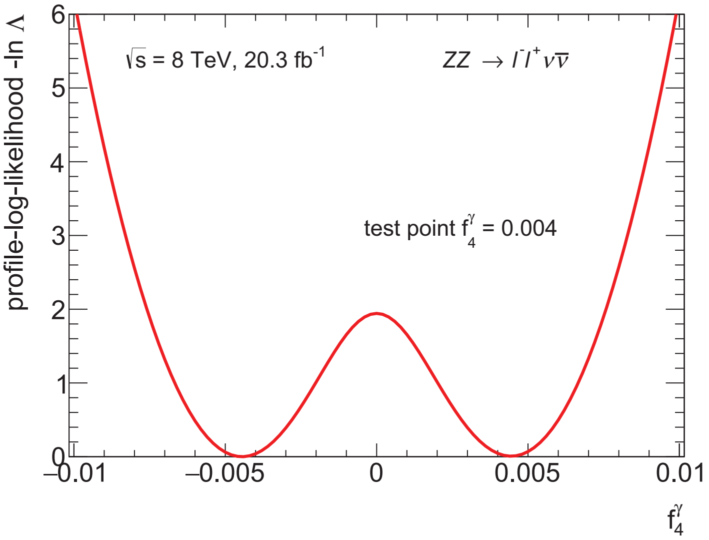

(b)

Fig. 8.5 The profile-log-likelihood ($-\ln\Lambda$) as a function of f_4^γ in a small sample of pseudo-experiments at the test point (a) 0.0 and (b) 0.004, showing the quadratic nature of the likelihood function. Pseudo-experiments can give rise to a likelihood with either a single minimum or a double-minimum (or two very close minima which cannot be resolved).

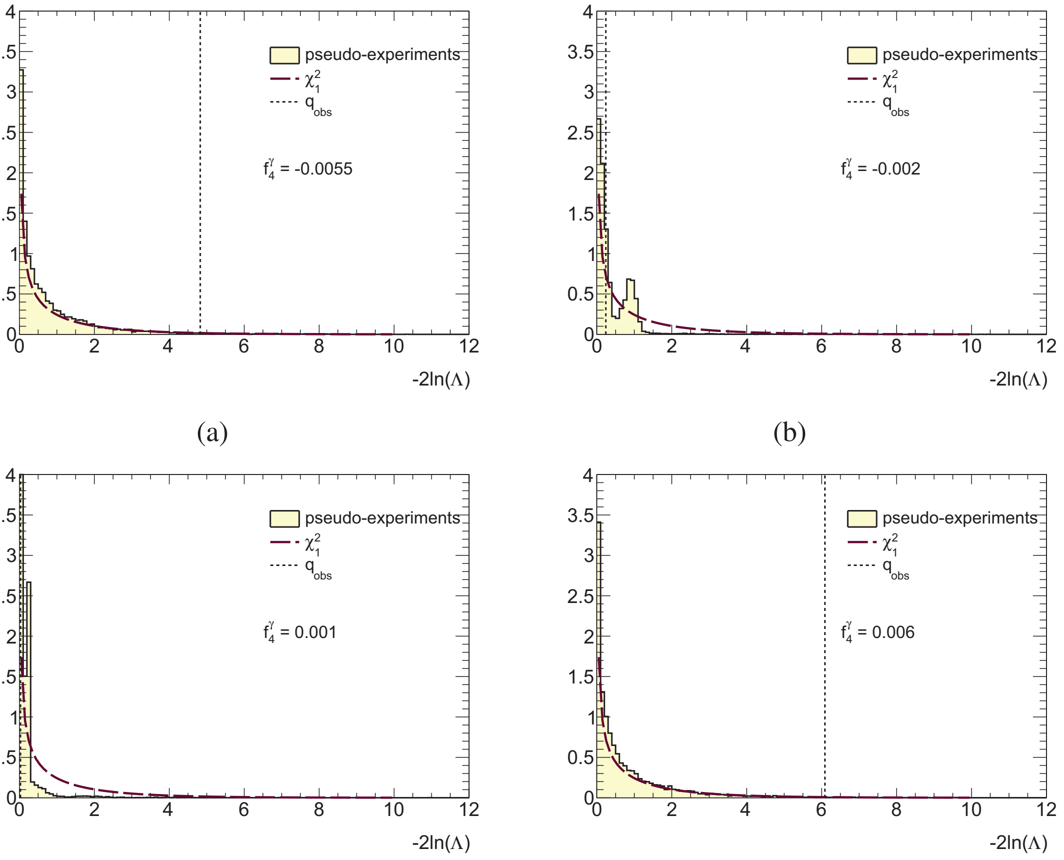

(a) (b)

(c) (d)

Fig. 8.6 The sampling distributions of the test statistic in 10,000 pseudo-experiments and the test statistic in data at selected scanned points for the coupling f_4^γ. The sampling distributions are each normalised to unit area and can be interpreted as a probability distribution. Superimposed on these distributions is a χ^2 distribution with one degree of freedom. The dashed vertical line indicates the value of the test statistic $q = -2\ln(\Lambda)$ observed in the data at that point in the raster scan. The p-value at a given point in the scan is calculated as the integral from the value of the test statistic observed in data outward to infinity of the sampling distribution according to Eq. (8.23).

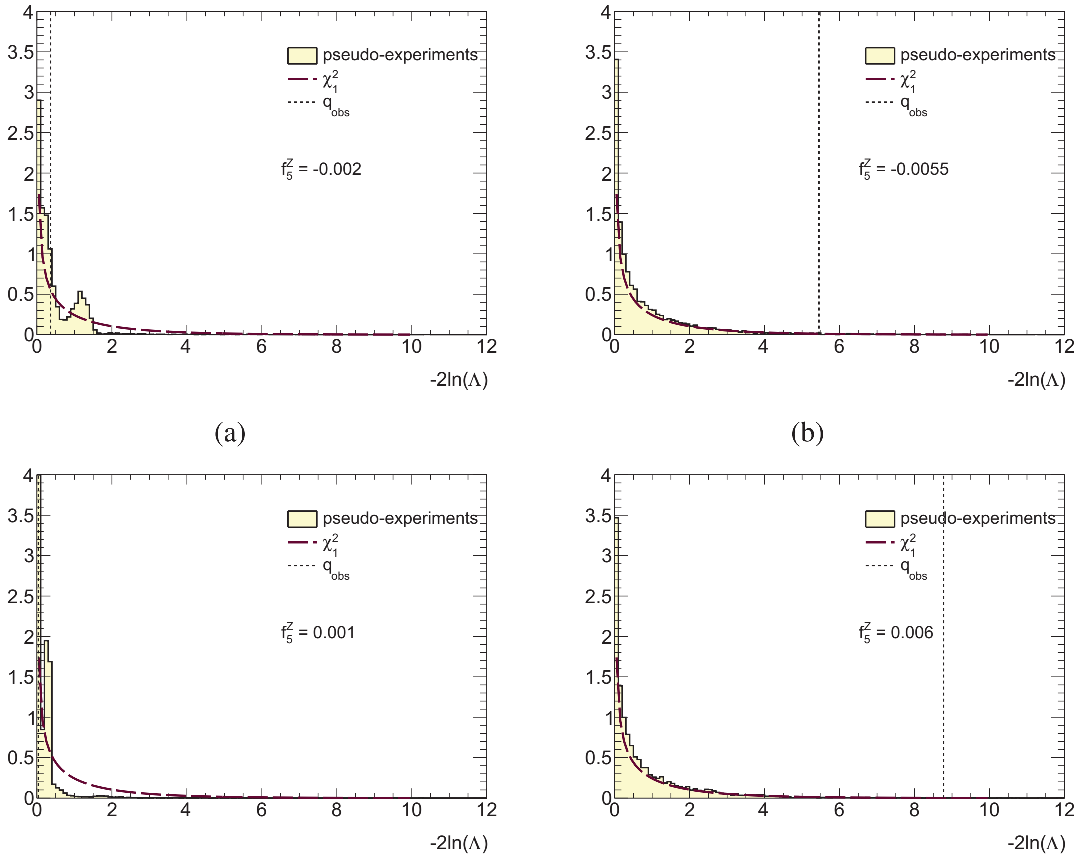

(a) (b)

(c) (d)

Fig. 8.7 The sampling distributions of the test statistic in 10,000 pseudo-experiments and the test statistic in data at selected scanned points for the coupling f_5^Z.

8.2.3 Expected limits using the delta log-likelihood method

Observed limits of a parameter (or parameters) in a model are often compared against expected limits under the assumption of a certain signal strength. One method of calculating expected limits is via the delta log-likelihood method. This method of limit calculations is much less computationally intensive compared to the full frequentist approach by calculating p-values. This method involves performing pseudo-experiments and building up a distribution of limits under the background-only ($\mu = 0$) hypothesis. For each pseudo-experiment, the data are replace by pseudo-data drawn from a Poisson distribution generated about the Standard Model point ($\mu = 0$) for a given coupling. The upper and lower limits for a given pseudo-experiment are found by where the test statistic q increases by 1.92 (3.84/2) from its minimum value. The resulting distributions are plotted for upper and lower limits. The means of the distributions are taken as the expected limits, while the uncertainty on the mean is taken as the statistical uncertainty on the expected limit.

8.2.4 Frequentist observed limits in one dimension

Frequentist observed limits are obtained through a similar method as presented in Section 8.2.2, by performing a one-dimensional scan over a range of suitable values for the aTGC couplings. At each point, an initial fit is performed to the data to set the conditional maximum likelihood estimators of the nuisance parameters. For a given pseudo-experiment, pseudo-data are generated using the value of the coupling equal to the current point being tested. The nuisance parameters are varied randomly within their uncertainties, and the test statistic is subsequently calculated. This procedure is repeated once for each pseudo-experiment. The distribution of the test statistic is built from the pseudo-experiments and compared to the value of the test statistic obtained for N_{observed} in data at that test point to calculate the p-value. A point is accepted at 95% confidence if the p-value is greater than 5%, while a point is rejected if the p-value at that point is less than 5%. The limit is calculated as a numerical interpolation between the first-rejected and last-accepted points. Sample distributions of p-values as a function of scanned point are shown in Figs. 8.8 and 8.9.

The expected and observed limits are summarised in Table 8.3. These constitute limits on the bare couplings themselves, as no form-factor is used ($\Lambda_{\text{FF}} = \infty$). The limits presented are a factor of two tighter constraint on anomalous couplings than the ATLAS measurement at 7 TeV, which used a combination of both the $ZZ \to \ell^-\ell^+\nu\bar{\nu}$ and $ZZ \to \ell^-\ell^+\ell^-\ell^+$ channels [77]. The CMS collaboration have reported limits using the full 8 TeV dataset and limits combining the 7 and 8 TeV datasets [231]. The expected limits presented are comparable to those presented in this thesis, while the observed limits using the 8 TeV dataset are,

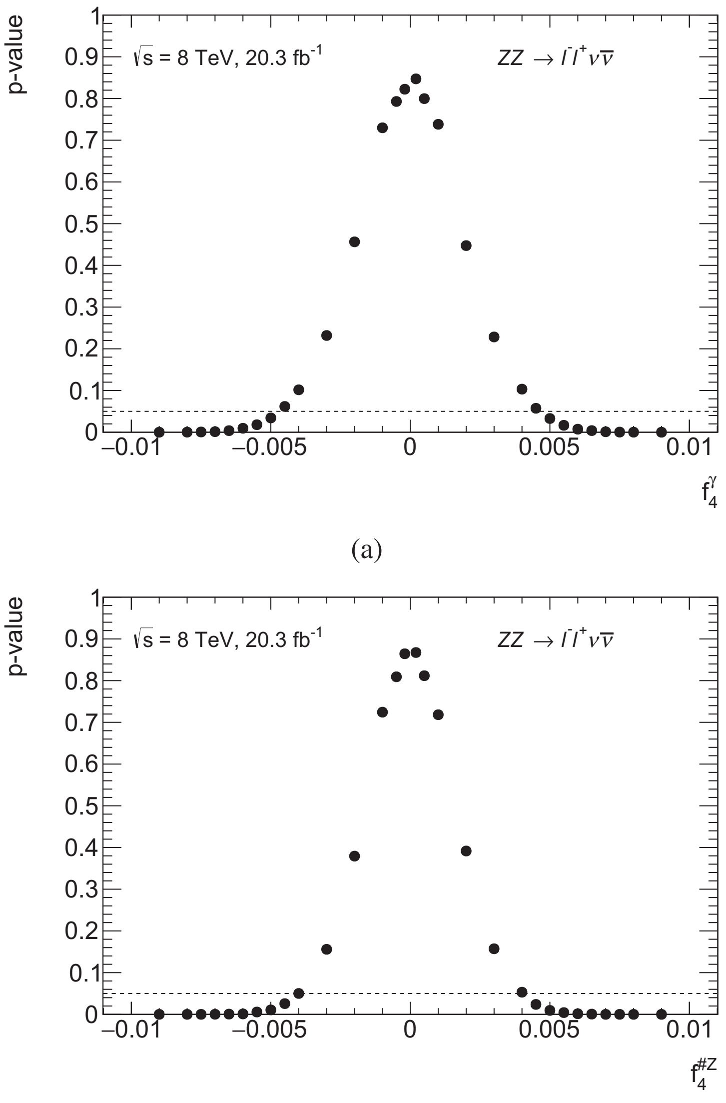

(a)

(b)

Fig. 8.8 A sampled distribution of p-values as a function of test point in the raster scan used to obtain observed limits for each aTGC parameter. The 95% confidence-level limit on each parameter is taken as the value of the coupling where the p-value falls below 5% as indicated by the dashed lines. The p-value sharply increases at values close to zero, indicating a low probability of observing a test statistic in the pseudo-experiments that is greater than that observed in data at that given point.

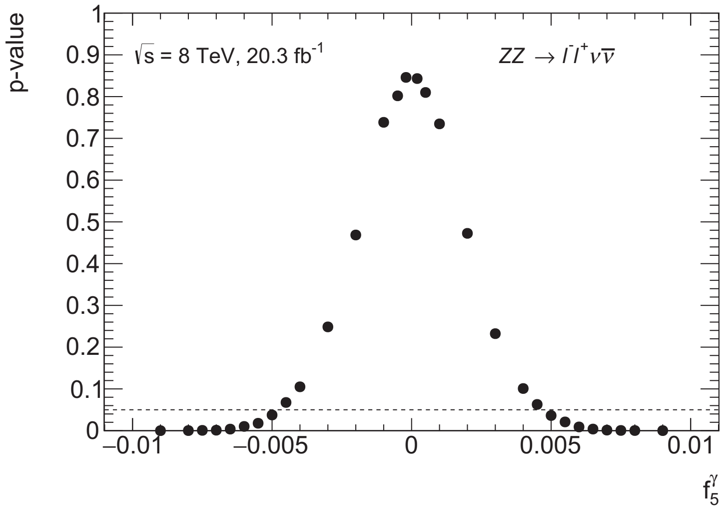

(a)

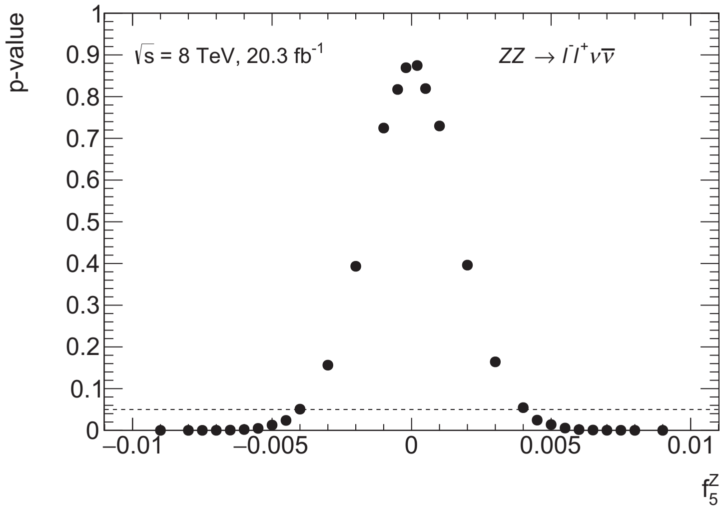

(b)

Fig. 8.9 A sampled distribution of p-values as a function of test point in the raster scan used to obtain observed limits for $f_5^{\gamma}$and f_5^{Z}. The 95% confidence-level limit on each parameter is taken as the value of the coupling where the p-value falls below 5% as indicated by the dashed lines. The p-value sharply increases at values close to zero, indicating a low probability of observing a test statistic in the pseudo-experiments that is greater than that observed in data at that given point.

in general about 25% tighter, and the combined limits are approximately 35% tighter. The ATLAS limits could be further tightened with a corresponding combination of channels and datasets from different runs.

Coupling	Expected	Observed
f_4^γ	[-0.0055 , 0.0055]	[-0.0047 , 0.0046]
f_4^Z	[-0.0046 , 0.0046]	[-0.0040 , 0.0040]
f_5^γ	[-0.0054 , 0.0055]	[-0.0048 , 0.0047]
f_5^Z	[-0.0046 , 0.0047]	[-0.0040 , 0.0041]

Table 8.3 One-dimensional expected and observed limits at 95% confidence-level on the anomalous ZZV gauge boson couplings in the $ZZ \to \ell\ell\nu\bar{\nu}$ channel, where the limit for each coupling assumes the other couplings fixed at their SM value. The scale of the form factor $\Lambda_{\mathrm{FF}} = \infty$.

8.3 Conclusions and outlook

This chapter presented limits on neutral anomalous gauge couplings obtained with the full ATLAS dataset at 8 TeV as measured in the two $\ell^-\ell^+\nu\bar{\nu}$ sub-channels. A method of parametrising the signal yield by reweighting diboson events generated at an aTGC point back to the Standard Model by the ratio of differential cross sections was also presented. A statistical model was constructed to calculate the profile likelihood ratio, which was used as the test statistic for a frequentist limit-setting procedure. One-dimensional frequentist observed and expected limits were presented. The limits are compatible with the one-dimensional limits measured by the CMS collaboration using the $ZZ \to \ell^-\ell^+\ell^-\ell^+$ channel (with τ leptons included in the signal definition) [83]. However, these limits are larger than the most recent limits obtained by a combination of the $ZZ \to \ell^-\ell^+\nu\bar{\nu}$ and $ZZ \to \ell^-\ell^+\ell^-\ell^+$ decay channels. Similar combination of decay channels by ATLAS to enhance the observed limits could lead to limits that are about 10% to 20% tighter than those presented here, although this has yet to be explored fully.

Chapter 9

Conclusions

This analysis presented a measurement of the ZZ production cross section in proton-proton collisions at a centre-of-mass energy of $\sqrt{s} = 8$ TeV collected in 2012 by the ATLAS experiment at the LHC. The data used for the analysis corresponds to an integrated luminosity of $20.3\,\text{fb}^{-1}$. The event selection is consistent with selecting one pair of opposite-sign, same-flavour leptons from the decay of an on-shell Z boson and a significant amount of missing energy consistent with a Z boson decaying invisibly. Dominant backgrounds, such as WZ, $t\bar{t}$, WW, Wt, $W+$jets and $Z+$jets were estimated using a mixture of data-driven techniques and simulation. The fiducial efficiency correction C_{ZZ} and the acceptance factor A_{ZZ} were estimated from simulation using a next-to-leading order prediction from POWHEG-BOX to model the $q\bar{q} \to ZZ$ component and gg2VV to model the $gg \to ZZ$ at lowest order in the gluon-induced process. An unbinned likelihood-based fit to the cross section was performed using a statistical model constructed from the total number of background events, C_{ZZ}, A_{ZZ}, and the observed events passing all selection criteria. Separate measurements of the cross section were measured in a fiducial phase space using the $e^-e^+\nu\bar{\nu}$ and $\mu^-\mu^+\nu\bar{\nu}$ sub-channels in the $ZZ \to \ell^+\ell^- + E_{\mathrm{T}}^{\mathrm{miss}}$ decay mode, and the $e^-e^+e^-e^+$, $e^-e^+\mu^-\mu^+$, and $\mu^-\mu^+\mu^-\mu^+$ sub-channels in the $ZZ \to \ell^-\ell^+\ell^-\ell^+$ decay mode. Measured cross sections were extrapolated to a phase space defined by both Z bosons in the mass range $66 < m_{\ell^-\ell^+} < 116$ GeV and corrected for branching fraction to obtain an extrapolated measurement of the $pp \to ZZ$ cross section using each sub-channel. The fiducial and extrapolated cross sections in the $e^-e^+\nu\bar{\nu}$ and $\mu^-\mu^+\nu\bar{\nu}$ sub-channels were measured to be

$$\begin{aligned}
\sigma^{\text{fid}}_{pp\to ZZ} &= 4.99\,^{+0.76}_{-0.71}\,(\text{stat})\,^{+0.45}_{-0.38}\,(\text{syst})\,^{+0.20}_{-0.15}\,(\text{lumi})\ \text{fb}\ (ZZ\to e^-e^+\nu\bar{\nu}),\\
\sigma^{\text{fid}}_{pp\to ZZ} &= 4.67\,^{+0.70}_{-0.65}\,(\text{stat})\,^{+0.45}_{-0.35}\,(\text{syst})\,^{+0.19}_{-0.15}\,(\text{lumi})\ \text{fb}\ (ZZ\to \mu^-\mu^+\nu\bar{\nu}),\\
\sigma^{\text{extrapolated}}_{pp\to ZZ} &= 8.99\,^{+1.37}_{-1.28}\,(\text{stat})\,^{+0.95}_{-0.78}\,(\text{syst})\,^{+0.36}_{-0.28}\,(\text{lumi})\ \text{pb}\ (ZZ\to e^-e^+\nu\bar{\nu}),\\
\sigma^{\text{extrapolated}}_{pp\to ZZ} &= 8.68\,^{+1.29}_{-1.21}\,(\text{stat})\,^{+0.94}_{-0.73}\,(\text{syst})\,^{+0.35}_{-0.27}\,(\text{lumi})\ \text{pb}\ (ZZ\to \mu^-\mu^+\nu\bar{\nu}),
\end{aligned} \tag{9.1}$$

while in the $e^-e^+e^-e^+$, $e^-e^+\mu^-\mu^+$, and $\mu^-\mu^+\mu^-\mu^+$ sub-channels, the cross sections were measured to be

$$\begin{aligned}
\sigma^{\text{fid}}_{pp\to ZZ} &= 5.90\,^{+0.83}_{-0.76}\,(\text{stat})\,^{+0.29}_{-0.23}\,(\text{syst})\,^{+0.19}_{-0.15}\,(\text{lumi})\ \text{fb}\ (ZZ\to e^-e^+e^-e^+),\\
\sigma^{\text{fid}}_{pp\to ZZ} &= 12.35\,^{+1.03}_{-0.98}\,(\text{stat})\,^{+0.38}_{-0.33}\,(\text{syst})\,^{+0.37}_{-0.32}\,(\text{lumi})\ \text{fb}\ (ZZ\to e^-e^+\mu^-\mu^+),\\
\sigma^{\text{fid}}_{pp\to ZZ} &= 4.87\,^{+0.56}_{-0.52}\,(\text{stat})\,^{+0.21}_{-0.17}\,(\text{syst})\,^{+0.15}_{-0.12}\,(\text{lumi})\ \text{fb}\ (ZZ\to \mu^-\mu^+\mu^-\mu^+),\\
\sigma^{\text{extrapolated}}_{pp\to ZZ} &= 6.38\,^{+0.90}_{-0.83}\,(\text{stat})\,^{+0.32}_{-0.25}\,(\text{syst})\,^{+0.20}_{-0.16}\,(\text{lumi})\ \text{pb}\ (ZZ\to e^-e^+e^-e^+),\\
\sigma^{\text{extrapolated}}_{pp\to ZZ} &= 7.52\,^{+0.63}_{-0.60}\,(\text{stat})\,^{+0.25}_{-0.21}\,(\text{syst})\,^{+0.23}_{-0.20}\,(\text{lumi})\ \text{pb}\ (ZZ\to e^-e^+\mu^-\mu^+),\\
\sigma^{\text{extrapolated}}_{pp\to ZZ} &= 6.66\,^{+0.77}_{-0.71}\,(\text{stat})\,^{+0.30}_{-0.24}\,(\text{syst})\,^{+0.21}_{-0.17}\,(\text{lumi})\ \text{pb}\ (ZZ\to \mu^-\mu^+\mu^-\mu^+).
\end{aligned} \tag{9.2}$$

A measurement of the extrapolated cross section was measured combining information from both $\ell^-\ell^+\nu\bar{\nu}$ sub-channels, and three $ZZ\to\ell^-\ell^+\ell^-\ell^+$ sub-channels to give

$$\sigma^{\text{extrapolated}}_{pp\to ZZ} = 7.30\,^{+0.38}_{-0.37}\,(\text{stat})\,^{+0.28}_{-0.25}\,(\text{syst})\,^{+0.23}_{-0.20}\,(\text{lumi})\ \text{pb}\ (\text{all sub-channels}). \tag{9.3}$$

The measured cross section is compared to the calculated theoretical prediction of the cross section in the specified mass range from the summed contributions from the POWHEGBOX and gg2VV generators was found to be

$$\sigma^{\text{predicted}}_{pp\to ZZ} = 6.69 \pm 0.01\,(\text{stat})\,^{+0.67}_{-0.56}\,(\text{theory})\ \text{pb}, \tag{9.4}$$

where the theoretical uncertainties include the QCD scale and the uncertainty associated with the parton distribution function used to produce the samples of ZZ events. The measurement is in agreement with the Standard Model prediction within experimental and theoretical uncertainties.

The model used to extract the cross sections was extended to place limits on anomalous neutral ZZZ and $ZZ\gamma$ couplings within the framework of an effective Lagrangian. Limits were set using a profile-likelihood-based test statistic to build probability distributions in 10,000 pseudo-experiments at various scanned points in the parameter space. The observed limits at 95% confidence level were calculated to be

$$\begin{aligned}
&-0.0047 < f_4^\gamma < 0.0046, -0.0040 < f_4^Z < 0.0040\,,\\
&-0.0048 < f_5^\gamma < 0.0047, -0.0040 < f_5^Z < 0.0041\,,
\end{aligned} \tag{9.5}$$

where a form-factor with cutoff scale $\Lambda = \infty$.

References

[1] Brock, Ian and Schörner-Sadenius, Thomas, *Setting the Scene*, in *Physics at the Terascale*, Brock, Ian and Schörner-Sadenius, Thomas, ed. Wiley-VCH, Weinheim, Germany, 2011.

[2] E598 Collaboration, J. Aubert et al., *Experimental observation of a heavy particle J*, Phys. Rev. Lett. **33** (1974) 1404–1406.

[3] G. Abrams, D. Briggs, W. Chinowsky, C. Friedberg, G. Goldhaber, et al., *The discovery of a second narrow resonance in* e^+e^- *annihilation*, Phys. Rev. Lett. **33** (1974) 1453–1455.

[4] F. Hasert, H. Faissner, W. Krenz, J. Von Krogh, D. Lanske, et al., *Search for elastic* ν_μ *electron scattering*, Phys. Lett. **B46** (1973) 121–124.

[5] Gargamelle Neutrino Collaboration, F. Hasert et al., *Observation of neutrino like interactions without muon or electron in the Gargamelle neutrino experiment*, Phys. Lett. **B46** (1973) 138–140.

[6] S. Herb, D. Hom, L. Lederman, J. Sens, H. Snyder, et al., *Observation of a dimuon resonance at 9.5 GeV in 400-GeV proton-nucleus collisions*, Phys. Rev. Lett. **39** (1977) 252–255.

[7] M. L. Perl et al., *Evidence for anomalous lepton production in* $e^+ - e^-$ *annihilation*, Phys. Rev. Lett. **35** (1975) 1489–1492.

[8] CDF Collaboration, F. Abe et al., *Evidence for top quark production in* $\bar{p}p$ *collisions at* $\sqrt{s} = 1.8$ *TeV*, Phys.Rev. **D50** (1994) 2966–3026.

[9] DONUT Collaboration, K. Kodama et al., *Observation of tau neutrino interactions*, Phys. Lett. **B504** (2001) 218–224, `arXiv:hep-ex/0012035 [hep-ex]`.

[10] M. Diehl and W. Hollik, *The Standard Model: Our picture of the microcosm*, in *Physics at the Terascale*, I. Brock and T. Schörner-Sadenius, eds. Wiley-VCH, Weinheim, Germany, 2011.

[11] H. Fritzsch, M. Gell-Mann, and H. Leutwyler, *Advantages of the color octet gluon picture*, Phys. Lett. **B47** (1973) 365–368.

[12] Y. Nagashima, *Elementary particle physics, Vol. 2: Foundations of the Standard Model.* Wiley-VCH, Weinheim, Germany, 2013.

[13] R. K. Ellis, W. J. Stirling, and B. R. Webber, *QCD and collider physics*. Cambridge monographs on particle physics, nuclear physics, and cosmology. Cambridge University Press, Cambridge, UK, 2003.

[14] T. Hebbeker, *Tests of quantum chromodynamics in hadronic decays of* Z^0 *bosons produced in* e^+e^- *annihilation*, Phys. Rept. **217** (1992) 69–157.

[15] Particle Data Group Collaboration, K. Olive et al., *Review of particle physics*, Chin. Phys. **C38** (2014) 090001.

[16] J. Bardeen, L. N. Cooper, and J. R. Schrieffer, *Microscopic theory of superconductivity*, Phys. Rev. **106** (1957) 162–164.

[17] Y. Nambu, *Axial vector current conservation in weak interactions*, Phys. Rev. Lett. **4** (1960) 380–382.

[18] F. Englert and R. Brout, *Broken symmetry and the mass of gauge vector mesons*, Phys. Rev. Lett. **13** (1964) 321–323.

[19] P. W. Higgs, *Broken symmetries, massless particles and gauge fields*, Phys. Lett. **12** (1964) 132–133.

[20] P. W. Higgs, *Broken symmetries and the masses of gauge bosons*, Phys. Rev. Lett. **13** (1964) 508–509.

[21] J. Ellis, M. K. Gaillard, and D. V. Nanopoulos, *A historical profile of the higgs boson*, `arXiv:1201.6045 [hep-ph]`.

[22] S. Weinberg, *A model of leptons*, Phys. Rev. Lett. **19** (1967) 1264–1266.

[23] A. Salam, *Weak and electromagnetic interactions*, in *8^{th} Nobel Symposium Lerum, Sweden*, vol. C680519, 367–377. 1968.

[24] J. Goldstone, *Field theories with «Superconductor» solutions*, Il Nuovo Cimento **19** no. 1, (1961) 154–164. http://dx.doi.org/10.1007/BF02812722.

[25] P. D. B. Collins, *Particle physics and cosmology*. Wiley, Chichester, UK, 1989.

[26] F. Halzen, *Quarks and leptons: An introductory course in modern particle physics*. Wiley, Chichester, 1984.

[27] M. Veltman, *Second threshold in weak interactions*, Acta Phys. Polon. **B8** (1977) 475.

[28] B. W. Lee, C. Quigg, and H. B. Thacker, *Strength of weak interactions at very high energies and the Higgs boson mass*, Phys. Rev. Lett. **38** (1977) 883–885.

[29] UA1 Collaboration, G. Arnison et al., *Experimental observation of isolated large transverse energy electrons with associated missing energy at* $\sqrt{s} = 540$ *GeV*, Phys. Lett. **B122** (1983) 103–116.

[30] UA2 Collaboration Collaboration, M. Banner et al., *Observation of single isolated electrons of high transverse momentum in events with missing transverse energy at the CERN $\bar{p}p$ Collider*, Phys. Lett. **B122** (1983) 476–485.

[31] UA1 Collaboration, G. Arnison et al., *Experimental observation of lepton pairs of invariant mass around* 95 *GeV/c*^{2} *at the CERN SPS Collider*, Phys. Lett. **B126** (1983) 398–410.

[32] LEP Working Group for Higgs boson searches, ALEPH Collaboration, DELPHI Collaboration, L3 Collaboration, OPAL Collaboration, R. Barate et al., *Search for the Standard Model Higgs boson at LEP*, Phys. Lett. **B565** (2003) 61–75, `arXiv:hep-ex/0306033 [hep-ex]`.

[33] TEVNPH (Tevatron New Phenomina and Higgs Working Group), CDF, DØ Collaboration, *Combined CDF and DØ Search for Standard Model Higgs boson production with up to 10.0 fb^{-1} of data*, `arXiv:1203.3774 [hep-ex]`.

[34] CERN Press Office, “CERN releases analysis of LHC incident.” press.web.cern.ch/press-releases/2008/10/cern-releases-analysis-lhc-incident, 2008. (Press Release).

[35] ATLAS Collaboration, *Combination of the searches for the Higgs boson in 1 fb^{-1} of data taken with the ATLAS detector at 7 TeV center-of-mass energy*, Tech. Rep. ATLAS-CONF-2011-112, CERN, Geneva, Aug, 2011.

[36] CMS Collaboration, *SM Higgs combination*, Tech. Rep. CMS-PAS-HIG-11-011, CERN, Geneva, Jul, 2011.

[37] CERN, *Press Conference: Update on the search for the Higgs boson at CERN on 4 July 2012.*, Jul, 2012.

[38] ATLAS Collaboration, *Observation of an excess of events in the search for the Standard Model Higgs boson with the ATLAS detector at the LHC*, Tech. Rep. ATLAS-CONF-2012-093, CERN, Geneva, Jul, 2012.

[39] ATLAS Collaboration, *Observation of an excess of events in the search for the Standard Model Higgs boson in the $\gamma\gamma$ channel with the ATLAS detector*, Tech. Rep. ATLAS-CONF-2012-091, CERN, Geneva, Jul, 2012.

[40] ATLAS Collaboration, *Evidence for the spin-0 nature of the Higgs boson using ATLAS data*, Phys. Lett. **B726** (2013) 120–144, `arXiv:1307.1432 [hep-ex]`.

[41] ATLAS Collaboration, *Differential cross sections of the Higgs boson measured in the diphoton decay channel using 8 TeV pp collisions*, tech. rep., Jul, 2013.

[42] ATLAS Collaboration, *Measurements of the properties of the Higgs-like boson in the two photon decay channel with the ATLAS detector using 25* fb^{-1} *of proton-proton collision data*, Tech. Rep. ATLAS-CONF-2013-012, CERN, Geneva, Mar, 2013.

[43] CMS Collaboration, *Constraints on the Higgs boson width from off-shell production and decay to $ZZ \to \ell\ell\ell'\ell'$ and $\ell\ell\nu\nu$*, Tech. Rep. CMS-PAS-HIG-14-002, CERN, Geneva, 2014.

[44] H. Murayama, *Supersymmetry phenomenology*, in *Proceedings of the summer school, Trieste, Italy, June 21-July 9, 1999*, 296–335. 2000. `arXiv:hep-ph/0002232 [hep-ph]`.

[45] G. L. Kane, *TASI lectures on weak scale supersymmetry: A top motivated bottom up approach*, `arXiv:hep-ph/0202185 [hep-ph]`.

[46] S. P. Martin, *A supersymmetry primer*, `arXiv:hep-ph/9709356 [hep-ph]`.

[47] A. Lipniacka, *Understanding SUSY limits from LEP*, `arXiv:hep-ph/0210356 [hep-ph]`.

[48] CDF, DØ Collaboration, T. Adams, *SUSY searches at the Tevatron*, in *Hadron collider physics. Proceedings, 19th symposium, HCP2008, Galena, USA, May 27-31, 2008*. 2008. `arXiv:0808.0728 [hep-ex]`.

[49] CDF, D0 Collaboration, M. Jaffre, *SUSY searches at the Tevatron*, EPJ Web Conf. **28** (2012) 09006, `arXiv:1202.0712 [hep-ex]`.

[50] H. P. Nilles, *Supersymmetry, supergravity and particle physics*, Phys. Rept. **110** (1984) 1–162.

[51] H. E. Haber and G. L. Kane, *The search for supersymmetry: probing physics beyond the Standard Model*, Phys. Rept. **117** (1985) 75–263.

[52] R. Barbieri, *Looking beyond the Standard Model: the supersymmetric option*, Riv. Nuovo Cim. **11** (1988) 1–45.

[53] MSSM Working Group Collaboration, A. Djouadi et al., *The minimal supersymmetric Standard Model: Group summary report*, in *GDR (Groupement De Recherche) - Supersymetrie Montpellier, France, April 15-17, 1998*. 1998. `arXiv:hep-ph/9901246 [hep-ph]`.

[54] ALEPH, DELPHI, L3, OPAL, LEP Electroweak Collaboration, S. Schael et al., *Electroweak measurements in electron-positron collisions at W-boson-pair energies at LEP*, Phys.Rept. **532** (2013) 119–244, `arXiv:1302.3415 [hep-ex]`.

[55] CDF Collaboration, F. Abe et al., *Observation of W^+W^- production in $\bar{p}p$ collisions at $\sqrt{s} = 1.8$ TeV*, Phys. Rev. Lett. **78** (1997) 4536–4540.

[56] CDF Collaboration, A. T. Goshaw, *Di-boson physics at the Tevatron*, in *Proceedings, 1st Symposium on hadron collider physics (HCP 2005)*, vol. 108, 86–90. 2006.

[57] CDF, DØ Collaboration, M. S. Neubauer, *Diboson physics at the Tevatron*, in *41st Rencontres de Moriond: QCD and hadronic interactions, La Thuile, Italy, March 18-25, 2006*. 2006. `arXiv:hep-ex/0605066 [hep-ex]`.

[58] CDF, D0 Collaboration, J. Sjolin, *Diboson physics at the Tevatron*, in *41st Rencontres de Moriond on electroweak interactions and unified theories La Thuile, Aosta Valley, Italy, March 11-18, 2006*. 2006. `arXiv:hep-ex/0605094 [hep-ex]`.

[59] A. Robson, *Diboson physics at the Tevatron*, EPJ Web Conf. **28** (2012) 06001, `arXiv:1201.4771 [hep-ex]`.

[60] M. Bauce, *Diboson physics at the Tevatron*, in *48th Rencontres de Moriond on electroweak interactions and unified theories*, J. T. T. V. Etienne Augé, Jacques Dumarchez, ed., 459–464. ARISF, La Thuile, Italy, Mar, 2013.

[61] H. Georgi, S. Glashow, M. Machacek, and D. V. Nanopoulos, *Higgs bosons from two gluon annihilation in proton proton collisions*, Phys. Rev. Lett. **40** (1978) 692–694.

[62] LHC Higgs Cross Section Working Group Collaboration, S. Dittmaier et al., *Handbook of LHC Higgs cross sections: 1. inclusive observables*, `arXiv:1101.0593 [hep-ph]`.

[63] S. Dittmaier, C. Mariotti, G. Passarino, R. Tanaka, et al., *Handbook of LHC Higgs cross sections: 2. differential distributions*, `arXiv:1201.3084 [hep-ph]`.

[64] G. Gounaris, J. Layssac, and F. Renard, *New and standard physics contributions to anomalous Z and γ self couplings*, Phys. Rev. **D62** (2000) 073013, `arXiv:hep-ph/0003143 [hep-ph]`.

[65] K. Hagiwara, R. Peccei, D. Zeppenfeld, and K. Hikasa, *Probing the weak boson sector in $e^+e^- \to W^+W^-$*, Nucl. Phys. **B282** (1987) 253.

[66] G. Gounaris, J. Layssac, and F. Renard, *Signatures of the anomalous $Z\gamma$ and ZZ production at the lepton and hadron colliders*, Phys. Rev. **D61** (2000) 073013 PM-99-39, THES-TP-99-11, `arXiv:hep-ph/9910395 [hep-ph]`.

[67] G. Gounaris, J. Layssac, and F. Renard, *Off-shell structure of the anomalous Z and γ self-couplings*, Phys. Rev. **D62** (2000) 073012, `arXiv:hep-ph/0005269 [hep-ph]`.

[68] U. Baur and E. L. Berger, *Probing the weak boson sector in $Z\gamma$ production at hadron colliders*, Phys. Rev. **D47** (1993) 4889–4904.

[69] U. Baur and D. L. Rainwater, *Probing neutral gauge boson self-interactions in ZZ production at hadron colliders*, Phys. Rev. **D62** (2000) 113011, `arXiv:hep-ph/0008063 [hep-ph]`.

[70] L3 Collaboration, M. Acciarri et al., *Study of neutral current four fermion and ZZ production in e^+e^- collisions at $\sqrt{s} = 183$ GeV*, Phys. Lett. **B450** (1999) 281–293.

[71] ALEPH and DELPHI and L3 and OPAL, LEP Electroweak Working Group Collaboration, J. Alcaraz et al., *A combination of preliminary electroweak measurements and constraints on the standard model*, `arXiv:hep-ex/0612034 [hep-ex]`.

[72] DØ Collaboration, *Measurement of the ZZ production cross section and search for the Standard Model Higgs boson in the four lepton final state in $p\bar{p}$ collisions*, Phys. Rev. **D88** (2013) 032008, `arXiv:1304.5422 [hep-ex]`.

[73] "CDF Run 2 Electroweak public results." http://www-cdf.fnal.gov/physics/ewk.

[74] ATLAS Collaboration, *Measurement of the $W \to \ell\nu$ and $Z/\gamma^* \to \ell\ell$ production cross sections in proton-proton collisions at $\sqrt{s} = 7$ TeV with the ATLAS detector*, JHEP **1012** (2010) 060, `arXiv:1010.2130 [hep-ex]`.

[75] ATLAS Collaboration, *Measurement of the WW cross section in $\sqrt{s} = 7$ TeV pp collisions with ATLAS*, Phys. Rev. Lett. **107** (2011) 041802, `arXiv:1104.5225 [hep-ex]`.

[76] ATLAS Collaboration, *Measurement of the ZZ production cross section and limits on anomalous neutral triple gauge couplings in proton-proton collisions at $\sqrt{s} = 7$ TeV with the ATLAS detector*, Phys. Rev. Lett. **108** (2012) 041804, `arXiv:1110.5016 [hep-ex]`.

[77] ATLAS Collaboration, *Measurement of ZZ production in pp collisions at $\sqrt{s} = 7$ TeV and limits on anomalous ZZZ and $ZZ\gamma$ couplings with the ATLAS detector*, JHEP **1303** (2013) 128, `arXiv:1211.6096 [hep-ex]`.

[78] ATLAS Collaboration, *Measurement of the total ZZ production cross section in proton-proton collisions at $\sqrt{s}$ = 8 TeV in 20 fb^{-1} with the ATLAS detector*, Tech. Rep. ATLAS-CONF-2013-020, CERN, Geneva, Mar, 2013.

[79] J. M. Campbell, R. K. Ellis, and C. Williams, *Vector boson pair production at the LHC*, JHEP **1107** (2011) 018, `arXiv:1105.0020 [hep-ph]`.

[80] CMS Collaboration, *Measurement of the WW, WZ and ZZ cross sections at CMS*, Tech. Rep. CMS-PAS-EWK-11-010, CERN, Geneva, 2011.

[81] CMS Collaboration, *Measurement of W^+W^- and ZZ production cross sections in pp collisions at $sqrt(s) = 8TeV$*, Phys. Lett. **B721** (2013) 190–211, `arXiv:1301.4698 [hep-ex]`.

[82] CMS Collaboration, S. Chatrchyan et al., *Measurement of the ZZ production cross section and nomalous gauge couplings limits in search for anomalous couplings in $2\ell2\ell'$ final states in pp collisions at $\sqrt{s} = 7$* TeV, JHEP **1301** (2013) 063, `arXiv:1211.4890 [hep-ex]`.

[83] CMS Collaboration, V. Khachatryan et al., *Measurement of the $pp \to ZZ$ production cross section and constraints on anomalous triple gauge couplings in four-lepton final states at $\sqrt{s}$ =8 TeV*, Phys. Lett. **B740** (2014) 250–272, `arXiv:1406.0113 [hep-ex]`.

[84] ATLAS, "Summary plots from the ATLAS Standard Model physics group." https://atlas.web.cern.ch/Atlas/GROUPS/PHYSICS/CombinedSummaryPlots/SM/index.html.

[85] CERN Press Office, "CERN Council gives go-ahead for Large Hadron Collider." http://press.web.cern.ch/press-releases/1994/12/cern-council-gives-go-ahead-large-hadron-collider, 1994.

[86] O. S. Brüning, P. Collier, P. Lebrun, S. Myers, R. Ostojic, et al., *LHC Design Report Vol.1: The LHC main ring*, Tech. Rep. CERN-2004-003-V1, CERN, Geneva, 2004.

[87] ATLAS Collaboration, *Technical proposal for a general-purpose pp experiment at the Large Hadron Collider at CERN*, tech. rep., CERN, Geneva, 1994.

[88] CMS Collaboration, *The Compact Muon Solenoid : technical proposal*, tech. rep., Geneva, 1994.

[89] CERN Press Office, "First beam in the LHC - accelerating science." http://press.web.cern.ch/press-releases/2008/09/first-beam-lhc-accelerating-science, Sept, 2008.

[90] CERN Timelines, "The Large Electron-Positron Collider: LEP's final shutdown." http://timeline.web.cern.ch/timelines/The-Large-Electron-Positron-Collider.

[91] S. Dailler, "Map of the Geneva region and of the LHC/Carte de la region lemanique avec l'emplacemen du LHC." AC Collection. Pictures from 1992 to 2002., Jul, 1997.

[92] Brüning, O. and Chohan, V. and Chattopadhyay, S., *Accelerator physics and technological challenges of the LHC*, in *Physics at the Large Hadron Collider*, A. Datta, B. Mukhopadhyaya, et al., eds. Springer India, 2009.

[93] A. Straessner, *Electroweak physics at LEP and LHC*, Springer Tracts Mod.Phys. **235** (2010) 1–211.

[94] D. Green, *At the leading edge: the ATLAS and CMS LHC experiments*. World Scientific, Singapore, 2010.

[95] http://public.web.cern.ch/public/en/research/AccelComplex-en.html.

[96] CERN Press Office, "CERN member states prepare for a decision on the Large Hadron Collider in June 1994." http://press.web.cern.ch/press-releases/1994/04/cern-member-states-prepare-decision-large-hadron-collider-june-1994.

[97] LARP Collaboration, A. P. Verweij et al., *Performance of the main dipole magnet circuits of the LHC during commissioning*, in *Particle accelerator. Proceedings, 11th European Conference, EPAC Genoa, Italy, June 23-27, 2008*, vol. C0806233, WEPD029.

[98] CERN Accelerators Coordination Unit, "Diagram of an LHC dipole magnet/Schéma d'un aimant dipôle du LHC." Jun, 1999.

[99] CERN, "Radiofrequency cavities." http://home.web.cern.ch/about/engineering/radiofrequency-cavities.

[100] M. Lamont, *The LHC's first long run*, CERN Courrier (2013).

[101] ATLAS Luminosity Group. https://twiki.cern.ch/twiki/bin/view/AtlasPublic/LuminosityPublicResults, 2008.

[102] CMS Luminosity Group. https://twiki.cern.ch/twiki/bin/view/CMSPublic/LumiPublicResults, 2008.

[103] ATLAS Collaboration, *The ATLAS experiment at the CERN Large Hadron Collider*, JINST **3** (2008) S08003.

[104] CMS Collaboration, *The CMS experiment at the CERN LHC*, JINST **3** (2008) S08004.

[105] LHCb Collaboration, J. Alves, A. Augusto et al., *The LHCb detector at the LHC*, JINST **3** (2008) S08005.

[106] ALICE Collaboration, K. Aamodt et al., *The ALICE experiment at the CERN LHC*, JINST **3** (2008) S08002.

[107] http://cdsweb.cern.ch/record/1095924.

[108] C. Wong, *Introduction to high-energy heavy-ion collisions*. World Scientific, Singapore, 1994.

[109] ATLAS Collaboration, *ATLAS high-level trigger, data-acquisition and controls: Technical design report*, Tech. Rep. CERN-LHCC-2003-022, ATLAS-TRD-016, CERN, Geneva, 2003.

[110] J. Haller, *The first-level trigger of ATLAS*, in *Proceedings, 2005 Europhysics Conference on High Energy Physics (EPS-HEP 2005)*, vol. HEP2005, 391. 2006. `arXiv:physics/0512195 [physics]`.

[111] ATLAS TDAQ Collaboration, T. Bold, *Commissioning ATLAS trigger*, `arXiv:0810.3269 [physics.ins-det]`.

[112] ATLAS Collaboration, T. Kono, *The ATLAS trigger menu for early data-taking*, in *Hadron collider physics. Proceedings, 19th Symposium, HCP2008, Galena, USA, May 27-31, 2008*. 2008. `arXiv:0808.4102 [hep-ex]`. http://inspirehep.net/record/794052/files/arXiv:0808.4102.pdf.

[113] http://atlas.web.cern.ch/Atlas/SUB_DETECTORS/DetStatus/DetStatus.html.

[114] ATLAS Collaboration, *ATLAS computing: Technical design report*, tech. rep., CERN, Geneva, 2005.

[115] G. Barrand, I. Belyaev, P. Binko, M. Cattaneo, R. Chytracek, et al., *GAUDI - A software architecture and framework for building HEP data processing applications*, Comput. Phys. Commun. **140** (2001) 45–55.

[116] W. Liebig, D. Rousseau, P. Calafiura, W. Lavrijsen, P. Loch, and A. Salzburger, *Physics-level job configuration*, in *15th International Conference on Computing in High Energy and Nuclear Physics (CHEP 06)*, S. Banerjee, ed., vol. 1 of *Macmillan Advanced Series*, 446–449. Macmillan, Mumbai, India, Feb, 2006.

[117] A. Buckley, J. Butterworth, S. Gieseke, D. Grellscheid, S. Hoche, et al., *General-purpose event generators for LHC physics*, Phys.Rept. **504** (2011) 145–233, `arXiv:1101.2599 [hep-ph]`.

[118] C. Ay, A. Buckley, J. Butterworth, J. Ferland, I. Hinchliffe, et al., *Monte Carlo generators in ATLAS software*, J. Phys. Conf. Ser. **219** (2010) 032001.

[119] S. Alioli, P. Nason, C. Oleari, and E. Re, *A general framework for implementing NLO calculations in shower Monte Carlo programs: the POWHEG BOX*, JHEP **1006** (2010) 043, `arXiv:1002.2581 [hep-ph]`.

[120] S. Frixione, P. Nason, and C. Oleari, *Matching NLO QCD computations with parton shower simulations: the POWHEG method*, JHEP **0711** (2007) 070, `arXiv:0709.2092 [hep-ph]`.

[121] N. Kauer, *Interference effects for* $H \to WW/ZZ \to \ell\bar{\nu}_\ell\bar{\ell}\nu_\ell$ *searches in gluon fusion at the LHC*, JHEP **1312** (2013) 082, `arXiv:1310.7011 [hep-ph]`.

[122] T. Binoth, N. Kauer, and P. Mertsch, *Gluon-induced QCD corrections to* $pp \to ZZ \to \ell\bar{\ell}\ell'\bar{\ell}'$, `arXiv:0807.0024 [hep-ph]`.

[123] T. Gleisberg, S. Hoeche, F. Krauss, M. Schonherr, S. Schumann, et al., *Event generation with SHERPA 1.1*, JHEP **0902** (2009) 007, `arXiv:0811.4622 [hep-ph]`.

[124] S. Frixione, F. Stoeckli, P. Torrielli, B. R. Webber, and C. D. White, *The MC@NLO 4.0 event generator*, `arXiv:1010.0819 [hep-ph]`.

[125] S. Frixione and B. R. Webber, *Matching NLO QCD computations and parton shower simulations*, JHEP **0206** (2002) 029, `arXiv:hep-ph/0204244 [hep-ph]`.

[126] T. Sjostrand, S. Mrenna, and P. Z. Skands, *A brief introduction to* PYTHIA *8.1*, Comput. Phys. Commun. **178** (2008) 852–867, `arXiv:0710.3820 [hep-ph]`.

[127] G. Corcella, I. Knowles, G. Marchesini, S. Moretti, K. Odagiri, et al., *HERWIG 6: An Event generator for hadron emission reactions with interfering gluons (including supersymmetric processes)*, JHEP **0101** (2001) 010, `arXiv:hep-ph/0011363 [hep-ph]`.

[128] M. Bahr, S. Gieseke, M. Gigg, D. Grellscheid, K. Hamilton, et al., *Herwig++ physics and manual*, Eur. Phys. J. **C58** (2008) 639–707, `arXiv:0803.0883 [hep-ph]`.

[129] J. Alwall, A. Ballestrero, P. Bartalini, S. Belov, E. Boos, et al., *A standard format for Les Houches event files*, Comput. Phys. Commun. **176** (2007) 300–304, `arXiv:hep-ph/0609017 [hep-ph]`.

[130] M. Dobbs and J. B. Hansen, *The HepMC C++ Monte Carlo event record for high energy physics*, Comput. Phys. Commun. **134** (2001) 41–46.

[131] GEANT4 Collaboration, S. Agostinelli et al., *GEANT4: A Simulation toolkit*, Nucl. Instrum. Meth. **A506** (2003) 250–303.

[132] J. Allison, K. Amako, J. Apostolakis, H. Araujo, P. Dubois, et al., *Geant4 developments and applications*, IEEE Trans. Nucl. Sci. **53** (2006) 270.

[133] K. Assamagan, G. Azuelos, S. Bahinipati, P. Banerjee, A. B. Galtieri, J. Collot, M. Davies, A. Gaponenko, A. Haas, J. Kraus, G. Lima, W. Lockman, A. Solodkov, G. Unal, A. Watson, and Y. Zhu, *Overlay for ATLAS Simulation*, Tech. Rep. ATL-SOFT-INT-2011-001, CERN, Geneva, Jul, 2011.

[134] G. Piacquadio, K. Prokofiev, and A. Wildauer, *Primary vertex reconstruction in the ATLAS experiment at LHC*, J. Phys. Conf. Ser. **119** (2008) 032033.

[135] ATLAS Collaboration, *Performance of primary vertex reconstruction in proton-proton collisions at* $\sqrt{s} = 7$ *TeV in the ATLAS experiment*, Tech. Rep. ATLAS-CONF-2010-069, CERN, Geneva, 2010.

[136] ATLAS Collaboration, *Performance of the ATLAS inner detector track and vertex reconstruction in the high pile-up LHC environment*, Tech. Rep. ATLAS-CONF-2012-042, CERN, Geneva, 2012.

[137] V. Lacuesta, *Track and vertex reconstruction in the ATLAS Experiment*, JINST **8** (2013) C02035.

[138] T. Cornelissen et al., *The new ATLAS track reconstruction (NEWT)*, J. Phys. Conf. Ser. **119** (2008) 032014.

[139] Frühwirth, R., *Application of Kalman filtering to track and vertex fitting*, Nucl. Instrum. Meth. **A262** (1987) 444–450.

[140] K. Benslama et al., *Tau trigger at the ATLAS experiment*, in *Proceedings, 34th International Conference on High Energy Physics (ICHEP 2008).* 2008. `arXiv:0810.0465 [hep-ex]`. http://weblib.cern.ch/abstract?ATL-DAQ-PROC-2008-001.

[141] ATLAS Collaboration, *Calorimeter clustering algorithms: description and performance*, Tech. Rep. ATL-LARG-PUB-2008-002, CERN, Geneva, Apr, 2008.

[142] ATLAS Collaboration, *Improved electron reconstruction in ATLAS using the Gaussian Sum Filter-based model for bremsstrahlung*, tech. rep., CERN, Geneva, 2012.

[143] ATLAS Collaboration, *Electron efficiency measurements with the ATLAS detector using the 2012 LHC proton-proton collision data,*. http://cds.cern.ch/record/1706245.

[144] M. Hance, *Measurement of inclusive isolated prompt photon production in proton-proton collisions at* $\sqrt{s} = 7$ *TeV with the ATLAS Detector.* PhD thesis, University of Pennsylvania, Philadelphia, Pennsylvania, USA, 2011.

[145] S. Laplace and J. de Vivie, *Calorimeter isolation and pile-up*, Tech. Rep. ATL-COM-PHYS-2012-467, CERN, Geneva, May, 2012. https://cds.cern.ch/record/1444890.

[146] ATLAS Collaboration, *Performance of the ATLAS trigger system in 2010*, Eur. Phys. J. **C72** (2012) 1849, `arXiv:1110.1530 [hep-ex]`.

[147] R. Nicolaidou et al., *Muon identification procedure for the ATLAS detector at the LHC using MuonBoy reconstruction package and tests of its performance using cosmic rays and single beam data*, J. Phys. Conf. Ser. **219** (2010) 032052.

[148] ATLAS Collaboration, *Measurement of the muon reconstruction performance of the ATLAS detector using 2011 and 2012 LHC proton-proton collision data*, Eur.Phys.J. **C74** no. 11, (2014) 3130, `arXiv:1407.3935 [hep-ex]`.

[149] M. Cacciari, G. P. Salam, and G. Soyez, *FastJet User Manual*, Eur.Phys.J. **C72** (2012) 1896, `arXiv:1111.6097 [hep-ph]`.

[150] T. J. Khoo, *The hunting of the squark: Experimental strategies in the search for supersymmetry at the Large Hadron Collider*. PhD thesis, University of Cambridge, Cambridge, UK, 2013.

[151] ATLAS Collaboration, *Performance of missing transverse momentum reconstruction in proton-proton collisions at 7 TeV with ATLAS*, Eur. Phys. J. **C72** (2012) 1844, `arXiv:1108.5602 [hep-ex]`.

[152] ATLAS Collaboration, *Performance of missing transverse momentum reconstruction in ATLAS studied in Proton-Proton Collisions recorded in 2012 at 8 TeV*, Tech. Rep. ATLAS-CONF-2013-082, CERN, Geneva, Aug, 2013.

[153] ATLAS Collaboration, *Pile-up suppression in missing transverse momentum reconstruction in the ATLAS experiment in proton-proton collisions at* $\sqrt{s} = 8$ *TeV*, Tech. Rep. ATLAS-CONF-2014-019, CERN, Geneva, May, 2014.

[154] ATLAS Collaboration, *Preliminary results on the muon reconstruction efficiency, momentum resolution, and momentum scale in ATLAS 2012 pp collision data*, Tech. Rep. ATLAS-CONF-2013-088, CERN, Geneva, Aug, 2013.

[155] ATLAS Collaboration, *Search for invisible decays of a Higgs boson produced in association with a Z boson in ATLAS*, Phys. Rev. Lett. **112** (2014) 201802, `arXiv:1402.3244 [hep-ex]`.

[156] M. Lamont, *Status of the LHC*, J. Phys. Conf. Ser. **455** no. 1, (2013) 012001. http://stacks.iop.org/1742-6596/455/i=1/a=012001.

[157] M. Kuhn, *LHC beam operations: past, present and future*, in *48th Rencontres de Moriond on QCD and High Energy Interactions*, J. Dumarchez, E. Augé, and J. Trân Thanh Vân, eds., 55–60. ARISF, La Thuile, Italy, Mar, 2013.

[158] S. van der Meer, *Calibration of the effective beam height in the ISR*, Tech. Rep. CERN-ISR-PO-68-31. ISR-PO-68-31, CERN, Geneva, 1968.

[159] ATLAS Luminosity Group, *Preliminary luminosity determination in pp collisions at* $\sqrt{s} = 8$ *TeV using the ATLAS detector in 2012*, Tech. Rep. ATL-COM-LUM-2012-013, CERN, Geneva, Nov, 2012.

[160] ATLAS Collaboration, *Luminosity determination in pp collisions at* $\sqrt{s} = 7$ *TeV using the ATLAS detector at the LHC*, Eur. Phys. J. **C71** (2011) 1630, `arXiv:1101.2185 [hep-ex]`.

[161] ATLAS Collaboration, *Improved luminosity determination in pp collisions at* $\sqrt{s} = 7$ *TeV using the ATLAS detector at the LHC*, Eur. Phys. J. **C73** no. 8, (2013) 2518, `arXiv:1302.4393 [hep-ex]`.

[162] W. Kozanecki, "Luminosity for physics." https://twiki.cern.ch/twiki/bin/view/Atlas/LuminosityForPhysics, 2015.

[163] T. Melia, P. Nason, R. Rontsch, and G. Zanderighi, *W^+W^-, WZ and ZZ production in the POWHEG BOX*, JHEP **1111** (2011) 078, `arXiv:1107.5051 [hep-ph]`.

[164] H.-L. Lai, M. Guzzi, J. Huston, Z. Li, P. M. Nadolsky, et al., *New parton distributions for collider physics*, Phys. Rev. **D82** (2010) 074024, `arXiv:1007.2241 [hep-ph]`.

[165] ATLAS Collaboration, *Summary of ATLAS Pythia 8 tunes*,. https://cds.cern.ch/record/1474107.

[166] P. Golonka and Z. Was, *Next to leading logarithms and the PHOTOS Monte Carlo*, Eur. Phys. J. **C50** (2007) 53–62, `arXiv:hep-ph/0604232 [hep-ph]`.

[167] N. Kauer, *Inadequacy of zero-width approximation for a light Higgs boson signal*, Mod.Phys. Lett. **A28** (2013) 1330015, `arXiv:1305.2092 [hep-ph]`.

[168] Kretzschmar, Jan. https://svnweb.cern.ch/trac/atlasoff/browser/Generators/MC12JobOptions/trunk/common/MultiLeptonFilter.py.

[169] D. Schaefer and E. Lipeles, *Evidence for the Higgs boson in the $H \rightarrow WW^{(*)} \rightarrow \ell\nu\ell\nu$ decay channel.* PhD thesis, University of Pennsylvania, Philadelphia, Pennsylvania, USA, 2014.

[170] Aoki, Masato. Private communication.

[171] ATLAS Collaboration, M. J. Woudstra, *Performance of the ATLAS muon trigger in pp collisions at $\sqrt{s} = 8$ TeV*, J. Phys. Conf. Ser. **513** (2014) 012040.

[172] M. Delmastro. https://twiki.cern.ch/twiki/bin/view/AtlasProtected/PhotonIDTool.

[173] Q. Buat. Private communication.

[174] K. Tackmann. Private communication.

[175] D. Olivito. Private communication.

[176] B. Lenzi, C. Royon, and M. Saimpert, *Data-driven corrections for the calorimeter isolation energy of photons computed from topological clusters*, Tech. Rep. ATL-COM-PHYS-2015-258, CERN, Geneva, Apr, 2015. https://cds.cern.ch/record/2008664.

[177] ATLAS Collaboration, *Expected performance of the ATLAS Experiment - detector, trigger and physics*, `arXiv:0901.0512 [hep-ex]`.

[178] M. Cacciari, G. P. Salam, and G. Soyez, *The anti-k_t jet clustering algorithm*, JHEP **0804** (2008) 063, `arXiv:0802.1189 [hep-ph]`.

[179] A. Vest. Private communication.

[180] S. Schramm. Private communication.

[181] E. Gozani. Private communication.

[182] ATLAS Collaboration, *Electron reconstruction and identification efficiency measurements with the ATLAS detector using the 2011 LHC proton-proton collision data*, Eur. Phys. J. **C74** no. 7, (2014) 2941, `arXiv:1404.2240 [hep-ex]`.

[183] DØ Collaboration, *High-p_T jets in $\bar{p}p$ collisions at $\sqrt{s} = 630$ GeV and 1800 GeV*, Phys.Rev. **D64** (2001) 032003, `arXiv:hep-ex/0012046 [hep-ex]`.

[184] UA2, Bern-CERN-Copenhagen-Orsay-Pavia-Saclay Collaboration, P. Bagnaia et al., *Measurement of jet production properties at the CERN $\bar{p}p$ collider*, Phys.Lett. **B144** (1984) 283.

[185] S. Ask, M. Parker, T. Sandoval, M. Shea, and W. Stirling, *Using γ+jets production to calibrate the Standard Model $Z(\to \nu\nu)$+jets background to new physics processes at the LHC*, JHEP **1110** (2011) 058, `arXiv:1107.2803 [hep-ph]`.

[186] ATLAS Collaboration, *Search for squarks and gluinos with the ATLAS detector in final states with jets and missing transverse momentum using 4.7 fb^{-1} of $\sqrt{s} = 7$ TeV proton-proton collision data*, Phys.Rev. **D87** no. 1, (2013) 012008, `arXiv:1208.0949 [hep-ex]`.

[187] J. M. Kunkle, *A search for dark matter through invisible decays of the Higgs boson with the ATLAS detector at the LHC*. PhD thesis, University of Pennsylvania, Philadelphia, Pennsylvania, USA, Jul, 2013. Presented 11 Jul 2013.

[188] ATLAS Collaboration, *Background studies for top-pair production in lepton plus jets final states in $\sqrt{s} = 7$ TeV ATLAS data*, Tech. Rep. ATLAS-CONF-2010-087, CERN, GENEVA, 2010.

[189] ATLAS Collaboration, B. Abi, *Top quark pair production cross section in ATLAS with early data*, `arXiv:1010.0148 [hep-ex]`.

[190] ATLAS Collaboration, *Search for a heavy neutral particle decaying into an electron and a muon using 1 fb^{-1} of ATLAS data*, Eur. Phys. J. **C71** (2011) 1809, `arXiv:1109.3089 [hep-ex]`.

[191] R. Barbieri and G. Giudice, *Upper bounds on supersymmetric particle masses*, Nucl. Phys. **B306** (1988) 63.

[192] B. de Carlos and J. Casas, *One loop analysis of the electroweak breaking in supersymmetric models and the fine tuning problem*, Phys. Lett. **B309** (1993) 320–328, `arXiv:hep-ph/9303291 [hep-ph]`.

[193] L. Randall and R. Sundrum, *A Large mass hierarchy from a small extra dimension*, Phys. Rev. Lett. **83** (1999) 3370–3373, `arXiv:hep-ph/9905221 [hep-ph]`.

[194] H. Davoudiasl, J. Hewett, and T. Rizzo, *Bulk gauge fields in the Randall-Sundrum model*, Phys. Lett. **B473** (2000) 43–49, `arXiv:hep-ph/9911262 [hep-ph]`.

[195] N. Arkani-Hamed, S. Dimopoulos, and G. Dvali, *The hierarchy problem and new dimensions at a millimeter*, Phys. Lett. **B429** (1998) 263–272, `arXiv:hep-ph/9803315 [hep-ph]`.

[196] G. Altarelli, B. Mele, and M. Ruiz-Altaba, *Searching for new heavy vector bosons in $p\bar{p}$ colliders*, Z. Phys. **C45** (1989) 109.

[197] E. Eichten and K. Lane, *Low-scale technicolor at the Tevatron and LHC*, Phys. Lett. **B669** (2008) 235–238, `arXiv:0706.2339 [hep-ph]`.

[198] M. T. Frandsen, *Minimal walking technicolor*, `arXiv:0710.4333 [hep-ph]`.

[199] J. Andersen, O. Antipin, G. Azuelos, L. Del Debbio, E. Del Nobile, et al., *Discovering technicolor*, Eur. Phys. J. Plus **126** (2011) 81, `arXiv:1104.1255 [hep-ph]`.

[200] K. Agashe, H. Davoudiasl, G. Perez, and A. Soni, *Warped gravitons at the LHC and beyond*, Phys. Rev. **D76** (2007) 036006, `arXiv:hep-ph/0701186 [hep-ph]`.

[201] G. Corcella, I. Knowles, G. Marchesini, S. Moretti, K. Odagiri, et al., *HERWIG 6.3 release note*, Tech. Rep. CAVENDISH-HEP-01-08, CERN-TH-2001-173, DAMTP-2001-61, 2001. `arXiv:hep-ph/0107071 [hep-ph]`.

[202] ATLAS Collaboration, *Measurements of four-lepton production at the Z resonance in pp collisions at $\sqrt{s} = 7$ and 8 TeV with ATLAS*, Phys. Rev. Lett. **112** no. 23, (2014) 231806, `arXiv:1403.5657 [hep-ex]`.

[203] ATLAS Collaboration, *Measurement of WZ production in proton-proton collisions at $\sqrt{s} = 7$ TeV with the ATLAS detector*, Eur. Phys. J. **C72** (2012) 2173, `arXiv:1208.1390 [hep-ex]`.

[204] ATLAS Collaboration, *Measurement of W^+W^- production in pp collisions at $\sqrt{s} = 7$ TeV with the ATLAS detector and limits on anomalous WWZ and $WW\gamma$ couplings*, Phys. Rev. **D87** no. 11, (2013) 112001, `arXiv:1210.2979 [hep-ex]`.

[205] F. Cascioli, T. Gehrmann, M. Grazzini, S. Kallweit, P. Maierhöfer, et al., *ZZ production at hadron colliders in NNLO QCD*, Phys. Lett. **B735** (2014) 311–313, `arXiv:1405.2219 [hep-ph]`.

[206] A. Martin, W. Stirling, R. Thorne, and G. Watt, *Heavy-quark mass dependence in global PDF analyses and 3- and 4-flavour parton distributions*, Eur.Phys.J. **C70** (2010) 51–72, `arXiv:1007.2624 [hep-ph]`.

[207] Duehrssen, Michael and others, *Supporting documentation for the off-shell Higgs signal strength measurements in $ZZ \to 4\ell$ and $ZZ \to 2\ell 2\nu$*, Tech. Rep. ATL-COM-PHYS-2014-1403, CERN, Geneva, Oct, 2014. https://cds.cern.ch/record/1957696.

[208] A. Bierweiler, T. Kasprzik, and J. H. Kühn, *Vector-boson pair production at the LHC to $\mathcal{O}(\alpha^3)$ accuracy*, JHEP **1312** (2013) 071, `arXiv:1305.5402 [hep-ph]`.

[209] J. Baglio, L. D. Ninh, and M. M. Weber, *Massive gauge boson pair production at the LHC: a next-to-leading order story*, Phys. Rev. **D88** (2013) 113005, `arXiv:1307.4331`.

[210] Gieseke, Stefan and Kasprzik, Tobias and Kühn, Johann H., *Vector-boson pair production and electroweak corrections in Herwig++*, Eur. Phys. J. **C74** no. 8, (2014) 2988, `arXiv:1401.3964 [hep-ph]`.

[211] J. Meyer and T. Kasprzik, *Reweighting method to incorporate higher order electroweak corrections into resonant heavy gauge boson pair production predictions*, Tech. Rep. ATL-COM-PHYS-2014-152, CERN, Geneva, Feb, 2014.

[212] W. Verkerke and D. P. Kirkby, *The RooFit toolkit for data modeling*, in *Statistical problems in particle physics, astrophysics and cosmology. Proceedings, Conference, PHYSTAT05, Oxford, UK, September 12-15, 2005*, vol. C0303241, MOLT007. 2005. `arXiv:physics/0306116 [physics]`. [,186(2003)].

[213] F. James and M. Roos, *Minuit: A system for function minimization and analysis of the parameter errors and correlations*, Comput. Phys. Commun. **10** (1975) 343–367.

[214] I. W. Stewart and F. J. Tackmann, *Theory uncertainties for Higgs and other searches using jet bins*, Phys.Rev. **D85** (2012) 034011, `arXiv:1107.2117 [hep-ph]`.

[215] ATLAS Collaboration, *Constraints on the off-shell Higgs boson signal strength in the high-mass ZZ and WW final states with the ATLAS detector*, Eur. Phys. J. **C75** no. 7, (2015) 335, `arXiv:1503.01060 [hep-ex]`.

[216] D. Curtin, P. Meade, and P.-J. Tien, *Natural SUSY in Plain Sight*, Phys.Rev. **D90** no. 11, (2014) 115012, `arXiv:1406.0848 [hep-ph]`.

[217] P. Jaiswal and T. Okui, *Explanation of the WW excess at the LHC by jet-veto resummation*, Phys.Rev. **D90** no. 7, (2014) 073009, `arXiv:1407.4537 [hep-ph]`.

[218] E. S. Protopapadaki, *ZZ diboson measurements with the ATLAS detector at the LHC and study of the toroidal magnetic field sensors*. PhD thesis, Université Paris-Sud, Orsay, France, 2014.

[219] K. Gregersen, *Anomalous trilinear gauge couplings in ZZ production at the ATLAS experiment*. PhD thesis, University of Copenhagen, Copenhagen, Denmark, Jul, 2013.

[220] J. B. Hansen and K. Gregersen. Private communication.

[221] G. Bella, *Weighting di-boson Monte Carlo events in hadron colliders*, `arXiv:0803.3307 [hep-ph]`.

[222] U. Baur, T. Han, and J. Ohnemus, *QCD corrections to hadronic $W\gamma$ production with nonstandard $WW\gamma$ couplings*, Phys.Rev. **D48** (1993) 5140–5161, `arXiv:hep-ph/9305314 [hep-ph]`.

[223] U. Baur, T. Han, and J. Ohnemus, *WZ production at hadron colliders: Effects of nonstandard WWZ couplings and QCD corrections*, Phys.Rev. **D51** (1995) 3381–3407, `arXiv:hep-ph/9410266 [hep-ph]`.

[224] U. Baur, T. Han, and J. Ohnemus, *QCD corrections and nonstandard three vector boson couplings in W^+W^- production at hadron colliders*, Phys.Rev. **D53** (1996) 1098–1123, `arXiv:hep-ph/9507336 [hep-ph]`.

[225] D. Casadei, *Statistical methods used in ATLAS for exclusion and discovery*, Tech. Rep. ATL-PHYS-SLIDE-2011-015, 2011. `arXiv:1108.2288 [physics.data-an]`.

[226] ATLAS Statistics Forum, "Frequentist limit recommendation." https://twiki.cern.ch/twiki/pub/AtlasProtected/StatisticsTools/Frequentist_Limit_Recommendation.pdf, 2011.

[227] J. Neyman and E. S. Pearson, *On the problem of the most efficient tests of statistical hypotheses*, Royal Society of London Philosophical Transactions Series A **231** (1933) 289–337.

[228] https://root.cern.ch/root/html/RooProfileLL.html.

[229] G. Cowan, K. Cranmer, E. Gross, and O. Vitells, *Asymptotic formulae for likelihood-based tests of new physics*, Eur. Phys. J. **C71** (2011) 1554, `arXiv:1007.1727 [physics.data-an]`.

[230] S. S. Wilks, *The large-sample distribution of the likelihood ratio for testing composite hypotheses*, Ann. Math. Statist. **9** no. 1, (1938) 60–62. http://dx.doi.org/10.1214/aoms/1177732360.

[231] CMS Collaboration, V. Khachatryan et al., *Measurements of the ZZ production cross sections in the $2\ell 2\nu$ channel in proton-proton collisions at $\sqrt{s}$ = 7 and 8 TeV and combined constraints on triple gauge couplings*, `arXiv:1503.05467 [hep-ex]`.

[232] J. Robinson, "Luminosity working group." https://twiki.cern.ch/twiki/bin/view/Atlas/LuminosityGroup, 2014.

[233] ATLAS Collaboration, *Observation of a new particle in the search for the Standard Model Higgs boson with the ATLAS detector at the LHC*, Phys. Lett. **B716** (2012) 1–29, `arXiv:1207.7214 [hep-ex]`.

[234] ATLAS Collaboration, *Measurements of the properties of the Higgs-like boson in the $WW^{(*)} \to \ell\nu\ell\nu$ decay channel with the ATLAS detector using 25 fb^{-1} of proton-proton collision data*, Tech. Rep. ATLAS-CONF-2013-030, CERN, Geneva, Mar, 2013.

[235] ATLAS Collaboration, *Search for Higgs boson decays to a photon and a Z boson in pp collisions at $\sqrt{s}$ =7 and 8 TeV with the ATLAS detector*, Phys. Lett. **B732** (2014) 8–27, `arXiv:1402.3051 [hep-ex]`.

[236] DØ Collaboration, *Observation of ZZ production in $p\bar{p}$ collisions at $\sqrt{s} = 1.96$ TeV*, Phys. Rev. Lett. **101** (2008) 171803, `arXiv:0808.0703 [hep-ex]`.

[237] Fermilab, "Prelude to the higgs: A work for two bosons in the key of z." http://www.fnal.gov/pub/presspass/press_releases/Dzero_zzdiboson.html, 2008.

[238] DØ Collaboration, *$ZZ \to \ell^+\ell^-\nu\bar{\nu}$ Production in $p\bar{p}$ Collisions at $\sqrt{s} = 1.96$ TeV*, Phys. Rev. **D78** (2008) 072002, `arXiv:0808.0269 [hep-ex]`.

[239] DØ Collaboration, *Search for ZZ and* $Z\gamma^*$ *production in* $p\bar{p}$ *collisions at* $\sqrt{s} = 1.96$ *TeV and limits on anomalous ZZZ and* $ZZ\gamma^*$ *couplings*, Phys. Rev. Lett. **100** (2008) 131801, `arXiv:0712.0599 [hep-ex]`.

[240] OPAL Collaboration, W^+W^- *production and triple gauge boson couplings at LEP energies up to 183 GeV*, Eur. Phys. J. **C8** (1999) 191–215, `arXiv:hep-ex/9811028 [hep-ex]`.

[241] ALEPH Collaboration, R. Barate et al., *Measurement of the W mass in* e^+e^- *collisions at production threshold*, Phys. Lett. **B401** (1997) 347–362.

[242] V. Barger, *Collider Physics*. Addison-Wesley, Redwood City, California, 1987.

[243] U. Baur, R. K. Ellis, and D. Zeppenfeld, *QCD and weak boson physics in Run II. Proceedings, Batavia, USA, March 4-6, June 3-4, November 4-6, 1999*, Tech. Rep. FERMILAB-PUB-00-297, December, 2000.

[244] I. Brock and T. e. Sadenius, *Physics at the terascale*. Wiley-VCH, Weinheim, Germany, 2011.

[245] R. D. Field, *Applications of perturbative QCD*. Addison-Wesley, Redwood City, California, 1989.

[246] J. Ellison and J. Wudka, *Study of trilinear gauge boson couplings at the Tevatron collider*, Ann. Rev. Nucl. Part. Sci. **48** (1998) 33–80, `arXiv:hep-ph/9804322 [hep-ph]`.

[247] M. S. Bilenky, J. Kneur, F. Renard, and D. Schildknecht, *Trilinear couplings among the electroweak vector bosons and their determination at LEP-200*, Nucl. Phys. **B409** (1993) 22–68.

[248] D. J. Griffiths, *Introduction to elementary particles; 2nd rev. ed.* Wiley, New York, 2008.

[249] D. Ross, *Foundations of the Standard Model*, in *Large Hadron Collider phenomenology: proceedings of the fifty seventh Scottish Universities summer school in physics, St. Andrews, 17 August to 29 August 2003*, M. Krämer and F. Soler, eds. Scottish Universities Summer School in Physics; Institute of Physics Pub, Edinburgh, 2004.

[250] E. Leader, *Introduction to gauge theories and modern particle physics*. Cambridge University Press, Cambridge, UK, 1996.

[251] Y. Nagashima, *Elementary particle physics, Vol. 1: Quantum Field Theory and Particles*. Wiley-VCH, Weinheim, Germany, 2010.

[252] M. E. Peskin and D. V. Schroeder, *An introduction to quantum field theory*. Westview, Boulder, Colorado, 1995.

[253] S. Roth, *Precision electroweak physics at electron-positron colliders*. Springer Tracts in Modern Physics. Springer, Berlin, Germany, 2007.

[254] R. Stock, *Encyclopedia of applied high energy and particle physics*. Wiley-VCH, Weinheim, Germany, 2009.

[255] Tevatron New Physics Higgs Working Group, CDF Collaboration, DØ Collaboration, *Updated combination of CDF and DØ searches for Standard Model Higgs boson production with up to 10.0 fb*$^{-1}$ *of data*, `arXiv:1207.0449 [hep-ex]`.

[256] J. M. Campbell, R. K. Ellis, and C. Williams, *Gluon-gluon contributions to* W^+W^- *production and Higgs interference effects*, JHEP **1110** (2011) 005, `arXiv:1107.5569 [hep-ph]`.

[257] E. N. Glover and J. van der Bij, *Vector boson pair production via gluon fusion*, Phys. Lett. **B219** (1989) 488.

[258] E. N. Glover and J. van der Bij, *Z boson pair production via gluon fusion*, Nucl. Phys. **B321** (1989) 561.

[259] N. Kauer, *Signal-background interference in* $gg \to H \to VV$, in *RADCOR 2011, 10*th *international symposium on radiative corrections (applications of quantum field theory to phenomenology)*, R. Basu et al., eds. Mahabalipuram, India, Sep, 2011. `arXiv:1201.1667 [hep-ph]`.

[260] C. F. Berger, J. S. Gainer, J. L. Hewett, and T. G. Rizzo, *Supersymmetry Without Prejudice*, JHEP **02** (2009) 023, `arXiv:0812.0980 [hep-ph]`.

[261] P. Fayet, *Supersymmetry and weak, electromagnetic and strong interactions*, Phys. Lett. **B64** (1976) 159.

[262] P. Fayet, *Spontaneously broken supersymmetric theories of weak, electromagnetic and strong interactions*, Phys. Lett. **B69** (1977) 489.

[263] G. R. Farrar and P. Fayet, *Phenomenology of the production, decay, and detection of new hadronic states aAssociated with Supersymmetry*, Phys. Lett. **B76** (1978) 575–579.

[264] P. Fayet, *Relations between the masses of the superpartners of leptons and quarks, the goldstino couplings and the ceutral currents*, Phys. Lett. **B84** (1979) 416.

[265] S. Dimopoulos and H. Georgi, *Softly broken supersymmetry and SU(5)*, Nucl. Phys. **B193** (1981) 150.

[266] S. Weinberg, *Implications of dynamical symmetry breaking*, Phys. Rev. **D13** (1976) 974–996.

[267] L3 Collaboration, P. Achard et al., *Study of the* $e^+e^- \to Z\gamma$ *process at LEP and limits on triple neutral-gauge-boson couplings*, Phys. Lett. **B597** (2004) 119–130, `arXiv:hep-ex/0407012 [hep-ex]`.

[268] CDF Collaboration, *First measurement of ZZ production in* $p\bar{p}$ *collisions at* $\sqrt{s} = 1.96$ *TeV*, Phys. Rev. Lett. **100** (2008) 201801, `arXiv:0801.4806 [hep-ex]`.

[269] CERN Press Office, “The first LHC protons run ends with new milestone.” http://press.web.cern.ch/press-releases/2012/12/first-lhc-protons-run-ends-new-milestone, 2012.

[270] O. S. Brüning, P. Collier, P. Lebrun, S. Myers, R. Ostojic, et al., *LHC Design Report. 2. The LHC infrastructure and general services*, Tech. Rep. CERN-2004-003-V-2, CERN, Geneva, 2004.

[271] CERN, *ATLAS: Letter of intent for a general-purpose pp experiment at the Large Hadron Collider at CERN*, Tech. Rep. CERN-LHCC-92-04, CERN-LHCC-I-2, CERN, Geneva, 1992.

[272] L. Evans and P. Bryant, *LHC machine*, JINST **3** (2008) S08001.

[273] ATLAS Collaboration, *Electron performance measurements with the ATLAS detector using the 2010 LHC proton-proton collision data*, Eur. Phys. J. **C72** (2012) 1909, `arXiv:1110.3174 [hep-ex]`.

[274] ATLAS Collaboration, *A measurement of the muon reconstruction efficiency in 2010 ATLAS data using jpsi decays*, Tech. Rep. ATLAS-CONF-2012-125, CERN, Geneva, Aug, 2012.

[275] ATLAS Collaboration, *Muon reconstruction efficiency and momentum resolution of the ATLAS experiment in proton-proton collisions at* $\sqrt{s}$ *= 7 TeV in 2010*, Eur.Phys.J. **C74** no. 9, (2014) 3034, `arXiv:1404.4562 [hep-ex]`.

[276] ATLAS Collaboration, *Jet energy scale and its systematic uncertainty for jets produced in proton-proton collisions at rts* $= 7$ *TeV and measured with the ATLAS detector*, Tech. Rep. ATLAS-CONF-2010-056, CERN, Geneva, 2010.

[277] ATLAS Collaboration, *Jet energy scale and its systematic uncertainty in proton-proton collisions at* $\sqrt{s} = 7$ *TeV in ATLAS 2010 data*, Tech. Rep. ATLAS-CONF-2011-032, CERN, Geneva, 2011.

[278] ATLAS Collaboration, *Jet energy scale and its systematic uncertainty in proton-proton collisions at rts* $= 7$ *TeV with ATLAS 2011 data*, Tech. Rep. ATLAS-CONF-2013-004, ATLAS-COM-CONF-2012-171, CERN, Geneva, 2013.

[279] ATLAS Collaboration, *Jet energy measurement with the ATLAS detector in proton-proton collisions at* $\sqrt{s} = 7$ *TeV*, Eur.Phys.J. **C73** no. 3, (2013) 2304, `arXiv:1112.6426 [hep-ex]`.

[280] ATLAS Collaboration, *Jet energy resolution in proton-proton collisions at* $\sqrt{s} = 7$ *TeV recorded in 2010 with the ATLAS detector*, Eur.Phys.J. **C73** no. 3, (2013) 2306, `arXiv:1210.6210 [hep-ex]`.

[281] T. Barillari, *Jet Energy Scale Uncertainties in ATLAS*, CERN. CERN, Geneva, 2012. http://cdsweb.cern.ch/record/1473875/files/ATL-PHYS-PROC-2012-137.pdf.

[282] P. Loch, *Jet measurements in ATLAS*, in *Jet reconstruction and spectroscopy at hadron colliders. Proceedings, Workshop, Pisa, Italy, April 18-19, 2011*, vol. 323, 012002. 2011.

[283] ATLAS Collaboration, *Single hadron response measurement and calorimeter jet energy scale uncertainty with the ATLAS detector at the LHC*, Eur.Phys.J. **C73** no. 3, (2013) 2305, `arXiv:1203.1302 [hep-ex]`.

[284] T. Barber, *New physics searches in the ZZ sector with the ATLAS experiment*. PhD thesis, University of Cambridge, Cambridge, UK, February, 2011.

[285] C. Bierlich, *Limits on triple gauge boson couplings: Limits on the TGCs of the WWZ vertex using 827.87 pb^{-1} of data, recorded with the ATLAS detector at the LHC at $\sqrt{s} = 7$ TeV*. PhD thesis, University of Copenhagen, Copenhagen, Denmark, 2012.

[286] W. Buttinger, *ZZ production and limits on anomalous triple gauge couplings with the ATLAS experiment at the LHC*. PhD thesis, University of Cambridge, Cambridge, UK, 2013.

[287] M. Dobbs, *Probing the three gauge-boson couplings in 14 TeV proton-proton collisions*. PhD thesis, University of Victoria, Victoria, British Columbia, Canada, 2002.

[288] C. Doglioni, *Measurement of the inclusive jet cross section with the ATLAS detector at the Large Hadron Collider*. PhD thesis, University of Oxford, Oxford, UK, 2011.

[289] N. Edwards, *Measurement of the ZZ production cross section and limits on anomalous neutral triple gauge couplings with the ATLAS detector*. PhD thesis, University of Glasgow, Glasgow, UK, Jul, 2013. Presented 13 Jun 2013.

[290] D. Hall, *Discovery and measurement of the Higgs boson in the WW decay channel*. PhD thesis, University of Oxford, Oxford, UK, Aug, 2014.

[291] ATLAS Collaboration, *Performance of missing transverse momentum reconstruction in ATLAS with 2011 proton-proton collisions at $\sqrt{s} = 7$ TeV*, Tech. Rep. ATLAS-CONF-2012-101, CERN, Geneva, Jul, 2012.

[292] D. J. Gross and F. Wilczek, *Ultraviolet behavior of non-abelian gauge theories*, Physical Review Letters **30** (1973) 1343–1346. http://link.aps.org/doi/10.1103/PhysRevLett.30.1343.

[293] D. Gross and F. Wilczek, *Asymptotically free gauge theories. I*, Phys.Rev. **D8** (1973) 3633–3652.

[294] D. Gross and F. Wilczek, *Asymptotically free gauge theories. II.*, Phys.Rev. **D9** (1974) 980–993.

[295] ATLAS Statistics Forum, *The CL_s method: information for conference speakers*, Jul, 2011. www.pp.rhul.ac.uk/~cowan/stat/cls/CLsInfo.ps.

[296] ATLAS Statistics Forum, *Frequentist limit recommendation Implementation*, 2012. https://twiki.cern.ch/twiki/bin/viewauth/AtlasProtected/FrequentistLimitRecommendationImplementation.

[297] M. Kayl, *Tracking performance of the ATLAS inner detector and observation of known hadrons*, `arXiv:1010.1091 [physics.ins-det]`.

[298] K. Prokofiev, *Reconstruction of primary vertices in pp collisions at energies of 900 GeV and 7 TeV with the ATLAS detector*, `arXiv:1010.1483 [physics.ins-det]`.

[299] A. Martin, W. Stirling, R. Thorne, and G. Watt, *Uncertainties on α_S in global PDF analyses and implications for predicted hadronic cross sections*, Eur. Phys. J. **C64** (2009) 653–680, `arXiv:0905.3531 [hep-ph]`.

[300] A. Martin, W. Stirling, R. Thorne, and G. Watt, *Parton distributions for the LHC*, Eur. Phys. J. **C63** (2009) 189–285, `arXiv:0901.0002 [hep-ph]`.

[301] ATLAS Collaboration, K. Nagano, *Algorithms, performance, development of the ATLAS High-Level Trigger*, in *Proceedings, 20^{th} international conference on computing in high energy and nuclear physics (CHEP 2013)*, vol. 513, 012026. 2014.

[302] Matsushita, Takashi. Private communication.

[303] ATLAS Collaboration Collaboration, *ATLAS detector and physics performance: Technical design report, 1*. CERN, Geneva, 1999. https://cds.cern.ch/record/391176.

[304] ATLAS Collaboration Collaboration, *ATLAS detector and physics performance: Technical Design Report, 2*. CERN, Geneva, 1999. https://cds.cern.ch/record/391177.

[305] ATLAS Collaboration, *Expected photon performance in the ATLAS experiment*, Tech. Rep. ATL-PHYS-PUB-2011-007, ATL-COM-PHYS-2010-1051, CERN, Geneva, 2011.

[306] S. Maxfield. Private communication.

[307] CMS Collaboration, *Measurement of ZZ production cross section at 7 and 8 TeV and anomalous gauge couplings limits in $2\ell2\nu$ decay channel*, Tech. Rep. CMS-PAS-SMP-12-016, CERN, Geneva, 2013.

[308] F. James, *Determining the statistical significance of experimental results*, in *CERN School of Computing 1980*, no. CERN-DD-81-02, C80-09-14-3, 182. 1981.

[309] ATLAS Collaboration, *Search for an invisibly decaying Higgs boson produced via vector boson fusion pp collisions at $\sqrt{s} = 8$ TeV using the ATLAS Detector at the LHC*, Tech. Rep. ATLAS-COM-CONF-2015-004, CERN, Geneva, 2015.

[310] A. Collaboration, *SUSY searches with dileptons and high missing transverse momentum*, Tech. Rep. ATL-COM-PHYS-2010-1045, CERN, Geneva, Dec, 2010. https://cds.cern.ch/record/1314226.

[311] J. A. Bagger and L. S. Littenberg, *Physics beyond the standard model*, in *1990 DPF Summer Study on high-energy physics: Research directions for the decade (Snowmass 90) Snowmass, Colorado, June 25-July 13, 1990*, 179–181. 1990.

[312] Particle Data Group Collaboration, C. Amsler et al., *Review of particle physics*, Phys. Lett. **B667** (2008) 1–1340.

[313] Atlas Collaboration, *Performance of the ATLAS detector using first collision data*, JHEP **1009** (2010) 056, `arXiv:1005.5254 [hep-ex]`.

[314] F. Campabadal, C. Fleta, M. Key, M. Lozano, C. Martinez, et al., *Design and performance of the ABCD3TA ASIC for readout of silicon strip detectors in the ATLAS semiconductor tracker*, Nucl. Instrum. Meth. **A552** (2005) 292–328.

[315] S. Terada, H. Kobayashi, H. Sengoku, Y. Kato, K. Hara, et al., *Design and development of a work robot to place ATLAS SCT modules onto barrel cylinders*, Nucl. Instrum. Meth. **A541** (2005) 144–149.

[316] S. Dawson and H. E. Haber, *Electroweak symmetry breaking and physics beyond the Standard Model*, in *Electroweak symmetry breaking and new physics at the TeV scale*, T. Barklow, S. Dawson, H. Haber, and J. L. Siegrist, eds., vol. 16 of *Advanced Series on Directions in High Energy Physics*. World Scientific, 1996. `arXiv:hep-ph/9604354 [hep-ph]`.

[317] E. Abat et al., *The ATLAS TRT barrel detector*, JINST **3** (2008) P02014.

[318] Sandaker, H., *The read-out and control system for the ATLAS SemiConductor Tracker*, Nucl. Instrum. Meth. **A541** (2005) 96–103.

[319] M. P. Giordani, *Top physics at the LHC*, in *Deep inelastic scattering. Proceedings, 14th International Workshop, DIS 2006, Tsukuba, Japan, April 20-24, 2006*, 317–320. 2006.

[320] CDF, DØ Collaboration, T. Aaltonen et al., *Combined CDF and DØ upper limits on Standard Model Higgs boson production with up to 8.2 fb^{-1} of data*, `arXiv:1103.3233 [hep-ex]`.

[321] M. Wielers, *Simulation studies of the jet and missing transverse energy performance of the ATLAS calorimeters*, in *Calorimetry in particle physics. Proceedings, 10th International Conference, CALOR 2002, Pasadena, USA, March 25-29, 2002*, 367–374. 2002.

[322] L. Tompkins, *Performance of the ATLAS Minimum bias trigger in p-p collisions at the LHC*, Tech. Rep. ATL-DAQ-SLIDE-2010-242, Aug, 2010. `arXiv:1009.6133 [hep-ex]`.

[323] A. Abdesselam, *ATLAS SCT endcap module production*, Tech. Rep. ATL-INDET-PUB-2006-007. ATL-COM-INDET-2006-008, CERN, Geneva, Jul, 2006.

[324] A. Abdesselam, T. Akimoto, P. Allport, J. Alonso, B. Anderson, et al., *The barrel modules of the ATLAS semiconductor tracker*, Nucl. Instrum. Meth. **A568** (2006) 642–671.

[325] ATLAS Collaboration, A. Abdesselam et al., *The ATLAS semiconductor tracker end-cap module*, Nucl. Instrum. Meth. **A575** (2007) 353–389.

[326] ATLAS SCT Collaboration, L. Feld, *Detector modules for the ATLAS SCT endcaps*, Nucl. Instrum. Meth. **A511** (2003) 183–186.

[327] ATLAS Collaboration, *The ATLAS simulation infrastructure*, Eur. Phys. J. **C70** (2010) 823–874. 53 p, `arXiv:1005.4568 [physics.ins-det]`.

[328] ATLAS Collaboration, *The ATLAS Inner Detector commissioning and calibration*, Eur. Phys. J. **C70** (2010) 787–821, `arXiv:1004.5293 [physics.ins-det]`.

[329] ATLAS Collaboration, P. Haefner, *The ATLAS silicon microstrip tracker. Operation and performance*, JINST **5** (2010) C12050. http://stacks.iop.org/1748-0221/5/i=12/a=C12050.

[330] N. P. Konstantinidis et al., *Architecture of the ATLAS High Level trigger event selection software*, in *Frontier detectors for frontier physics. Proceedings, 9th Pisa Meeting on advanced detectors, La Biodola, Italy, May 25-31, 2003.* 2003. http://weblib.cern.ch/abstract?ATL-DAQ-2003-046.

[331] ATLAS High Level Trigger Collaboration, M. Grothe et al., *Architecture of the ATLAS High Level Trigger event selection software*, Nucl. Instrum. Meth. **A518** (2003) WEPT004, `arXiv:physics/0306097 [physics]`.

[332] A. Abdesselam, T. Barber, A. Barr, P. Bell, J. Bernabeu, et al., *The data acquisition and calibration system for the ATLAS Semiconductor Tracker*, JINST **3** (2008) P01003.

[333] B. Demirköz, *Construction and performance of the ATLAS SCT barrels and cosmic tests*. PhD thesis, University of Oxford, Oxford, UK, April, 2007.

[334] E. Coniavitis, A. Okamoto, and R. Tanaka, *Lorentz angle and cluster width studies for the ATLAS SCT*, Tech. Rep. ATL-COM-INDET-2009-039, CERN, Geneva, Jun, 2009. Reviewed several times in the SCT. Approved by PL.

[335] T. Lari, *Lorentz angle variation with electric field for ATLAS silicon detectors*, Tech. Rep. ATL-INDET-2001-004, CERN, Geneva, Apr, 2001.

[336] T. Lari, *A Geant4 simulation of not irradiated and irradiated pixel detectors*, Tech. Rep. ATL-INDET-2003-015, CERN, Geneva, Aug, 2003.

[337] P. Vankov, *ATLAS silicon microstrip tracker operation and performance*, Tech. Rep. ATL-COM-INDET-2010-152, CERN, Geneva, Nov, 2010.

[338] S. Gadomski, *Model of the SCT detectors and electronics for the ATLAS simulation using Geant4*, Tech. Rep. ATL-SOFT-2001-005, CERN, Geneva, May, 2001.

[339] A. Ahmad et al., *The silicon microstrip sensors of the ATLAS Semiconductor Tracker*, Nucl. Instrum. Meth. **A578** (2007) 98–118.

[340] N. Amapane, *Precision electroweak measurements at ATLAS and CMS*, Springer Proc.Phys. **108** (2006) 91–95.

[341] T. Virdee, *Particle Detection at the LHC: an Introduction*,.

[342] J. W. Rohlf, *Physics with jets at the LHC*, Acta Phys. Pol. B **36** (2005) 469–479.

[343] http://cms.web.cern.ch/cms/Media/Images/Detector/index.html.

[344] A. Christos, “Atlas regular computing tutorial.” https://twiki.cern.ch/twiki/bin/viewauth/Atlas/PatTutorial1520.

[345] S. Fratina. https://twiki.cern.ch/twiki/bin/viewauth/Atlas/TRTEventPhase.

[346] H.-A. Gustafsson, *Status of the ALICE detector at LHC*, in *Hadron Collider Physics 2005: Proceedings of the 1st Hadron Collider Physics Symposium, Les Diablerets, Switzerland, July 4-9, 2005*, M. Campanelli, A. Clark, and X. Wu, eds., vol. 108 of *Springer Proceedings in Physics*. Springer, 2006.

[347] D0 Collaboration, M. A. Strang, *Diboson Production at D0*, in *Particles and fields. Proceedings, Meeting of the Division of the American Physical Society, DPF 2009, Detroit, USA, July 26-31, 2009*. 2009. `arXiv:0912.1622 [hep-ex]`. http://lss.fnal.gov/cgi-bin/find_paper.pl?conf-09-620.

[348] A. Salam and J. C. Ward, *Weak and electromagnetic interactions*, Nuovo Cim. **11** (1959) 568–577.

[349] A. Salam and J. C. Ward, *On a gauge theory of elementary interactions*, Nuovo Cim. **19** (1961) 165–170.

[350] A. Salam and J. C. Ward, *Electromagnetic and weak interactions*, Phys. Lett. **13** (1964) 168–171.

[351] J. Goldstone, A. Salam, and S. Weinberg, *Broken Symmetries*, Phys. Rev. **127** (1962) 965–970.

[352] http://cms.web.cern.ch/cms/Media/Images/Detector/index.html.

[353] A. Massafferri Rodrigues et al. http://cms.web.cern.ch/cms/Media/Images/Detector/index.html.

[354] http://aliceinfo.cern.ch/Public/en/Chapter2/Chap2Experiment-en.html.

[355] https://twiki.cern.ch/twiki/bin/viewauth/Atlas/InnerDetector.

[356] http://project\discretionary-atlas\discretionary-lucid.web.cern.ch/project\discretionary-atlas\discretionary-lucid/taskforce/main.html.

[357] http://dept.physics.upenn.edu/hepex/atlasoverview.html.

[358] S. Sjöstrand, S. Mrenna, and P. Skands, *PYTHIA 6.4 physics and manual*, J. High Energy Phys. **05** no. 026, (2006), `arXiv:0603175 [hep-ph]`.

[359] M. Mangano et al., *ALPGEN, a generator for hard multiparton processes in hadronic collisions*, J. High Energy Phys. **07** no. 001, (2003), `arXiv:0206293 [hep-ph]`.

[360] C. Corcella et al., *HERWIG 6: An event generator for hadron emission reactions with interfering gluons (including supersymmetric processes)*, J. High Energy Phys. **01** no. 010, (2001), `arXiv:0011363 [hep-ph]`.

[361] T. Gleisberg et al., *Sherpa 1.alpha, A proof-of-concept version*, J. High Energy Phys. **02** no. 056, (2004), `arXiv:0311263 [hep-ph]`.

[362] F. Cascioli, P. Maierhofer, and S. Pozzorini, *Scattering amplitudes with open loops*, Phys. Rev. Lett. **108** (2012) 111601, `arXiv:1111.5206 [hep-ph]`.

[363] A. van Hameren, *Multi-gluon one-loop amplitudes using tensor integrals*, JHEP **0907** (2009) 088, `arXiv:0905.1005 [hep-ph]`.

[364] J. Bystrický and J. C. Vermeulen, *Paper modelling of the ATLAS LVL2 trigger system*, Tech. Rep. ATL-DAQ-2000-030, CERN, Geneva, Mar, 2000.

[365] F. Gianotti, *ATLAS Has Recorded 1/fb*, 2011. Internal communication to ATLAS collaboration.

[366] CDF, DØ Collaboration, M. P. Sanders, *Measuring the W boson mass at the Tevatron*, in *22nd Rencontres de Blois on Particle Physics and Cosmology Blois, Loire Valley, France, July 15-20, 2010*. 2010. `arXiv:1009.2903 [hep-ex]`. http://lss.fnal.gov/cgi-bin/find_paper.pl?conf-10-363.

[367] CDF Collaboration, E. D. Lipeles, *WW and WZ production at the Tevatron*, in *Proceedings of the 33rd international conference on high energy physics (ICHEP ’06)*, 689–692. 2006. `arXiv:hep-ex/0701038 [hep-ex]`.

Appendix A

Simulated signal and background samples for the ZZ analysis

This appendix lists the simulated samples used for the ZZ signal and background estimates, as well as samples used to make performance plots.

MCID	Process	Generator	N_{events}	k-factor	$\varepsilon_{\text{filter}}$	cross section [pb]
108343	Single top s-channel $W \to e\nu$	MC@NLO	199997	1	1	0.606
108344	Single top s-channel $W \to e\nu$	MC@NLO	200000	1	1	0.606
108345	Single top s-channel $W \to \tau\nu$	MC@NLO	199999	1	1	0.606
117360	Single top t-channel	AcerMC/PYTHIA	299899	1	1	9.48
117361	Single top t-channel	AcerMC/PYTHIA	300000	1	1	9.48
117362	Single top t-channel	AcerMC/PYTHIA	293499	1	1	9.48
108346	Single top Wt inclusive	MC@NLO/Jimmy	1999194	1	1	22.37
110001	$t\bar{t}$ with lepton filter	MC@NLO/Jimmy	9988449	1	0.105	252.89
105200	$t\bar{t}$ with lepton filter	MC@NLO/Jimmy	14990603	1	0.543	252.89
105204	$t\bar{t}$ all hadronic	MC@NLO/Jimmy	1199990	1	0.457	252.89

Table A.1 MC samples used to model single top, and $t\bar{t}$ production. Separate $t\bar{t}$ samples are produced for fully leptonic decays and all hadronic decays to reduce overlap between samples. The MCID refer to the identification number of the sample as given by the ATLAS Monte Carlo production framework.

MCID	Process	Generator	N_{events}	k-factor	$\varepsilon_{\text{filter}}$	cross section [pb]
110805	$Z \to ee + 0$ partons	Alpgen/PYTHIA	604398	1.18	1	15.107
110806	$Z \to ee + 1$ parton	Alpgen/PYTHIA	260000	1.18	1	7.2131
110807	$Z \to ee + 2$ partons	Alpgen/PYTHIA	110000	1.18	1	3.032
110808	$Z \to ee + 3$ partons	Alpgen/PYTHIA	40000	1.18	1	1.1767
110809	$Z \to \mu\mu + 0$ partons	Alpgen/PYTHIA	600000	1.18	1	15.115
110810	$Z \to \mu\mu + 1$ parton	Alpgen/PYTHIA	265000	1.18	1	7.198
110811	$Z \to \mu\mu + 2$ partons	Alpgen/PYTHIA	115000	1.18	1	3.0303
110812	$Z \to \mu\mu + 3$ partons	Alpgen/PYTHIA	40000	1.18	1	1.1738
110813	$Z \to \tau\tau + c\bar{c} + 0$ partons	Alpgen/PYTHIA	599999	1.18	1	15.119
110814	$Z \to \tau\tau + c\bar{c} + 1$ partons	Alpgen/PYTHIA	265000	1.18	1	7.2016
110815	$Z \to \tau\tau + c\bar{c} + 2$ partons	Alpgen/PYTHIA	115000	1.18	1	3.0385
110816	$Z \to \tau\tau\ + 3$ partons	Alpgen/PYTHIA	40000	1.18	1	1.1677
110817	$Z \to ee + \bar{b} + 0$ partons	Alpgen/PYTHIA	150000	1.18	1	8.0397
110818	$Z \to ee + \bar{b} + 1$ parton	Alpgen/PYTHIA	80000	1.18	1	3.2353
110819	$Z \to ee + \bar{b} + 2$ partons	Alpgen/PYTHIA	45000	1.18	1	1.1388
110820	$Z \to ee + \bar{b} + 3$ partons	Alpgen/PYTHIA	4500	1.18	1	0.49066

Continued on next page

110821	$Z \rightarrow \mu\mu + b\bar{b} + 0$ partons	Alpgen/PYTHIA	150000	1.18	1	8.0422
110822	$Z \rightarrow \mu\mu + b\bar{b} + 1$ parton	Alpgen/PYTHIA	80000	1.18	1	3.2155
110823	$Z \rightarrow \mu\mu + b\bar{b} + 2$ partons	Alpgen/PYTHIA	45000	1.18	1	1.14
110824	$Z \rightarrow \mu\mu + b\bar{b} + 3$ partons	Alpgen/PYTHIA	5000	1.18	1	0.50943
110825	$Z \rightarrow \tau\tau + \bar{b} + 0$ partons	Alpgen/PYTHIA	150000	1.18	1	8.0358
110826	$Z \rightarrow \tau\tau + \bar{b} + 0$ partons	Alpgen/PYTHIA	80000	1.18	1	3.2299
110827	$Z \rightarrow \tau\tau + \bar{b} + 0$ partons	Alpgen/PYTHIA	44999	1.18	1	1.1445
110828	$Z \rightarrow \tau\tau + \bar{b} + 0$ partons	Alpgen/PYTHIA	5000	1.18	1	0.49266
117650	$Z \rightarrow ee + 0$ partons	Alpgen/PYTHIA	6619984	1.18	1	718.89
117651	$Z \rightarrow ee + 1$ partons	Alpgen/PYTHIA	1329498	1.18	1	175.6
117652	$Z \rightarrow ee + 2$ partons	Alpgen/PYTHIA	404998	1.18	1	58.849
117653	$Z \rightarrow ee + 3$ partons	Alpgen/PYTHIA	109999	1.18	1	15.56
117654	$Z \rightarrow ee + 4$ partons	Alpgen/PYTHIA	30000	1.18	1	3.9322
117655	$Z \rightarrow ee + 5$ partons	Alpgen/PYTHIA	10000	1.18	1	1.1994
117660	$Z \rightarrow \mu\mu + 0$ partons	Alpgen/PYTHIA	6608490	1.18	1	718.91
117661	$Z \rightarrow \mu\mu + 1$ partons	Alpgen/PYTHIA	1334697	1.18	1	175.81
117662	$Z \rightarrow \mu\mu + 2$ partons	Alpgen/PYTHIA	404995	1.18	1	58.805
117663	$Z \rightarrow \mu\mu + 3$ partons	Alpgen/PYTHIA	110000	1.18	1	15.589

Continued on next page

117664	$Z \rightarrow \mu\mu + 4$ partons	Alpgen/PYTHIA	30000	1.18	1	3.9072
117665	$Z \rightarrow \mu\mu + 5$ partons	Alpgen/PYTHIA	10000	1.18	1	1.1933
117670	$Z \rightarrow \tau\tau + 0$ partons	Alpgen/PYTHIA	6615490	1.18	1	718.85
117671	$Z \rightarrow \tau\tau + 1$ partons	Alpgen/PYTHIA	1334998	1.18	1	175.83
117672	$Z \rightarrow \tau\tau + 2$ partons	Alpgen/PYTHIA	405000	1.18	1	58.63
117673	$Z \rightarrow \tau\tau + 3$ partons	Alpgen/PYTHIA	108999	1.18	1	15.508
117674	$Z \rightarrow \tau\tau + 4$ partons	Alpgen/PYTHIA	30000	1.18	1	3.9526
117675	$Z \rightarrow \tau\tau + 5$ partons	Alpgen/PYTHIA	10000	1.18	1	1.1805
145161	$Z \rightarrow ee + \gamma$	SHERPA	8844673	1.0	1	32.261
145162	$Z \rightarrow \mu\mu + \gamma$	SHERPA	9198579	1.0	1	32.317
126854	$Z \rightarrow \tau\tau + \gamma$	SHERPA	3999409	1.0	1	32.331

Table A.2 MC samples processes used to model $Z + X$.

MCID	Process	Generator	N_{events}	k-factor	$\varepsilon_{\text{filter}}$	cross section [pb]
107680	$W \rightarrow e\nu$+0 parton	Alpgen/Jimmy	3459718	1.19	1	8037.1
107681	$W \rightarrow e\nu$+1 parton	Alpgen/Jimmy	2499797	1.19	1	1579.2
107682	$W \rightarrow e\nu$+1 parton	Alpgen/Jimmy	3769889	1.19	1	477.2
107683	$W \rightarrow e\nu$+1 parton	Alpgen/Jimmy	1009965	1.19	1	133.93
107684	$W \rightarrow e\nu$+1 parton	Alpgen/Jimmy	249999	1.19	1	35.622
107685	$W \rightarrow e\nu$+1 parton	Alpgen/Jimmy	70000	1.19	1	10.553
107690	$W \rightarrow \mu\nu+0$	Alpgen/Jimmy	3469591	1.19	1	8040
107691	$W \rightarrow \mu\nu+1$ parton	Alpgen/Jimmy	2499893	1.19	1	1580.3
107692	$W \rightarrow \mu\nu+2$ parton	Alpgen/Jimmy	3769890	1.19	1	477.5
107693	$W \rightarrow \mu\nu+3$ parton	Alpgen/Jimmy	1009896	1.19	1	133.94
107694	$W \rightarrow \mu\nu+4$ parton	Alpgen/Jimmy	255000	1.19	1	35.636
107695	$W \rightarrow \mu\nu+5$ parton	Alpgen/Jimmy	20000	1.19	1	10.571
107700	$W \rightarrow \tau\nu+0$ parton	Alpgen/Jimmy	3364789	1.19	1	8035.8
107701	$W \rightarrow \tau\nu+1$ parton	Alpgen/Jimmy	2449991	1.19	1	1579.8
107702	$W \rightarrow \tau\nu+2$ parton	Alpgen/Jimmy	3719888	1.19	1	477.55
107703	$W \rightarrow \tau\nu+3$ parton	Alpgen/Jimmy	1009993	1.19	1	133.79
107704	$W \rightarrow \tau\nu+4$ parton	Alpgen/Jimmy	249898	1.19	1	35.583
107705	$W \rightarrow \tau\nu+5$ parton	Alpgen/Jimmy	65000	1.19	1	10.54

Table A.3 MC Samples used to measure $Z \rightarrow ee$+jets $Z \rightarrow \mu\mu+$ jets as an alternative to the AlpgenPythia samples. These samples are also used to measure the jet veto efficiency and calculating the jet veto scale factor.

MCID	Process	Generator	PDF	N_{events}	k-factor	$\varepsilon_{\text{filter}}$	cross section [pb]
126928	$W^+W^- \to e^+\bar{\nu}e^-\nu$	POWHEGBOX/PYTHIA8	CT10	299700	1	1	0.631
126929	$W^+W^- \to \mu^+\bar{\nu}e^-\nu$	POWHEGBOX/PYTHIA8	CT10	300000	1	1	0.631
126930	$W^+W^- \to \tau^+\bar{\nu}e^-\nu$	POWHEGBOX/PYTHIA8	CT10	299999	1	1	0.631
126931	$W^+W^- \to e^+\bar{\nu}mu^-\nu$	POWHEGBOX/PYTHIA8	CT10	299999	1	1	0.631
126932	$W^+W^- \to \mu^+\bar{\nu}\mu^-\nu$	POWHEGBOX/PYTHIA8	CT10	300000	1	1	0.631
126933	$W^+W^- \to \tau^+\bar{\nu}e^-\nu$	POWHEGBOX/PYTHIA8	CT10	300000	1	1	0.631
126934	$W^+W^- \to e^+\bar{\nu}\tau^-\nu$	POWHEGBOX/PYTHIA8	CT10	299996	1	1	0.631
126935	$W^+W^- \to \mu^+\bar{\nu}\tau^-\nu$	POWHEGBOX/PYTHIA8	CT10	299999	1	1	0.631
126936	$W^+W^- \to \tau^+\bar{\nu}\tau^-\nu$	POWHEGBOX/PYTHIA8	CT10	299999	1	1	0.631

Table A.4 MC Samples used to for the WW contribution. No additional lepton filters are used for these samples.

MCID	Process	Generator	PDF	N_{events}	k-factor	$\varepsilon_{\text{filter}}$	cross section [pb]
129477	$WZ \to e^+ \nu e^+ e^-$	POWHEGBOX/PYTHIA8	CT10	190000	1	0.29456	1.407
129478	$WZ \to e^+ \nu \mu^+ \mu^-$	POWHEGBOX/PYTHIA8	CT10	190000	1	0.35211	0.9382
129479	$WZ \to e^+ \nu \tau^+ \tau^-$	POWHEGBOX/PYTHIA8	CT10	76000	1	0.16682	0.1746
129480	$WZ \to \mu^+ \nu e^+ e^-$	POWHEGBOX/PYTHIA8	CT10	189999	1	0.29351	1.399
129481	$WZ \to \mu^+ \nu \mu^+ \mu^-$	POWHEGBOX/PYTHIA8	CT10	190000	1	0.35132	0.9537
129482	$WZ \to \mu^+ \nu \tau^+ \tau^-$	POWHEGBOX/PYTHIA8	CT10	76000	1	0.16863	0.1746
129483	$WZ \to \tau^+ \nu e^+ e^-$	POWHEGBOX/PYTHIA8	CT10	75400	1	0.14289	1.399
129484	$WZ \to \tau^+ \nu \mu^+ \mu^-$	POWHEGBOX/PYTHIA8	CT10	76000	1	0.18256	0.9382
129485	$WZ \to \tau^+ \nu \tau^+ \tau^-$	POWHEGBOX/PYTHIA8	CT10	19000	1	0.058517	0.1719
129486	$WZ \to e^- \nu e^+ e^-$	POWHEGBOX/PYTHIA8	CT10	189899	1	0.29694	0.9795
129487	$WZ \to e^- \nu \mu^+ \mu^-$	POWHEGBOX/PYTHIA8	CT10	190000	1	0.35302	0.639
129488	$WZ \to e^- \nu \tau^+ \tau^-$	POWHEGBOX/PYTHIA8	CT10	76000	1	0.15969	0.1125
129489	$WZ \to \mu^- \nu e^+ e^-$	POWHEGBOX/PYTHIA8	CT10	190000	1	0.29766	0.9359
129490	$WZ \to \mu^- \nu \mu^+ \mu^-$	POWHEGBOX/PYTHIA8	CT10	190000	1	0.35414	0.6488
129491	$WZ \to \mu^- \nu \tau^+ \tau^-$	POWHEGBOX/PYTHIA8	CT10	76000	1	0.16023	0.1125
129492	$WZ \to \tau^- \nu e^+ e^-$	POWHEGBOX/PYTHIA8	CT10	76000	1	0.14803	0.9359
129493	$WZ \to \tau^- \nu \mu^+ \mu^-$	POWHEGBOX/PYTHIA8	CT10	76000	1	0.18657	0.639
129494	$WZ \to \tau^- \nu \tau^+ \tau^-$	POWHEGBOX/PYTHIA8	CT10	19000	1	0.056651	0.1107

Table A.5 MC Samples used to measure WZ background. All samples are generated with POWHEGBOX and showered with PYTHIA8 using the AU2 tune of the CT10 PDF set. A cut is placed on all same-flavour-opposite sign pairs produced from the Z of $m_{\ell^-\ell^+} > 2m_{Z\to\ell^+\ell^-} + 250$ MeV. A multilepton filter is placed during production in athena (not at generator-level) requiring a minimum two leptons with a $p_{\text{T}}$of 5 GeVwithin a range of $|\eta| < 2.7$.

MCID	Process	Generator	PDF	N_{events}	k-factor	$\varepsilon_{\text{filter}}$	cross section [pb]
147806	$Z \rightarrow ee$ without lepton filter	POWHEGBOX/PYTHIA8	CT10	9994580	1	1	1109.9
147807	$Z \rightarrow \mu\mu$ without lepton filter	POWHEGBOX/PYTHIA8	CT10	9988282	1	1	1109.8

Table A.6 MC Samples used to measure $Z \rightarrow ee$+jets $Z \rightarrow \mu\mu$+ jets as an alternative to the AlpgenPythia samples. These samples are also used to measure the jet veto efficiency and calculating the jet veto scale factor.

MCID	Process	Generator	PDF	f_4^γ	f_4^Z	f_5^γ	f_5^Z	N_{events}	k-factor	$\varepsilon_{\text{filter}}$	cross section [pb]
147211	$ZZ \to \ell\ell\nu\bar{\nu}$, SM sample, up to 1 jet with ME+PS	SHERPA	CT10	0	0	0	0	199999	1	1	0.231574
147212	$ZZ \to \ell\ell\nu\bar{\nu}$, TGC sample, up to 1 jet with ME+PS	SHERPA	CT10	0.1	0	0	0	199799	1	1	1.0557
147213	$ZZ \to \ell\ell\nu\bar{\nu}$, TGC sample, up to 1 jet with ME+PS	SHERPA	CT10	0.1	0	0	0.1	394992	1	1	2.1111
147214	$ZZ \to \ell\ell\nu\bar{\nu}$, TGC sample, up to 1 jet with ME+PS	SHERPA	CT10	0.1	0.1	0.1	0.1	799396	1	1	5.4263

Table A.7 MC samples/processes used to model ZZ signal with anomalous triple gauge couplings. All samples are produced with SHERPA using the CT10 PDF set. The values of the couplings. In order to use the afterburner reweighting method, at least three samples must be used, one sample generated at the Standard Model point of , one sample with one coupling non-zero, and another sample with at least one coupling non-zero.

Appendix B

Uncertainty breakdowns of measured fiducial and total cross sections

This appendix gives the breakdowns of the uncertainties of the measured fiducial and total cross sections in the $ZZ \to e^-e^+\nu\bar{\nu}$ and $ZZ \to \mu^-\mu^+\nu\bar{\nu}$ sub-channels.

Uncertainty	$e^-e^+\nu\bar{\nu}$	$\mu^-\mu^+\nu\bar{\nu}$
statistical uncertainty	$^{+15.21\%}_{-14.23\%}$	$^{+14.91\%}_{-13.97\%}$
luminosity	$^{+3.94\%}_{-3.10\%}$	$^{+3.97\%}_{-3.16\%}$
electron identification	$^{+2.27\%}_{-1.72\%}$	$^{+0.00\%}_{-0.04\%}$
electron isolation	$^{+0.41\%}_{-0.31\%}$	$^{+0.00\%}_{-0.04\%}$
electron reconstruction	$^{+0.98\%}_{-0.74\%}$	$^{+0.00\%}_{-0.04\%}$
electron energy resolution	$^{+0.00\%}_{-0.07\%}$	$^{+0.00\%}_{-0.05\%}$
electron energy scale	$^{+0.07\%}_{-0.08\%}$	$^{+0.05\%}_{-0.06\%}$
muon momentum resolution	$^{+0.00\%}_{-0.04\%}$	$^{+0.19\%}_{-0.22\%}$
muon momentum scale	$^{+0.00\%}_{-0.04\%}$	$^{+0.34\%}_{-0.28\%}$
muon reconstruction efficiency	$^{+0.00\%}_{-0.06\%}$	$^{+0.97\%}_{-0.74\%}$
muon identification effieicney	$^{+0.00\%}_{-0.04\%}$	$^{+0.09\%}_{-0.08\%}$

muon isolation	$^{+0.00\%}_{-0.04\%}$	$^{+4.33\%}_{-3.29\%}$
- BJES	$^{+0.00\%}_{-0.04\%}$	$^{+0.00\%}_{-0.04\%}$
- CloseBy	$^{+0.00\%}_{-0.04\%}$	$^{+0.00\%}_{-0.04\%}$
- FlavorComp	$^{+3.20\%}_{-2.71\%}$	$^{+2.87\%}_{-2.18\%}$
- FlavorResponse	$^{+1.85\%}_{-1.51\%}$	$^{+1.75\%}_{-1.27\%}$
- NPVOffset	$^{+0.94\%}_{-0.72\%}$	$^{+0.94\%}_{-0.68\%}$
- MuOffset	$^{+0.34\%}_{-0.24\%}$	$^{+0.62\%}_{-0.48\%}$
- PileupPt	$^{+0.00\%}_{-0.04\%}$	$^{+0.00\%}_{-0.04\%}$
- PileupRho	$^{+1.90\%}_{-1.48\%}$	$^{+1.86\%}_{-1.38\%}$
- EtaIntercalibration_Modelling	$^{+2.47\%}_{-1.91\%}$	$^{+2.47\%}_{-1.84\%}$
- EtaIntercalibration_StatAndMethod	$^{+0.71\%}_{-0.55\%}$	$^{+0.69\%}_{-0.53\%}$
- EffectiveNP_1	$^{+1.45\%}_{-1.13\%}$	$^{+1.20\%}_{-0.88\%}$
- EffectiveNP_2	$^{+2.34\%}_{-1.88\%}$	$^{+2.30\%}_{-1.70\%}$
- EffectiveNP_3	$^{+1.03\%}_{-0.79\%}$	$^{+0.93\%}_{-0.66\%}$
- EffectiveNP_4	$^{+0.32\%}_{-0.26\%}$	$^{+0.28\%}_{-0.24\%}$
- EffectiveNP_5	$^{+0.46\%}_{-0.37\%}$	$^{+0.38\%}_{-0.31\%}$
- EffectiveNP_6restTerm	$^{+0.23\%}_{-0.20\%}$	$^{+0.19\%}_{-0.18\%}$
- SingleParticle_HighPt	$^{+0.00\%}_{-0.04\%}$	$^{+0.00\%}_{-0.04\%}$
jet energy scale (total)	$^{+5.82\%}_{-4.69\%}$	$^{+5.52\%}_{-4.11\%}$
jet energy resolution	$^{+3.22\%}_{-2.73\%}$	$^{+4.12\%}_{-3.19\%}$
jet vertex fraction	$^{+0.39\%}_{-0.31\%}$	$^{+0.35\%}_{-0.28\%}$
$E_{\mathrm{T}}^{\mathrm{miss}}$ resolution (soft terms)	$^{+0.71\%}_{-0.68\%}$	$^{+0.75\%}_{-0.61\%}$

$E_{\mathrm{T}}^{\mathrm{miss}}$ scale (soft terms)	+1.43% −1.24%	+1.47% −1.00%
trigger	+0.10% −0.09%	+0.75% −0.57%
electroweak corrections	+0.39% −0.28%	+0.42% −0.30%
MC generator difference	+1.08% −0.76%	+2.57% −1.81%
PDF		
C_{ZZ} statistical uncertainty	+2.50% −1.77%	+2.49% −1.76%
A_{ZZ} statistical uncertainty	+0.00% −0.04%	+0.00% −0.04%
WZ background - QCD scale	+1.62% −1.69%	+1.63% −1.67%
WZ background statistical uncertainty	+1.54% −1.69%	+1.43% −1.53%
$ZZ \to \ell\ell\ell'\ell'$ background statistical	+0.03% −0.07%	+0.05% −0.08%
WW background statistical uncertainty	+0.08% −0.10%	+0.09% −0.10%
WW background total systematic	+0.55% −0.55%	+0.60% −0.59%
$W+X$ background statistical uncertainty	+1.58% −1.56%	+0.00% −0.04%
$W+X$ background total systematic	+0.80% −0.80%	+0.00% −0.04%
$Z+X$ background statistical uncertainty	+0.00% −0.04%	+0.00% −0.04%
$Z+X$ background total systematic	+0.00% −0.06%	+0.00% −0.06%
total systematic uncertainty	+8.95% −7.58%	+9.59% −7.57%

Table B.1 Uncertainty breakdown of the fiducial cross section in the $ZZ \to e^-e^+\nu\bar{\nu}$ and $ZZ \to \mu^-\mu^+\nu\bar{\nu}$ sub-channels.

	$e^-e^+\nu\bar{\nu}$	$\mu^-\mu^+\nu\bar{\nu}$
statistical uncertainty	$^{+15.16\%}_{-14.19\%}$	$^{+14.88\%}_{-13.94\%}$
luminosity	$^{+3.90\%}_{-3.11\%}$	$^{+3.94\%}_{-3.17\%}$
electron identification	$^{+2.30\%}_{-1.79\%}$	$^{+0.00\%}_{-0.06\%}$
electron isolation	$^{+0.40\%}_{-0.32\%}$	$^{+0.00\%}_{-0.06\%}$
electron reconstruction	$^{+0.96\%}_{-0.75\%}$	$^{+0.00\%}_{-0.06\%}$
electron energy resolution	$^{+0.00\%}_{-0.09\%}$	$^{+0.00\%}_{-0.07\%}$
electron energy scale	$^{+2.63\%}_{-2.19\%}$	$^{+0.00\%}_{-0.14\%}$
muon momentum resolution	$^{+0.00\%}_{-0.06\%}$	$^{+0.18\%}_{-0.22\%}$
muon momentum scale	$^{+0.00\%}_{-0.06\%}$	$^{+0.34\%}_{-0.29\%}$
muon reconstruction efficiency	$^{+0.00\%}_{-0.08\%}$	$^{+0.95\%}_{-0.75\%}$
muon identification effieicney	$^{+0.00\%}_{-0.06\%}$	$^{+0.08\%}_{-0.10\%}$
muon isolation	$^{+0.00\%}_{-0.06\%}$	$^{+4.44\%}_{-3.48\%}$
- BJES	$^{+0.00\%}_{-0.06\%}$	$^{+0.00\%}_{-0.06\%}$
- CloseBy	$^{+0.00\%}_{-0.06\%}$	$^{+0.00\%}_{-0.06\%}$
- FlavorComp	$^{+1.55\%}_{-1.36\%}$	$^{+1.04\%}_{-0.77\%}$
- FlavorResponse	$^{+0.92\%}_{-0.77\%}$	$^{+0.68\%}_{-0.47\%}$
- NPVOffset	$^{+0.61\%}_{-0.48\%}$	$^{+0.19\%}_{-0.14\%}$
- MuOffset	$^{+0.00\%}_{-0.06\%}$	$^{+0.23\%}_{-0.20\%}$
- PileupPt	$^{+0.00\%}_{-0.06\%}$	$^{+0.00\%}_{-0.06\%}$
- PileupRho	$^{+0.92\%}_{-0.73\%}$	$^{+0.74\%}_{-0.54\%}$

- EtaIntercalibration_Modelling	$^{+0.96\%}_{-0.73\%}$	$^{+0.61\%}_{-0.41\%}$
- EtaIntercalibration_StatAndMethod	$^{+0.34\%}_{-0.28\%}$	$^{+0.26\%}_{-0.21\%}$
- EffectiveNP_1	$^{+0.73\%}_{-0.58\%}$	$^{+0.40\%}_{-0.28\%}$
- EffectiveNP_2	$^{+1.07\%}_{-0.87\%}$	$^{+0.86\%}_{-0.61\%}$
- EffectiveNP_3	$^{+0.49\%}_{-0.38\%}$	$^{+0.31\%}_{-0.21\%}$
- EffectiveNP_4	$^{+0.12\%}_{-0.12\%}$	$^{+0.02\%}_{-0.09\%}$
- EffectiveNP_5	$^{+0.21\%}_{-0.19\%}$	$^{+0.09\%}_{-0.11\%}$
- EffectiveNP_6restTerm	$^{+0.10\%}_{-0.11\%}$	$^{+0.03\%}_{-0.10\%}$
- SingleParticle_HighPt	$^{+0.00\%}_{-0.06\%}$	$^{+0.00\%}_{-0.06\%}$
jet energy scale (total)	$^{+2.74\%}_{-2.26\%}$	$^{+1.90\%}_{-1.38\%}$
jet energy resolution	$^{+0.54\%}_{-0.60\%}$	$^{+0.86\%}_{-0.61\%}$
jet vertex fraction	$^{+0.14\%}_{-0.13\%}$	$^{+0.06\%}_{-0.09\%}$
$E_{\mathrm{T}}^{\mathrm{miss}}$ resolution (soft terms)	$^{+0.69\%}_{-0.67\%}$	$^{+0.74\%}_{-0.61\%}$
$E_{\mathrm{T}}^{\mathrm{miss}}$ scale (soft terms)	$^{+1.40\%}_{-1.26\%}$	$^{+1.45\%}_{-1.00\%}$
trigger	$^{+0.09\%}_{-0.10\%}$	$^{+0.73\%}_{-0.58\%}$
electroweak corrections	$^{+0.38\%}_{-0.28\%}$	$^{+0.41\%}_{-0.31\%}$
MC generator difference	$^{+1.06\%}_{-0.78\%}$	$^{+2.52\%}_{-1.85\%}$
PDF	$^{+0.71\%}_{-0.78\%}$	$^{+0.62\%}_{-0.72\%}$
C_{ZZ} statistical uncertainty	$^{+2.67\%}_{-1.95\%}$	$^{+2.62\%}_{-1.92\%}$
A_{ZZ} statistical uncertainty	$^{+0.00\%}_{-0.06\%}$	$^{+0.00\%}_{-0.06\%}$
WZ background - QCD scale	$^{+1.59\%}_{-1.67\%}$	$^{+1.59\%}_{-1.67\%}$
WZ background statistical uncertainty	$^{+1.53\%}_{-1.64\%}$	$^{+1.43\%}_{-1.51\%}$

$ZZ \to \ell\ell\ell'\ell'$ background statistical	$^{+0.00\%}_{-0.08\%}$	$^{+0.00\%}_{-0.09\%}$
jet veto scale factor statistical uncertainty	$^{+0.12\%}_{-0.13\%}$	$^{+0.00\%}_{-0.07\%}$
WW background statistical uncertainty	$^{+0.06\%}_{-0.11\%}$	$^{+0.07\%}_{-0.12\%}$
WW background total systematic	$^{+0.54\%}_{-0.55\%}$	$^{+0.59\%}_{-0.60\%}$
$W+X$ background statistical uncertainty	$^{+1.56\%}_{-1.57\%}$	$^{+0.00\%}_{-0.06\%}$
$W+X$ background total systematic	$^{+0.79\%}_{-0.80\%}$	$^{+0.00\%}_{-0.06\%}$
$Z+X$ background statistical uncertainty	$^{+0.00\%}_{-0.06\%}$	$^{+0.00\%}_{-0.06\%}$
$Z+X$ background total systematic	$^{+0.00\%}_{-0.08\%}$	$^{+0.00\%}_{-0.08\%}$
total systematic uncertainty	$^{+6.33\%}_{-5.54\%}$	$^{+6.82\%}_{-5.53\%}$

Table B.2 Uncertainty breakdown of the fiducial cross section in the $ZZ \to e^-e^+\nu\bar{\nu}$ and $ZZ \to \mu^-\mu^+\nu\bar{\nu}$ sub-channels with the jet veto scale factor applied to the $q\bar{q}$ component of C_{ZZ} for each sub-channel.

	$e^-e^+\nu\bar{\nu}$	$\mu^-\mu^+\nu\bar{\nu}$
statistical uncertainty	$^{+15.21\%}_{-14.23\%}$	$^{+14.91\%}_{-13.97\%}$
luminosity	$^{+3.96\%}_{-3.08\%}$	$^{+3.99\%}_{-3.14\%}$
electron identification	$^{+2.28\%}_{-1.71\%}$	$^{+0.14\%}_{-0.00\%}$
electron isolation	$^{+0.43\%}_{-0.28\%}$	$^{+0.14\%}_{-0.00\%}$
electron reconstruction	$^{+0.99\%}_{-0.73\%}$	$^{+0.14\%}_{-0.00\%}$
electron energy resolution	$^{+0.14\%}_{-0.00\%}$	$^{+0.14\%}_{-0.00\%}$
electron energy scale	$^{+2.67\%}_{-2.12\%}$	$^{+0.29\%}_{-0.00\%}$

muon momentum resolution	$^{+0.14\%}_{-0.00\%}$	$^{+0.24\%}_{-0.17\%}$
muon momentum scale	$^{+0.14\%}_{-0.00\%}$	$^{+0.37\%}_{-0.24\%}$
muon reconstruction efficiency	$^{+0.20\%}_{-0.00\%}$	$^{+1.00\%}_{-0.72\%}$
muon identification effieicney	$^{+0.14\%}_{-0.00\%}$	$^{+0.17\%}_{-0.00\%}$
muon isolation	$^{+0.14\%}_{-0.00\%}$	$^{+4.34\%}_{-3.28\%}$
- BJES	$^{+0.17\%}_{-0.00\%}$	$^{+0.17\%}_{-0.00\%}$
- CloseBy	$^{+0.15\%}_{-0.00\%}$	$^{+0.15\%}_{-0.00\%}$
- FlavorComp	$^{+3.22\%}_{-2.69\%}$	$^{+2.88\%}_{-2.16\%}$
- FlavorResponse	$^{+1.86\%}_{-1.50\%}$	$^{+1.76\%}_{-1.26\%}$
- NPVOffset	$^{+0.95\%}_{-0.71\%}$	$^{+0.95\%}_{-0.67\%}$
- MuOffset	$^{+0.37\%}_{-0.20\%}$	$^{+0.64\%}_{-0.46\%}$
- PileupPt	$^{+0.14\%}_{-0.00\%}$	$^{+0.14\%}_{-0.00\%}$
- PileupRho	$^{+1.91\%}_{-1.47\%}$	$^{+1.87\%}_{-1.37\%}$
- EtaIntercalibration_Modelling	$^{+2.49\%}_{-1.90\%}$	$^{+2.48\%}_{-1.83\%}$
- EtaIntercalibration_StatAndMethod	$^{+0.73\%}_{-0.53\%}$	$^{+0.70\%}_{-0.52\%}$
- EffectiveNP_1	$^{+1.46\%}_{-1.11\%}$	$^{+1.21\%}_{-0.87\%}$
- EffectiveNP_2	$^{+2.36\%}_{-1.87\%}$	$^{+2.31\%}_{-1.69\%}$
- EffectiveNP_3	$^{+1.05\%}_{-0.77\%}$	$^{+0.95\%}_{-0.65\%}$
- EffectiveNP_4	$^{+0.35\%}_{-0.22\%}$	$^{+0.31\%}_{-0.20\%}$
- EffectiveNP_5	$^{+0.49\%}_{-0.34\%}$	$^{+0.40\%}_{-0.28\%}$

- EffectiveNP_6restTerm	$^{+0.28\%}_{-0.14\%}$	$^{+0.24\%}_{-0.12\%}$
- SingleParticle_HighPt	$^{+0.14\%}_{-0.00\%}$	$^{+0.14\%}_{-0.00\%}$
jet energy scale (total)	$^{+5.88\%}_{-4.64\%}$	$^{+.\%}_{-.\%}$
jet energy resolution	$^{+3.24\%}_{-2.72\%}$	$^{+4.13\%}_{-3.18\%}$
jet vertex fraction	$^{+0.42\%}_{-0.28\%}$	$^{+0.38\%}_{-0.24\%}$
$E_{\mathrm{T}}^{\mathrm{miss}}$ resolution (soft terms)	$^{+0.73\%}_{-0.66\%}$	$^{+0.77\%}_{-0.59\%}$
$E_{\mathrm{T}}^{\mathrm{miss}}$ scale (soft terms)	$^{+1.44\%}_{-1.22\%}$	$^{+1.48\%}_{-0.99\%}$
trigger	$^{+0.18\%}_{-0.00\%}$	$^{+0.76\%}_{-0.55\%}$
electroweak corrections	$^{+0.69\%}_{-0.48\%}$	$^{+0.74\%}_{-0.53\%}$
MC generator difference	$^{+1.09\%}_{-0.75\%}$	$^{+2.58\%}_{-1.81\%}$
QCD scale ($q\bar{q}$ only)	$^{+1.52\%}_{-1.28\%}$	$^{+1.67\%}_{-1.15\%}$
PDF	$^{+2.12\%}_{-1.44\%}$	$^{+2.00\%}_{-1.40\%}$
parton shower	$^{+4.92\%}_{-3.57\%}$	$^{+4.08\%}_{-3.00\%}$
C_{ZZ} statistical uncertainty	$^{+2.51\%}_{-1.76\%}$	$^{+2.50\%}_{-1.75\%}$
A_{ZZ} statistical uncertainty	$^{+1.33\%}_{-0.94\%}$	$^{+1.35\%}_{-0.97\%}$
WZ background - QCD scale	$^{+1.65\%}_{-1.67\%}$	$^{+1.64\%}_{-1.66\%}$
WZ background statistical uncertainty	$^{+1.56\%}_{-1.67\%}$	$^{+1.45\%}_{-1.52\%}$
$ZZ \to \ell\ell\ell'\ell'$ background statistical	$^{+0.15\%}_{-0.00\%}$	$^{+0.15\%}_{-0.00\%}$
WW background statistical uncertainty	$^{+0.16\%}_{-0.00\%}$	$^{+0.17\%}_{-0.00\%}$
WW background total systematic	$^{+0.58\%}_{-0.53\%}$	$^{+0.62\%}_{-0.58\%}$

$W+X$ background statistical uncertainty	$^{+1.60\%}_{-1.54\%}$	$^{+0.14\%}_{-0.00\%}$
$W+X$ background total systematic	$^{+0.82\%}_{-0.78\%}$	$^{+0.14\%}_{-0.00\%}$
$Z+X$ background statistical uncertainty	$^{+0.14\%}_{-0.00\%}$	$^{+0.14\%}_{-0.00\%}$
$Z+X$ background total systematic	$^{+0.20\%}_{-0.00\%}$	$^{+0.20\%}_{-0.00\%}$
total systematic uncertainty	$^{+10.58\%}_{-8.65\%}$	$^{+10.78\%}_{-8.40\%}$

Table B.3 Uncertainty breakdown of the total cross section in the $ZZ \to e^-e^+\nu\bar{\nu}$ and $ZZ \to \mu^-\mu^+\nu\bar{\nu}$ sub-channels.

	$e^-e^+\nu\bar{\nu}$	$\mu^-\mu^+\nu\bar{\nu}$
statistical uncertainty	$^{+15.16\%}_{-14.19\%}$	$^{+14.88\%}_{-13.94\%}$
luminosity	$^{+3.92\%}_{-3.10\%}$	$^{+3.96\%}_{-3.16\%}$
electron identification	$^{+2.31\%}_{-1.79\%}$	$^{+0.02\%}_{-0.00\%}$
electron isolation	$^{+0.41\%}_{-0.31\%}$	$^{+0.02\%}_{-0.00\%}$
electron reconstruction	$^{+0.96\%}_{-0.75\%}$	$^{+0.02\%}_{-0.00\%}$
electron energy resolution	$^{+0.04\%}_{-0.06\%}$	$^{+0.04\%}_{-0.02\%}$
electron energy scale	$^{+2.64\%}_{-2.18\%}$	$^{+0.10\%}_{-.\%}$
muon momentum resolution	$^{+0.02\%}_{-0.00\%}$	$^{+0.20\%}_{-0.21\%}$
muon momentum scale	$^{+0.02\%}_{-0.00\%}$	$^{+0.34\%}_{-0.28\%}$
muon reconstruction efficiency	$^{+0.03\%}_{-0.00\%}$	$^{+0.96\%}_{-0.75\%}$
muon identification effieicney	$^{+0.02\%}_{-0.00\%}$	$^{+0.10\%}_{-0.07\%}$
muon isolation	$^{+0.02\%}_{-0.00\%}$	$^{+4.46\%}_{-3.48\%}$

- BJES	+0.03% −0.01%	+0.03% −0.02%
- CloseBy	+0.01% −0.00%	+0.01% −0.00%
- FlavorComp	+1.56% −1.35%	+1.04% −0.76%
- FlavorResponse	+0.93% −0.76%	+0.68% −0.47%
- NPVOffset	+0.61% −0.47%	+0.20% −0.12%
- MuOffset	+0.05% −0.00%	+0.24% −0.19%
- PileupPt	+0.03% −0.00%	+0.03% −0.00%
- PileupRho	+0.92% −0.73%	+0.75% −0.54%
- EtaIntercalibration_Modelling	+0.97% −0.73%	+0.62% −0.41%
- EtaIntercalibration_StatAndMethod	+0.34% −0.27%	+0.27% −0.20%
- EffectiveNP_1	+0.74% −0.57%	+0.40% −0.27%
- EffectiveNP_2	+1.07% −0.86%	+0.86% −0.61%
- EffectiveNP_3	+0.49% −0.37%	+0.32% −0.20%
- EffectiveNP_4	+0.13% −0.10%	+0.07% −0.07%
- EffectiveNP_5	+0.22% −0.18%	+0.11% −0.09%
- EffectiveNP_6restTerm	+0.12% −0.09%	+0.08% −0.07%
- SingleParticle_HighPt	+0.02% −0.00%	+0.02% −0.00%
jet energy scale (total)	+2.75% −2.24%	+1.92% −1.36%
jet energy resolution	+0.55% −0.59%	+0.86% −0.60%
jet vertex fraction	+0.15% −0.11%	+0.09% −0.06%
$E_{\mathrm{T}}^{\mathrm{miss}}$ resolution (soft terms)	+0.70% −0.67%	+0.74% −0.61%
$E_{\mathrm{T}}^{\mathrm{miss}}$ scale (soft terms)	+1.41% −1.25%	+1.46% −1.00%

trigger	$^{+0.11\%}_{-0.08\%}$	$^{+0.74\%}_{-0.57\%}$
electroweak corrections	$^{+0.68\%}_{-0.50\%}$	$^{+0.73\%}_{-0.55\%}$
MC generator difference	$^{+1.07\%}_{-0.78\%}$	$^{+2.53\%}_{-1.85\%}$
QCD scale ($q\bar{q}$ only)	$^{+1.50\%}_{-1.30\%}$	$^{+1.66\%}_{-1.16\%}$
PDF	$^{+2.00\%}_{-1.53\%}$	$^{+1.84\%}_{-1.47\%}$
parton shower	$^{+4.89\%}_{-3.60\%}$	$^{+4.06\%}_{-3.02\%}$
C_{ZZ} statistical uncertainty	$^{+2.68\%}_{-1.95\%}$	$^{+2.63\%}_{-1.92\%}$
A_{ZZ} statistical uncertainty	$^{+1.32\%}_{-0.96\%}$	$^{+1.33\%}_{-0.98\%}$
WZ background - QCD scale	$^{+1.61\%}_{-1.65\%}$	$^{+1.61\%}_{-1.65\%}$
WZ background statistical uncertainty	$^{+1.55\%}_{-1.63\%}$	$^{+1.44\%}_{-1.50\%}$
$ZZ \rightarrow \ell\ell\ell'\ell'$ background statistical	$^{+0.06\%}_{-0.05\%}$	$^{+0.07\%}_{-0.06\%}$
jet veto SF statistical uncertainty	$^{+0.14\%}_{-0.11\%}$	$^{+0.05\%}_{-0.03\%}$
WW background statistical uncertainty	$^{+0.09\%}_{-0.08\%}$	$^{+0.10\%}_{-0.09\%}$
WW background total systematic	$^{+0.55\%}_{-0.55\%}$	$^{+0.60\%}_{-0.59\%}$
$W+X$ background statistical uncertainty	$^{+1.58\%}_{-1.56\%}$	$^{+0.02\%}_{-0.00\%}$
$W+X$ background total systematic	$^{+0.80\%}_{-0.79\%}$	$^{+0.02\%}_{-0.00\%}$
$Z+X$ background statistical uncertainty	$^{+0.02\%}_{-0.00\%}$	$^{+0.02\%}_{-0.00\%}$
$Z+X$ background total systematic	$^{+0.03\%}_{-0.00\%}$	$^{+0.03\%}_{-0.00\%}$
total systematic uncertainty	$^{+8.45\%}_{-6.95\%}$	$^{+8.39\%}_{-6.62\%}$

Table B.4 Uncertainty breakdown of the total cross section in the $ZZ \rightarrow e^-e^+\nu\bar{\nu}$ and $ZZ \rightarrow \mu^-\mu^+\nu\bar{\nu}$ sub-channels with the jet veto scale to the $q\bar{q}$ component of C_{ZZ} for each sub-channel.